AN EXPERIMENTAL AND COMPUTATIONAL STUDY ON CO-CURED METAL−POLYMER MATRIX COMPOSITE INTERFACES IN HIGH TEMPERATURE HYBRID LAMINATES

A Dissertation

by

HIEU THI XUAN TRUONG

Submitted to the Office of Graduate and Professional Studies of
Texas A&M University
in partial fulfillment of the requirements for the degree of

DOCTOR OF PHILOSOPHY

Chair of Committee,	Ozden O. Ochoa
Co-Chair of Committee,	Dimitris C. Lagoudas
Committee Members,	J.N. Reddy
	Ibrahim Karaman
Head of Department,	Andreas A. Polycarpou

May 2016

Major Subject: Mechanical Engineering

ABSTRACT

Due to the increasing needs for lightweight and multifunctional materials and structures that can perform in extreme environment such as high temperature and pressure, hybrid composite laminates that are comprised of both metallic and polymeric constituents are under development. Because of the mismatch in properties of different layers in these hybrid laminates, the interfacial regions between polymer and metal are critical for durability and reliability. The objective of this work is to develop a robust and multifunctional interface between metallic foils and carbon fabric reinforced polymer matrix composite (PMC) for hybrid materials that can maintain mechanical properties at high temperature temperature, i.e. up to 200 - 300 ^oC. The major focus of this Ph.D. dissertation is the fabrication and characterization of the high temperature hybrid interface between Ti/NiTi with high temperature thermosetting polymer matrix composites. Approaches derived from experimental techniques for manufacturing and characterizing are utilized. In particular, the highlight of this work is the employment of the novel laser ablation method in combination with a custom-synthesized sol-gel treatment technique to prepare the surfaces of metallic foils for strong adhesion with the polymer matrix composites. The mode I and mode II fracture toughness of the hybrid interfaces is characterized at various temperatures up to the glass transition temperature onset of the polymer matrix. To achieve this, the double cantilever beam (DCB) and four-point end notch flexure (4-ENF) tests were performed. In-situ distributed strain measurements using Rayleigh back-scattered fiber optics and digital image correlation (DIC) are carried out during the fracture toughness tests at both room and elevated temperatures. Extensive characterization of the hybrid interface cross-section is performed using optical mi-

croscopy, scanning electron microscopy/energy dispersive spectroscopy and atomic force microscopy/nano-infrared spectra analysis. Other thermal-mechanical characterization methods employed in this work include dynamic mechanical analysis, thermomechanical analyzer, differential scanning calorimetry, and thermal gravimetric analysis. Finite element analyses (FEA) are conducted in parallel with experiments to provide assistance to understanding the fracture behavior of the hybrid metal-composite interfaces. The virtual crack closure technique with mixed-mode fracture criterions is used to model crack propagation in double cantilever beams. The influence of thermal residual stress due to curing on the crack growth at the hybrid interface is investigated. The effect of laser ablated pattern on the fracture behavior of the hybrid interfaces is studied via the extended finite element method (XFEM).

DEDICATION

To my loved ones

ACKNOWLEDGEMENTS

I am happy to have another chance to reflect on what has happened in my life and to whom I am grateful.

My first and foremost thanks are to my advisors, Professors Ozden O. Ochoa and Dimitris C. Lagoudas for their impeccable guidance. They are the best advisors I could ever ask for. Professor Ochoa has led me from a novice undergraduate student to who I am today. Her technical challenges set the bar high for me. She constantly provided me support both academically and emotionally through all the difficult times during my Ph.D. study. Professor Lagoudas has always made me feel special, thanks to his high expectation, encouragement and generosity. His advice has many times broadened my view and will have long-lasting impacts on me. As an old saying goes "no pain no gain", this dissertation, however modest it is, would have been much worse without the challenges my advisors have given me. Especially, I am thankful to both of them for giving me a big academic family, from which I received tremendous support throughout the years.

I also thank Professors J.N. Reddy and Ibrahim Karaman for being so kind to serve as my Ph.D. committee members and their help during the years. Dr. Reddy has taught me two courses in finite element analysis, which my research greatly benefits from. Dr. Karaman's recommendation helped me to obtain the NASA NSTRF and Amelia Earhart fellowships.

I am grateful to Dr. Miladin Radovic for serving in Dr. Karaman's role during my defense and his especially enjoyable class in Ceramics Materials. Sincere thanks are also extended to Dr. Terry Creasy and Dr. H.J. Sue. Dr. Creasy, besides a fantastic professor of Composite Materials class, was instrumental in establishing the Society

for the Advanced Materials and Process Engineering (SAMPE) student chapter at Texas A & M. My activities with SAMPE have been a rewarding experience, for which I received the SAMPE Student Leadership and the University Research Symposium awards to attend two prestigious SAMPE conferences. Dr. Sue's class in Fracture of Polymers plays an essential role in my research. I am indebted to his class for the explanation of the glass and sub-glass transitions in this dissertation. He has many times generously allowed me to use his laboratory for characterizations using thermal gravimetric analyzer and laser confocal microscope. I also thank my friends and classmates, Spencer Hawkins and Peng Liu, who many times helped me with using those equipments and shared with me their knowledge and experience about polymers and experimental characterization techniques.

My five years at Texas A & M have been a vivid experience. I am grateful to everyone who made it happened: my professors, classmates, officemates, and many friends. I put here a random list of people who wasted their time to entertain me academically and non-academically (I would be surprised if I didn't forget some important names). They are my academic brothers: Dr. Brian Lester, Edwin Peraza-Hernandez, Dr. Majid Tabesh, Dr. Frank Gardea, John Rohmer, Mahdi Mohajer, Sameer Jape, and Dr. Norimichi Nanami, who, despite their "wicked" nature, have been real gentlemen to me. They are my friends and collaborators from the AFOSR MURI team, Dr. Ross McLendon, Dr. Yu-Hung Li, and Dr. Ankush Kothalkar, whom I worked with and learned from tremendously. They also include my Vietnamese fellows, with whom I share endless passions for food and nonsense jokes/rumors.

My time at Texas A & M was divided between Departments of Mechanical Engineering and Aerospace Engineering. I am thankful to both departments for their hospitality. I have been also fortunate to have a chance to visit and perform re-

search at several places during my Ph.D.: Structures and Composite Laboratory at Stanford University, the Structural Integrity & Composites Laboratory at the Delft University of Technology, and NASA Langley Research Center. My Ph.D. research and research visits would not have been made possible without various financial supports. I am grateful for the generous support by the NASA Space Technology Research Fellowship Grant No. NNX14AM41H, the AFOSR MURI Award No. FA9550-09-1-0686, the International Institute for Multifunctional Materials for Energy Conversion (IIMEC) established by NSF Grant No. DMR-0844082 as well as Zonta International Amelia Earhart fellowship.

My mentor at NASA, Dr. John Connell is definitely one of the nicest persons I have ever met. No word can describe how fortunate I am to have met him. Many results in this dissertation are only possible due to his unrivaled expertise. My second mentor Dr. Frank Palmieri and NSTRF program coordinator at NASA LaRC, Dr. Liz Ward also deserve my special thanks for what they had done for me.

NASA Langley research center, where I have spent six months last year, was my true home. Everyone there was friendly and wonderful. I especially mention here my cheerful and helpful crew: Hoa Luong, Sean Briton, John Hopkins, Clay Claytor, Jim Baughman and Crystal Chamberlain. They were not only of great assistance but also true friends that lighted me up from the depression of constant failures. I will carry the fun memories with them for the rest of my life.

Another person that I owe so much is Dr. Marcias Martinez, who was my mentor at TU Delft. From him, I have learned so many interesting experimental and computational techniques. I also thank the TU Delft Faculty of Aerospace Engineering, especially the Structural Integrity & Composites Laboratory for a fantastic three-month research visit. At TU Delft, I met many wonderful friends: Dr. Lars Bernhammer, Dr. Liaojun Yao, Lei Shi, Illias Tapeinos, Fabricio Abelha, Wandong

Wang, Niels Reurings, Lucas Amaral, and Thang Nguyen. Thanks to them, I had an opportunity to experience the authentic European culture: biking around the city in Delft, experiencing the German Christmas market and Gluhwein in Munster for the first time, just to name a few.

Twenty six years ago, I was born into a family of working class parents. They have labored so hard to give me the best opportunities. They, together with my brother and grandmother, have been with me through ups and downs. They are the anchors for me to fly high. Deep from my heart, this dissertation is dedicated to them.

I am also thankful to my husband, who has been the shoulder for me to lean on through the years, for his unconditional love and support. Without him, this work would not have been completed.

At the age of seventeen, I came to the US as a high school foreign exchange student. After one semester, an unfortunate incident almost sent me homeless. I was, fortunately, rescued by my kind-hearted teacher and his beautiful wife. Dennis and Linda, thank you for giving me a true American family.

Finally, I want to honor an old man, who was my best friend and first teacher on everything. He fought so hard to see the day I receive a doctoral degree. He did not make it. However, Grandpa, I am sure that you are very much happy and proud of me now.

NOMENCLATURE

DCB	Double Cantilever Beam
4-ENF	Four-point End Notched Flexure
SMA	Shape Memory Alloys
CFRP	Carbon Fiber/Fabric Reinforced Polymer
PMC	Polymer Matrix Composites
FEA	Finite Element Analysis
TGA	Thermal Gravimetric Analysis
DMA	Dynamic Mechanical Analysis
TMA	Thermal Mechanical Analysis
DSC	Differential Scanning Calorimetry
T_g	Glass transition temperature
AFM	Atomic Force Microscope
OM	Optical Microscope
SEM	Scanning Electron Microscope
FTIR	Fourier Transform Infrared Spectroscopy

TABLE OF CONTENTS

Page

LIST OF FIGURES

FIGURE Page

LIST OF TABLES

1. INTRODUCTION

1.1 Motivation and Background

Recent needs in developing technologies for aerospace vehicles necessitate lightweight and multifunctional structures and materials. Due to high operating speeds and the harsh environment surrounding the space vehicles, the entire structure has to undergo and be able to sustain the extreme conditions such as high temperature and high pressure. To satisfy the lightweight and structural integrity requirements, hybrid composites fabricated with ceramics, metal and polymer matrix composite (PMC) as well as nano-engineered materials are of significant interest and consideration in the design of these space vehicles.

Ceramics are well known for their chemically inert and heat resistant abilities while polymeric composites are famous for their high strength and stiffness as well as good corrosion resistance [7, 8, 9, 10]. Intermetallic shape memory alloys (SMAs) are increasingly utilized in actuation applications and aerospace structures where super elasticity and shape memory capability are of high benefits [11, 12]. Assembling SMA to the hybrid structure between ceramics and PMC can bring other advantages such as improved damping capability as well as addition of smart and active characteristics [13, 14]. Furthermore, when the composite material is composed of ceramic, SMA and PMC layers, where the ceramic is used as the skin and the PMC in the innermost layer, there is a thermal gradient throughout the entire material structure so that the structural functionality of the PMC can still be attained at temperature below the glass transition temperature of the matrix.

In addition, novel composite laminates where shape memory alloy foils are embedded inside polymer matrix composites are of significant interest for smart and

morphing applications [11, 15, 16, 17, 18, 19]. Beyond morphing capabilities, these unique material systems also imbue the structure with high damping capabilities, a tangible benefit by itself. Ogisu *et al.* investigated the use of embedded SMA foil in carbon fiber reinforced plastics (CFRP) for damage suppression [20]. In hybrid SMA-PMC composites, its active character is associated with thermo-mechanically induced phase transformation of the SMA constituent. Specifically, at elevated temperatures, the material has an austentitic structure while at lower temperatures a martensitic configuration is present [11]. Transforming between these two states may be accomplished through purely thermal loadings which leads to different thermoelastic properties as well as inelastic strains in the two conditions. Regardless of these differences, the structural integrity of the hybrid laminates must be maintained at both low (often room temperature) and elevated (typically 40-100 ^oC) temperatures.

In these hybrid systems, the interface between SMA and PMC is one of the most critical considerations for reliability. The interface has to be robust and able to maintain its functions at the operating temperatures and under cyclic loading. There has been a considerable amount of work done on adhesive joining reported in the literature [21, 22, 23, 24, 25, 26, 27, 28, 29, 30, 31, 32, 33]. However, there are limitations on the strength and temperature range of the currently available structural adhesives. In addition, structures created by adhesively joining metal and composite parts have two distinct interfaces, one is between the metal and the adhesive, and the other is between the composite and adhesive. Thus, significant efforts need to be made to control these interfaces for structural integrity.

In order create robust interfaces, the interfacial behaviors should be understood so that the interfaces/interphases can be tailored for better adhesion. The mechanisms of interfacial adhesion can be categorized into four categories: physical, chemical, diffusion bonding, and mechanical interlocking [34]. Of these, the most common method

to bond metal and polymer substrates is mechanical interlocking, although this bonding is rather weak. Chemical bonding provides the highest strength of the four listed; however, it is often difficult to obtain. Often, oxide layers are presented on the metallic surfaces and remain in the interfaces with polymer [35, 36, 37, 38, 39, 40, 41]. The oxide degrades at high temperature and can bring defects to the interface. Titanium and SMAs oxide layers can serve as crack initiators when the hybrid structures operate at elevated temperatures. Thus, surface treatment of the metallic components needs to be done properly prior to joining to polymeric structural components to reduce degradation and delamination of the hybrid interfaces at elevated temperature.

Molitor reviewed different surface treatment techniques employed for titanium alloy surfaces [42]. Traditional mechanical abrasion techniques such as sand and grit blasting as well as chemical methods like hydroxide and acid etching helps with the removal of the oxide layer on the metallic surface and create macro and micro roughness that facilitates mechanical interlocking adhesion. Laser and plasma etching techniques were reported to be the best to produce strong and durable adhesive joints. Sol-gel treatment on metallic surfaces such as aluminum, titanium and nickel-titanium alloys, which facilitates chemical bonding, developed by the Boeing Company [43] has been shown to be effective in creating strong and durable adhesive joints of metallic substrates. One successful application of the sol-gel surface treatment method is the adhesive joint of SMA actuator with polymer matrix composite in morphing structures as demonstrated in Zimmerman *et al.* [27]. The sol-gel treatment adds silane coupling agents to the metal surface thereby creating chemical bonding between the metal and silane group as well as between silane and polymer interfaces. Laser ablation is a new novel surface treatment technique that can be employed so that the use of toxic chemicals for acid etching can be eliminated and the surface roughness can be designed as patterns. Utilization of laser ablative sur-

face treatment method has been proved to improve the bond strength and durability in adhesive joints of titanium alloy [44, 45].

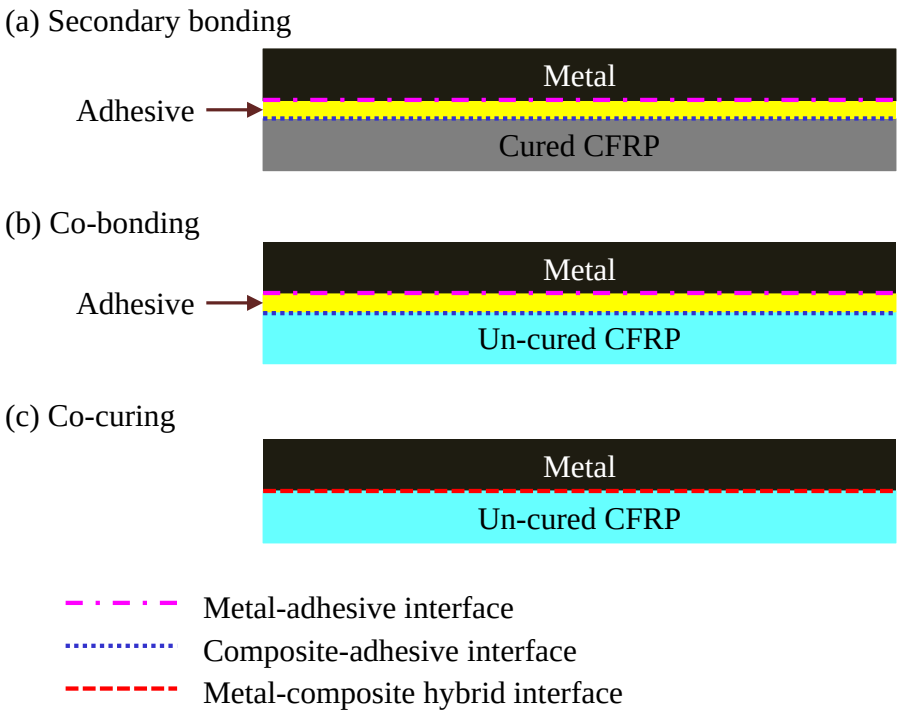

Figure 1.1: The hybrid joints between metallic and polymer matrix composite components (a) Secondary bonding. (b) Co-bonding. (c) Co-curing.

There are a variety of methods developed to join metallic to polymer matrix composites parts as illustrated in Figure 1.1. The most common method of joining is secondary bonding where the metallic part is bonded to a cured composite laminates with a layer of adhesive. In order to create a strong secondary bond, the surfaces of both the metallic and composite parts need to be pre-treated prior to bonding. Also, by undergoing the curing cycle of the adhesive, the metal and composite components

may be subjected to additional thermal residual stresses due to cooling from elevated temperature and changes in their thermal-mechanical properties. The second most common method is co-bonding where an adhesive is used to join the metal and uncured composite laminates. Using this method, both the adhesive and the composite undergo the same curing cycle and thus the additional changes in material properties issue is eliminated. However, in both of the discussed methods, there are two distinct interfaces, one between the metal and the adhesive, the other one between the adhesive and composite. To have a successful secondary-bonding or co-bonding joint, the development and use of a unique adhesive is required in order to form robust interfaces with both the metal and composite. By employing the co-curing method, where the metal is bonded directly to the composite without the use of an adhesive, both of the mentioned issues are eliminated. The hybrid joint created by this method is formed by adhesion between the metal and matrix of the composite. In order to have a strong hybrid co-cured joint, the metallic surface needs substantial pre-treatment before the bonding process takes place.

Regarding computational analyses, there has been a considerable amount of work reported in the literature modeling delamination and crack propagation in composites utilizing the virtual crack closure technique (VCCT) and cohesive zone method (CZM). The VCCT can differentiate between the different fracture modes (opening, scissoring and tearing) but cannot predict fracture initiation. The cohesive zone model, on the other hand, can facilitate predictions of where crack initiates as well as how it propagates. Krueger has done substantial work on using VCCT to model mode I, mode II as well as mixed mode delamination in composite laminates [46, 47]. Banea and colleagues have studied temperature-dependent fracture toughness of adhesive joints via both experimental and numerical investigation [25, 24, 26]. In their work, the interface was modeled with a cohesive zone. Viscoelastic and tempera-

ture dependent properties of the adhesive were taken into account. Banea's work, however, only dealt with adhesive joints of metal-to-metal such as stainless steel substrates. These adhesive joints were created by secondary bonding that required the use of high temperature adhesives. Mode I and mode II fracture toughness of co-cured hybrid Al/CFRP interface was studied experimentally and computationally by Ning *et al.* [48, 49]. The effect of nano-reinforcement (carbon nanofiber) on the improvement of fracture toughness was investigated in their work. However, they did not account for mode mixity presented at the hybrid interfaces during crack propagation nor considered the influence of elevated temperature on the fracture behavior of the interfaces.

There is published work on the influence of micro-roughness surfaces on adhesion and failure behavior of adhesive joints where the surface roughness of the substrates is presented [50, 51, 52]. Crack kinking due to surface roughness was studied by [50, 51]. Yao and Qu published a quantitative approach to predict the amount of cohesive failure in metal-polymer interface given a known surface roughness of the metallic part using analytical fracture mechanics [50]. They idealized the rough surface as a saw-tooth like profile. In their work, it was assumed that the crack first initiated at the metal-polymer interface due to weak adhesion and then kinked to the polymer. A crack kinking criteria was developed based on the calculated strain energy release rates of the interface and the polymer. Noijen *et al.* extended Yao and Qu's work and studied aluminum-epoxy interface using a numerical fracture mechanics approach [51]. They predicted the locations where the crack kinked from the interface into the polymer by performing a parametric study using finite element analysis of this interface. Similar to Yao and Qu's work, Noijen *et al.* also predicted crack kinking from calculation and comparison of the strain energy release rates. In both of the mentioned work, neither crack initiation nor propagation was modeled.

1.2 Research Objectives

In the present study, the objective is to understand the interfacial integrity of metal-carbon fiber reinforced polymer matrix composite at different temperatures via quasi-static testing.

Herein, the hybrid composite laminates are developed where metallic foils are incorporated in the layup together with carbon fiber reinforced polymer matrix composite laminae. The metal foils are inserted in the composite layup and then co-cured with the thermosetting polymer matrix composites. Consequently, the hybrid laminates are fabricated with only one curing cycle. The single interface between the metal foil and the prepreg layers that are carefully designed and controlled to assure both mechanical and chemical bonding. The details of material systems investigated in this work as well as hybrid laminate manufacturing methods are presented in section 2.1.

The hybrid interfaces investigated in this work are created mainly based on combining the mechanical and chemical bonding mechanisms. Traditional surface treatment techniques such as acid etching, hand-sanding and sand-blasting are investigated in the preliminary study. The highlight of experimental work carried out is the use of NiTi and Ti foils treated with laser ablation to create hybrid interfaces. To aid in chemical bonding, sol-gel treatments are utilized in combination with laser ablation. Various sol-gel surface treatment formulations are investigated in this dissertation work. The details of these sol-gel solutions are dicussed in section 2.2. Mode I and mode II fracture toughness of the hybrid interface between metal foil and PMC is investigated as a function of temperature using the double cantilever beam (DCB) and 4-point end notched flexure (4ENF) tests. Thermal-mechanical characterizations together with various microscopy techniques and on-line monitor-

ing methods such as fiber optics distributed strain measurement and digital image correlation are utilized to assist with the analysis and explanation of the hybrid interfaces fracture behaviors.

Furthermore, in this work, experimental effort is carried out side-by-side with computational analyses. The effect of laser ablated pattern on fracture behavior of the hybrid interfaces is studied via a combination of the extended finite element method and conventional finite element methods for crack propagation studies including the VCCT. Mode mixity is investigated with the assistance of VCCT models. The effect of high temperature is taken into account by performing analysis to calculate residual stresses in the hybrid laminates due to thermal cooling from the curing temperature to the test temperature.

In summary, herein we present a coupled experimental and computational research approach to develop strong hybrid metal and polymer interfaces in hybrid composite laminates for high temperature aerospace applications as well as to investigate fracture toughness of this interface under effects of temperature and different interfacial architecture. The specific aims of this research are to **experimentally**:

- create strong hybrid interfaces between metallic surfaces treated with a combination of newly-developed laser ablation and sol-gel techniques and bismaleimide as well as polyimide matrix composite laminates by co-curing,

- investigate the mode-I and mode-II fracture toughness of the created hybrid interfaces as a function of temperature,

  and to **computationally**

- investigate and predict the different modes of fracture of the hybrid interfaces via finite element analyses,

- quantify the pure mode I and mode II fracture toughness of hybrid interfaces as a function of temperature and calibrate parameters for mixed mode fracture criteria.

1.3 Dissertation Outline

The dissertation outline is as follows. Section 1 presents the motivation, background and research objectives for this work. Section 2 introduces the materials investigated in this work as well as the experimental and computational approach undertaken herein. Section 3 discusses the initial experimental and computational studies on developing and understanding the multifunctional hybrid interfaces. The material systems investigated in this section includes plain weave T300 carbon fabric, Matrimid 5292 bismaleimide matrix, equiatomic NiTi beam, and piezoelectric sensors. The four-point bending tests are performed to investigate the mechanical response of hybrid specimens with and without sensors. Combinations of different chemical, mechanical surface treatment techniques and sol-gel treatment for the NiTi surface are investigated. The EPII sol-gel is used in this preliminary work. Knowledge and experience gained from this preliminary study help guides the experimental work in the subsequent sections. In addition, impedance response of the piezoelectric sensors is characterized as a function of thermal and mechanical loading. Preliminary finite element analysis is performed that take into account the nonlinear material behaviors of both the NiTi beam that undergoes shape memory alloy phase transformation, and the composite laminate that experience damage upon loading. The preliminary study also includes a finite element analysis of piezoelectric sensor impedance response as a function of different boundary conditions.

In section 4, the fabrication of the epoxy matrix hybrid composite laminates using an out-of-autoclave processing technique is presented. The double-infusion VARTM

technique is developed to facilitate fabrication of hybrid laminates. The metallic constituents investigated in this section are aluminum, titanium and nickel-rich nickel titanium foil. The EPII sol-gel system is utilized for metal surface pretreatment. The composite constituent is epoxy matrix reinforced with plain weave T300 carbon fabric. The double cantilever beam tests are performed at room and elevated temperature to investigate the influence of temperature on the mode I fracture toughness of the epoxy matrix hybrid interfaces. One of the highlights of the work presented in this section is the use of an on-line monitoring technique to measure axial strain profiles along the specimen's length. This is done by using the Rayleigh backscattered fiber-optics method. Strain energy release upon crack propagation was captured by the Rayleigh fiber optic measurements.

In section 5, the fabrication details of the hybrid polyimide matrix composite laminates are presented. The constituents of the hybrid laminates created in this work include T650-8HS/AFR-PE-4 prepreg and Ti or NiTi foil. Combinations of the laser ablation method and sol-gel treatment are employed to prepared the Ti and NiTi foil. All three sol-gel formulations presented in section 2.2 are utilized herein. To activate the shape memory effect of the NiTi foil, various heat treatments on the as-received foil are performed and investigated. Results from physical and thermal-mechanical characterizations of the hybrid interfaces are presented in this section.

In section 6 and 7, the mode I and mode II fracture toughness of the fabricated hybrid laminates as described in section 5 are investigated as a function of temperature. Fractography using scanning electron microscopy/energy dispersive x-ray spectroscopy is carried out after the tests to investigate the failure modes at the hybrid interface and influence of different loading configurations, i.e. either mode I or mode II loading. Fourier transformed infrared spectroscopy is also performed on

the fracture surfaces obtained in section 5. Outlook for future work on utilizing the experimental measurement via digital image correlation to calibrate cohesive zone parameters for future finite element analysis effort is also presented and discussed.

In section 8, finite element analysis is carried out to model the double cantilever beam experiment performed in section 4 and 6. Axial strain profiles along the specimen's edge obtained from FEA are compared to those measured in the experiment in section 4 via optical fibers. Thermal residual stresses due to thermal curing and their effects on the strain energy release rates upon crack propagation are analyzed. In addition, shape memory alloy phase transformation in the hybrid DCB specimens containing NiTi foil occuring during the test at room temperature as observed and described in section 6. This phase transformation is captured and illustrated by the FEA performed in this section. The FEA results obtained in this section further support experimental observersions and explanation presented in section 4 and 6.

Section 9 presents the microscale finite element model to study the effect of micro-roughness pattern created by laser ablation of the metal surface on crack initiation and propagation behavior at the hybrid interface. The results obtained in this section support evidence of micro-crack formation on the fracture surfaces shown in sections 6 and 7.

Finally, concluding remarks and recommendations for future work are presented in section 10.

2. MATERIALS AND APPROACH

This section introduces the materials investigated in this work. The experimental and computational approach undertaken are also presented.

2.1 Material Constituent Investigated

The metallic components that were used for fracture toughness investigation in this work are aluminum, titanium and nickel-titanium (Ti-50.8 at% Ni) foils that have thickness of 400 μm, 127 μm, and 127 μm respectively. The composite laminate investigated in this work is either plain weave T300 carbon fabric in epoxy Epikote-Epikure 04908 matrix or 8-harness satin weave T650 carbon fabric in polyimide AFR-PE-4. The latter came as prepreg and was purchased from Renegade Materials Corp (AFR-PE-4-T650-35-3K-DEZ-8HS-50 prepreg). A major portion of this dissertation focuses on investigating the fracture toughness of the hybrid interfaces between Ti and NiTi foil with this high temperature composite system. The plane view and cross-section schematics of the plain and 8-harness satin weave fabric are illustrated in Figures 2.2 and 2.3. AFR-PE-4 is a phenylethynyl-encapped resin system that was developed at the Air Force Research lab. An initial study was performed by Lincoln [53]. Synthesis of AFR-PE-4 oligomer is shown in Figure 2.1 [1]. Mechanical and fracture characterization at room and elevated temperature of T650-8HS/AFR-PE-4 composite laminates were performed by [54, 55].

It should be noted that dynamic mechanical analysis of thermosetting resins such as epoxy and polyimides has shown that besides the primary transition of T_g, the polymers also exhibit a sub-T_g (sub-glass) transition, so-called β transition, or beta transition [56, 57, 58, 59, 60, 61, 62]. β transition is observed in the tan δ or loss modulus E'' curves. This transition occurs when the material is in the glassy state

and presents as a weak, broad peak before the strong and sharp glass transition peak. Different from the glass transition that is accompanied by a sharp decrease in the storage modulus E', a gradual decrease in E' is observed as the material undergoes the β transition. Previous studies indicated that β transitions are associated with the local movements of the side chains or adjacent atoms in the polymer main chains, and often correlates to, but not always an indicator of toughness in polymers [63, 64]. It has been concluded that the β transition must be related to either localized movement of in the backbone or the movement of side chains in order to sufficiently absorb energy [63, 65, 66, 67]. Yee *et al.* reported that for polycarbonate, the movement of large side chains can be related to toughness [68]. A study on amorphous and semi-crystalline polymers performed by Boyer [69] described the relationship between toughness and the room temperature frequency of the β transition, $f_{\beta,RT}$, where toughness increases as $f_{\beta,RT}$ increases. Schroeder *et al.* investigated β transition in several aromatic and aliphatic epoxy systems and demonstrated the relationship between β relaxation and tensile as well as impact toughness [70]. By definition, toughness of material is its ability to absorb or dissipate energy prior to fracture. For polymers, chains motion is required for energy to be absorbed. The energy absorbing mechanism associated with impact and toughness behavior of polymers in the glassy state has been identified to be the β transition [56, 57]. They concluded that at temperatures above T_β and below T_g, more energy can be absorbed than at temperature below T_g. They also found better impact properties can be obtained with lower T_β values.

β transition (or β relaxation) in dynamic mechanical behavior of aromatic polyimides has been studied by a number of researchers [58, 59, 60, 61, 62]. They reported the observation of β transition in dynamic mechanical analysis and ascribed this transition to the local change in the polyimide chains although no relation to physical

or mechanical properties were investigated. Sun and colleagues related the β transition in polyimides to the rotation of rigid segments of para-phenylene and amide groups around the $-O-$ and $-CH_2-$ hinges in diamines [61]. It was found by Bas *et al.* that the broadness of the β transition in aromatic polyimides is dependent on the intensity of the intramolecular charge transfer between the diamine and diimide segments or the flexibility of dianhydride and diamine links [62].

The above discussion on β transition in polymer matrix is beneficial for the analysis and discussions of dynamic mechanical analysis and mode I fracture toughness results presented in sections 5 and 6.

Besides the material mentioned above, in the preliminary study described in section 3, the hybrid composite laminate investigated utilized a resin system that is in the intermediate regime between the epoxy and polyimide resin systems. In this preliminary work, the hybrid interface between equiatomic NiTi beam and bismaleimide Matrimid 5292 matrix composite reinforced with plain weave T300 carbon fabric is investigated. In addition, to facilitate the fabrication and initial study of multifunctional hybrid composite, commercial APC PZT piezoelectric sensors as well as custom-fabricated high temperature BsPT sensors series, developed at Stanford University, are utilized. These materials and sensor details are described in section 3.

2.2 Sol-Gel Surface Treatment Formulations Employed

Three diffferent sol-gel surface treatment formulations are employed in this study. The first formulation, the BoeGel EPII, herein refered to as EPII sol-gel, was developed at Boeing and facilitates adhesion between metal and epoxy-based adhesives. The solution is a mixture of glycidoxypropyltrimethoxysilane, tetra-n-propoxyzirconium (TPOZ), propyl alcohol, acetic acid and deionized water [43, 27]. Representation of

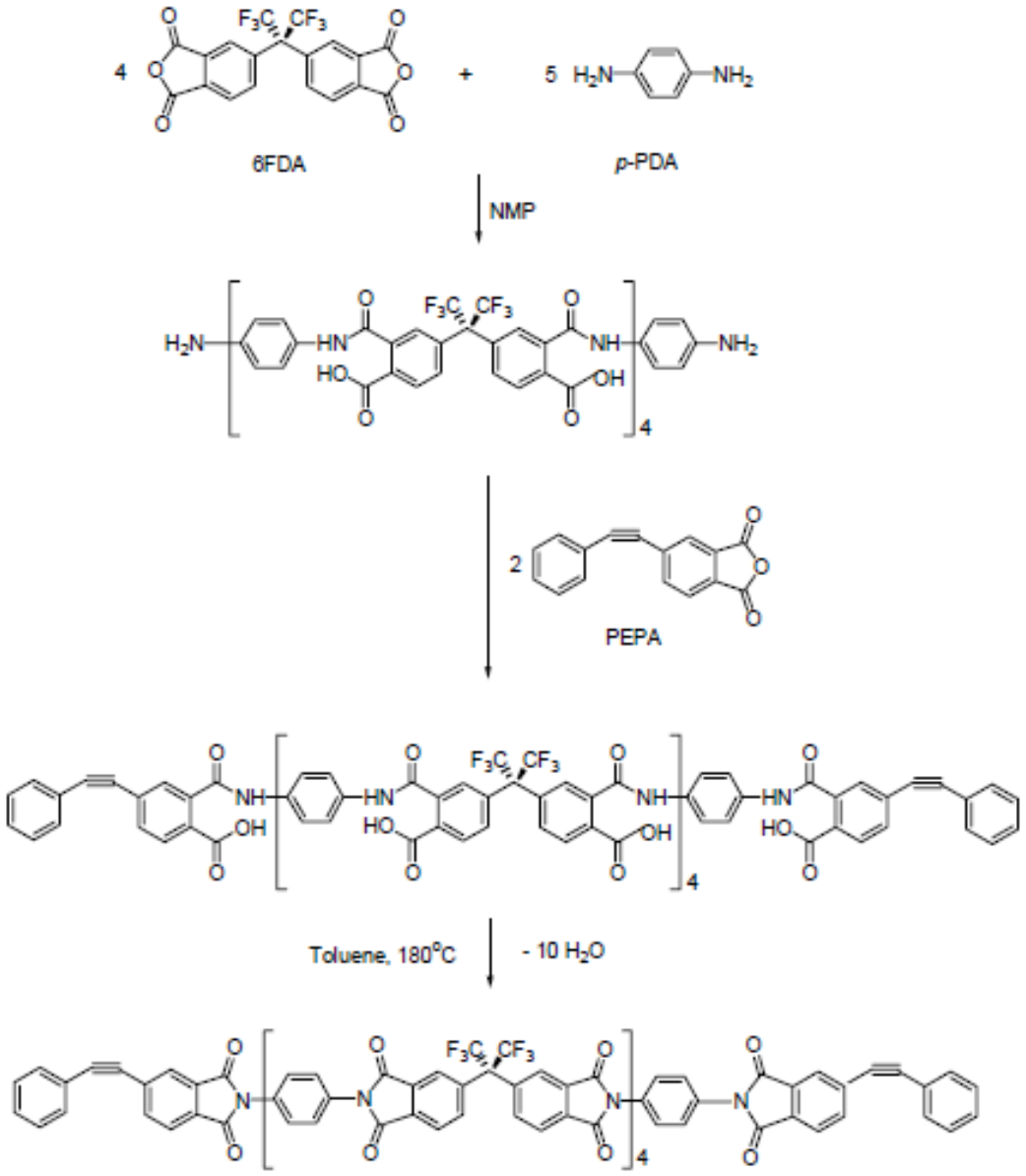

Figure 2.1: Synthesis of AFR-PE-4 oligomer [1]

the hybrid interface created using the EPII sol-gel as metallic surface treatment solution is presented in Figure 2.4.

In high temperature hybrid composite laminates, the use of glycidoxypropy-

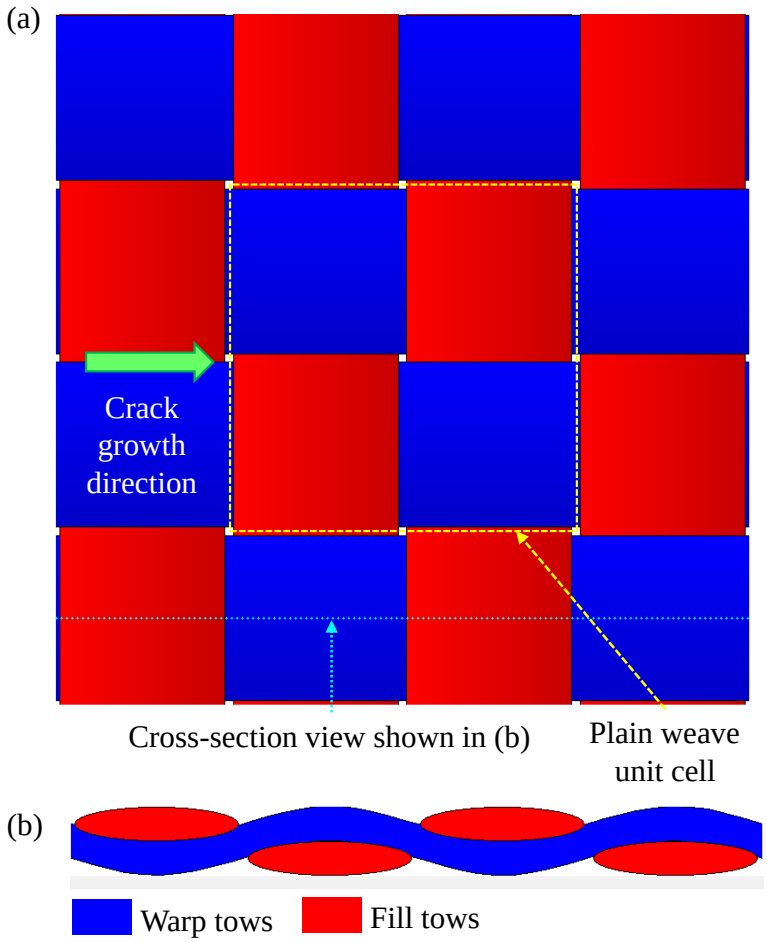

Figure 2.2: (a) Schematic of plain weave fabric (b) Cross-section view of one layer of plain weave fabric. *The weave pattern in this figure was generated using TexGen [2].*

ltrimethoxysilane is not suitable because it degrades and is unstable at the temperature that the hybrid laminates undergo during the curing cycle, i.e. 250 ^oC or above. Thus, it was recommended that aminophenyltrimethoxysilane is used in place of glycidoxypropyltrimethoxysilane to create a sol-gel solution that can be used to prepare metal surfaces for high temperature processing [43]. This is because aminophenyltrimethoxysilane is much more stable at high temperature due to the

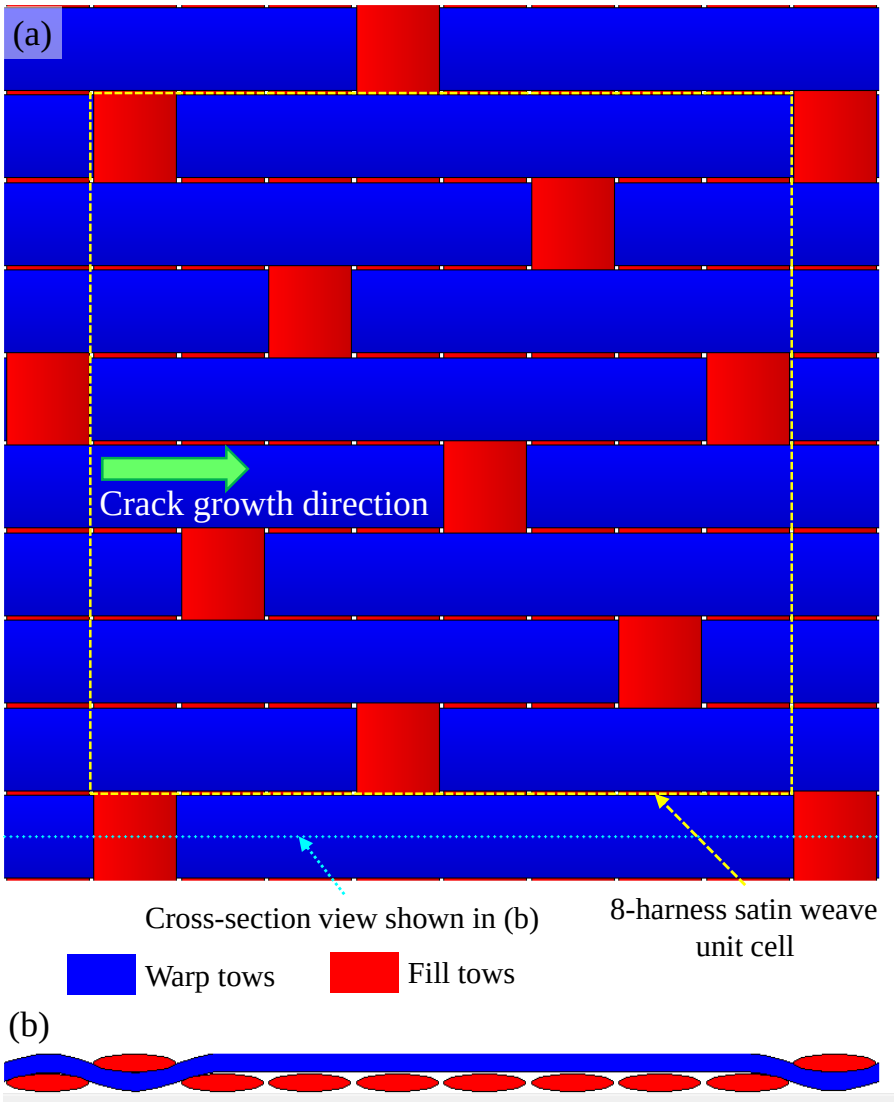

Figure 2.3: (a) 8-harness satin weave schematic (b) Cross-section view of one layer of 8HS fabric. *The weave pattern in this figure was generated using TexGen [2].*

presence of the bulky amino-phenyl side groups in the chemical structure. As a result, the aminophenyl sol-gel or AP sol-gel, is employed in this work. This sol-gel solution includes aminophenyltrimethoxysilane, tetra-n-propoxyzirconium (TPOZ), propyl alcohol, acetic acid and deionized water. Figure 2.5 presents the representa-

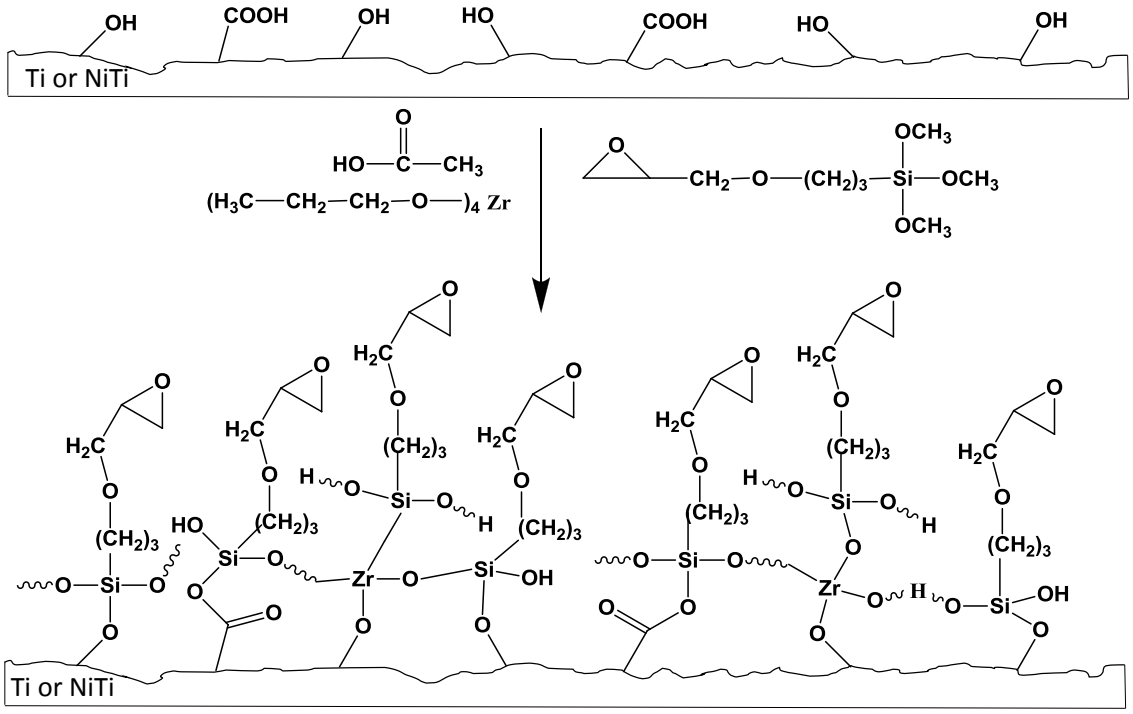

Figure 2.4: Synthesis and representation of covalent bonds formed at the Ti/NiTi foil surface treated with the EPII sol-gel chemistry

tion of the hybrid interface created using the modified-EPII sol-gel or AP sol-gel as metallic surface treatment solution.

In attempt to create lightweight, adhesively bonded structural components for use at high temperature, Park *et al.* developed a novel phenylethynyl imide silane sol-gel surface treatment that facilitates joining of titanium adherends using polyimide adhesive [71, 72]. This sol-gel solution, herein refered to as phenylethynyl imide (PEI) sol-gel, is a mixture of pendent phenylethynyl imide oligometric disilane and tetraethoxysilane. Details of the synthesis of this novel sol-gel surface treatment

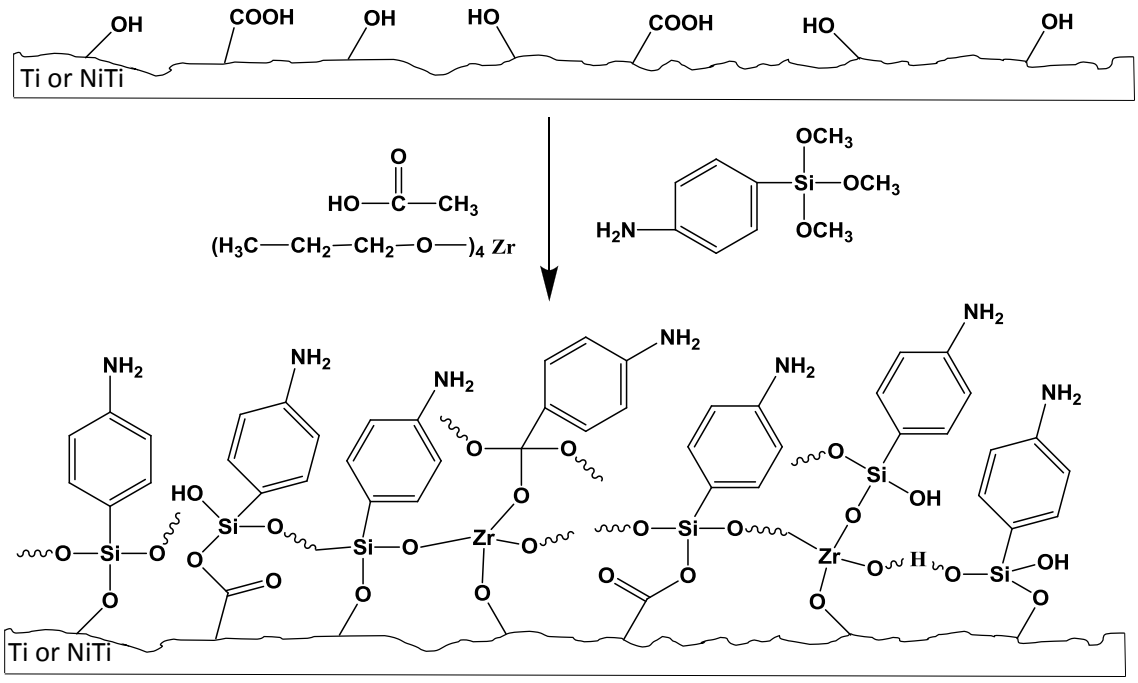

Figure 2.5: Synthesis and representation of covalent bonds formed at the Ti/NiTi foil surface treated with the modified EPII sol-gel chemistry (containing aminophenyl silane).

solution are presented in Figures A.1 and A.2 in Appendix A. Representation of the hybrid interface created using this new PEI sol-gel as metallic surface treatment solution is illustrated in Figure 2.6.

In summary, the use of EPII sol-gel, AP sol-gel and PEI sol-gel for metal surface pretreatment is investigated in this work. However, not all of these sol-gel treatments are employed for each of the hybrid material systems as presented in section 2.1. The use of the selected sol-gel treatment solutions is described accordingly in each of the subsequent sections.

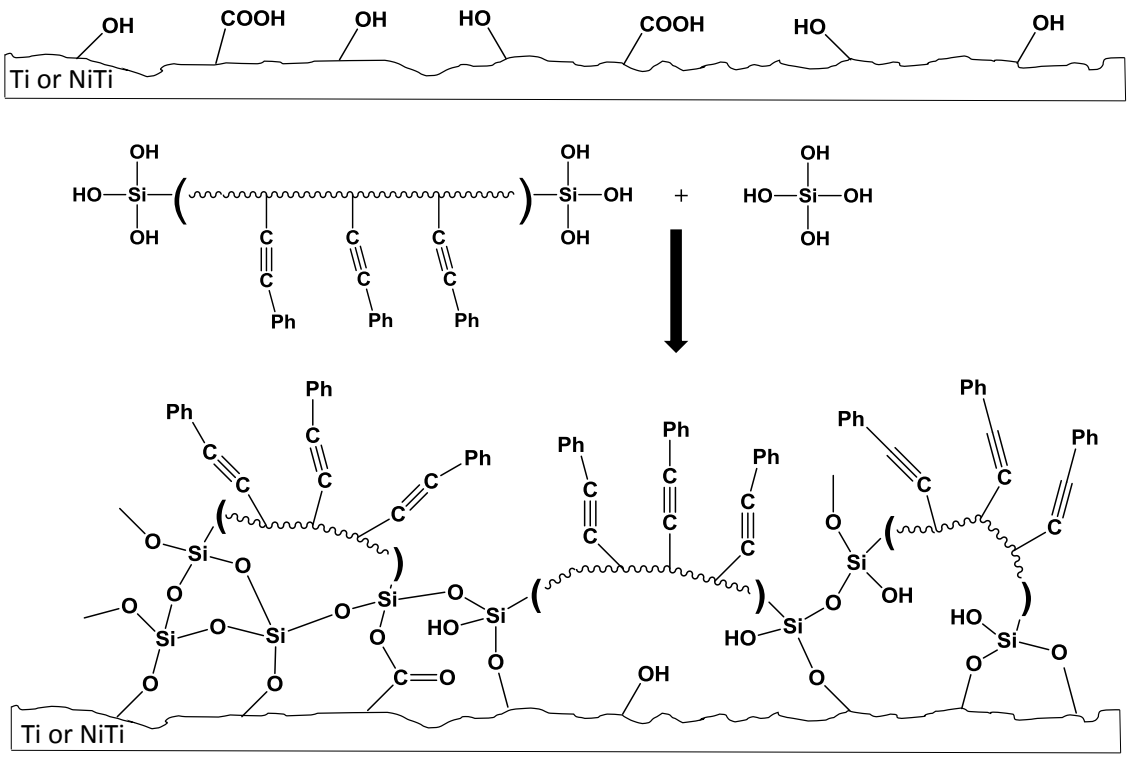

Figure 2.6: Synthesis and representation of covalent bonds formed at the Ti/NiTi foil surface treated with the custom-synthesized phenylethynyl imide containing (PEI) sol-gel chemistry that was developed at NASA Langley Research Center.

2.3 Hybrid Laminates Fabrication Methods

Current out-of-autoclave composite manufacturing techniques are used to fabricate the hybrid laminates in this work. For the epoxy matrix composite, a modified vacuum assisted resin transfer molding (VARTM) technique was developed to fabricate the hybrid laminates. This technique is discussed in details in section 3. For the polyimide matrix panel, since pre-manufactured prepreg is used, the hybrid laminates are fabricated by curing in a hot-press. Details of the high temperature laminates

processing are presented in section 5. Table 2.1 summarizes the materials will be used for the PMC part of the hybrid laminates, as well as processing techniques and temperature range for different polymer matrix systems.

In the preliminary study presented in section 3, the Matrimid matrix composite laminates are fabricated using the resin film infusion (RFI) method. The hybrid specimens are created by joining bulk equiatomic NiTi beam to cured Matrimid matrix laminates using neat Matrimid resin as the adhesive. The hybrid specimens were cured in a hot-press. The fabrication details of these specimens are presented in section 3.

Table 2.1: Hybrid composite material systems investigated in this work and corresponding composite manufacturing method

Reinforcement Type	**Matrix**	**Metal Foil (thickness)**	**Processing Technique**	T_g
T300 plain weave carbon fabric (T300-PW)	Epikote-Epikure 04908	Al (0.4 mm), Ti (0.127 mm), Ti-50.8 at%Ni (0.127 mm)	VARTM	83.2 ^{o}C
T300 plain weave carbon fabric (T300-PW)	Matrimid 5292	Equiatomic NiTi (2.5 mm)	RFI and hot-press	201.4 ^{o}C
T650 8-harness satin weave carbon fabric (T650-8HS)	AFR-PE-4 (prepreg)	Ti (0.127 mm), Ti-50.8 at%Ni (0.127 mm)	Hot press	390 ^{o}C

2.4 Hybrid Laminates/Interfaces Characterization Approach

Characterization techniques including mechanical testing including mode I and mode II fracture toughness tests will be done at both room temperature and elevated temperature up to the onset of glass transition temperature of the PMC. In-situ distributed strain measurement using Raleigh backscattering fiber optics and/or digital image correlation are employed during the fracture toughness tests to provide more information for further analysis and verification of finite element analysis.

Besides mechanical tests of composite laminates, other characterizations to be done include:

1. Performing optical microscopy (OM), scanning electron microscopy/energy dispersive x-ray spectroscopy (SEM/EDS), and contact angle measurement on metallic surface after laser ablation treatment

2. Performing thermal mechanical tests (differential scanning calorimetry (DSC) and isobaric tensile) on NiTi foil to examine if heat and surface treatment process affects properties of NiTi

3. Performing C-scan after fabrication of the laminate to determine the hybrid panel quality

4. Performing thermal-mechanical characterization on the PMC using dynamic mechanical analysis (DMA), thermomechanical analysis (TMA), and thermal gravimetric analysis (TGA)

5. Characterizing the cross-section at the hybrid metal-PMC interface with OM, SEM and atomic force microscope infrared spectroscopy (AFM-IR)

6. Characterizing fracture surfaces with OM, SEM/EDS, and Fourier transformed infrared spectroscopy (FTIR)

2.5 Computational Analysis Approach

Multiscale finite element analyses are conducted to model the mode-I and mode-II dominated crack propagation behavior of hybrid interfaces investigated in this study. The commercial FE software ABAQUS is used. First, FEA is carried out to obtain the homogenized properties of the PMC in the tow as well as in the woven composite lamina. Finally, at the macroscale, the double cantilever beam is modelled. It should be noted that even though the specimens are symmetric about the mid-plane, they are asymmetric with respect to the plane of the initial crack. Thus, the macroscale analyses are performed on specimens herein referred to as asymmetric double cantilever beam (ADCB). Homogenized properties obtained from the weave scale are used in the macroscale model. The virtual crack closure technique is used to assist with the determination of the mode mixity presented during crack propagation at the hybrid interfaces. Moreover, the effect of the patterned micro-roughness created by laser ablation on the crack path and failure modes of hybrid interfaces is investigated.

3. HIGH TEMPERATURE MULTIFUNCTIONAL HYBRID INTERFACES: INITIAL INSIGHTS

This section presents the preliminary work that was performed to study the different perspectives of interfacial behaviors of the multifunctional hybrid interface between NiTi and Matrimid matrix composites. These perspectives include experimental and computational investigations of flexural response of NiTi-PMC bimaterial beams. In addition, aspects of integrating piezoelectric sensors in the hybrid composite system for structural health moninoring purposes were explored.

3.1 Joining and Characterization of the Interface between Shape Memory Alloy to Matrimid Matrix Composite[1]

The constituents of the hybrid specimens fabricated and tested in this section are bulk equiatomic NiTi beam of dimensions 10.0 x 40.0 x 2.5 mm^3 and cured T300-PW/Matrimid 5292 beam (8 layers of carbon fabric through the thickness) of dimensions 10.0 x 40.0 x 1.9 mm^3. These specimens were created by joining the pre-cured composite beam that has a layup of $[0/90]_{2s}$[2] to NiTi beam using Matrimid 5292 (same as the matrix resin) as the adhesive and cured using a hot press under a pressure of 20 MPa. The schematic of the bonding process is shown in Figure 3.1(a). The curing cycle for this bonding process is as follows.

- Heat to 177 ^oC at a rate of 2 ^oC/min
- Hold at 177 ^oC for 150 min

[1]The experimental work presented in this section was performed in collaboration with Dr. Ankush Kothalkar and Prof. Ibrahim Karaman at Texas A & M University.

[2]The T300-PW/Matrimid5292 laminates were fabricated using the resin film infusion (RFI) process by Dr. G.P. Tandon at the Air Force Research Laboratory, Dayton, OH.

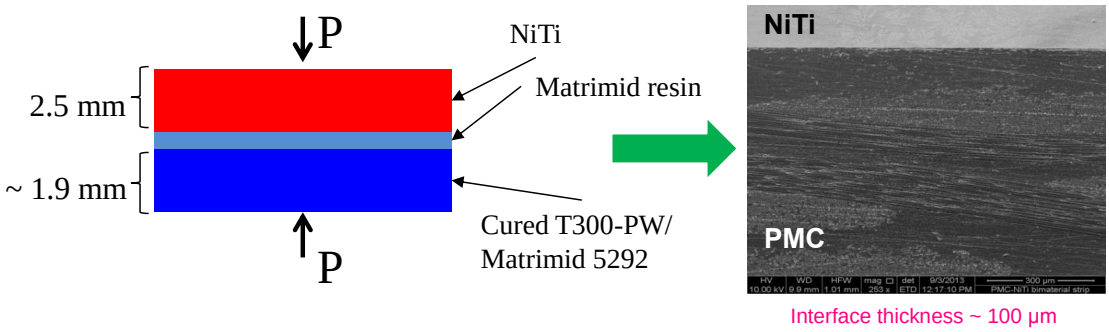

Figure 3.1: (a) Schematic of the joining method. (b) Cross-section image of the hybrid NiTi-T300_PW/Matrimid interface.

- Heat to 204 ^oC at a rate of 2.5 ^oC/min
- Hold at 204 ^oC for 4 hours
- Cool to room temperature at a rate of 5 ^oC/min.

To surface treat the NiTi beam, either sand blasting alone or a combination of sand blasting and sol-gel was used. In this work, the EPII sol-gel system was utilized. Mechanical sanding using 400-grit sand papers and ultra-sonication cleaning were employed to prepare the PMC surfaces for joining. Figure 3.1(b) shows the cross-section of the created hybrid specimen. It should be noted that the secondary bonding method was adopted to created the hybrid joints in this section. The adhesive used for hybrid bonding was the same as the matrix resin. Thus, the adhesive needs to go the same curing cycle as the composite. As a result, in the hybrid specimens fabricated in this section, the composite underwent curing cycle twice before mechanical testing. To ensure the second curing cycle did not significantly alternate the properties of the PMC, differential scanning calorimetry was performed on specimens before and after undergoing the second curing cycle. It was found that the

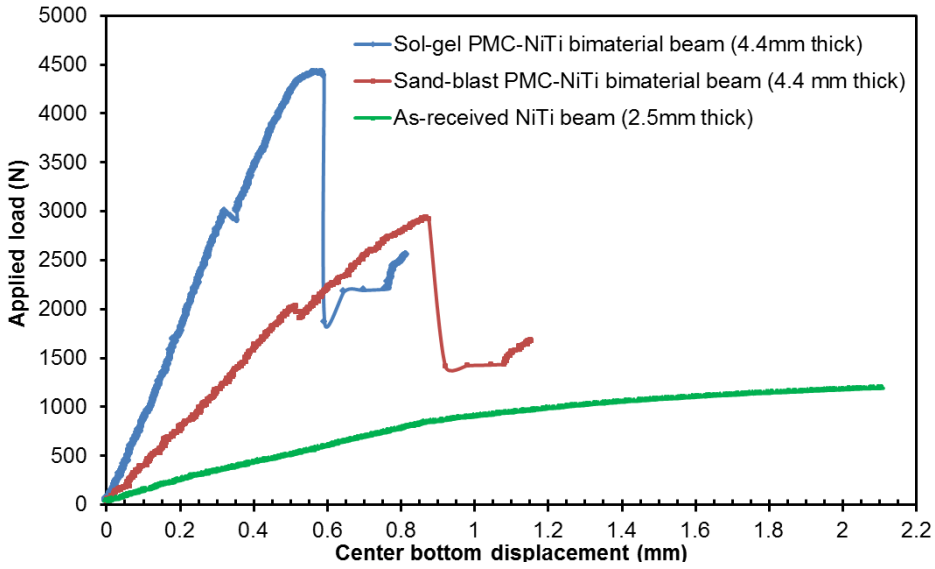

Figure 3.2: Load-displacement results from four-point bending tests of NiTi-PMC hybrid specimens and monolithic equiatomic NiTi beam.

specimen that experienced additional curing exhibited glass transition temperature of 221 ^oC as compared to a T_g of 204 ^oC of the composite that was cured once. Thus, it was concluded that the second cycle served as post-curing process that assisted the formation of more cross-links in the thermosetting matrix, hence, increased the material T_g.

Four-point bending tests at room temperature are undertaken with NiTi-T300-PW/ Matrimid5292 laminates (PMC) with the layup of $[0/90]_{2s}$ as well as monolithic equiatomic NiTi beam. In-situ digital image correlation was performed during the four-point bending tests. The strain profiles obtained in this work are compared to those obtained from finite element analysis and presented in the following section. Load-displacement curves together with loading schematic for 4-point bending test are presented in Figure 3.2. It is observed that the specimen in which the NiTi surface treated with a combination of sand blasting and EPII sol-gel yields a stiffer

load-displacement response and can sustain higher load compare to that of the specimen with sand-blasted NiTi surface. This is due to the more effective load transfer between NiTi and thanks to a stronger interface between the two constituents.

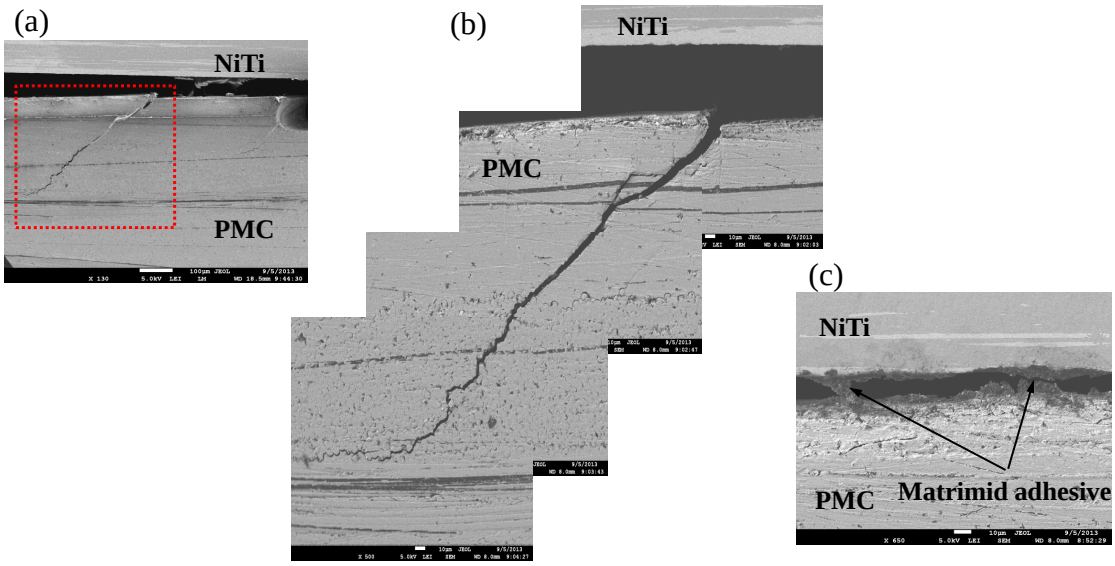

Figure 3.3: Cross-section view of a NiTi-T300-PW/ Matrimid5292 bimaterial beam after 4-point bending test showing (a) delamination and 45 ^{o} crack initiated at the hybrid NiTi-PMC interface. (b) close-up view of the 45 ^{o} crack. (c) residual Matrimid adhesive adhere to both the NiTi and PMC beams after delamination occurs.

SEM images of the delaminated specimen, whose NiTi layer was treated with the combination of sand-blasting and sol-gel methods, are shown in Figures 3.3 and 3.4. It is clearly observed that the interfacial separation evolves into typical 45 ^{o} matrix cracks in the composite layers. Residual of the composite (note that this composite was pre-cured and the hybrid interface was created via co-bonding using Matrimid 5292 resin as adhesive) with imprints of fiber on delaminated NiTi surface, and fracture of fiber on delaminated PMC surface show evidence of a good interface.

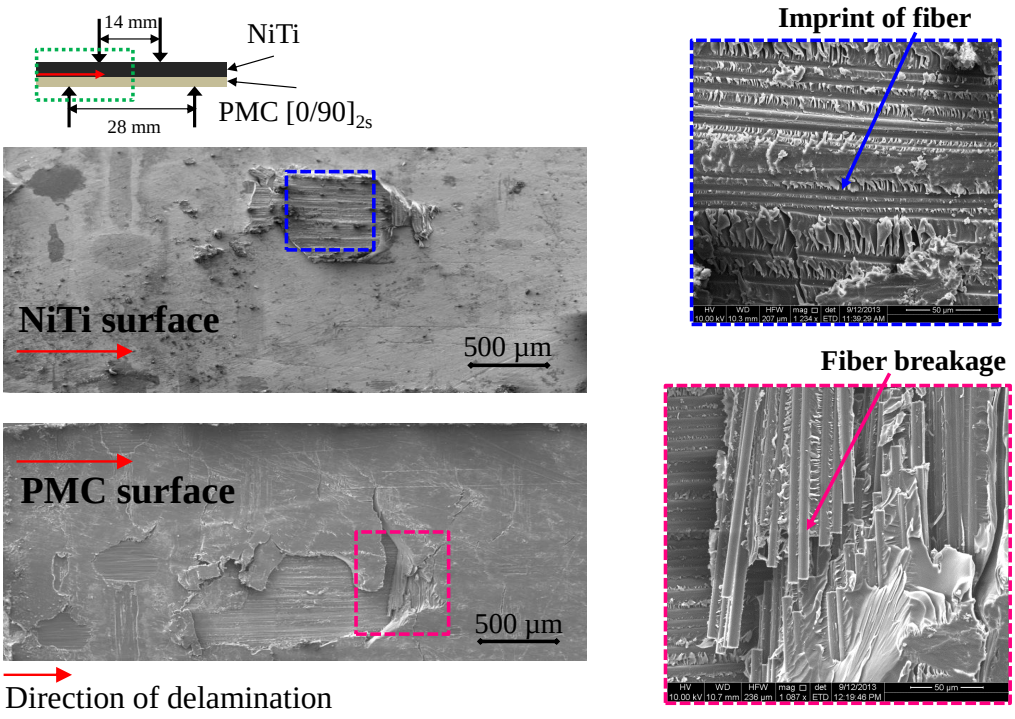

Figure 3.4: Delaminated surfaces of a NiTi-T300-PW/ Matrimid 5292 bimaterial beam (NiTi surface treated with a combination of sand blasting and EPII sol-gel) after a 4-point bending test showing evidences of a strong hyrbid interface: residual of the composite containing fiber imprints on the NiTi fracture surface, and fracture of fiber on the delaminated composite surface.

3.2 Nonlinear Finite Element Analysis of Four-point Bending SMA-PMC Bimaterial Beam

Finite element analysis of the 4-point bending bimaterial beam (NiTi-T300-PW/ Matrimid 5292) were carried out using ABAQUS. Strain profile obtained from the model was verified with digital image correlation (DIC) experiment. Due to symmetry, only a quarter of the beam was modeled with symmetry about the x and y planes through the origin, placed at the center of the beam. The homogenized properties of the T300-PW/Matrimid5292 composite used in the model are summarized in Table 8.1. Shape memory alloy behavior was captured using a UMAT user subroutine for SMA constitutive model developed by Lagoudas *et al.* [73]. Properties of equiatomic NiTi beam used in this model are shown in Table 3.2.

Table 3.1: Thermal-mechanical and damage initiation properties of PMC

$E_{11} = E_{22}$ (GPa)	56.5
E_{33} (GPa)	10.6
G_{12} (GPa)	4.13
$G_{23} = G_{13}$ (GPa)	3.13
ν_{12}	0.148
$\nu_{23} = \nu_{13}$	0.392
$\alpha_{11} = \alpha_{22}$ ($1/^oC$)	2.17 x 10^{-5}
α_{33} ($1/^oC$)	-3.62 x 10^{-7}
$\sigma_{L,t} = \sigma_{T,t}$ (MPa)	610
$\sigma_{L,c} = \sigma_{T,c}$ (MPa)	420
τ_{LT}	106

Table 3.2: Thermal-mechanical properties of equiatomic NiTi

E^T (GPa)	24.5
E^D (GPa)	56.31
M_s (^{o}C)	23.06
M_f (^{o}C)	-31.50
A_s (^{o}C)	78.94
A_f (^{o}C)	108.14
$\nu_A = \nu_M$	0.33
$C_A = C_M$ (MPa/^{o}C)	11.41
α_A (1/^{o}C)	32.0 x 10^{-6}
α_M (1/^{o}C)	21.0 x 10^{-6}

Figure 3.5(a) shows a comparison of load-displacement results obtained from FEA and experiment for a specimen with NiTi surface treated with sand-blasting and sol-gel method that underwent four-point bend loading. In the model, displacement was applied on top the bimaterial beam, unloaded by releasing the applied displacement, and heated to temperature above Austenitic finished temperature of NiTi to recover the shape. The NiTi-PMC interface was assumed perfectly bonded using tie constraint. Nonlinearity in the FE model was then considered to include damage behavior of PMC. A UMAT describing damage behavior in PMC provided by ABAQUS was utilized together with the SMA UMAT. Figure 3.5(b) shows load-displacement predictions from a model using a combination of SMA and PMC damage UMATs with perfectly bonded interface assumption and cohesive interface. The models captured the large drop in load as observed in the experiment, however, still could not capture the first small drop at about 3000 N. This small drop observed in the ex-

periment could be due to experimental instablity and thus cannot be accounted for in this FE model. Figure 3.6 shows a comparison of strain profile obtained from FE analysis with full-field strain profiles from experiment with DIC.

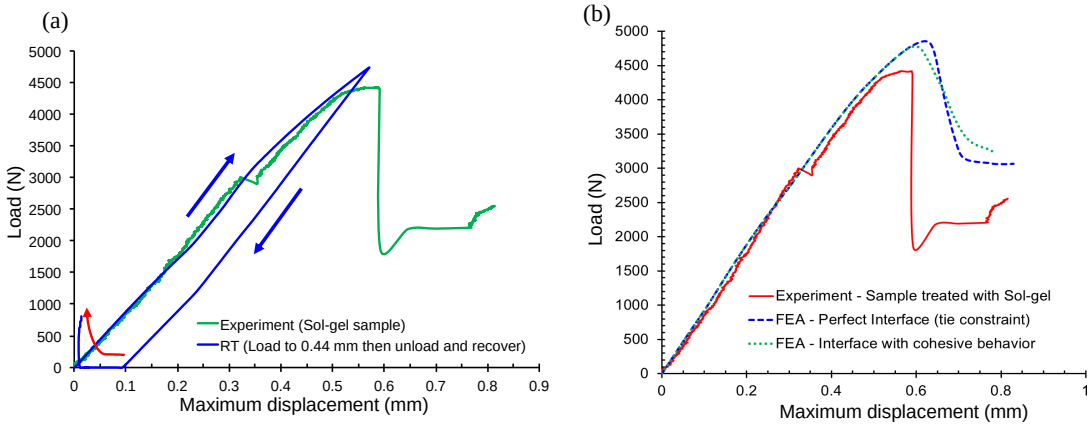

Figure 3.5: (a) Model used SMA UMAT, loaded to 0.44 mm, unloaded and then recovered by heating to temperature above A_f (b) Model used SMA UMAT and PMC damage UMAT.

The interfacial stresses through thickness at the center of the beam for perfect interface and cohesive interface are shown in Figure 3.7. These values were obtained at the time step where the specimen is subjected to maximum load, i.e. before the large load drop.

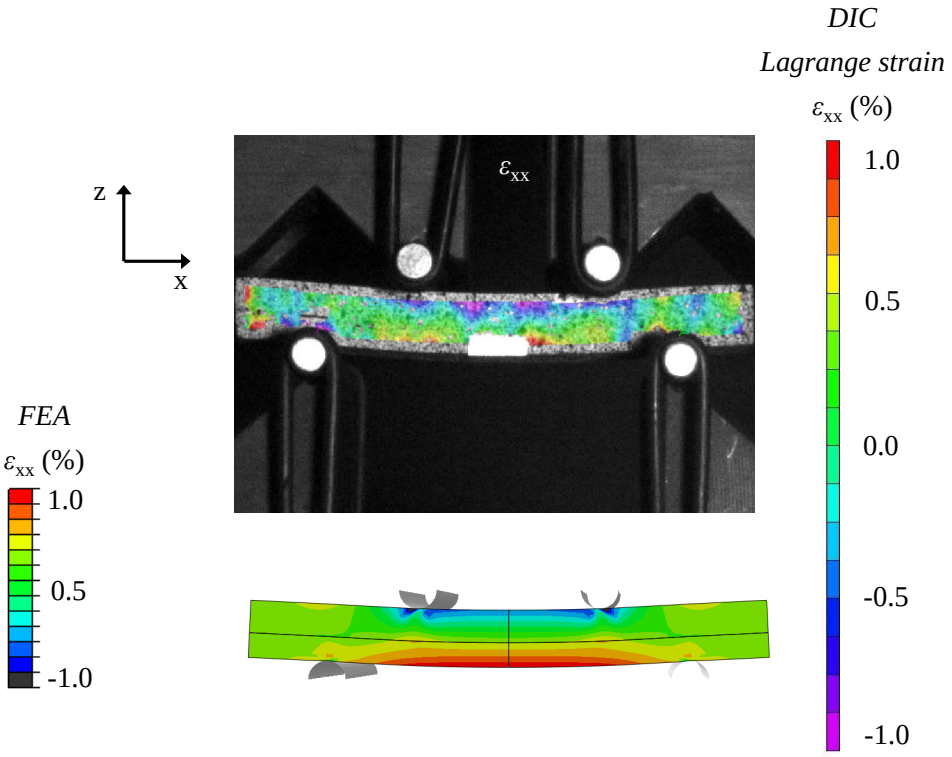

Figure 3.6: Strain profile from 4-point bending test with DIC versus strain profile from FE model.

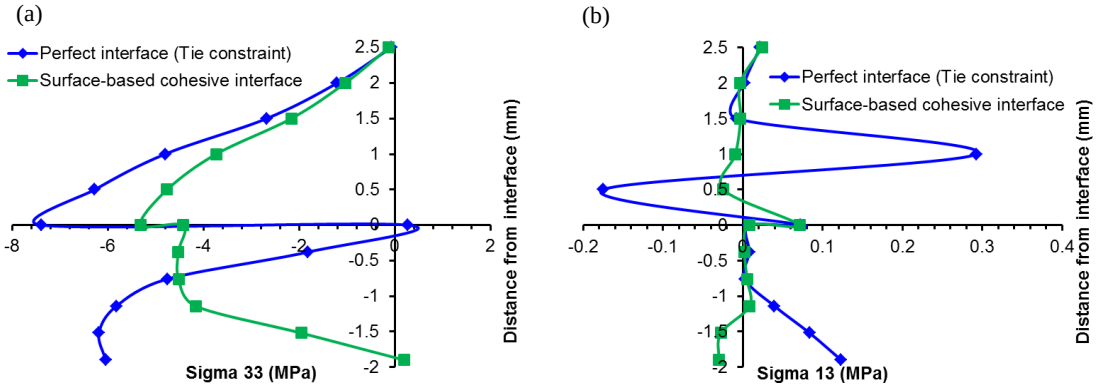

Figure 3.7: (a) σ_{33} and (b) σ_{13} as functions of through-thickness distance from the hybrid interface.

3.3 Integration of Piezoelectric Sensors to the Interface Between Shape Memory Alloy to High Temperature Polymer Matrix Composites

As an attempt on developing and investigating multifunctional hybrid interfaces, piezoelectric sensors were embedded at the NiTi-PMC and PMC-PMC interfaces. These sensors were integrated for structural health monitoring purpose. However, besides investigating the sensor response before and after this integration, the effect of sensor integration on the mechanical properties of the overall structure also requires attention.

3.3.1 Investigating Mechanical Response of Hybrid Composite Beam with Embedded Piezoelectric Sensors[3]

High temperature flexible piezoelectric sensors fabricated at Stanford University were integrated at the NiTi-PMC and PMC-PMC interfaces. PMC used here is also pre-cured T300-PW/Matrimid5292. Matrimid 5292 resin was used as adhesive and the specimens were cured with a hot press. The NiTi beam was first sand-blasted, cleaned in a sonicator and then EPII sol-gel solution was applied. Surface treatment employed on the cured Matrimid matrix composite beam was mechanical abrasion using 400 grit sand papers followed by thorough cleaning with propyl alcohol. Figure 3.8 demonstrates the joining and sensor integration steps as well as a cross-section view of the hybrid composite beam with integrated piezoelectric sensors at the NiTi-PMC interface. The specimens fabricated via secondary bonding in this study include PMC-PMC and NiTi-PMC with and without sensor series.

[3]The experimental work presented herein was performed in collaboration with Dr. Yu-Hung Li and Prof. Fu-Kuo Chang of Stanford University, as a part of the AFOSR Multi-university Research Initative.

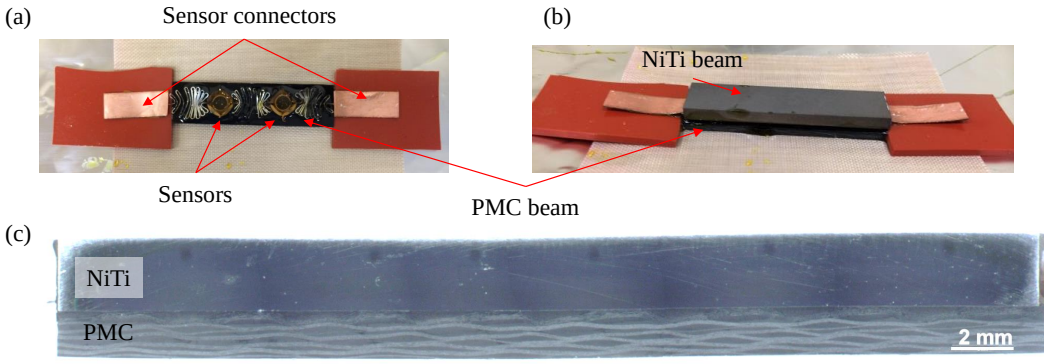

Layup of sample: [0/90/0/90/0/90/0/90$_{CNT}$]-sensor-NiTi

Figure 3.8: (a) High temperature flexible piezoelectric sensor series, fabricated at Stanford University, were placed on top of a cured T300-PW/ Matrimid 5292 beam prior to the hybrid specimen joining process. (b) Equiatomic NiTi beam was placed on top of the assembly presented in Figure (a). (c) Cross-section view of the hybrid composite beam with integrated piezoelectric sensors at the NiTi-PMC interface.

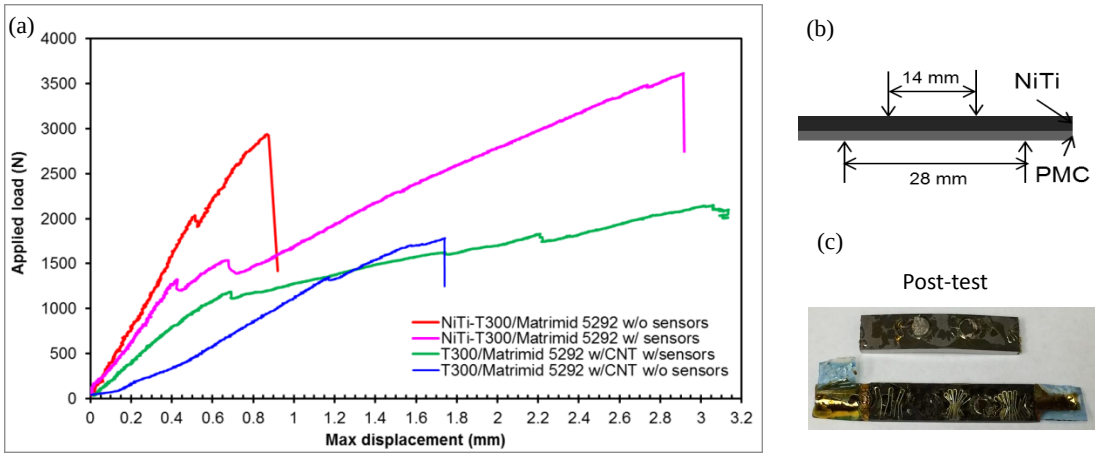

Figure 3.9: (a) Load-displacement results from four-point bending tests of secondary bonded PMC-PMC and NiTi-PMC beam with and without sensors. (b) Schematic of the four-point bending test. (c) Delaminated surfaces from a NiTi-PMC specimen that contained sensor series at the hybrid interface.

Preliminary results of the four-point bending tests at room temperature for specimens with and without sensors suggest that the presence of a thin sensors layer does not significantly alter the mechanical behaviors of the hybrid composite beams in terms of effective stiffness of the beams and maximum load they can sustain. In addition, adding a thin sensor layer increases the flexibility of the hybrid system because samples with sensors deflect approximately 3.5 times more than those without sensors before final failure occurs. Figure 3.9 shows sensor series on top of PMC prior to joining, delaminated surfaces after four-point bending test and experimental load-displacement results.

3.3.2 Investigating Impedance Response of Piezoelectric Sensors[4]

Hybrid specimens where piezoelectric sensors were sandwiched between two aluminum plates, and between two pre-cured neat Matrimid plates were fabricated. Matrimid 5292 was used as adhesive; and curing was done using a hot press. Measurements of the sensors' impedance were done before and after sample fabrication to ensure functionality of the sensors after being embedded between two plates and cured. The sensors in the samples with Al plates did not give output signals after being embedded due to electrical shortage when the sensors wires in contact with metal surfaces, while the sensors embedded between two insulating Matrimid plates still function after the curing cycle. Specimens where sensors were embedded between two neat Matrimid 5292 plates underwent four-point bending tests at room temperature with in-situ impedance measurement. Figure 3.10(a) show the four-point bending test setup in this work. Signals from the sensors were measured at different load applied until the specimens failed. Since the sensors were placed at the

[4]The experimental work presented in this section was performed by Hieu Truong and Dr. Yu-Hung Li at the Structures and Composites Laboratory, Department of Aeronautics and Astronautics, Stanford University, Stanford, CA in collaboration with Prof. Fu-Kuo Chang.

midplane, and only one sensor was presented in each four-point bending specimen, located at the center of each specimen, zero stress was experienced at the location of the sensor. As a result, no change in signals was observed for different load applied. The sensors embedded between two Matrimid plates, however, could detect change in temperature. At zero applied load, signals was measured at 25^oC and 90^oC. The impedance peak in signals measured at 90^oC shift to a lower frequency compared to that of the signals measured at 25^oC. This suggests that the sensors could be used to detect temperature change when placed anywhere in the specimens, and should be placed off-neutral plane in order to detect displacement/deformation in bending. The embedded PZT sensor impedance response to mechanical and thermal loading are presented in Figure 3.10(b)-(d).

Finite element analyses were carried out to study impedance response of piezoelectric sensor in the free and clamped configurations. Commercial APC-850 circular sensor of 3.175 mm diameter and 254 μm thickness was studied. Poling direction is through the thickness of the sensor. Direct steady-state dynamics analyses were carried out where zero potential was applied on one face of the sensor as the ground electrode and harmonic potential signal of magnitude 50 mV was applied on the other side. Complex charges output from the model was used to the frequency response of the sensor's impedance Z using the formula $Z = \dfrac{V}{jwQ}$,
where V is the applied voltage, Q is the complex charge output, and ω is the frequency at which the voltage was applied and charge calculated. The impedance peaks obtained from the analyses occurred at the frequencies that agree with experimental observations. There are frequency shifts in the impedance peaks from the free to the clamped sensor as shown in Figure 3.11 (d). Electrical resonances are unique properties of piezoelectric materials. Upon any changes in the loads or boundary conditions of the sensor, impedance peaks shift to different frequencies.

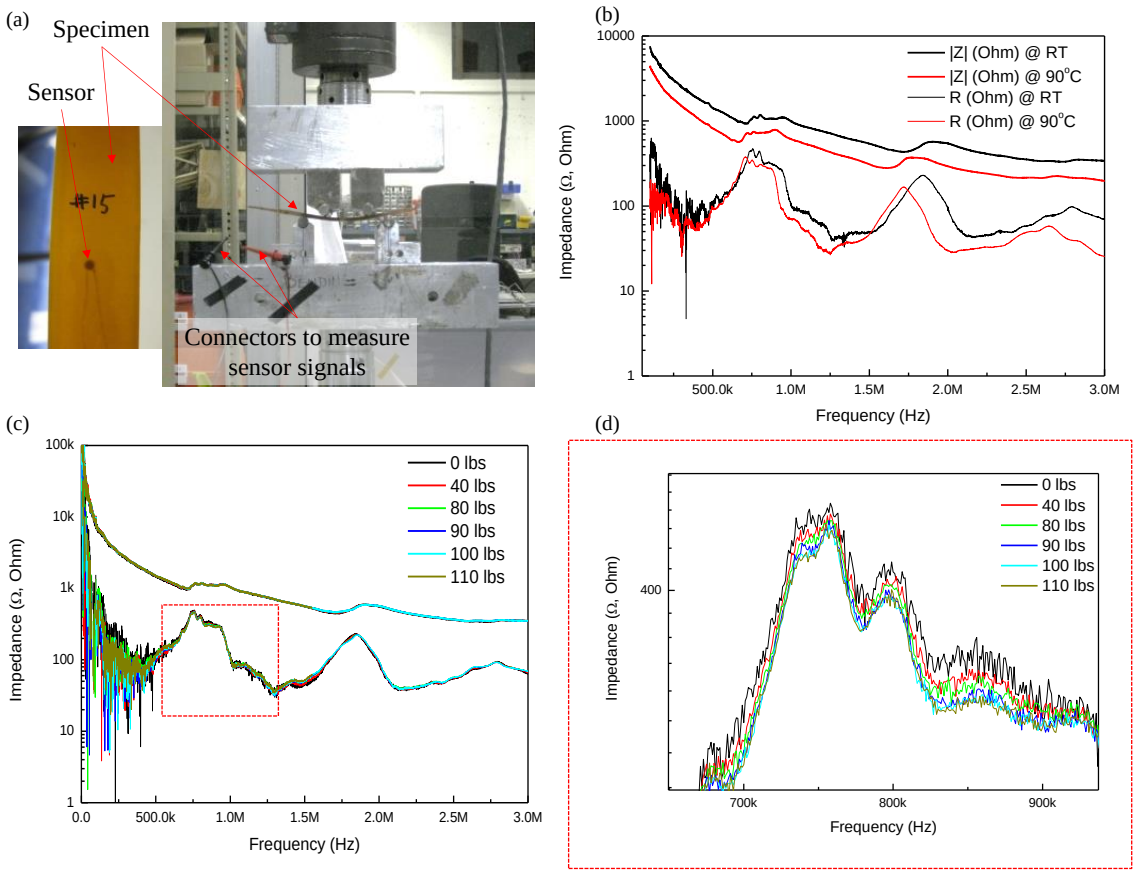

Figure 3.10: (a) Four-point bending test setup for specimens containing piezoelectric sensor with in-situ impedance measurement. (b) Impedance response to temperature stimulus of the embedded PZT sensor when no load was applied. The impedance peaks in signals measured at 90 ^{o}C shift to a lower frequency compared to that of the signals measured at 25 ^{o}C. (c) and (d) Impedance response to various applied load of the embedded PZT sensor at room temperature. All the signals collapse and no changes in impedance peak was observed.

This behavior will be used to study how the applied thermal-mechanical load and how damage on the host structures affect the impedance response of piezoelectric sensor using FE analyses.

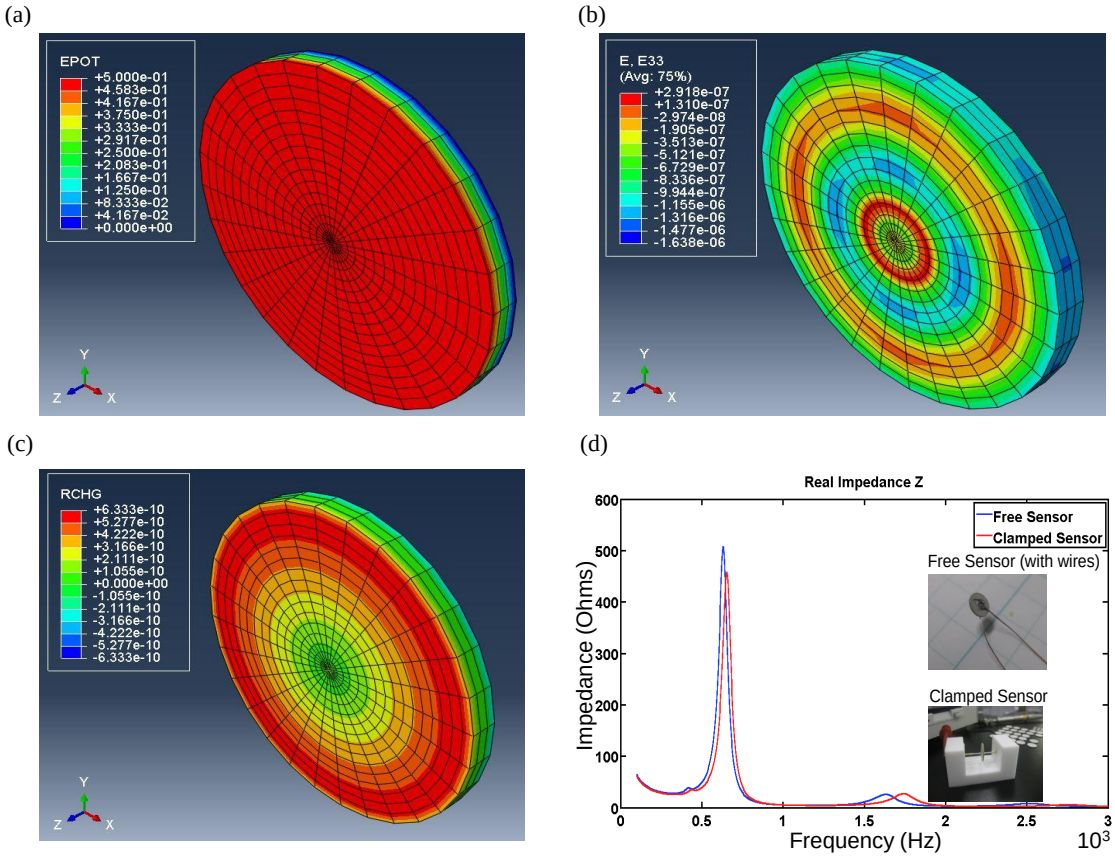

Figure 3.11: (a) Applied potential in FE analysis of PZT sensor (b) Calculated strain field in the poling direction of PZT sensor (c) Real values of charges calculated from FE analysis (d) Real Impedance response of a free and clamped PZT sensor.

3.4 Summary

In this section, the initial experimental and computational effort to develop and study the multifunctional hybrid interfaces was presented. Surface treatment methods that facilitate adhesion via mechanical interlocking and chemical bonding were employed to prepare the NiTi and cured Matrimid matrix composite prior to joining. Although the hybrid joints created in this section used the secondary bonding method, the adhesive used was Matrimid 5292 resin, the same as the matrix of the

cured composite. It was observed that chemical bonding formed at the interface between NiTi and Matrimid resin by using the EPII sol-gel treatment resulted in a strong hybrid interface. Thus in the subsequent sections, the sol-gel surface treatments are employed to prepare the metal surfaces before fabrication hybrid laminates.

The integration of piezoelectric sensors at the hybrid interfaces were also performed. Investigation on the effect of thin piezoelectric sensors presence at the interface on flexural response of the overall integrated structure shows that it did not significantly alter the mechanical behaviors of the hybrid composite beams in terms of effective stiffness of the beams and maximum load they can sustain. Impedance response of embedded PZT sensors was characterized as a function of thermal and mechanical loading. The results obtained in this preliminary shows these sensors were not sensitive to mechanical stimulus. Suggested future work regarding this aspect includes identifying the locations through the thickness of the sensors where the sensors can be more sensitive to mechanical loads. This can be performed both via experimental and computational effort. The contribution of this preliminary study was to confirm that no significant sacrifice in the mechanical response of the overall integrated structure was found as a result of integrating thin sensor series in the hybrid laminates. Since the focus of this study is to create and investigate the fracture behavior of hybrid interface as a function of temperature, in the subsequent sections, the use of piezoelectric sensors is eliminated.

4. HYBRID TI/NITI-EPOXY MATRIX COMPOSITE INTERFACE: PROCESSING AND CHARACTERIZATION*

This section presents our approach in utilizing an out-of-autoclave manufacturing process to fabricate hybrid composite laminates. The mode I fracture toughness of the hybrid metal-PMC interfaces were investigated at room and elevated temperature via the double cantilever beam test with on-line monitoring using Rayleigh backscattering fiber optics technique.[1]

4.1 Processing

4.1.1 Introduction to Hybrid Laminates Processing and Materials

To provide an understanding of the out-of-autoclave fabrication procedure as well as effect of elevated temperature on interfacial behavior of the hybrid co-cured metal/alloy-PMC interface, the epoxy matrix was utilized. The constituent materials for hybrid laminates investigated in this section are 3K plain weave T300 carbon fabric, metallic foil and epoxy Epikote-Epikure 04908 matrix. Three hybrid composite laminates were fabricated. Each hybrid laminate contained one layer of metallic foil, either Al (400 μm thick), or Ti (127 μm thick) or NiTi (127 μm thick). Layup of each laminate is as follows: $[0/90]_4$/Al/$[90/0]_4$, or $[0/90]_4$/Ti/$[90/0]_4$, or $[0/90]_4$/NiTi/$[90/0]_4$. It should be noted that even though the composite panel's reinforcements are not unidirectional laminae but rather carbon fabric layers, the

*Part of this section was reprinted from "An Investigation on Hybrid Interface Using On-line Monitoring Experiment and Finite Element Analyses" by Truong, H. T., Martinez, M. J., Ochoa, O. O., and Lagoudas, D. C. in *ICCM 20: 20th International Conference on Composite Materials, Copenhagen, Denmark, 19-24 July 2015.* and "Experimental and Computational Investigations of Hybrid Interfaces in Hybrid Composite Laminates" by Truong, H. T., Martinez, M. J., Ochoa, O. O., and Lagoudas, D. C. in *American Society of Composites-30th Technical Conference. 2015.*

[1]The experimental work presented in this section was performed at the Structural Integrity & Composite Laboratory, Faculty of Aerospace Engineering, the Delft University of Technology, Delft, the Netherlands, in collaboration with Prof. Marcias Martinez.

notation 0 and 90 was adopted to show that the fabric layers were oriented in direction along the warp and weft yarns, respectively. A 12 μm thick fluorinated ethylene propylene (FEP) film was placed adjacent to one side of the NiTi foil to create the initial crack.

4.1.2 Metal Surface Preparation Methods

Different surface treatment methods were employed on different metal foils selected for investigation in this study. The aluminum foil surfaces were prepared using the standard surface treatment procedure for Al in GLARE, performed at TU Delft where the foil underwent chromic acid anodization followed by priming with BR-127 primer. For the NiTi and Ti foils, acid etching followed by application of EPII sol-gel solution was employed to treat the surfaces. Acid etching was done following ASTM standard D2651-01 [74] by immersing the Ti and NiTi foils in an acid solution (1 liter of H_3PO_4 (83% concentration) and 75 milliliter HF (40% concentration)) for 2 minutes, then rinsing in distilled water and drying at 90 ^oC in an oven for 30 minutes. The sol-gel treatment done in this study used the commercial EPII sol-gel as described in Section 2.2. The solution was applied on the metal surfaces by brushing. The Ti and NiTi foils were then dried in ambient condition for 30 minutes and in an oven at 120 ^oC for 25 minutes followed by slow cooling to room temperature in the same oven.

4.1.3 Hybrid Laminate Manufacturing: An Out-of-Autoclave Process

A modified vacuum assisted resin tranfer molding process was performed to fabricate the epoxy hybrid laminates in this study. To ensure that the epoxy resin wet the entire laminate, both on the top and bottom sides with respect to the metal foil placed in the center, the layup was done so that two independent infusion flows were created. Although the resin flow on the top side is separated from that of the bottom

side, one resin inlet and one resin outlet were used for the entire panel. One flow mesh was placed on the bottom and one was placed on the top of the panel preform. The two flow mesh layers met at the resin inlet tube. Two peel ply layers separated the top and bottom flow mesh layers from the panel. A vacuum bag was placed on top of the bottom 8-layer carbon fabric stack and adjacent to the initial crack film to separate the top and bottom flow. Figure 4.1 demonstrates the partial layup of the hybrid laminates that shows the separation of the resin flow was achieved by using a layer of vacuum bag. The dashed blue lines in Figure 4.1(a) indicate the edges of this vacuum bag layer.

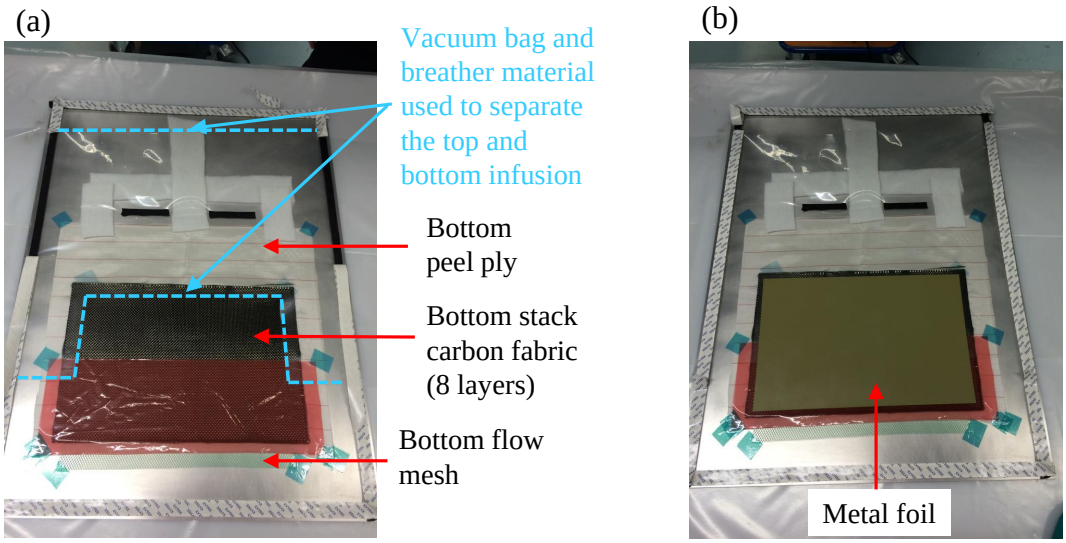

Figure 4.1: (a) Panel layup for bottom part of the double-infusion VARTM process. (b) Panel layup after the metal foil was placed on top of the bottom stack containing 8 layers of fabric and pre-crack film.

The Epikote 04908 resin and Epikure 04908 hardener, both of which are in liquid form at room temperature, were mixed with a resin-to-hardener ratio of 100:30. The

resin mixture was then degassed under full vacuum for 20 minutes. The degassed resin was infused when the panel preform was under 50 mbar vacuum. When the resin fronts of both the top and bottom flows were observed outside the panel preform, a reduction in vacuum was performed to allow more resin to flow into the panel at a slower rate and to increase the resin content in the panel. The vacuum was maintained at 300 mbar during the reduction. Figure 4.2 shows the infused panel ready for vacuum reduction and curing. Two resin fronts were observed near the resin outlet indicating that the double infusion was successful and two resin flows were achieved both on top and bottom of the panel with respect to the metal foil. Once infusion was finished, the panel was cured at 80 ^{o}C for 6 hours. The vacuum pressure was kept at 300 mbar pressure during the entire curing cycle. Two thermocouples were used to monitor temperature of the panel during the curing cycle. The locations of these temperature measurement sites are indicated in Figure 4.2. C-scan was subsequently performed on the cured laminate after manufacturing. No indication of big voids or dry spots was observed.

4.1.4 Thermal Characterizations of the Composite

Differential scanning calorimetry measurements were performed on the fabricated hybrid composite laminates. The measured glass transition temperature (T_g) is 83.2 $\pm$ 0.9 ^{o}C with the lower onset of 76.5 ^{o}C. To avoid softening of the polymer matrix, 60 ^{o}C was selected for elevated temperature testing. In addition, thermal gravimetric analysis was performed on the composite part of the hybrid laminates. It was found that the composite had a fiber volume fraction of 66 %.

4.2 Mode I Fracture Toughness Testing

The DCB specimens prepared from the fabricated hybrid composite laminates containing Al−T300-PW/ Epoxy 04908, Ti−T300-PW/ Epoxy 04908, and NiTi−T300-

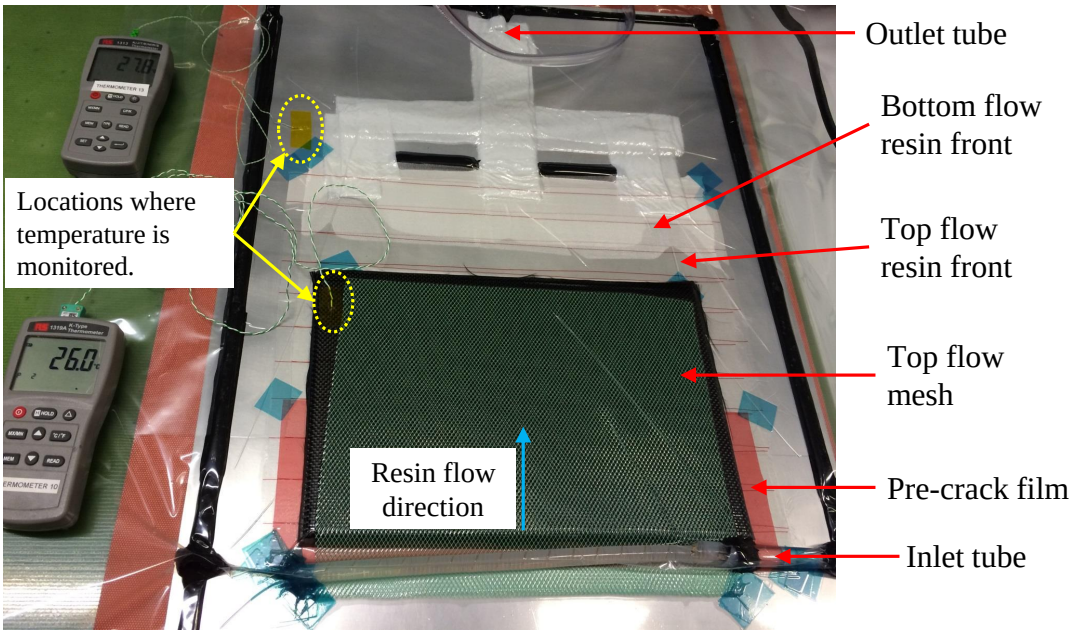

Figure 4.2: Hybrid panel after the infusion completed. Two resin flow fronts were observed indicating the double infusion was successful and resin flows were achieve on both sides of the laminate with respect to the metal foil.

PW/ Epoxy 04908 interfaces were tested at room and elevated temperature. These tests were performed to investigate the effect of temperature on mode I fracture toughness of these hybrid laminates. Table 4.1 presented the test matrix for mode I fracture toughness characterization performed in this section.

4.2.1 DCB Specimen Preparation

Strips of 25 mm nominal width were cut from all four edges of the fabricated panel before cutting the DCB specimens to ensure uniform thickness in all specimens. Piano hinges were bonded onto the specimens using adhesive 3M Scotch-Weld 9323. The specimens were painted white on one edge to facilitate observation of the crack tip during testing. A scale created by millimeter paper was adhesively bonded on

Table 4.1: Test matrix for mode I fracture toughness characterization of hybrid Al/Ti/NiTi−T300-PW/ Epoxy 04908 interfaces. The 3^{rd} and 4^{th} columns show the number of specimens tested at 25 ^oC and 60 ^oC, respectively. The numbers in () in these columns indicate the number of specimens tested with in-situ fiber optic distributed strain measurement.

Interface name	**Layup**	**25** ^oC	**60** ^oC
Al−T300-PW/Epoxy04908	$[90/0]_4/Al/_{\mathbf{ICF}}/[0/90]_4$	3(1)	3(1)
Ti−T300-PW/Epoxy04908	$[90/0]_4/Ti/_{\mathbf{ICF}}/[0/90]_4$	3	3
NiTi−T300-PW/Epoxy04908	$[90/0]_4/NiTi/_{\mathbf{ICF}}/[0/90]_4$	3(1)	3(1)

the painted edge of the DCB specimen to aid the measurement of crack length. Based on DSC measurements of the fabricated hybrid composite, glass transition temperature (Tg) is 83.2 ± 0.9^{o}C with the lower onset of 76.5^{o}C. As a result, 60^{o}C was selected for elevated temperature investigation for the studied material system to avoid softening effect of the matrix when heated near its T_g. DCB tests were carried out at 25^{o}C and 60^{o}C following ASTM D5528 guidance [75]. The loading and loading rates for all tests were 2 mm/min and 10 mm/min with a data acquisition rate of 10 Hz. Elevated temperature tests were carried out in an environmental chamber. Thermocouples were taped to the top and bottom sides of the specimens prior to being loaded to the test frame. Temperature of the specimen was monitored during heating and upon loading. When each elevated specimen's temperature reached 60 ± 1^{o}C, it was let stable for 15 minutes to make sure that temperature profile in the specimen was uniform before being tested. Pre-cracking step was done to create a natural crack front instead of a straight crack created by the FEP film. Thus, each specimen was loaded in displacement-controlled mode at 2 mm/min rate until

a crack extension of 3 to 5 mm was observed. The specimen was then unloaded at a rate of 10 mm/min then reloaded at 2 mm/min for further crack propagation. The crack length was monitored using a camera placed outside the environmental testing chamber, which has a glass door for visual observation of its interior.

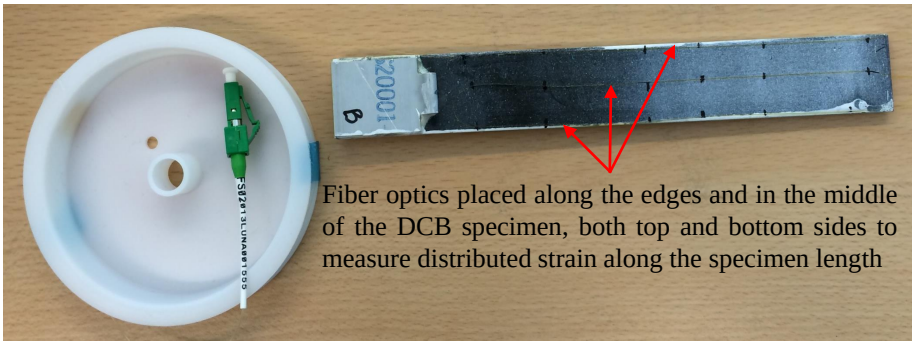

Figure 4.3: DCB specimen with fiber optics bonded on the surfaces

4.2.2 On-line Monitoring with Raleigh Backscattering Fiber Optics

Besides visual observation of the crack propagation along the side of the DCB specimen as described above, an on-line monitoring technique using fiber optics was performed during the DCB tests to provide additional information for the location of crack tip across the specimen's width. This technique is based on the Rayleigh backscattering phenomenon and allows the users to measure axial strain along the specimen length. Strain measurements were obtained with a spacial resolution of 1.3 mm at a data acquisition rate of 1 Hz. The data acquisition system used for distributed strain measurements in this study is the commercial Optical Frequency Domain Reflectometry (ODISI-B) manufactured by Luna Technologies, Inc. Comparisons between this new technique and traditional strain gauges were studied by

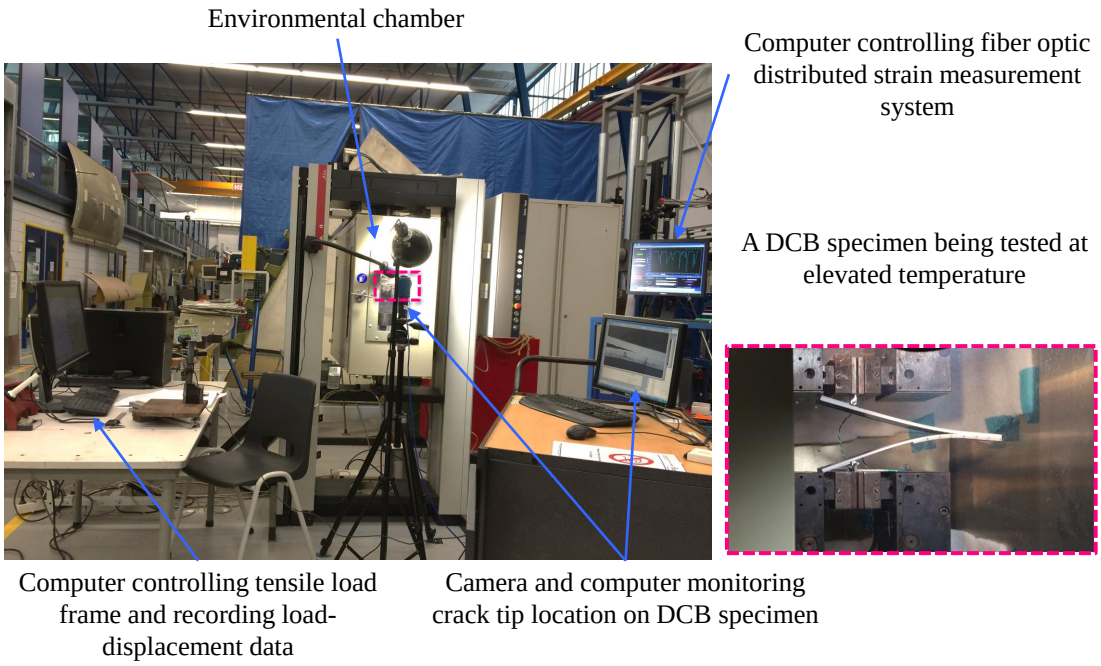

Figure 4.4: High temperature DCB test setup

Martinez *el al.* [76]. It was shown that the two methods of strain measurements are in good agreement with each other.

Rayleigh backscattering fiber optics sensors were glued along the longitudinal edges, both on the top and bottom sides of the DCB specimen for in-situ distributed strain measurements. An example of a DCB specimen with fiber optics bonded on the surface is shown on Figure 4.3(a). A schematic of the fiber optics path on the top surface of the DCB specimen is illustrated by Figure 4.3(b). An illustration of the test set-up with in-situ strain measurement system is shown in Figure 4.4.

4.2.3 Results and Discussion

4.2.3.1 Al– T300-PW/Epoxy04908 Interface

Representative load-displacement response from the DCB tests on the hybrid specimens containing Al foil both at 25 ^oC and 60 ^oC are presented in Figure 4.5. Unstable crack propagation, i.e. the repeated crack advancing and arresting behavior due to the weave architecture in the PMC, is observed at both room and elevated temperature as indicated by the saw-tooth behavior in the load-displacement curves. In addition, at 60 ^oC, delamination at the hybrid interface was more unstable than at 25 ^oC. This is revealed by the larger saw-tooth patterns in the load-displacement curves from tests at 60 ^oC compared to the patterns observed from test load-displacement curves at room temperature. At elevated temperature, the crack propagated longer distances and there are fewer number of crack propagations in comparison with crack progression behavior at room temperature.

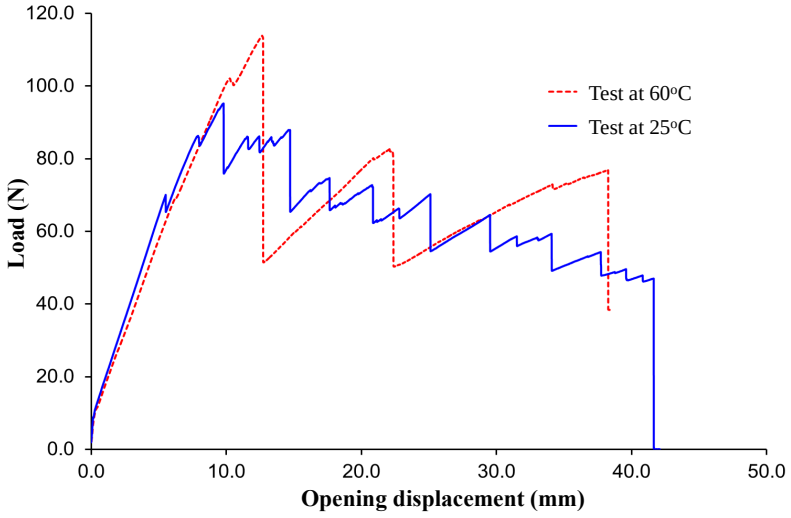

Figure 4.5: Representative load-displacement response from DCB tests at 25 ^{o}C and 60 ^{o}C of Al-T300-PW/ Epoxy 04908 interface.

From the FEA results, the ratio of mode-II to mode-I strain energy release rates was calculated to be 3.1%. The calculated mode-I dominant strain energy release rate values for DCB tests performed at both 25 ^oC and 60 ^oC are presented in Figure 4.6. It is observed that fracture toughness of the hybrid interface at 60 ^oC is higher than that at 25 ^oC. The fracture surfaces of the Al−T300-PW/ Epoxy 04908 revealed 100 % cohesive failure. Thus, the fracture behavior of the composite as a function of temperature governed the fracture behavior of the hybrid Al−T300-PW/Epoxy04908 interface fabricated in this work. The high fracture toughness at elevated temperature compared to that obtained at room temperature is attributed to the softening of the epoxy matrix near its glass transition temperature.

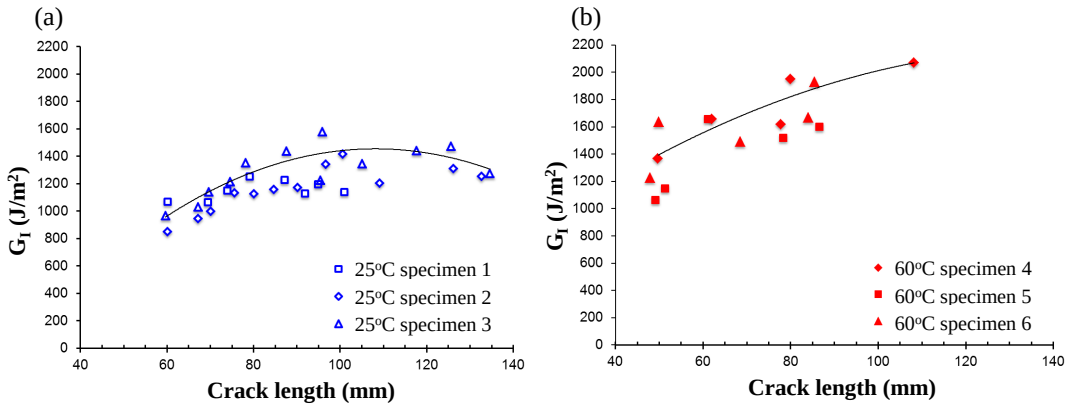

Figure 4.6: Resistance curve from DCB tests of Al−T300-PW/Epoxy04908 interface at (a) 25 ^oC and (b) 60 ^oC.

4.2.3.2 Ti−T300-PW/Epoxy04908 Interface

The load-displacement response and resistance curves from the DCB tests at both 25 ^{o}C and 60 ^{o}C of the Ti−T300-PW/Epoxy04908 interface are presented in Figure 4.7. The load-displacement curves at 25 ^{o}C presented in Figure 4.7(a) show some

saw-tooth features at the beginning of crack propagation. However, as the crack propagates further away from the pre-crack, the response became relatively smooth. Smooth load-displacement curves were also obtained from the test at 60 ^{o}C. Smooth load-displacement response implies that the crack propagated at a relatively smooth interface, showing minor influence of the composite and indicating adhesive failure. The fracture toughness values presented in Figure 4.7(b) shows a corresponding trend in the failure mode to that observed from the load-displacement results. At 25 ^oC, the R-curves show initial toughening behavior indicating cohesive failure mode. However, as the crack propagated, adhesive failure mode was revealed, as indicated by the decrease in fracture toughness values. At 60 ^oC, the R-curves are relatively flat. No toughening behavior was observed and the fracture toughness values are one-third time as low as that of the room temperature. This indicates that the adhesive failure mode overshadowed the fracture toughness measurement. That is, the Ti−T300-PW/Epoxy04908 hybrid interface in this work exhibited weak interfacial adhesion at 60 ^oC. It stably failed in adhesive mode as the crack propagated along the Ti surface and resulted in low fracture toughness. These observations were proved by visual inspection of the fracture surfaces post-fracture toughness tests.

4.2.3.3 NiTi− T300-PW/Epoxy04908 Interface

The load-displacement curves measured from the DCB tests of NiTi-PMC interface are shown on Figure 4.8. Unstable crack propagation, i.e. the repeated crack advancing and arresting behavior due to the weave architecture in the T300-PW/Epoxy04908 composite, is observed at both room and elevated temperature as indicated by the saw-tooth behavior in the load-displacement curves. In addition, similar to the Al−T300-PW/Epoxy04908 interface behavior, at 60^{o}C, delamination at the hybrid interface is more unstable than at 25^{o}C. This is revealed by the larger

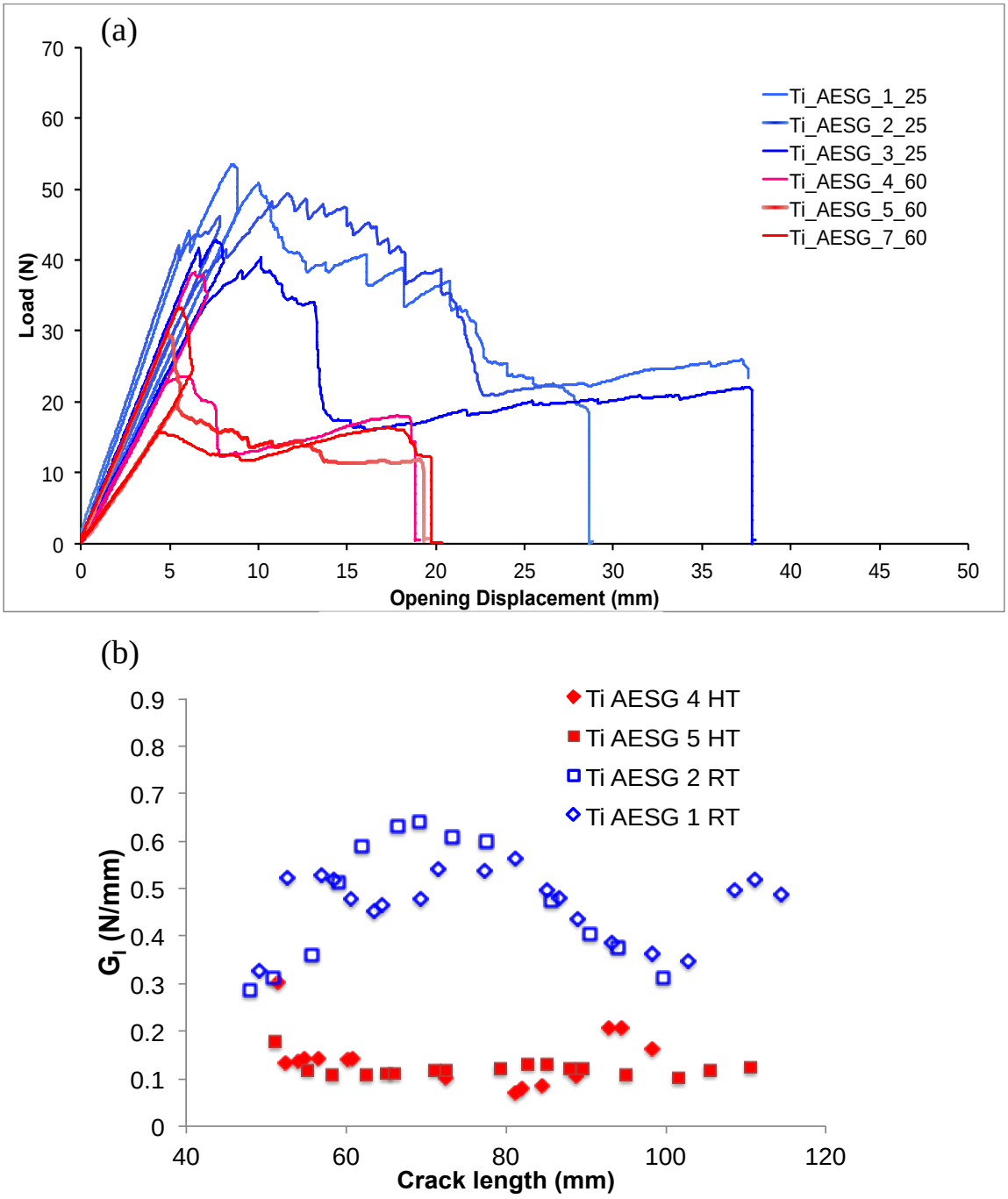

Figure 4.7: Results from DCB tests at 25 ^{o}C and 60 ^{o}C of Ti−T300-PW/ Epoxy 04908 interface: (a) Load-displacement response (b) Resistance curve.

saw-tooth patterns in the load-displacement curves from tests at 60^{o}C compared to the patterns observed from room temperature test load-displacement curves. At elevated temperature, the crack propagates longer distances and there are fewer number of crack propagations in comparison with crack progression behavior at room temperature. Example of unstable crack growth behavior at 60^{o}C is shown on Figure 4.10 where the crack propagates more than 10 mm at a time.

From FE analyses, the ratio between mode-I and mode-II strain energy release rates was calculated to be less than 2%. Thus, G_{IC} values for the hybrid interface in this study were calculated assuming symmetric configuration and following ASTM standard D5528 guidance. The calculated mode-I dominant strain energy release rate values for DCB tests done at both 25^{o}C and 60^{o}C are shown on Figure 4.9. It is observed that fracture toughness of the hybrid interface at 60^{o}C is higher than that at 25^{o}C. Visual inspection of the fracture surfaces reveal 100 % cohesive failure. As a result, similar to the observation from the Al−T300-PW/Epoxy04908 interface, the fracture behavior of the composite as a function of temperature governed the fracture behavior of the hybrid NiTi−T300-PW/Epoxy04908 interface fabricated in this work. Fracture toughness at higher temperature shows higher value because the epoxy matrix softened and toughened at temperature near its T_g.

4.2.3.4 Fracture Surfaces Investigation

Figure 4.11(a) and (b) shows the typical fracture surfaces of the NiTi−T300-PW/Epoxy04908 DCB specimens tested at 25 ^{o}C and 60 ^{o}C respectively. As illustrated by the cross-section schematic in Figure 4.11(c), the top side in 4.11(a) and (b) is the NiTi surface while the bottom side is the bottom T300-PW/Epoxy04908 composite surface. No adhesive failure, i.e. failure that occured adjacent to the NiTi surface, was observed from the fracture surfaces of specimens tested both 25 ^{o}C and

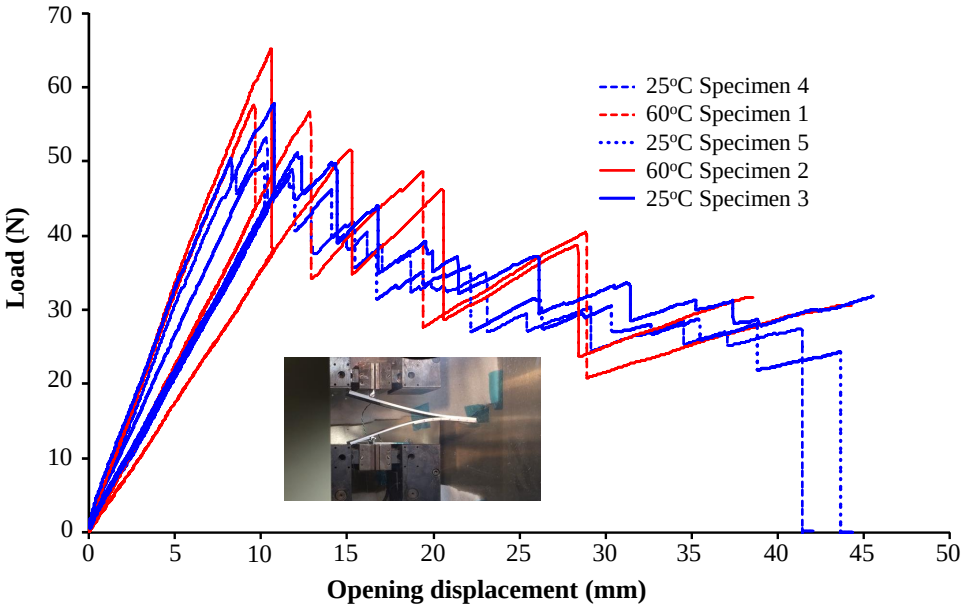

Figure 4.8: Load-displacement response from DCB tests at 25 ^{o}C and 60 ^{o}C of NiTi−T300-PW/Epoxy04908 interface.

60 ^{o}C. Failure mode was predominantly cohesive inside the resin-rich region toward the T300-PW/Epoxy04908 composite side or in the first carbon fabric layer of the T300-PW/Epoxy04908 composite. Figure 4.11(d) shows optical microscopic images of both top and bottom side of a DCB specimen tested at 60 ^{o}C. The difference in fracture behaviors of room and elevated test specimens was revealed by scanning electron microscopic fractographics shown on Figure 4.12. Both Figures 4.12(a) and 4.12(b) show the fracture surface on the NiTi side. As seen on Figures 4.12(a), at room temperature, there is more fracture of fibers observed on the NiTi surface. On the other hand, more imprints of fibers were seen on the NiTi fracture surface from the 60 ^{o}C tests. This indicates that at elevated temperature, failure occurs more at the fiber-matrix interface due to the softening of the polymer matrix. In addition, at higher temperature, the polymer matrix becomes softer and more ductile than at

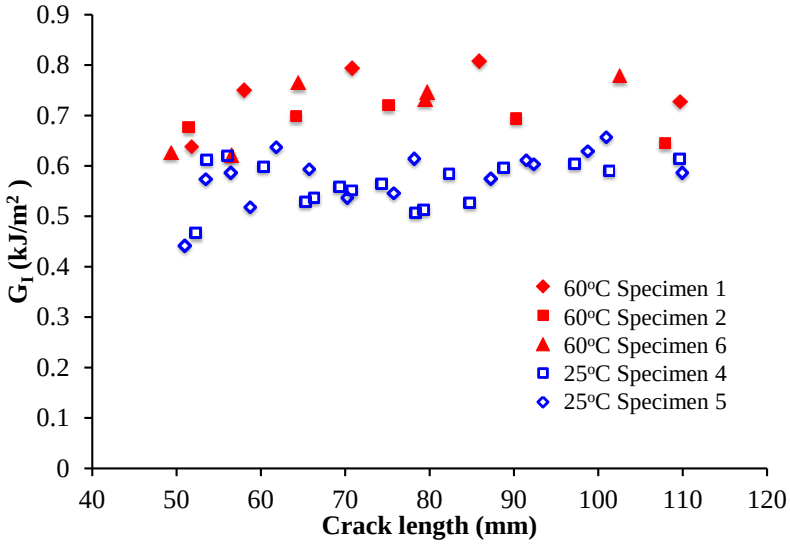

Figure 4.9: Mode I resistance curves from DCB tests at 25 ^{o}C and 60 ^{o}C of NiTi−T300-PW/Epoxy04908 interface.

room temperature. The cusps features observed on the 60 ^oC fracture surface were formed due to the shearing between the fiber and matrix as the fiber-matrix interface weakened at high temperature. The formation of these cusps is an additional failure mechanisms, requiring more energy to dissipate during the fracture process. This explains why the hybrid interfacial region is tougher at 60 ^{o}C than at 25 ^{o}C as observed earlier in Figure 4.9.

4.2.3.5 Distributed Strain Measurement Results

Figure 4.13 shows the distributed strain along the length of the DCB specimen using Rayleigh backscattering fiber optics measurements. In bending, the top and bottom sides of the loaded DCB specimen were under compression. As expected, negative strain values were obtained. It was observed that along the specimen's length, the compression strain magnitude increases from the delaminated end of the beam, or the loading pin, to the vicinity of the crack tip, where the maximum com-

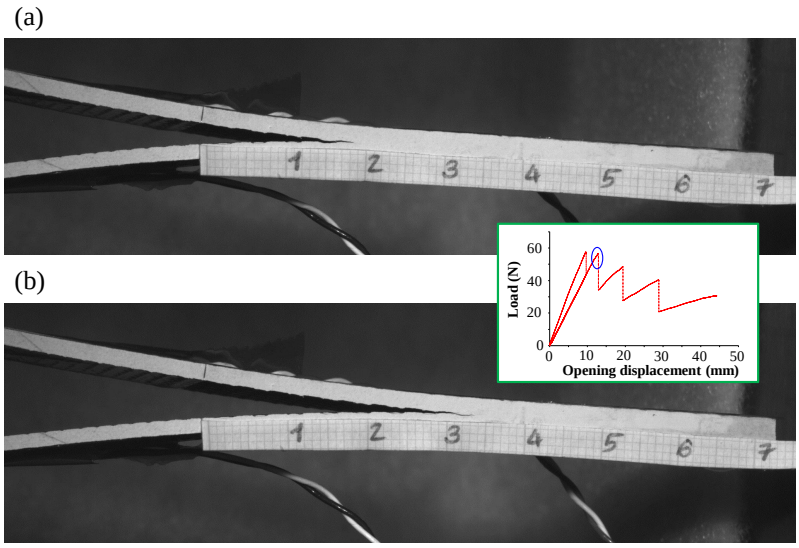

Figure 4.10: Highly unstable crack growth behavior observed in Al−T300-PW/ Epoxy 04908 and NiTi−T300-PW/ Epoxy 04908 interfaces tested at 60 ^oC (a) Before the crack propagated i.e. before the second peak load, highlighted by the blue oval on the load-displacement graph, was reached. (b) After the crack propagated.

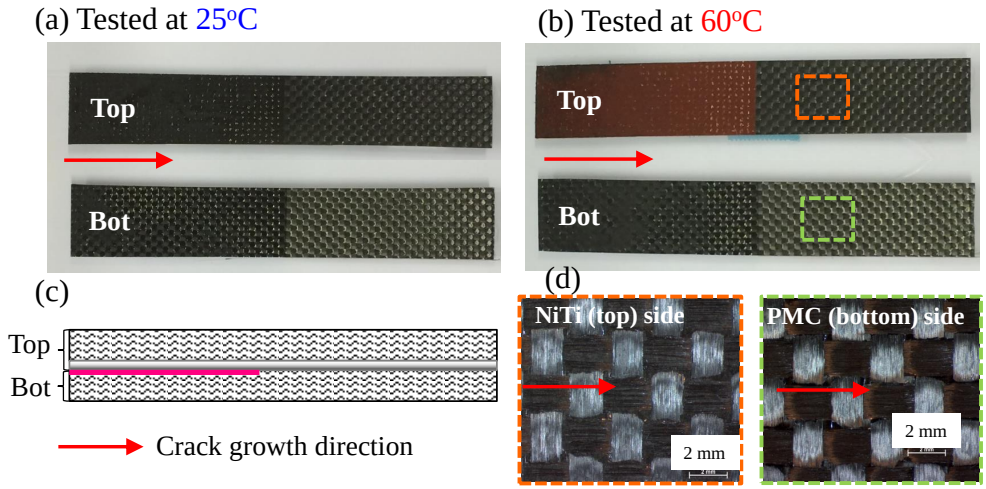

Figure 4.11: Fracture surfaces from NiTi−T300-PW/Epoxy04908 interface (a) 25^{o}C (b) 60^{o}C

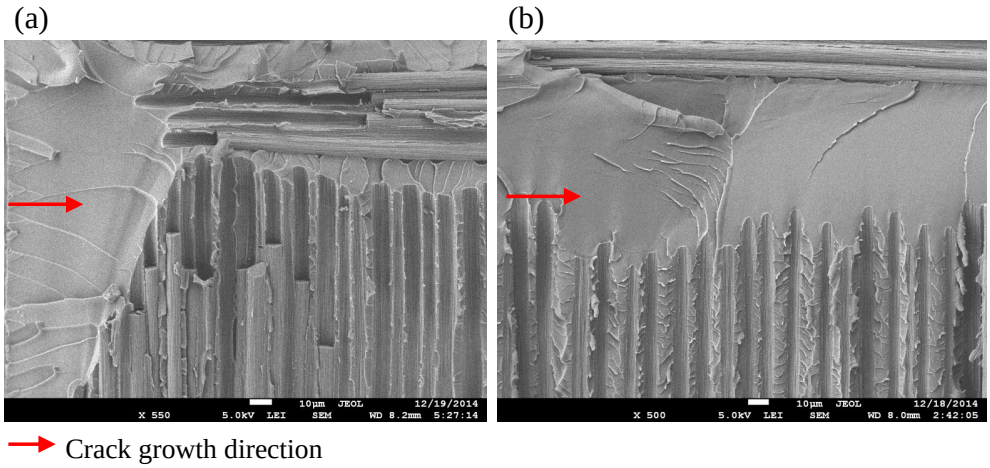

Figure 4.12: Fracture surface on NiTi side from specimens tested at (a) 25^{o}C (b) 60^{o}C

pression strain value was measured, and then immediately decayed to zero strain. Three examples of crack growth-arresting are shown on Figure 4.13. The evolution of crack progression follows the black arrows indicated on the strain profiles graph. As the crack tip experiences a critical strain value, the strain energy was released and the crack tip moved to a new location. At this new location, the magnitude of the compression strain that the crack tip undergoes resets back an amount of approximately 500 x 10^{-6}. This strain value then gradually increases to a critical value then the strain energy was released again and the crack propagates accordingly. This crack growth-arresting behavior repeats until the specimen was fully delaminated. The behavior observed from the distributed strain measurements supported the saw-tooth patterns seen on the load-displacement curve.

4.3 Summary

In this section, it was demonstrated that an effective out-of-autoclave manufacturing method, double-infusion VATRM, was successfully employed to create a

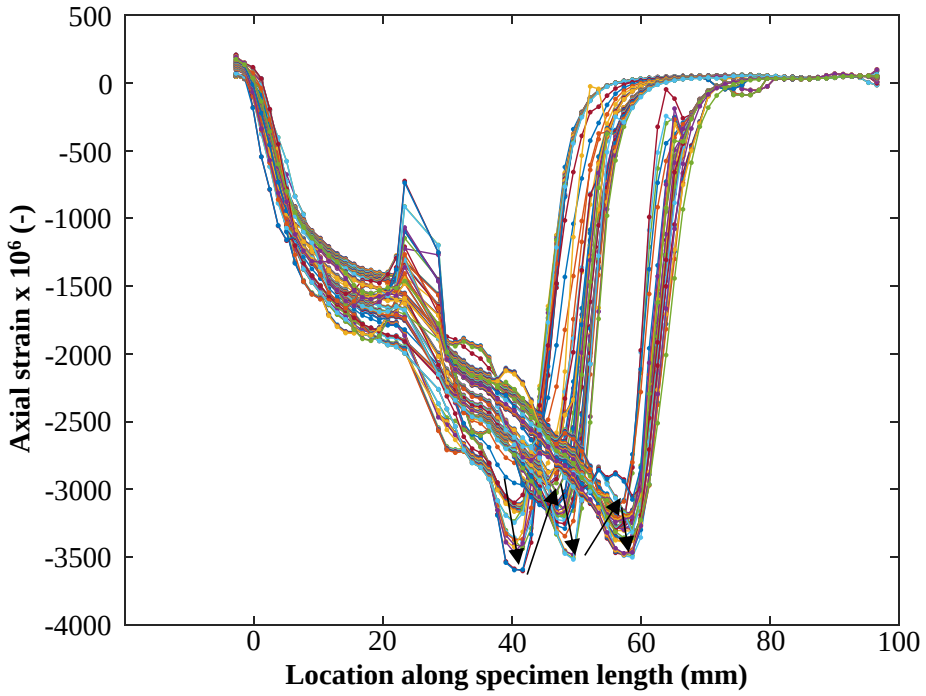

Figure 4.13: Strain profiles along the length of a NiTi−T300-PW/Epoxy04908 specimen undergoing DCB test as measured using fiber optics

hybrid composite laminate that was composed of a layer of metal foil (Al, Ti, or NiTi) placed at the center of sixteen layer plain weave T300 carbon fabric with epoxy Epikote-Epikure 04908 matrix. The hybrid interface between metal foil and the epoxy matrix composite was created by co-curing and without the use of any additional adhesive. The mode I fracture behavior of the fabricated hybrid interface was investigated at both room and elevated temperature. It was observed that at the interfaces where the mode of failure was cohesive, the crack propagation behavior at the hybrid interface was more unstable at elevated temperature compared to that at room temperature. The strain energy release rates required for the crack to propagate at elevated temperature was higher than that needed at room temperature. This observation is applicable to the NiTi−T300-PW/Epoxy04908 and

Al−T300-PW/Epoxy04908 interface. It was observed that the fracture behavior of the composite as a function of temperature governed the fracture behavior of the hybrid interfaces fabricated in this work. The fracture toughness at higher temperature shows higher value because the epoxy matrix softened and toughened at temperature near its T_g. The hybrid Ti−T300-PW/Epoxy04908 interface fabricated in this work was weak and exhibited adhesive failure mode, resulting in low G values on the resistance curves. It should be noted that the same surface treatment procedure that employed acid etching and EPII sol-gel treatment was performed on both the Ti and NiTi foil prior to fabrication of the laminates. Thus, it can be concluded that this surface treatment procedure was more effective on the NiTi than on the Ti foil. In addition, for the first time, in-situ Rayleigh backscattering fiber optics measurements were obtained during DCB experiments. This new technique to measure distributed strains allows us to interpret the DCB experiment in a new way and enables the visualization of strain energy release upon crack propagation.

5. HYBRID TI/NITI-POLYIMIDE MATRIX COMPOSITE INTERFACE: PROCESSING AND PHYSICAL CHARACTERIZATION[1]

This section details our approach to develop high temperature, hybrid composite material systems using a custom-designed robust interface to fabricate Ti/NiTi foil-polyimide matrix hybrid composites. The highlight of the experimental work carried out in this section is utilizing laser ablation and a custom-synthesized sol-gel treatment on Ti and NiTi foil. The treated metallic surfaces were co-cured in carbon fabric reinforced polyimide matrix composites to create the hybrid laminates. The results from microscopy and physical characterizations of the hybrid interface cross-section as well as composite laminates are presented herein.

5.1 Materials Descriptions

The materials used to fabricate the hybrid laminates include prepreg of 8-harness satin weave T650 carbon fabric AFR-PE-4 polyimide matrix and Ti or Ti-50.8at%Ni foil with thickness of 127 μm. Details of these materials were described in Section 2.1.

5.2 Surface Treatments: Laser Ablation and Custom Synthesized Sol-gel Treatments

5.2.1 Laser Ablating Metallic Surfaces

As an alternative to surface treatment methods that use toxic chemicals or produce non-uniformity in surface roughness, laser ablation was employed in this work. The effects of laser ablation performed on Ti and NiTi surfaces include cleaning oxide layer and creating patterned micro-roughness that can be designed and engineered

[1]The experimental work presented in this section was performed at NASA Langley Research Center, Hampton, VA in collaboration with Drs. John Connell and Frank Palmieri.

on the metal surfaces as well as increasing surface wettability for better adhesion with polymer resins. Adopting the approach presented by Palmieri *et al.*, a set of laser parameters were selected to ensure a full coverage of laser ablation on the entire Ti and NiTi foil surfaces [44, 45]. These parameters are presented in Table 5.1. Figure 5.3 show SEM images of the laser ablated Ti and NiTi foil surfaces. Prior to proceeding to the subsequent manufacturing process, the foils were laser ablated with full coverage on both sides.

Table 5.1: Selected laser ablation parameters

Laser Ablation Parameter	**Value**
Power	1.5 W
Pitch	1 mil
Frequency	80 kHz

5.2.2 Sol-gel Surface Treatment

All three sol-gel formulations presented in Section 2.2 were employed for surface treatment of Ti and NiTi foils in the hybrid laminates fabricated and discussed in this section. The compositions of these sol-gel solution are summarized as follows.

- EPII sol-gel (commercial sol-gel solution developed by the Boeing Company): mixture of glycidoxypropyltrimethoxysilane, tetra-n-propoxyzirconium (TPOZ), propyl alcohol, acetic acid and deionized water [43].
- AP sol-gel (modified EPII sol-gel): mixture of aminophenyltrimethoxysilane, TPOZ, propyl alcohol, acetic acid and deionized water [43].

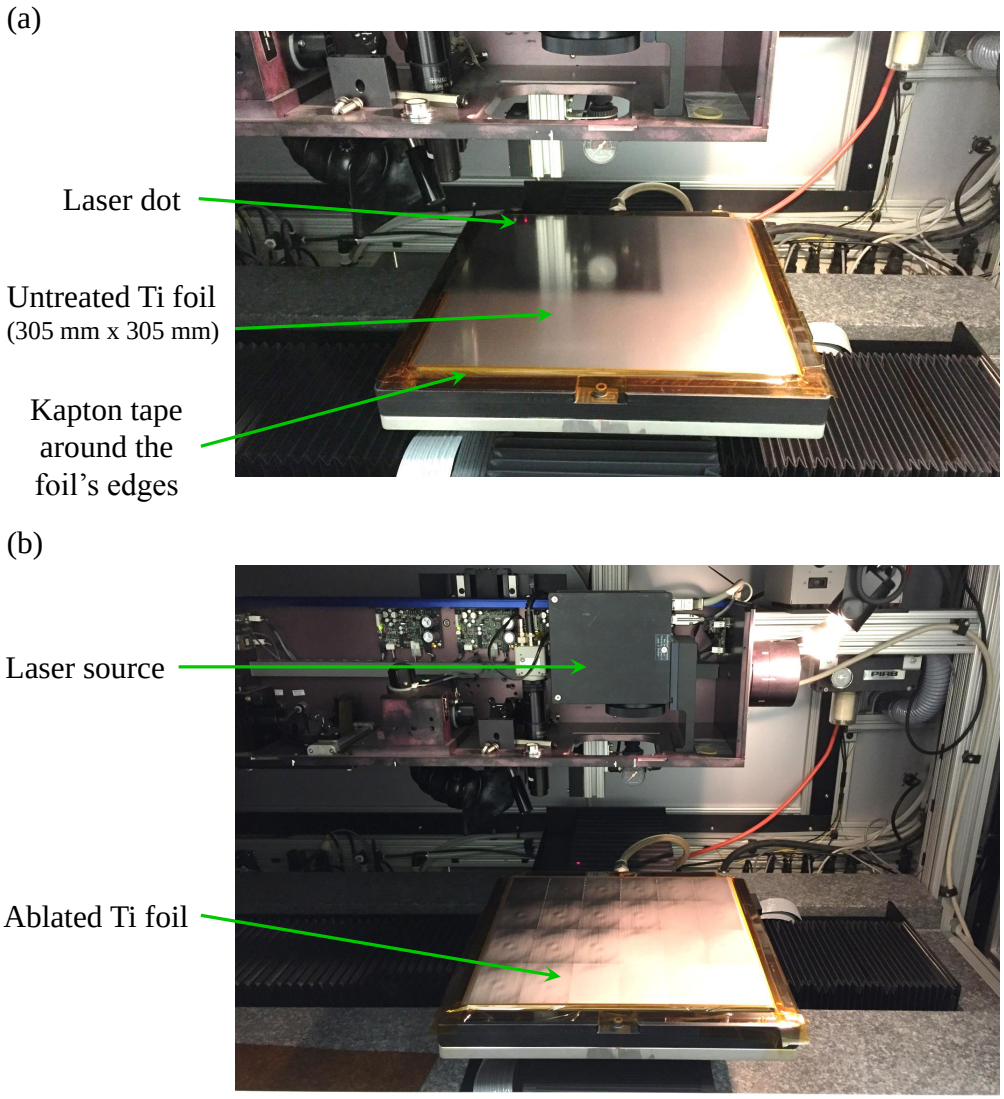

Figure 5.1: Laser ablation setup (a) before and (b) after the Ti foil laser ablated.

- PEI sol-gel (novel phenylethynyl imide silane sol-gel solution developed at NASA Langley Research Center): mixture of pendent phenylethynyl imide oligometric disilane and tetraethoxysilane [71, 72].

Details of the synthesis of PEI sol-gel are presented in Figure A.1 and A.2 in

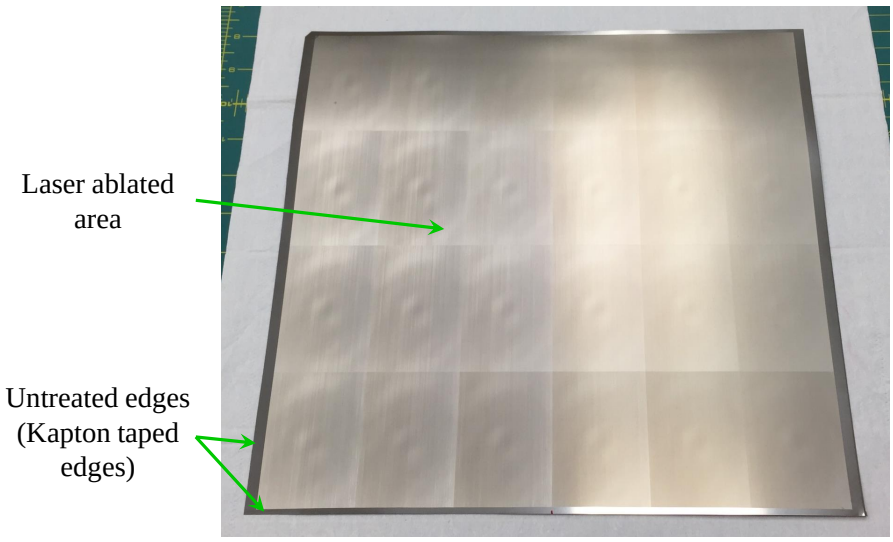

Figure 5.2: Image of one side of the Ti foil after undergoing laser ablation surface treatment.

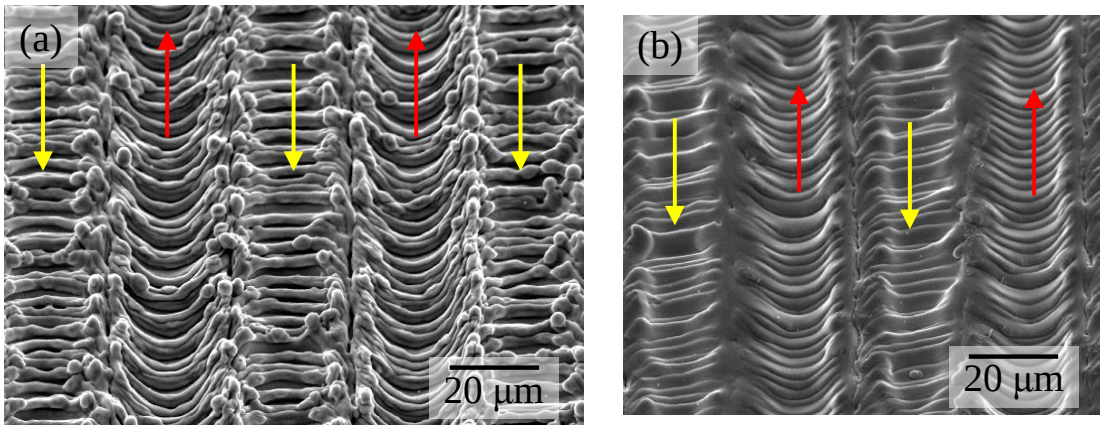

Figure 5.3: (a) Laser ablated Ti surface. (b) Laser ablated NiTi. *Arrows indicate laser ablation direction.*

Appendix A. It should be noted that a hydrolysis step took place in either 1 hour or 16 hour prior to the application of this sol-gel solution to the metal foil surfaces. The PEI sol-gel solutions hydrolyzed in the two different time are herein refered to as PEI_1-hour and PEI_16-hour.

The surface treatment procedure performed on each of the Ti and NiTi foils in this work is outlined as follows.

- Perform laser ablation on both sides
- Immediately after the laser ablation process completed, gently and thoroughly wipe both sides of the foil using lint-free cloth and isopropanol
- After the cleansing solvent dried, apply sol-gel solution onto ablated and cleaned surfaces by brushing or spraying both surfaces
- Allow the sol-gel layer to dry at room temperature in ambient condition for 30 minutes
- Cure the sol-gel layer in a pre-heated oven. For EPII and AP sol-gel systems, the sol-gel treated foils were cured at 120 ^oC for 30 minutes. For the PEI sol-gel, the foils were cured at 220 ^oC and 110 ^oC for 30 minutes at each temperature.
- Allow the sol-gel treated and cured foil to undergo control-cooling to room temperature in the same oven

5.3 Activating Shape Memory Effects in NiTi Foil

5.3.1 Heat Treatment Procedures

The as-received Ti-50.8 at%Ni foil did not possess any shape memory behavior as evidenced by the fact that no endothermic and exothermic peaks was observed from differential scanning calorimetry measurements. Thus, additional heat treatment

was required in order to activate the shape memory and/or pseudoelastic effects in the the NiTi foil prior to the fabrication of hybrid laminates containing NiTi foil. The effect of different thermomechanical processing parameters and heat treatment procedures on superelastic behavior and phase transformation temperature of Ni-rich NiTi alloys has been previously studied [77, 78]. Two different heat treatment procedures were employed on the specific NDC as-drawn superelastic Ti-50.8 at%Ni foil (127 μm thick) used in the present work. The heat treatment in this work was performed using an air-furnace. The detail procedures are described as follows.

- Heat treatment 1 (HT1): The air-furnace was pre-heated to 500 ^oC and allowed to stabilize for at least 30 minutes. The NiTi foil was then placed close to the center of the pre-heated furnace. Due to the heat loss when the furnace door was opened for the NiTi foil placement, temperature was dropped an amount of approximately $10 - 20$ ^oC. Once the furnace temperature reached back up to 500 ^oC, the foil was heat treated at 500 ^oC for 30 minutes, then taken out of the furnace and immediately water quenched.

- Heat treatment 2 (HT2): Similar to heat treatment 1, the NiTi foil was first heat treated at 500 ^oC in an air-furnace. However, the heat treatment time was 1 hour. Then, the foil was furnace-cooled and underwent aging at 400 ^oC for 45 minutes followed by water quenching.

It should be noticed that the NiTi foil being heat-treated for hybrid laminate fabrication has in-plane dimensions of 304.8 mm x 304.8 mm. In addition, it needs to be flat during and after the heat treatment. In order to avoid the formation of thick oxide layers on the foil's surfaces after its being subjected to high temperatures during the heat treatment, the use of a vacuum or inert gas furnace is desirable. However, no vacuum or inert gas furnace that could facilitate the foil's dimensions

was available or accessible. Thus, prior to being heat-treated, the foil was placed in between two 350 mm x 350 mm sheets of stainless steel foil, which were then seam-welded to create a metallic bag. The stainless steel bag was subsequently vacuumed and sealed to protect the NiTi foil from oxidation during the heat treatment in an air furnace. As a results, only the outer surfaces of the stainless steel vacuum bag was oxidized after the heat treatment.

5.3.2 Thermal Characterization of NiTi Foil Using Differential Scanning Calorimetry

Differential scanning calorimetry was performed to obtain the transformation temperature of the NiTi foil after undergoing each of the two different heat treatment procedures described in Section 5.3.1. In addition to the NiTi foil as-treated by HT1 and HT2, the influence of laser ablation and curing cycle of the T650-8HS/AFR-PE-4 composite laminates on the transformation temperature of the NiTi foil was investigated using DSC. Two DSC specimens for each combination of thermal-mechanical processing parameters were tested. The specimens were cut using a low-force diamond saw. The DSC experiments were carried out using a NETZSCH DSC 204 F1 machine. Each specimen was first cooled to -80 ^oC and allowed to equilibrate for 1 minute, then subjected to two heating (-80 ^oC to 150 ^oC) and cooling (150 ^oC to -80 ^oC) cycles. A heating and cooling rate of 10 $^oC/min$ was used.

Representative DSC result for each type of specimens tested is presented in Figure 5.4. For all cases, the results from the second heating and cooling cycle of each DSC experiment are reported. As seen in Figure 5.4(a), the NiTi foil undergoing heat treatment 1 exhibits two-step austenitic transformation upon heating and two-step martensitic transformation upon cooling. This is supported by the existence of two endothermic peaks and two exothermic peaks on the DSC curve. On cooling, the

first exothermic peak, which occurs at higher temperatures, is associated with the transformation from the austenite B2 phase to an unstable martensite R-phase while the second peak is attributed to the transformation from R-phase to a more stable martensite phase, B19'. Similarly, upon heating, the first and second endothermic peaks are respectively ascribed to the transformations from B19' to R-phase and from R-phase to B2. Multiple-step transformations in Ni-rich NiTi alloys have been previously observed and investigated by Carroll *et al.* [79] and Wang *et al.* [80]. It is well known that the presence of metastable Ni_4Ti_3 precipitates in Ni-rich NiTi and dislocation substructures created during processing results in a microstructure that favors the formation of the R-phase before stable B19' is formed during martensitic transformation [79].

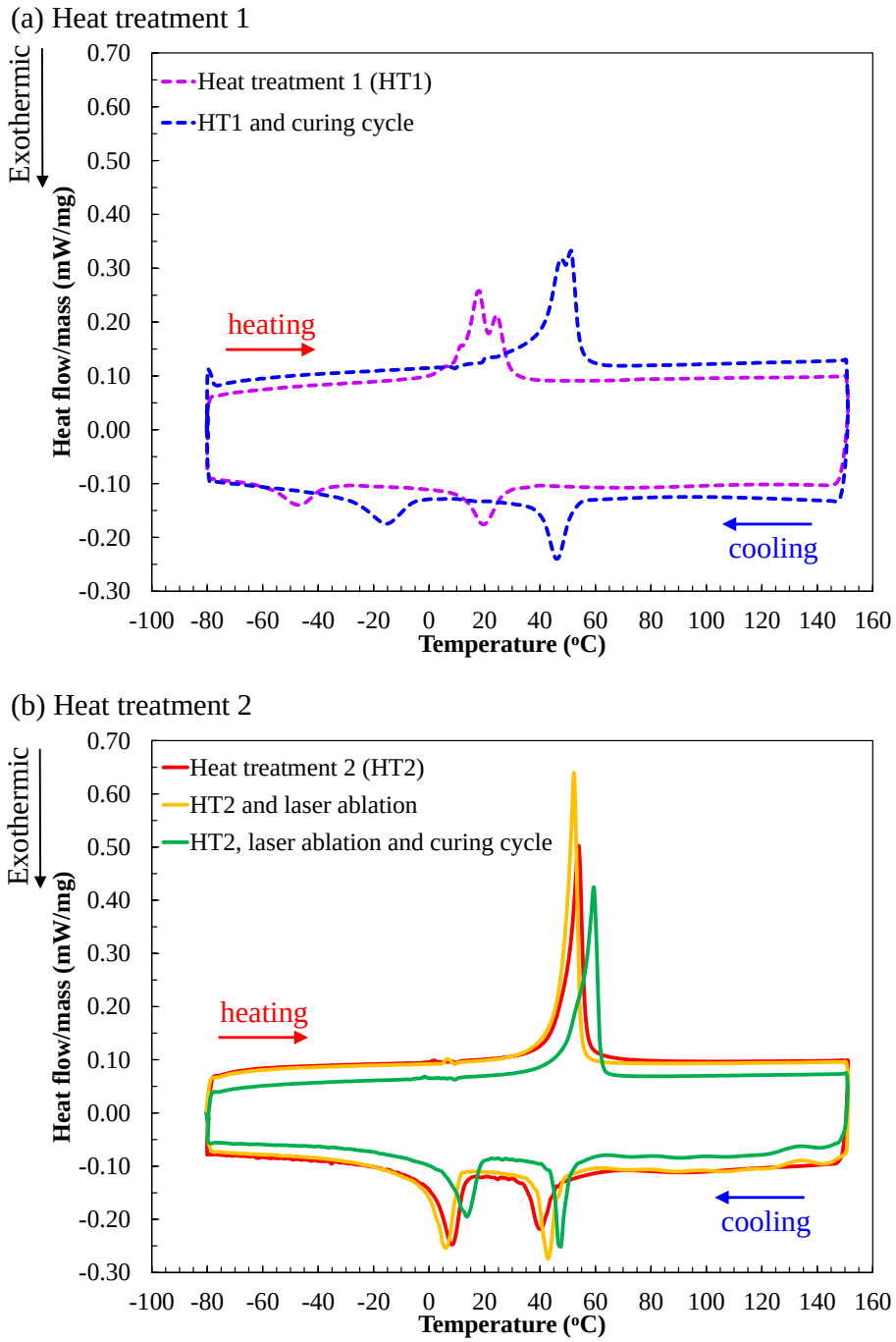

Figure 5.4: DSC analysis of Ti-50.8 at%Ni foil after undergoing (a) heat treatment 1 (heat treatment at 500 ^{o}C for 30 minutes followed by water quenching) and subsequent thermo-mechanical processing steps. (b) heat treatment 2 (heat treatment at 500 ^{o}C for 1 hour and aging for 45 minutes at 400 ^{o}C followed by water quenching) and subsequent thermo-mechanical processing steps.

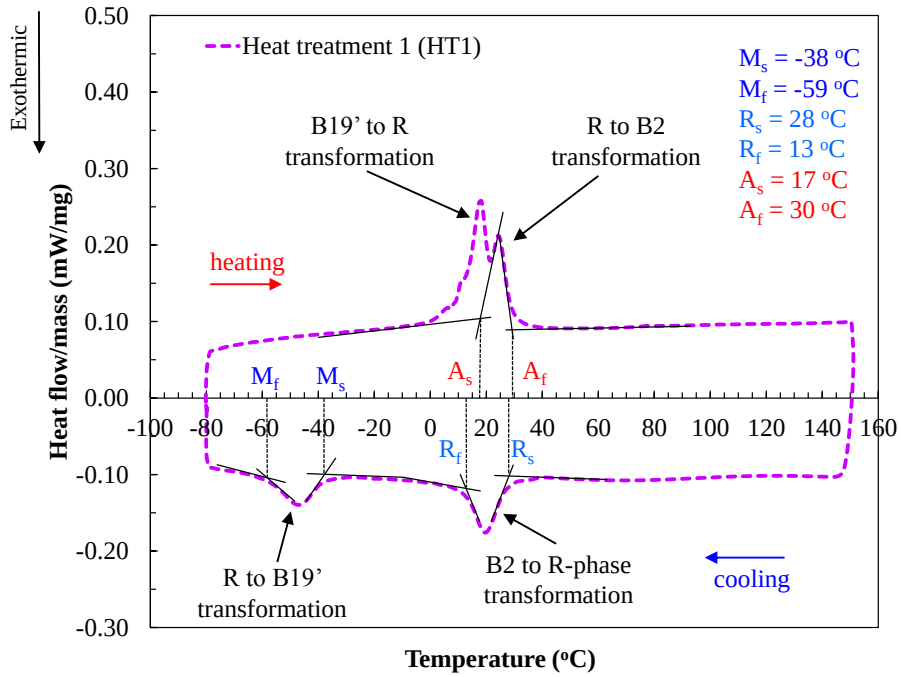

Figure 5.5: DSC analysis of Ti-50.8 at%Ni foil after undergoing heat treatment 1 (heat treatment at 500 ^{o}C for 30 minutes then water quenching).

The two-step austenitic and martensitic transformations are also observed in the NiTi foil that underwent heat treatment 1 and the AFR-PE-4 composite curing cycle. For the Ti-50.8 at%Ni foil subjected to heat treatment 2 and subsequent processing steps, Figure 5.4(b) shows that one-step austenitic phase transformation is observed while two-step martensitic transformation is present in all cases. In other words, only one endothermic peak is seen on all heating curves whereas two distinct exothermic peaks are still presented on all cooling curves in Figure 5.4(b).

Figures 5.5 and 5.6 show the detailed analysis that was carried out to obtain the transformation temperatures of the Ti-50.8 at%Ni foil after undergoing heat treatment 1 and 2, respectively. On these figures, the austenitic start and finish transformation temperatures are denoted as A_s and A_f. Similarly, the notations M_s, M_f, R_s

and R_f indicate the martensitic start and finish, R-phase start and finish transformation temperares. Detailed DSC analyses of the NiTi foil that experienced subsequent processing steps of laser ablation and/or thermal curing cycle of AFR-PE-4 matrix composite laminates are illustrated in Figures B.1, B.2 and B.3 in Appendix B. Table 5.2 summarizes the transformation temperatures for NiTi foil that underwent either heat treatment 1 or heat treatment 2, and subsequent thermal-mechanical processing steps. In summary, activating shape memory behavior in Ti-50.8 at%Ni foil was achieved by performing two different heat treatment procedures. DSC measurements indicate that HT2 resulted in a NiTi foil that has higher transformation temperatures than that obtained from HT1. Thus, heat treatment 2 was selected to be performed on the NiTi foil that was subsequently used to fabricate the hybrid laminates containing SMA. It was observed that the NiTi foil remained active after undergoing laser ablation and curing cycle of the AFR-PE-4 matrix composite. In addition, intensive laser ablation and AFR-PE-4 thermal curing cycle had some influence of the NiTi foil phase transformation behavior where the transformation peaks shift to different temperatures, indicating changes in transformation temperatures. However, the influence of laser ablation and thermal curing is not significant as the transformation temperatures changed less than 5 ^oC in most cases as a results of ablation and curing. It was found from the DSC results that the curing cycle served as an aging treatment that caused both the martensitic and austenitic the transformation peaks to shift to slightly higher temperatures. Finally, as evidenced in Figures 5.4(b) and B.3, after being heat-treated and surface-treated as well as integrated into the T650-8HS/AFR-PE-4 hybrid laminate, at room temperature, the Ti-50.8 at%Ni foil exhibited an unstable martensitic R-phase.

Table 5.2: Summary of transformation temperatures of Ti-50.8 at%Ni under the influence of thermo-mechanical processing parameters

	$\mathbf{M}_f$ (^oC)	$\mathbf{M}_s$ (^oC)	$\mathbf{R}_f$ (^oC)	$\mathbf{R}_s$ (^oC)	$\mathbf{A}_s$ (^oC)	$\mathbf{A}_f$ (^oC)
Heat treatment 1 (HT1)	-59	-38	13	28	17	30
HT1 and curing cycle	-28	-5	32	40	39	55
Heat treatment 2 (HT2)	0	13	35	47	45	57
HT2 and laser ablation	-3	10	38	47	45	55
HT2, laser ablation and curing cycle	4	19	44	51	47	62

5.3.3 Mechanical Characterization of NiTi Foil via Tensile Tests

5.4 Panel Layup and Manufacturing

The stacking sequences for the hybrid panels in this study are as follows,

$[90/0]_2$/Ti/$[0/90]_2$ and $[90/0]_2$/NiTi/$[0/90]_2$. Notations of 0 and 90 are adopted to indicate the orientation of the fabric in the warp and fill directions, respectively. Two layers of Kapton film of 50 μm thickness were used to create a pre-crack, and placed on one side of the Ti/NiTi foil. The panel preform including the prepreg and

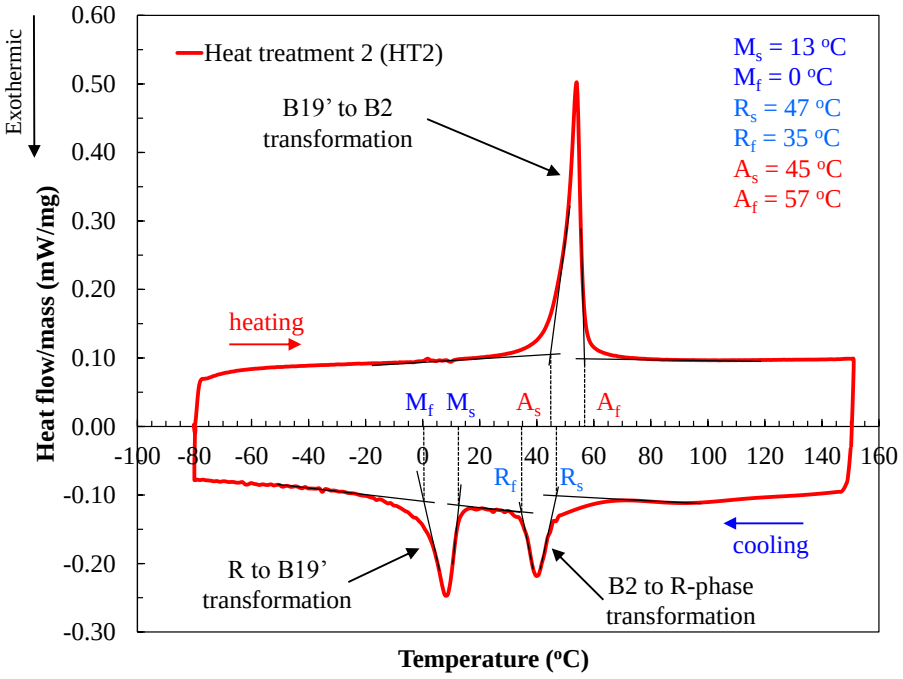

Figure 5.6: DSC analysis of Ti-50.8 at%Ni foil after undergoing heat treatment 2 (heat treatment at 500 °C for 1 hour and aging for 45 minutes at 400 °C followed by water quenching).

metal foil layers and supporting materials such as peel-plies and fiber glass breather layers was vacuum-bagged for 12 hours to remove excess solvent from the making of prepreg and air gaps induced during the hand-layup process. The panels were cured in a Wabash hot-press. The curing cycle is shown in Figure 5.8. Table 5.3 summarizes the composite panels fabricated and investigated in this section and sections 6 and 7.

5.5 Thermal and Mechanical Characterization of T650-8HS/AFR-PE-4 composites

It is important to understand the thermal and mechanical behavior with respect to temperature of the T650-8HS/AFR-PE-4 composite before characterizing and

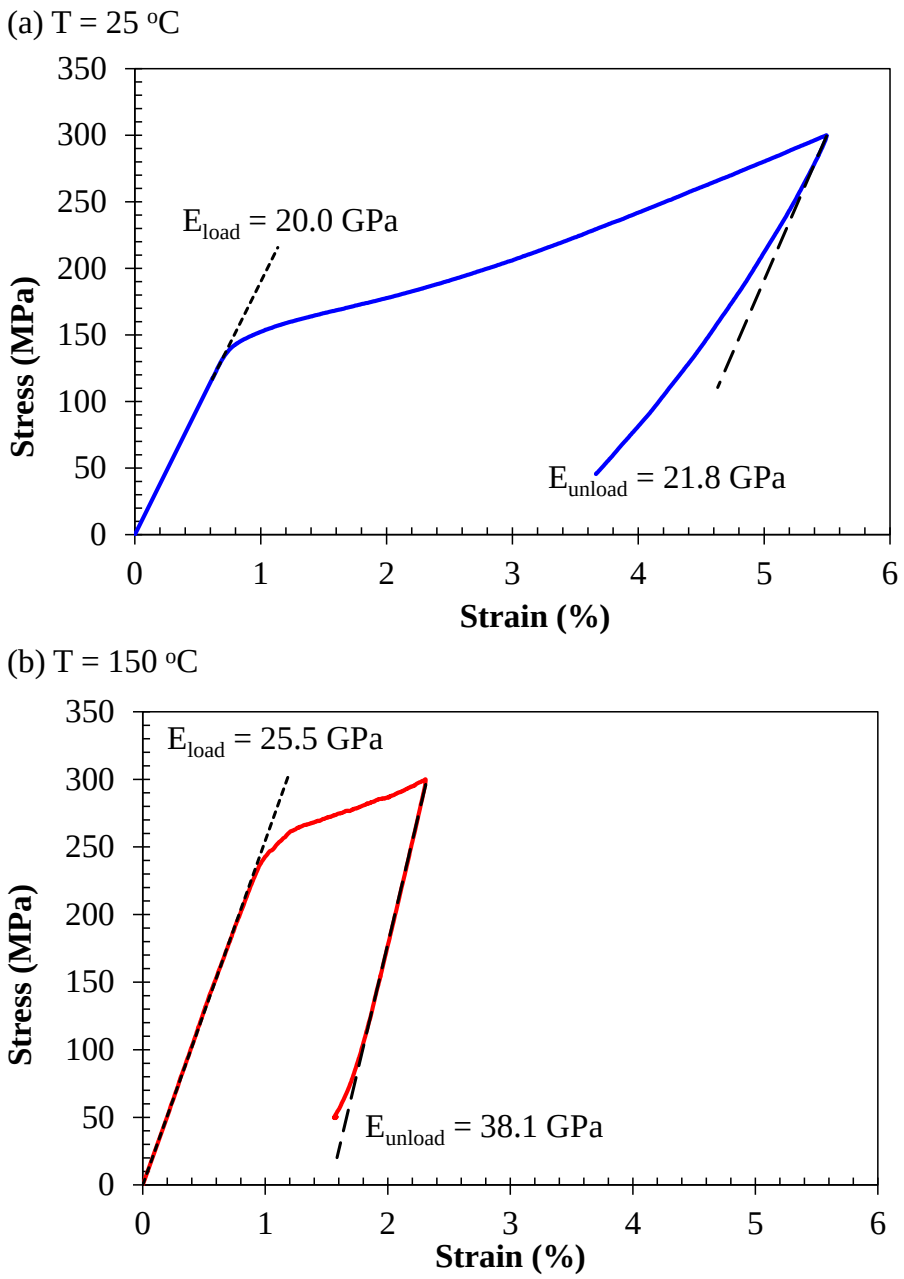

Figure 5.7: Stress-strain response of NiTi foil that underwent HT2, laser ablation and curing cycle from tensile test performed at (a) room temperature (25 ^oC). (b) 150 ^oC.

Table 5.3: Summary of composite panels fabricated and investigated(*)

Panel designation	**Layup**	**Sol-gel chemistry used for metal surface treatment**
Non-hybrid	$[0/90]_4/_{\mathbf{ICF}}/[0/90]_4$	N/A
Ti_EPII	$[90/0]_2/\text{Ti}/_{\mathbf{ICF}}/[0/90]_2$	EPII sol-gel: mixture of zirconium n-propoxide, acetic acid and glycidoxypropy-ltrimethoxysilane
Ti_AP	$[90/0]_2/\text{Ti}/_{\mathbf{ICF}}/[0/90]_2$	Modified EPII sol-gel: mixture of zirconium n-propoxide, acetic acid and aminophenyltrimethoxysi-lane
Ti_PEI_1-hour	$[90/0]_2/\text{Ti}/_{\mathbf{ICF}}/[0/90]_2$	Phenylethynyl imide containing silane (PEI) sol-gel: mixture of pendent phenylethynyl imide oligometric disilane and tetraethoxysilane (hydrolysis time: 1 hour)
Ti_PEI_16-hour	$[90/0]_2/\text{Ti}/_{\mathbf{ICF}}/[0/90]_2$	PEI sol-gel (hydrolysis time: 16 hours)
NiTi_PEI_16-hour	$[90/0]_2/\text{NiTi}/_{\mathbf{ICF}}/[0/90]_2$	PEI sol-gel (hydrolysis time: 16 hours)

testing the hybrid composite laminates and hybrid interfaces. Properties of the composite such as glass transition temperature, coefficients of thermal expansion, and thermal stability need to be obtained. The glass transition temperature is measured to determine the maximum temperature where fracture toughness tests were performed. The coefficients of thermal expansion obtained in this work are later used

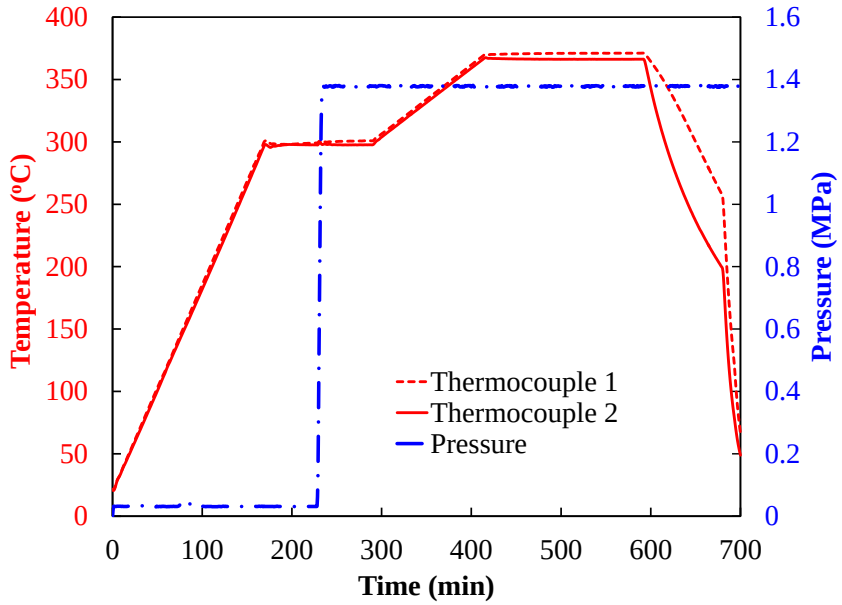

Figure 5.8: Curing cycle used for non-hybrid and hybrid laminates containing T650-8HS/AFR-PE-4 prepreg. Curing was performed using a Wabash hot-press.

finite element analysis and thermal residual stress calculations. Thermal characterization techniques for composites employed in this study include dynamic mechanical analysis, thermal mechanical analysis and thermal gravimetric analysis.

5.5.1 Dynamic Mechanical Analysis (DMA)

It has been found that dynamic mechanical analysis is more sensitive to the primary and second-order transitions in polymers that can be undetectable or difficult to be determined by other techniques such as differential scanning calorimetry or thermal mechanical analysis [63]. Thus, in order to accurately obtain the glass transition temperature (T_g) of non-hybrid and hybrid composite laminates with AFR-PE-4 matrix, DMA was performed using a TA Instruments Q800 machine.

Following ASTM guidance, the DMA tests were carried out in the three-point

bending configuration with a support span of 50.0 mm [81]. Each DMA specimen has a nominal width and length of 12.5 mm and 58.0 mm, respectively. Four specimens from the non-hybrid panel, which contained sixteen layers of T650-8HS/AFR-PE-4, were cut and tested. These specimens were cut from the regions of the panel that contained Kapton film. Thus, after cutting, the specimens had a nominal thickness of 3.05 mm, which was a half of that of the non-hybrid panel. In other words, each DMA specimen from the non-hybrid panel had eight layers of T650-8HS/AFR-PE-4 through the thickness. DMA tests were performed on the non-hybrid panel as well as hybrid panels that contain Ti foil treated with the EPII sol-gel solution (the Ti_EPII panel) and Ti foil treated with the modified EPII sol-gel (the Ti_AP panel). Two DMA specimens were prepared from each of the hybrid laminates. They were cut from areas of the panels that did not contain Kapton film. Thus, these specimens had eight layers of T650-8HS/AFR-PE-4 and one layer of Ti foil. The nominal thickness of these specimens was 3.2 mm.

The three-point bend DMA tests were carried out at a frequency of 1 Hz and oscillation amplitude of 20 μm. Each specimen was subjected to an equilibration at 30 ^{o}C for 1 minute then a temperature ramp from 30 ^{o}C to 500 ^{o}C at a heating rate of 2 ^{o}C/min. Since the tests were performed up to 500 ^{o}C, nitrogen was introduced as air bearing gas to protect the equipment from oxidation.

Representative DMA results from the three panels tested are presented in Figure 5.9. For ease of visualization, two separate plots were created. Figure 5.9(a) presents storage modulus and loss modulus results as functions of temperature while Figure 5.9(b) shows results for storage modulus and tan δ. The glass transition temperature of each specimen is depicted by the major peak of the tan δ or loss modulus curve. The average T_g together with standard deviation measured from each of the tested panels are summarized in Table 5.4.

Table 5.4: Summary of the average glass transition temperature (T_g) measured from DMA tests done on non-hybrid, Ti_EPII and Ti_AP laminates containing T650-8HS/AFR-PE-4

Panel	**T_g ± Std. Dev. (^{o}C)**
Non-hybrid	396.45 ± 8.76
Ti_EPII	403.66 ± 5.13
Ti_AP	407.59 ± 5.25

Figure 5.9 shows evidence of AFR-PE-4 matrix exhibiting β transition before the primary transition of T_g. It is observed in each of the tan δ or loss modulus E'' curves in Figure 5.9 a weak, broad peak before the strong and sharp glass transition peak. The β transition temperature, T_β, is determined as the temperature at which the secondary peak for β transition on the tan δ curve occurs. It has been reported that T_β for polyimides is observed in a temperature range between 80 ^{o}C and 150 ^{o}C [58, 61, 62]. In this work, T_β for T650-8HS/AFR-PE-4 composites was found to be 145 ^{o}C and 155 ^{o}C for the non-hybrid and hybrid panels, respectively. This information is important for the understanding of the mode I and mode II fracture toughness of the non-hybrid and hybrid (Ti_EPII and Ti_AP) interfaces as a function of temperature investigated and presented in sections 6 and 7. It is observed in Figure 5.9 that the T_β peak for the Ti_AP specimen was the strongest among the three types of specimens that were DMA tested, and the T_β peak for the Ti_EPII specimen was the weakest. The difference in the β transition strength could be attributed to the difference in the sol-gel chemistry that was used for surface treatment of the Ti foil and presented at the hybrid interfaces between the Ti foil and composite.

5.5.2 Thermal Mechanical Analysis (TMA)

Thermal mechanical analysis on T650-8HS/AFR-PE-4 composite was performed using a NETZSCH TMA 202 machine. The TMA specimens were cut from the non-hybrid panel. They had in-plane dimensions of 7.0 mm x 7.0 mm and thickness of 6.1 mm. The TMA tests were carried out in standard expansion mode and thermal expansion was measured in the through-thickness direction (zz- or 33-direction) as well as in the in-plane directions that are parallel to the warp tows (xx- or 11-direction) and the fill tows (yy- or 22-direction). During the test, each TMA specimen was subjected to a thermal cycle that included a cooling step from room temperature to 0 ^oC and a heating step from 0 ^oC to 400 ^oC at a heating rate of 5 ^oC/min. Nitrogen was used as purge gas with a flow rate of 60 ml/min.

The coefficient of thermal expansion (CTE) as a function of temperature, $\alpha(T)$, was calculated as follows,

$$\alpha(T) = \frac{1}{L_o}\left(\frac{\partial l}{\partial T}\right)_T \tag{5.1}$$

where L_o is the initial length or height of the specimen, $\left(\frac{\partial l}{\partial T}\right)_T$ is the slope of the expansion curve dL at temperature T.

The results from TMA tests for both thermal expansion dL/L_o and CTE as functions of temperature are presented in Figures 5.10, 5.11 and 5.12. Similar thermal expansion behavior was observed in the in-plane directions although the material expanded slightly more in the 11-direction (parallel to the fill tows) than in the 22-direction (parallel to the warp tows). In the through-thickness direction (33-direction), the composite expanded 15.5 % more than it did in the in-plane directions. The average CTEs were calculated for CTEs values in the temperature range from

50 ^oC to 300 ^oC. A summary of the average thermal expansion coefficients measured from TMA analysis of T650-8HS/AFR-PE-4 composite in 11-, 22-, and 33-direction is presented in Table 5.5. These calculated CTE values of T650-8HS/AFR-PE-4 composite were later used in the finite element analyses performed in section 8.

Table 5.5: Summary of thermal expansion coefficients measured from TMA analysis of T650-8HS/AFR-PE-4 composite

CTE	**Value ± Std. Dev. (x 10^{-6} $^oC^{-1}$)**
α_{11}	3.98 ± 0.96
α_{22}	3.49 ± 0.96
α_{33}	57.42 ± 5.89

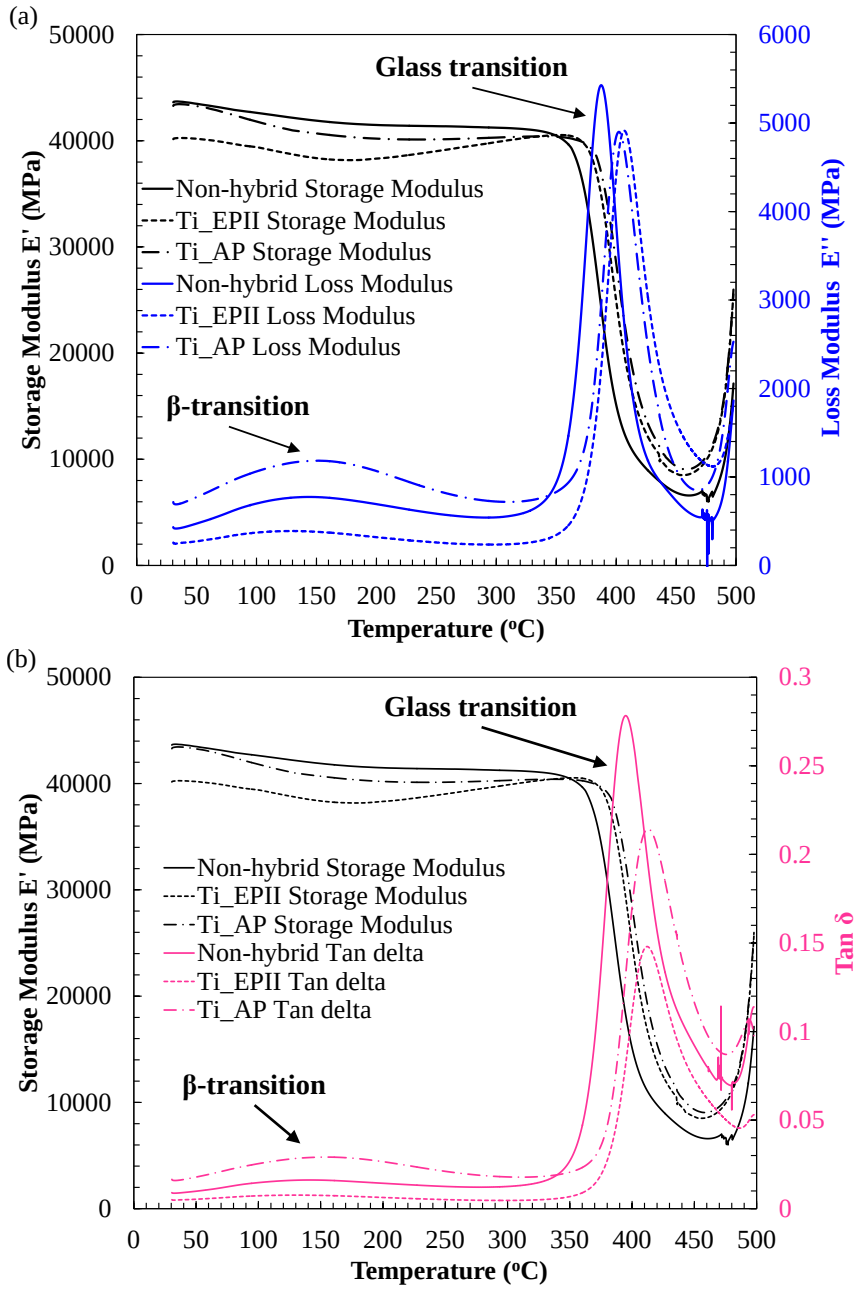

Figure 5.9: Representative dynamic mechanical analysis results for non-hybrid panel, hybrid panel containing Ti foil treated with EPII sol-gel and modified EPII (with aminophenyl silane) sol-gel solution (a) storage modulus (black lines) and loss modulus (blue lines) results are presented. (b) storage modulus (black lines) and tan δ (red lines) results are presented. Besides the primary glass transition, the second-order β transition was also observed as indicated by the broad and shallow peaks before the steep T_g peaks on the storage modulus and tan δ curves.

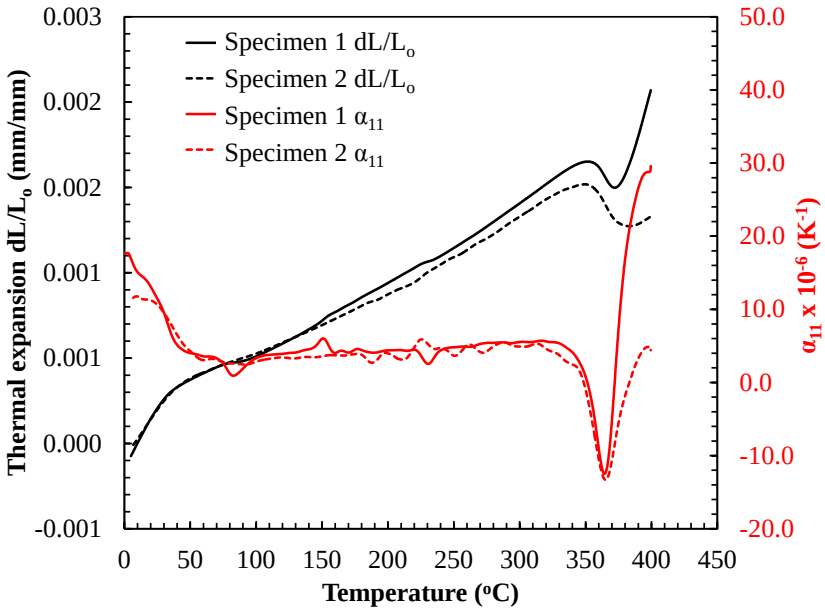

Figure 5.10: TMA results for measurements done in the 11-direction where thermal expansion dL/L_o (black lines) and coefficient of thermal expansion α_{11} (red lines) as functions of temperature are plotted.

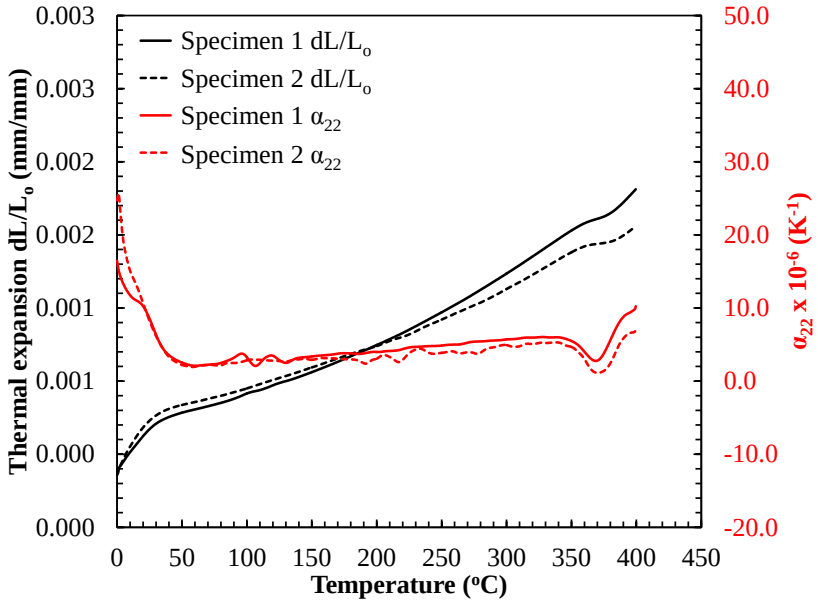

Figure 5.11: TMA results for measurements done in the 22-direction where thermal expansion dL/L_o (black lines) and coefficient of thermal expansion α_{22} (red lines) as functions of temperature are plotted.

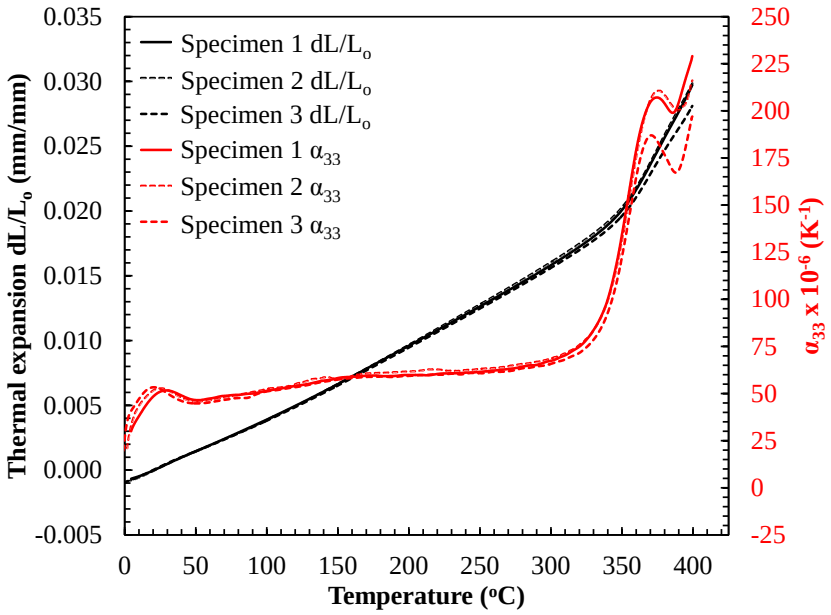

Figure 5.12: TMA results for measurements done in the 33-direction where thermal expansion dL/L_o (black lines) and coefficient of thermal expansion α_{33} (red lines) as functions of temperature are plotted.

5.5.3 Thermal Gravimetric Analysis (TGA)

To investigate the thermal stability of the T650-8HS/AFR-PE-4 composite laminates fabricated in this study, thermal gravimetric analysis was carried out. The TGA tests were performed using a NETZSCH TG 209F1 machine. Two specimens cut from the non-hybrid panel were tested. Each TGA test was carried out from 20 ^oC to 800 ^oC at a heating rate of 20 ^oC/min in air. The results from TGA measurements are shown in Figure 5.13. No weight loss, i.e. weight percent was 99.5 %, was observed at temperature up to 520 ^oC. The onset of weight loss was at 550 ^oC. At 800 ^oC, the average weight percent remained was 66.3 % with a standard deviation of 1.2 %.

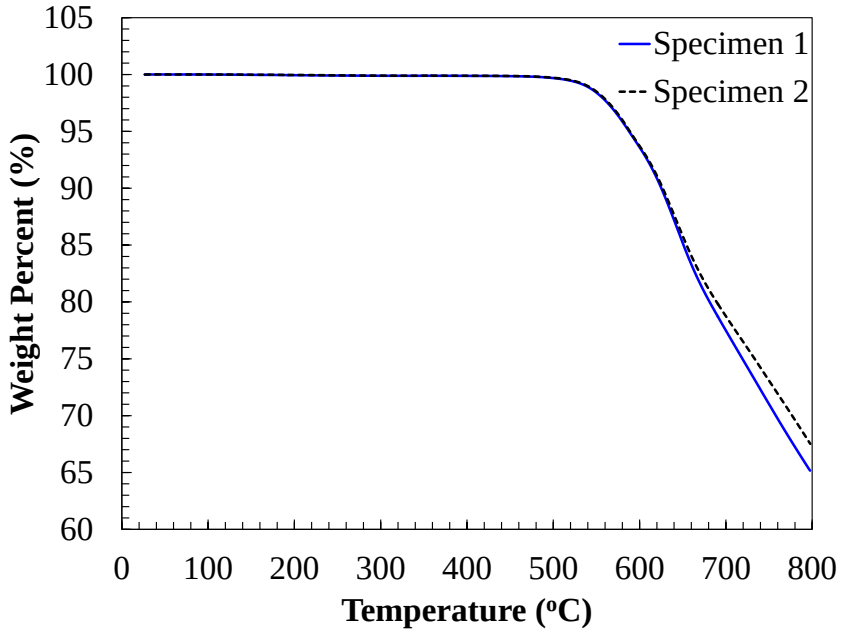

Figure 5.13: TGA analysis of cured T650-8HS/AFR-PE-4 composite shows that the material is thermally stable and only 0.5% weight loss was observed at temperature up to 520 ^oC.

5.6 Cross-section Characterizations

After the hybrid composite laminates were fabricated, the cross-section specimens from each of the laminates were prepared and examined using optical microscopy (SEM), scanning electron microscopy with energy dispersive x-ray spectroscopy (SEM/EDS) and nanoscale infrared (nanoIR) spectroscopy. The cross-section specimens were cut from regions of the panel that did not contain Kapton film and in directions perpendicular as well as parallel to the direction of laser ablation paths on the treated Ti and NiTi foil.

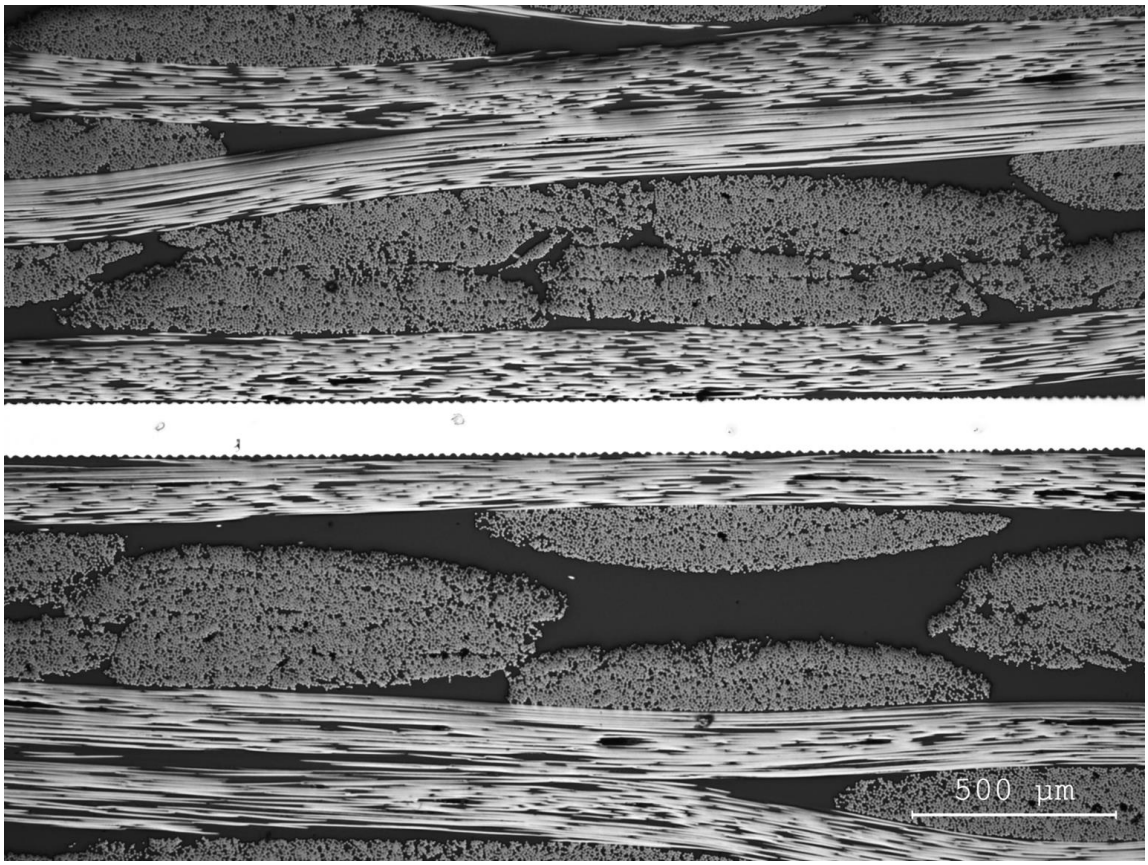

Figure 5.14: Cross-section view perpendicular to the direction of the laser ablation paths of hybrid Ti_PEI_1-hour interface.

5.6.1 Optical Microscopy

Representative images from optical microscopic analysis of the hybrid composite cross-sections are presented in this section. Figure 5.14 shows a cross-section view of the hybrid Ti-PMC in the hybrid T650-8HS/AFR-PE-4 laminate containing Ti foil treated with PEI sol-gel that underwent a 1-hour hydrolysis. This cross-section view is perpendicular to the direction of the laser ablation paths that are presented on the Ti foil surfaces. It can be seen that the fabricated high temperature hybrid laminate is of high quality although a few microscale porosities or voids are observed inside

the carbon fiber tows. The diameters of these voids are approximately $20-50\ \mu m$. The formation of these porosities could be due to the formation and vaporization of water or outgassing of residual solvent during the imidization and polymerization reactions upon curing at high temperature.

Close-up views of the cross-sections from the Ti_PEI_1-hour panel are shown in Figures 5.15 and 5.16 in directions perpendicular and parallel to the ablation path on Ti foil, respectively. Figures 5.15(a) and 5.16(a) capture the cross-sectional images from locations where a resin rich region is located near the Ti foil surface. Areas where the carbon fiber tows were found adjacent to the troughs of laser ablation pattern on the Ti foil are shown in Figures 5.15(b) and 5.16(b). It is observed from both Figures 5.15 and 5.16 that the resin from the T650-8HS/AFR-PE-4 prepreg fully infiltrated into the micro roughness patterns created by laser ablation even in locations where the Ti foil was bordered by the T650 fiber tows. No voids or porosities were detected at the hybrid Ti-matrix interfaces. The fact that the hybrid specimens remained intact, and no delamination was found in the metal-polymer neighborhoods after the cutting and polishing processes suggests strong adhesion between the metal and polyimide resin was achieved although the adhesion strength has to be determined by mechanical testing. This also indicates a larger surface area created by the laser ablation process was utilized for formation of the hybrid joint compared to the joints attained from using a metal substrate that has a flatter surface finish. Observations from the visual inspection of the hybrid laminates via optical microscopy reveal that mechanical interlocking plays an important role on the adhesion between the laser ablated metal foil and polyimide matrix in the hybrid laminates fabricated in this work. Evidence of chemical bonding at these hybrid interfaces are presented and discussed in Sections 5.6.2 and 5.6.3.

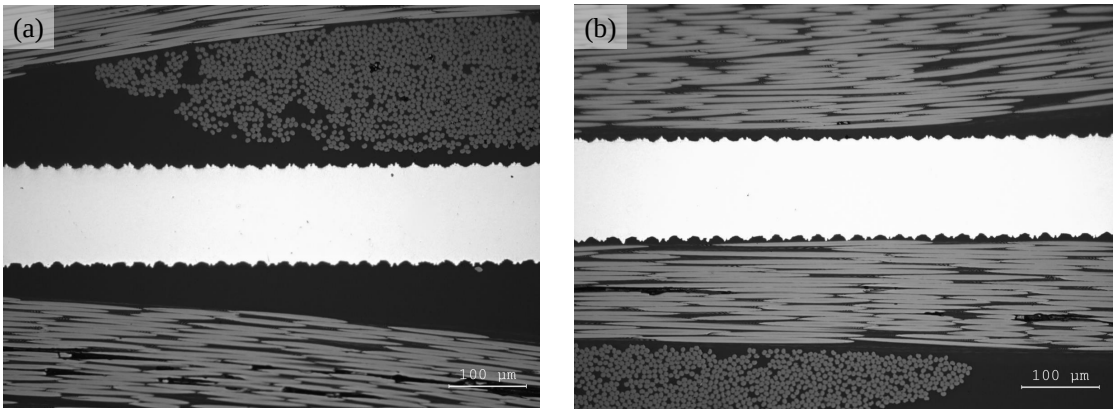

Figure 5.15: Close-up cross-section view of hybrid interface with laser ablated Ti foil with (a) interfaces near resin-rich regions. (b) interfaces where fiber tows are adjacent to Ti surfaces. *Cross-section view is perpendicular to the direction of laser ablation path.*

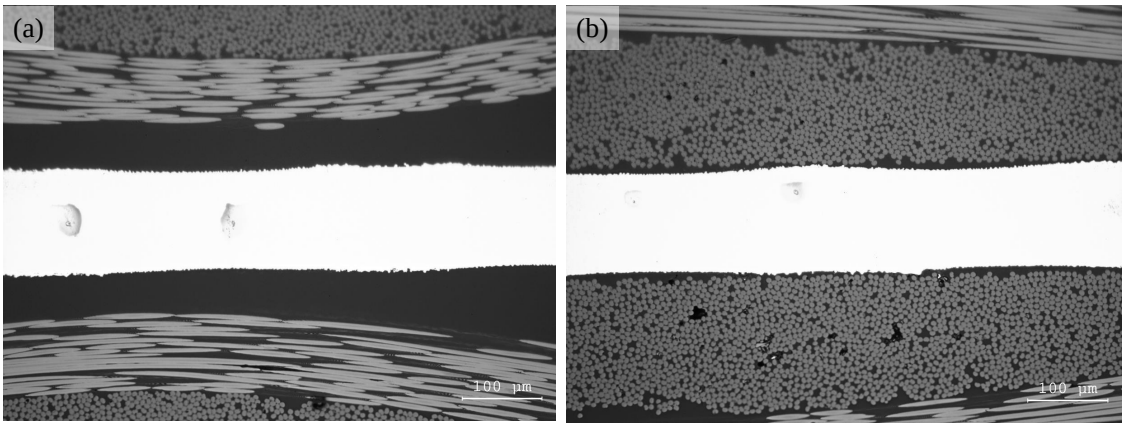

Figure 5.16: Cross-section of hybrid interface with laser ablated Ti foil with (a) interfaces near resin-rich regions. (b) interfaces where fiber tows are adjacent to Ti surfaces. *Cross-section view is parallel to the direction of laser ablation path.*

5.6.2 Scanning Electron Microscopy with Energy Dispersive X-ray Spectroscopy

Scanning electron microscopy (SEM) investigations of the hybrid interfaces were performed using an FEI/Phillips XL Field Emission ESEM. Elemental maps across the hybrid interfaces were obtained via energy dispersive X-ray spectroscopy (EDS) using an Oxford Instruments EDS with Aztec analysis software. Representative SEM/EDS results for the hybrid interface in panel Ti_PEI_16-hour are shown in Figures 5.17 and 5.18. In the grayscale images shown in Figures 5.17 and 5.18, the Ti layer is the light gray areas that situates on top of the darker polyimide resin. Besides the expected Ti, C and O elements, Si and F were detected from EDS analysis. F exists in the structure of AFR-PE-4 resin as previously discussed in Section 5.1. The presence of Si observed on the hybrid interface cross-section is attributed to use of the silane-containing sol-gel solution to treat the Ti surfaces prior to integrating the foil into the hybrid laminates. It can be seen from Figure 5.17 that Si, C, and F diffused into the ablated Ti layer. This could be due to the existence of porosities on the Ti foil surface caused by laser ablation. The SEM images that show porosities created on the laser ablated Ti surfaces are presented in Figure C.3[2] in Appendix C. High Si concentration was observed in Ti layer shown in Figure 5.17. It should be noted that the sol-gel solution has low viscosity and was sprayed onto the laser ablated Ti foil using an air-brush. After being sprayed with the solution containing silanes, the Ti foil was dried in air for 1 hour and subsequently cured in an oven at 110 ^oC and 220 ^oC for 30 minutes. Then, the foil was subjected to a 12 hours curing cycle at temperature up to 371 ^oC. The long processing time that the Ti foil underwent could be sufficient for the silane groups from the sol-gel treatment solution to diffuse into the Ti layer that has porosities on its surfaces. The interphase

[2]Courtesy of Dr. Yi Lin at NASA Langley Research Center

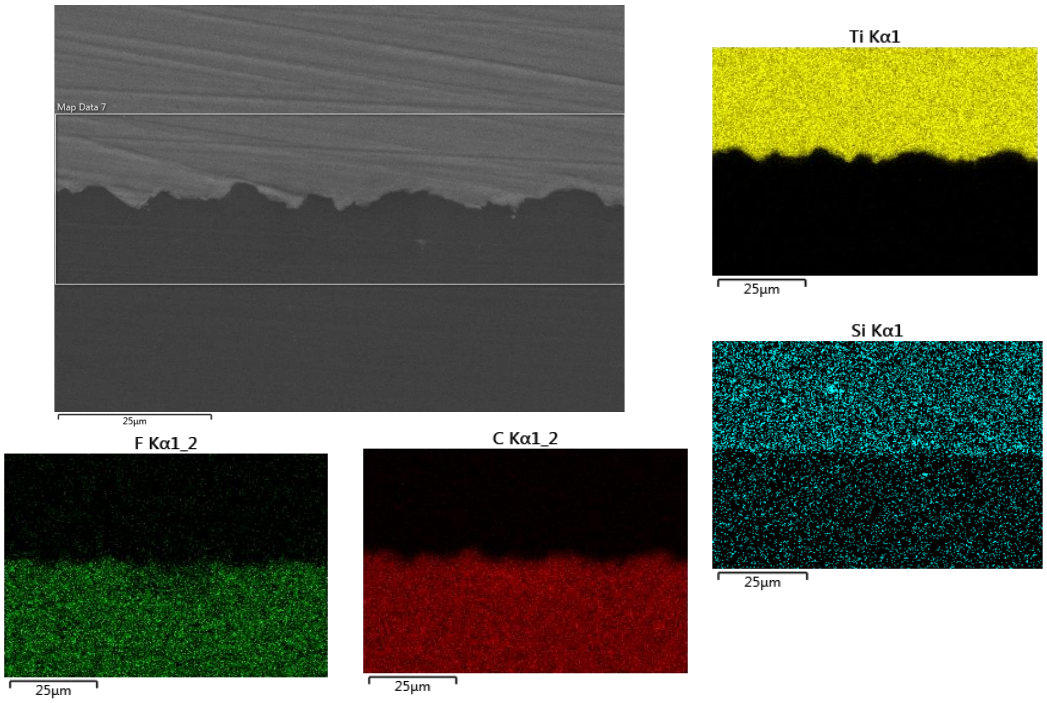

Figure 5.17: EDS analysis at the hybrid interface in panel Ti_PEI_16-hour. Elemental maps show Si penetrated into the composite side.

region where the sol-gel bridge presented in between the Ti foil and polyimide resin is approximately 2 μm as indicated by the area where the high concentration of Si is observed in Figure 5.18.

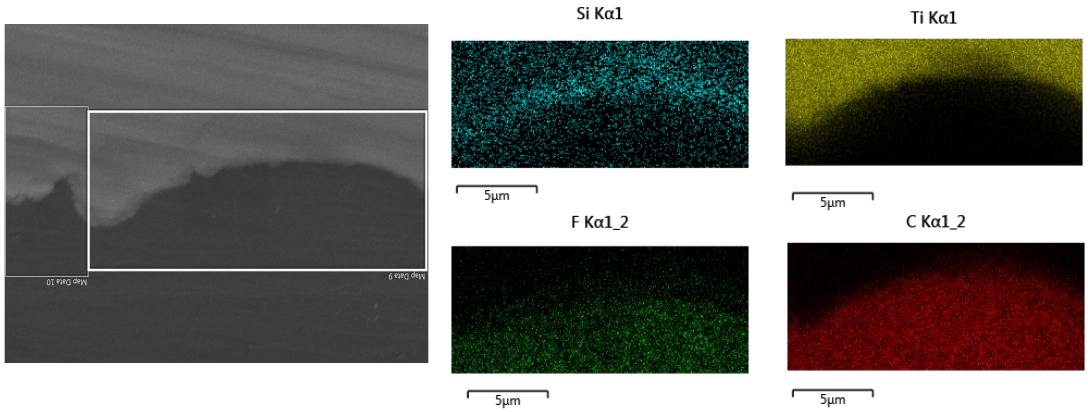

Figure 5.18: EDS analysis at the hybrid interface in panel Ti_PEI_16-hour (close-up view). The area where high concentration of Si is found around the boundary between Ti and resin indicates interphase region. The thickness of this interphase region is approximately 2 μm.

5.6.3 NanoIR Characterization at the Hybrid Ti-Polyimide Matrix Composite Interface

Nanoscale infrared analysis was carried out using a NanoIR2^{TM} with top side illumination system by Anasys Instruments. Atomic force microscope (AFM) images were first taken for areas of interest on the polished cross-section specimens [3]. The IR source induced rapid thermal expansion at the locations of interest on the AFM-imaged area. IR spectra were then detected by the deflection of the AFM probe cantilever. The hybrid interfaces analyzed via AFM-IR in the current study are Ti_EPII, Ti_AP and Ti_PEI_1-hour. The obtained nanoIR spectra for each of those hybrid interfaces are presented in the following sub-sections.

5.6.3.1 Hybrid Interface with Phenylethynyl imide-containing Sol-gel

NanoIR results from hybrid interface containing Ti foil treated with phenylethynyl amide sol-gel are presented in this section. Figure 5.19 shows a representative spectrum collected from AFM-IR analysis performed at a point in the resin region approximately 1 μm away from the Ti foil surface. The yellow dashed boundary shown in the attached AFM image in Figure 5.19 highlights the interface between the ablated Ti surface and the AFR-PE-4 resin at the cross-section. The yellow arrow on that image points to the specific location at which the nanoIR spectrum was obtained and analyzed in this figure. The major IR peaks occurring at wave numbers 1776 cm^{-1}, 1724 cm^{-1}, 1512 cm^{-1} and 1356 cm^{-1} are attributed to bond deformation in the polyimide matrix. Specifically, asymmetric and symmetric imide C=O bond stretching occurs at wave numbers 1776 cm^{-1} and 1724 cm^{-1}, respectively. The IR peaks at 1512 cm^{-1} and 1356 cm^{-1} are respectively associated with stretching

[3]The AFM-IR experiment presented in this section was performed by Dr. Dhriti Nepal at the Air Force Research Laboratory, Dayton, OH.

of benzene rings and imide C−N bonds. These observations from nanoIR spectra are consistent with the identification of imide peaks from Fourier transform infrared spectroscopy (FTIR) results for AFR-PEPA-4 oligomer previously analyzed and reported by Lincoln [53] and Li *et al.* [82].

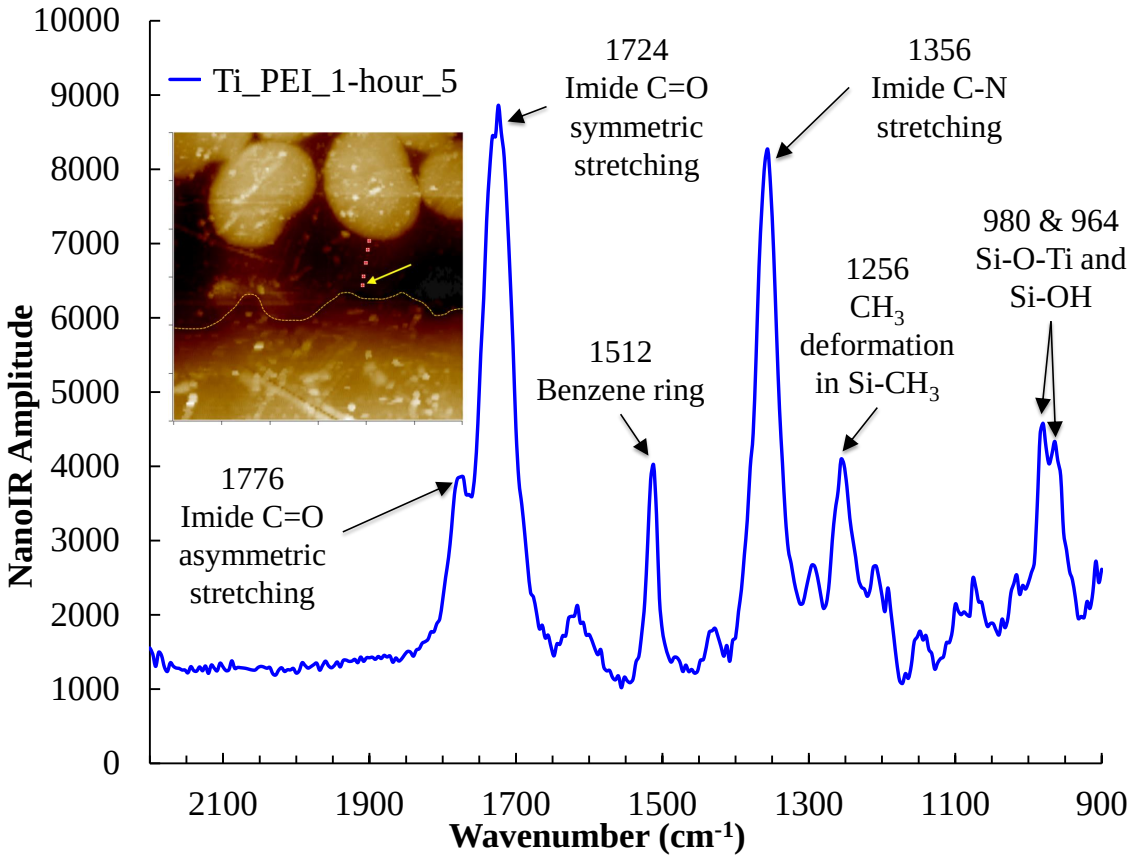

Figure 5.19: NanoIR spectrum obtained near the Ti-polyimide resin interface (highlighted by the dashed yellow boundary in the attached AFM image) from the Ti_PEI_1-hour panel with identification of the wave numbers where the IR peaks occur. Note that the Ti foil in this panel was surface-treated with laser ablation and 1-hour hydrolyzed PEI sol-gel prior to fabrication of the hybrid laminate.

According to the elemental EDS maps shown in Section 5.6.2, the presence of

Si in the vicinity of Ti-resin interface was observed. Thus, it is expected that the organosilicon groups be detected via infrared spectra. In accordance with the infrared analysis of organosilicon compounds reported in the literature [83, 84, 85, 86], the peak occurs at 1256 cm^{-1} is associated with deformation of the CH_3 group in $Si-CH_3$ bond. In addition, the double peak at wave numbers 980 cm^{-1} and 964 cm^{-1} can be attributed to bond deformation of the $Si-O-Ti$ and $Si-OH$ groups [83]. This double peak, indicating the existence of $Si-O-Ti$ at the hybrid interface, proves that covalent bonds were formed between the Ti surface that was activated via laser ablation and the silane-containing sol-gel treatment solution. It also reveals that some of the available $Si-OH$ groups did not react with the Ti foil surface.

Figure 5.20 shows the variation of nanoIR spectra from a location at the fiber-resin interface into a resin rich region and finally the neighborhood of Ti-resin interface. These spectra were taken at five consecutive points along a line at a spacing of approximately 1 μm. The specific locations of these points are illustrated by the numbered red dots in the AFM image in Figure 5.20. Spectrum 1 from the fiber-matrix interface shows a clear difference from the other four spectra plotted in this figure. Similarities are observed from spectra 2 to 5. The variation in the imide peaks intensity shows a decreasing trend as the IR spectra were obtained at locations that move closer and closer to the Ti-resin interface. This variation is consistent for all the detected imide peaks. That is, the imide peaks at 1776 cm^{-1}, 1724 cm^{-1}, 1512 cm^{-1} and 1356 cm^{-1} are strongest at location 2, then gradually decrease, and are weakest at location 5. This trend, however, is totally reversed for the peaks appear at 980 cm^{-1} and 964 cm^{-1}. The variation in nanoIR peaks intensity at 980 cm^{-1} and 964 cm^{-1} shows that for spectra taken at locations closer to the Ti surface, the peaks occur at these wave numbers appear to be. This implies more $Si-O-Ti$ groups were detected on the IR spectra collected at locations closer to the Ti-matrix interface.

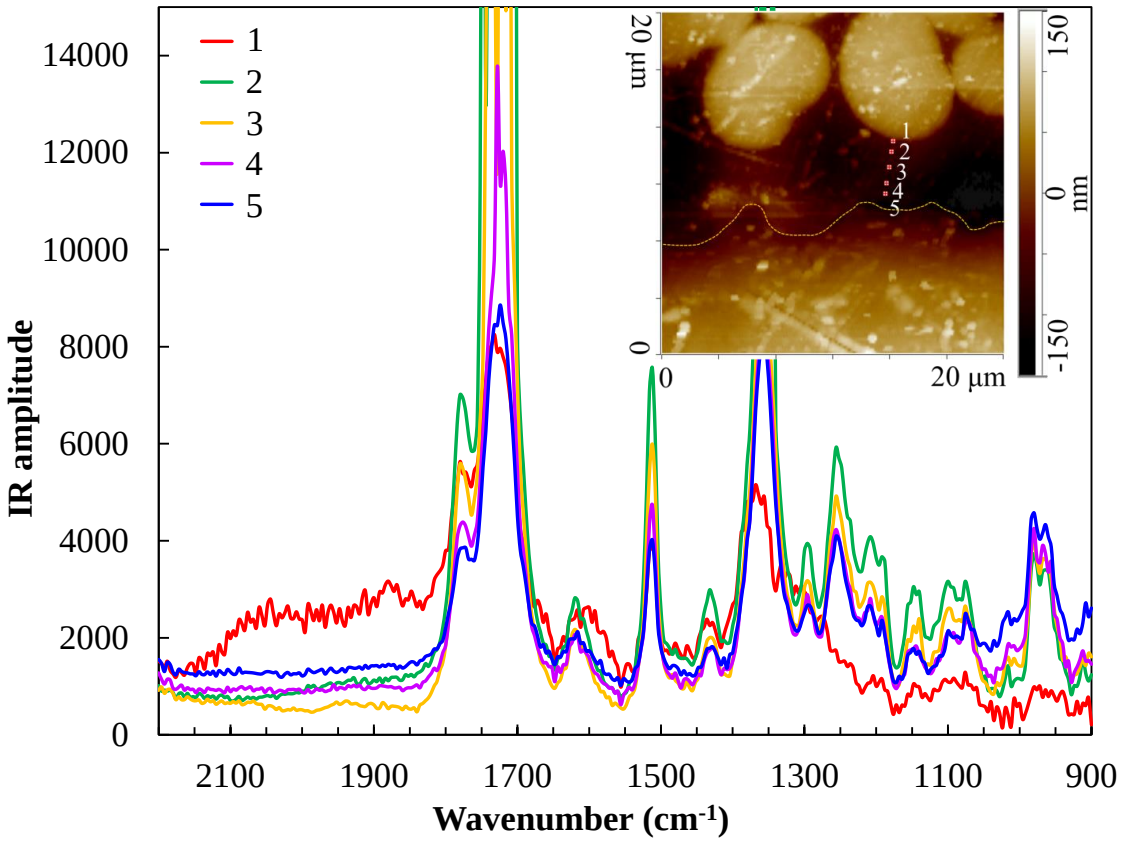

Figure 5.20: NanoIR results for a cross-section specimen from Ti_PEI_1-hour panel. The numbered red dots in the attached AFM image indicated the locations where the IR spectra presented herein was obtained. The dashed yellow line in the AFM image highlights the boundary between the Ti surface and AFR-PE-4 resin.

5.6.3.2 Hybrid Interface with EPII Sol-gel

Figure 5.21 shows the nano-IR results obtained near the hybrid Ti-composite interface in the Ti_EPII panel. The AFM image is presented to illustrate the location at which each of the plotted nanoIR spectrum was obtained. The area of interest that was imaged has dimensions of 20 μm x 20 μm. The interface between the Ti and the matrix is highlighted by the dashed yellow line. Similarity is observed in the peak intensities and the wave numbers where the peaks occur on spectra obtained in the resin region at locations 1, 3, 4, 5 and 6. This is ascribed to the homogeneous curing of the AFR-PE-4 matrix. Near the Ti surface that was treated with EPII sol-gel, the chemistry is slightly different from the chemistry of the AFR-PE-4 resin. Thus, nanoIR spectra for locations 7, 8 and 9, although similar to one another, slightly differ from that for the group of IR spectra discussed previously. The polyimide peaks at wave numbers 1778 cm^{-1}, 1732 cm^{-1} and 1360 cm^{-1} are still observed on the nanoIR spectra obtained near the Ti surface. However, for the wave numbers range from 900 cm^{-1} to 1200 cm^{-1}, this difference in chemistry is evidenced. The spectrum for location 2 that is near the T650 carbon fiber is distinctive from the other spectra presented in Figure 5.21.

Spectra 7 to 9 that were obtained in the Ti-resin neighborhood are re-plotted in Figure 5.22 for clarity and further analysis. The decreasing trend in imide peaks intensity variation as the spectra were collected closer to the Ti surface treated with EPII sol-gel is observed. The dashed arrows, both on the AFM image and the IR spectra plot, indicate the direction of this variation. This is similar to the trend observed from nanoIR analysis of the Ti_PEI_1-hour interface as discussed in Section 5.6.3.1. However, the reversed trend in the peaks intensity at 980 cm^{-1} and 968 cm^{-1} no longer holds in this case.

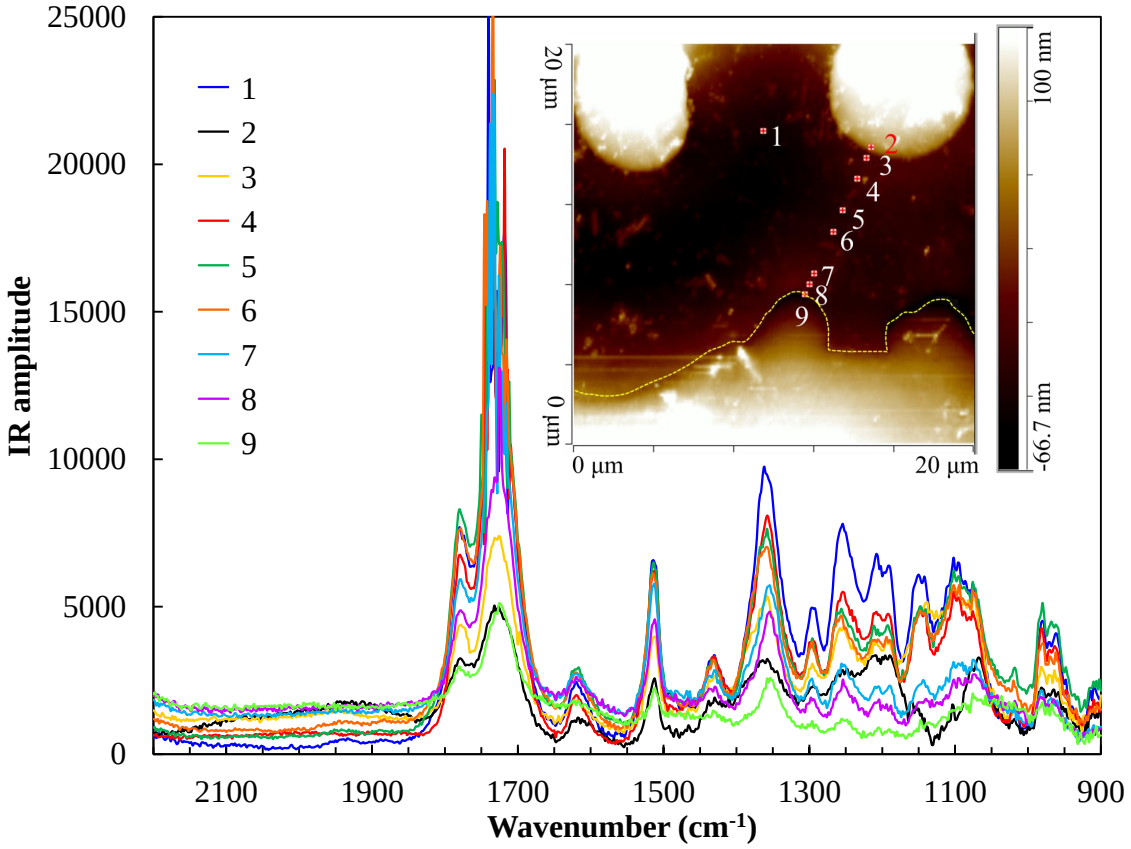

Figure 5.21: NanoIR results for a cross-section specimen from Ti_EPII panel. The numbered red dots in the attached AFM image indicated the locations where the IR spectra presented herein was obtained. The dashed yellow line in the AFM image highlights the boundary between the Ti surface and AFR-PE-4 resin. Note that the Ti foil in this panel was surface-treated with laser ablation and EPII sol-gel solution.

Figure 5.23 demonstrates the comparison of spectra obtained in the resin rich region (spectrum 1), near the fiber-matrix interface (spectrum 3) and near the Ti-matrix interface (spectrum 8). Similarity between spectrum 1 and spectrum 3 are observed while the nanoIR spectrum for location 8 is slightly different. As discussed, this difference is due to the dissimilarity in the chemistry presented near the Ti interface.

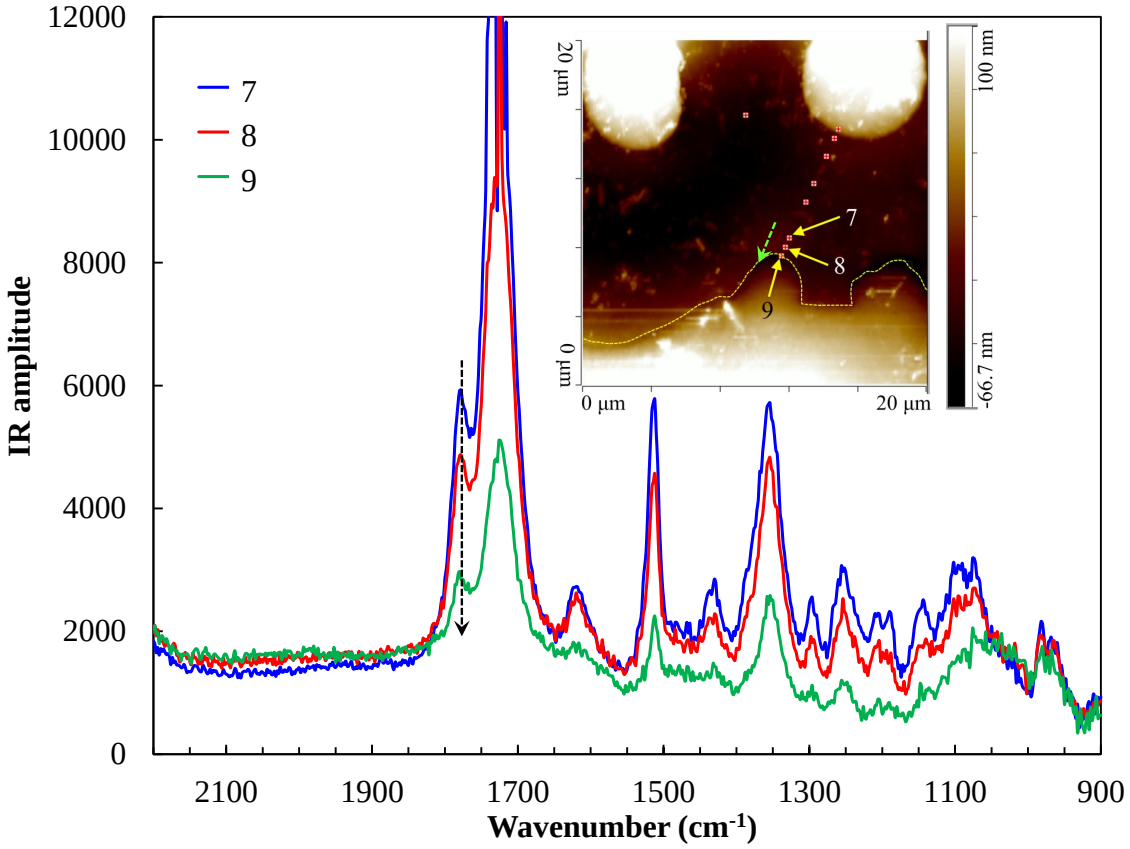

Figure 5.22: NanoIR spectra obtained in the vicinity of the Ti-matrix interface in the Ti_EPII panel. Dashed arrows indicate the direction of the variation peaks intensity.

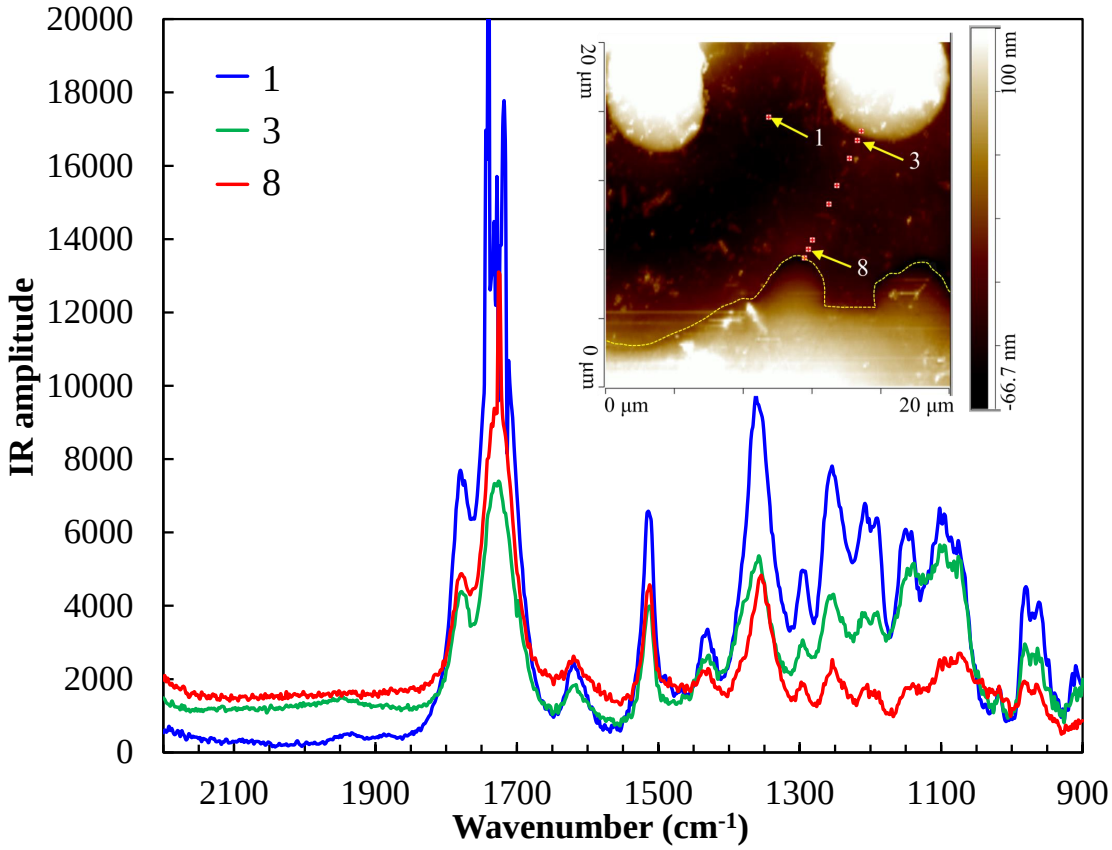

Figure 5.23: NanoIR results for cross-section specimen from the Ti_EPII panel showing comparison of spectra obtained in the resin rich region (spectrum 1), near the fiber-matrix interface (spectrum 3) and near the Ti-matrix interface (spectrum 8).

5.6.3.3 Hybrid Interface with Modified EPII (Aminophenyl Silane) Sol-gel

The nano-IR results obtained near the amino phenyl silane-containing hybrid Ti-polyimide matrix composite interface is presented in Figure 5.24. The nanoIR spectra were taken at five consecutive points along a line at spacing of approximately 1 μm. This line has a starting point in the resin-rich region at 8 μm away from the Ti-resin boundary, and an end point in the Ti layer at 0.5 μm away from that boundary. The specific locations at which the IR spectra were obtained are illustrated by the numbered red dots in the attached AFM image. The imide C=O, benzene ring and C−N peaks are observed at 1778 cm^{-1}, 1732 cm^{-1}, 1512 cm^{-1} and 1378 cm^{-1}. Besides the imide peaks, a strong and broad peak at 1080-1100 cm^{-1} are visible on each spectra. This peak could be attributed to the Si−phenyl-ring groups [83] that present in the sol-gel solution used to treat the Ti surface prior to integrating it to the hybrid composite. It is as expected that spectrum 5, which was collected at a location inside the Ti layer, exhibits no imide peaks. However, the broad peak at 1100 cm^{-1} is present on this spectrum, indicating the existence of the Si−phenyl-ring groups in the Ti layer. This is consistent with the observation discussed in Section 5.6.2 that Si penetrated into the Ti layer due to the porosities created on the Ti foil surface under the influence of laser ablation processing.

A large variation in the nanoIR peaks is observed in Figure 5.24. The variation in the imide peak intensity is shown as a gradient where the peak intensity decreases as the IR spectra were obtained at locations that move closer and closer to the Ti-resin interface. This gradient nature is consistent for all the detected imide peaks as well as the Si−phenyl-ring peak, and is illustrated by the dashed arrows in the figure. This indicates a curing heterogeneity in the polymer structures is presented in the vicinity of the hybrid Ti-resin interface that contains amino phenyl silane sol-gel.

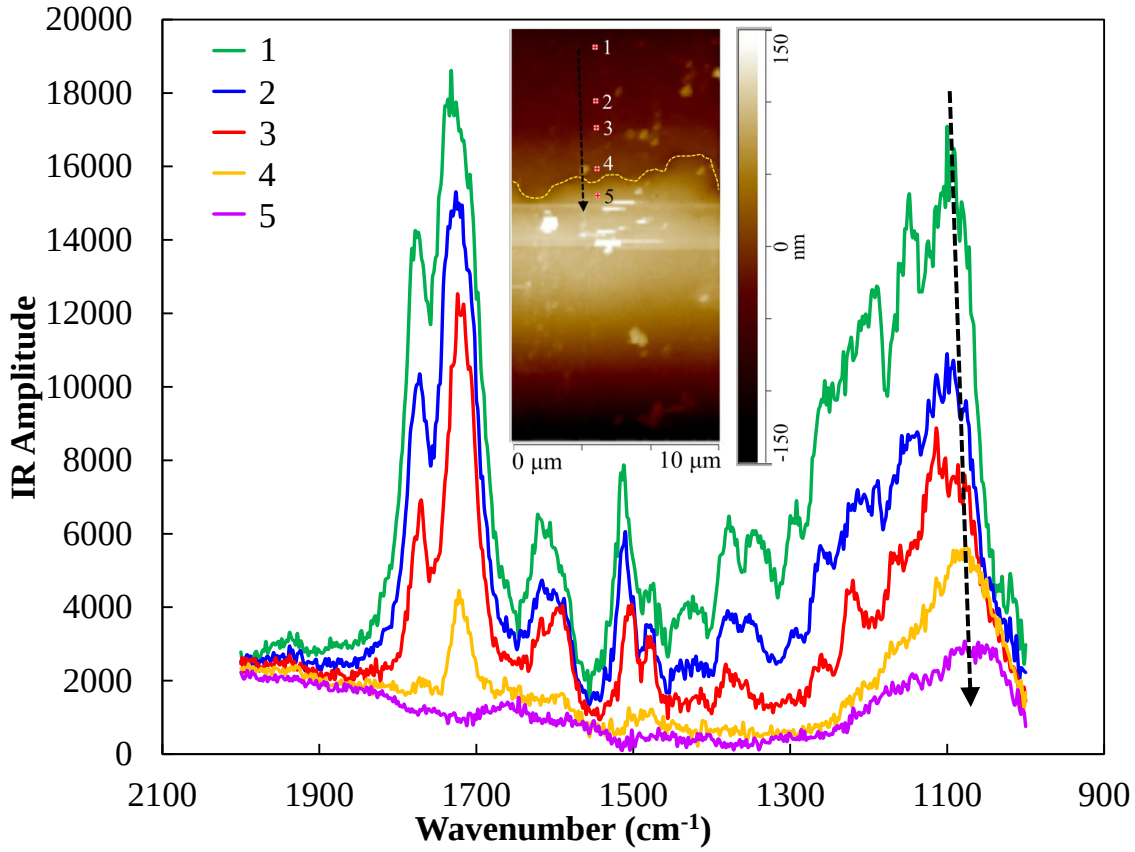

Figure 5.24: NanoIR spectra obtained in the vicinity of the Ti-matrix interface in the Ti_AP panel. The numbered red dots in the attached AFM image indicated the locations where the IR spectra presented herein was obtained. The dashed yellow line in the AFM image highlights the boundary between the Ti surface and AFR-PE-4 resin. Note that the Ti foil in this panel was surface-treated with laser ablation and the modified EPII sol-gel solution (containing amino phenyl silane). The dashed arrows indicate the direction of the variation peaks intensity.

5.6.3.4 Summary on NanoIR Analysis of Hybrid Ti-Polyimide Matrix Composite Interfaces

Figure 5.25 shows a comparison of nanoIR spectra that were obtained from all three panels investigated in this section. These spectra were collected at locations approximately 0.5 to 1 μm away from the hybrid Ti-polyimide matrix interface. The specific locations on the cross-section specimens are highlighted by the yellow arrows on the AFM images attached. The organosilicon groups are clearly present in the vicinity of the Ti-polyimide interface. Their existence was observed as far as 5 μm away from the ablated Ti surface. These organosilicon groups were detected at wave numbers between 900 cm^{-1} and 1100 cm^{-1}. The spectra presented in Figure 5.25 show similarity in the IR peaks representing imide bonds. Differences in these IR spectra are observed for peaks occurring at wave number ranging from 900 to 1200 cm^{-1}, where the organosilicon functional groups were detected. This difference arises from the use of different sol-gel surface treatment solutions on the ablated Ti foil surfaces. IR peaks associated with deformation of Si−O−Ti groups were also found, indicating the formation of covalent bonds between the Ti substrate and the sol-gel solution. In addition, nanoIR results provide further confirmation that the silane groups from the sol-gel solution penetrated into the ablated Ti layer, supporting the observations from SEM/EDS analysis discussed previously.

NanoIR spectra obtained from the Ti_PEI_1-hour panel hybrid interface will be compared to FTIR spectra collected on the fracture surfaces after a 4-point end notch flexure test. This will be presented and discussed in section 7. The effect of using different sol-gel chemistry on the adhesion between Ti and polyimide resin will also be revealed in that section.

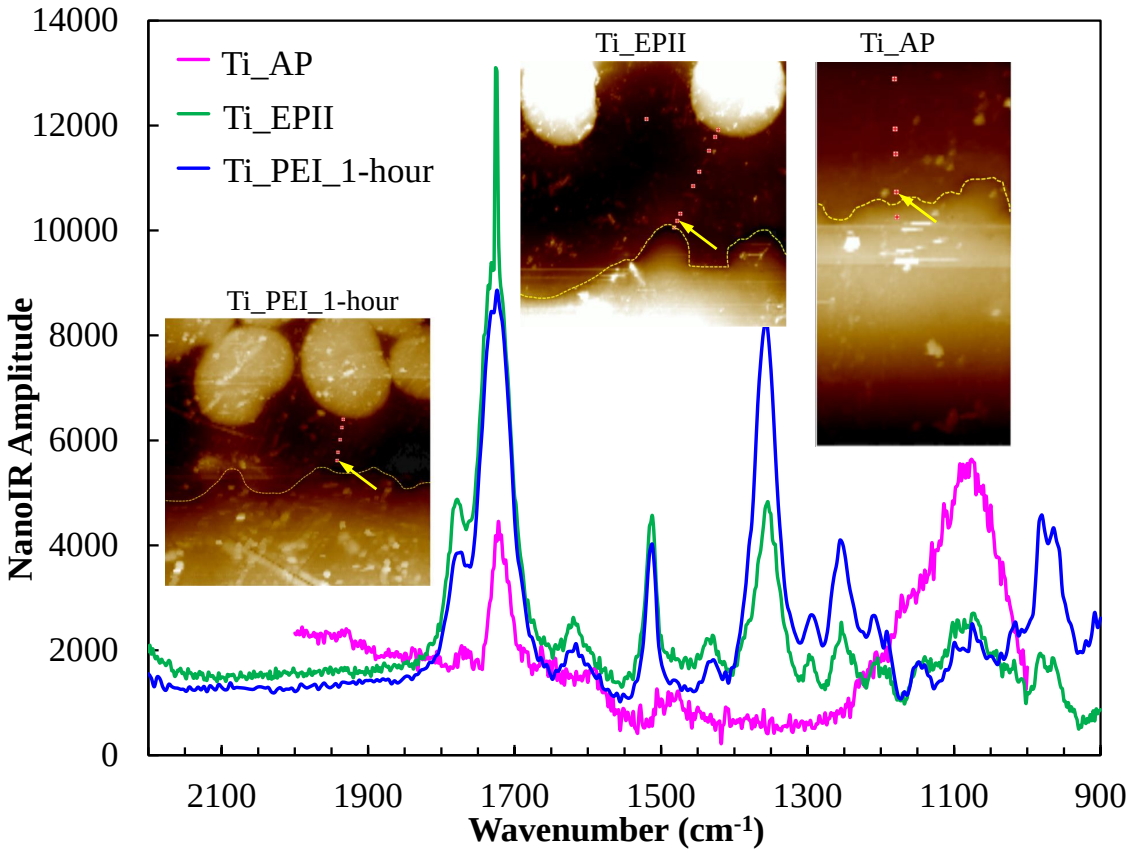

Figure 5.25: Comparison NanoIR results for specimens from Ti_PEI_1-hour panel, Ti_AP panel and Ti_EPII panel. *The yellow arrows on the AFM images indicate the location on each specimen where the nanoIR results are presented in this Figure.*

5.7 Summary

Hybrid laminates that are composed of Ti or NiTi foil and 8-harness satin weave T650 carbon fabric/AFR-PE-4 matrix prepreg were successfully fabricated. Heat treatments performed on Ni-rich NiTi foil to activate its shape memory behaviors prior to integrating it to the hybrid laminates were presented. The effect of thermal-mechanical processing conditions on the transformation temperatures of Ni-rich NiTi foil were investigated via DSC analysis. The surface treatments employed on the Ti and NiTi foil surfaces were laser ablation and sol-gel techniques. Three different sol-gel chemistry systems investigated in this work were the commercial BoeGel EPII, a modified EPII using aminophenyl silane in place of glycidoxypropyltrimethoxysilane, and a custom-synthesized sol-gel solution that contains phenylethynyl imides. Adhesion between ablated Ti surface and AFR-PE-4 matrix was directly achieved via both mechanical interlocking and chemical bonding. These bonding mechanisms were evidenced by the results presented and discussed from OM, SEM/EDS and nanoIR investigations. The micro roughness patterns created by laser ablation of the Ti/NiTi foil surfaces not only provided a larger contact area available for bonding with the resin, but also created porosities on the ablated surfaces. These porosities allowed the silane groups from the sol-gel solutions to penetrate into the Ti/NiTi layer. Evidence of Si presence in the ablated Ti layer was found via both SEM/EDS and nanoIR analysis performed on the cross-sections. Thermal-mechanical analyses were carried out using DMA, TMA and TGA. The coefficients of thermal expansion obtained from TMA experiment will be used in finite element analysis in section 8. Results from DMA analysis show that the non-hybrid and hybrid AFR-PE-4 matrix composite laminates fabricated in this work exhibit β transition prior to the glass transition. The temperatures at which β and glass transitions occur were $150 \pm 5\ ^oC$

and $402.6 \pm 6.4\ ^oC$, respectively. The understanding of these transitions and change in the polymer structure associated with these transitions are important for the analysis of the mode I and mode II fracture toughness as a function of temperature presented in sections 6 and 7.

6. HYBRID TI/NITI-POLYIMIDE MATRIX COMPOSITE INTERFACE: MODE I FRACTURE TOUGHNESS CHARACTERIZATION

It was presented in section 5 and observed that that strong hybrid interfaces were successfully fabricated. To assess the mode I fracture toughness of the hybrid interface as a function of temperature, the DCB tests are carried out [1]. This section presents the details of our approach to high temperature mode I fracture toughness testing up to 315 ^oC. DCB test results together with fractography and ultrasonic transducer inspection are presented herein.

6.1 The Double Cantilever Beam Test

6.1.1 Specimen Preparation

Double cantilever beam tests were carried out at temperature up to 315 ^oC, which is too high for most adhesives, bonding hinges for high temperature DCB tests is a challenge. In addition, DCB hinge bonding using high temperature adhesives requires curing at high temperature, which may cause changes in material properties, or degradation of the interface and and introduce additional residual stresses in the structure before the testing. Consequently, the DCB test results and analysis may be strongly influenced by the above changes. Thus, in this work, our approach is to mechanically attach DCB tabs to the specimens. Except for the specimen from NiTi-PMC panel, all specimens from both non-hybrid and hybrid panels as well as aluminum DCB tabs were drilled for mechanical tab bonding. Figure 6.1 shows an example of a drilled DCB for bonding hinges mechanically and a DCB with aluminum hinges mechanically attached ready for testing. The detail sketches that were used

[1]The experimental work presented in this section was performed at NASA Langley Research Center, Hampton, VA in collaboration with Drs. John Connell and Frank Palmieri.

for drilling the DCB tabs and specimens are presented in Figures D.1 and D.2 in Appendix D. Both longitudinal edges of each specimen were painted white with WiteOut liquid. To facilitate in-situ digital image correlation measurement, one longditudinal edge of each specimen was sprayed with Krylon black paint to create fine speckle patterns. The other white edge was used to measure crack length during the test. The specimens were UT scanned on both side prior to testing. The end of the Kapton film (pre-crack tip) was measured based on UT analysis and marked as 0 mm on the scale. A millimeter scale was marked directly on the white-painted edge using a sharp razor blade.

Due to the sensitivity of shape memory alloys to thermal-mechanical processing parameters, drilling or bonding DCB tabs at elevated temperature would mechanically and thermally introduce additional stresses and activate phase transformation in the NiTi-PMC specimens before testing. As a result, the SMA behavior may be altered and that could lead to a misinterpretation of the fracture toughness results. Thus, different from the DCB specimens from the non-hybrid and Ti-PMC panels described in the previous sections, the DCB aluminum tabs were adhesively bonded to the NiTi_PEI_16-hour specimens using the Henkel Hysol 9394 epoxy-based adhesive. The adhesive was allowed to cure at room temperature for five days. The curd adhesive can sustain test temperature up to 150 ^oC.

6.1.2 Test Setup and Procedure

The quasi-static DCB tests were performed using an MTS 858 table-top system with a 13.3 kN (3000 lbf) load cell and an MTS 458.20 MicroConsole analog controller. A ± 0.5 inches (± 12.7 mm) displacement cartridge and ± 300 lbf (± 1334 N) cartridge were used for the AC controller and DC controller respectively. With a few exceptions that will be described and discussed when applicable, each DCB

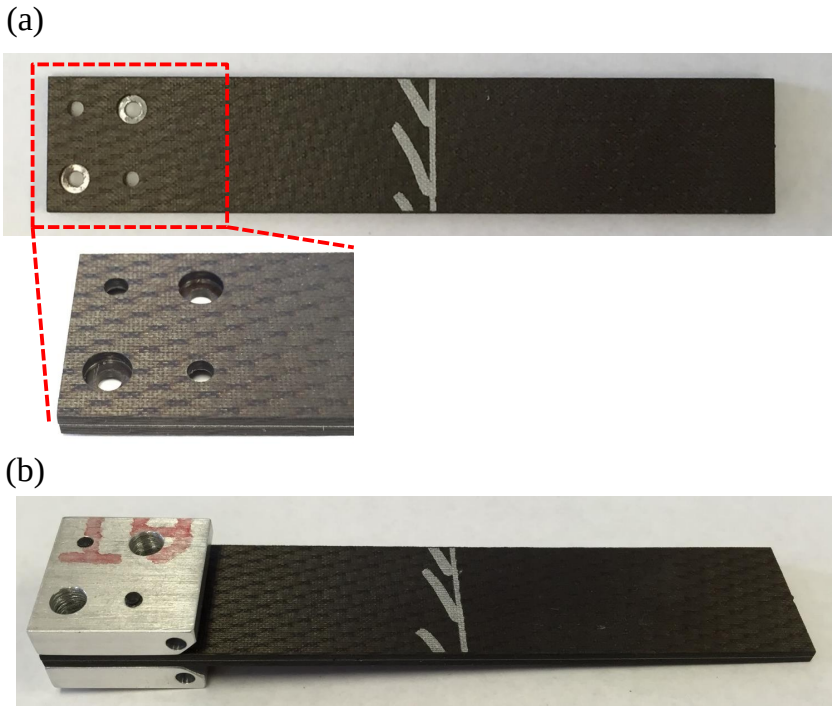

Figure 6.1: (a) Top view of a drilled double cantilever beam specimen for bonding hinges mechanically. (b) A double cantilever beam specimen with aluminum hinges mechanically attached.

specimen was tested by displacement-controlled loading to a maximum opening displacement of 25.4 mm. If the specimen did not fully failed (delaminated) when 25.4 mm was applied, it was unloaded to zero displacement. The loading and unloading rates were 1.02 mm/min and 5.08 mm/min respectively. Data acquisition for load and displacement was performed at a rate of 5 Hz. Figure 6.2(a) shows the test setup that faciliates DCB testing at elevated temperature and with in-situ digital image correlation. Two DIC cameras were used to obtained images for 3D-DIC analysis. These images were taken before and during the tests of the front side of the specimen that was speckle painted. Images for crack growth monitoring were taken by capturing the image on the mirror placed at the back of the environmental chamber,

reflecting the image of the real specimen's back side as shown in Figure 6.2(b).

Table 6.1: Test matrix for mode I fracture toughness characterization of non-hybrid and hybrid Ti/NiTi−T650-8HS/AFR-PE-4 interfaces. Except for the first column, the numbers in each column show the number of specimens tested at 25 ^oC, 150 ^oC, 250 ^oC, and 315 ^oC, respectively.

Panel name	**25** ^oC	**150** ^oC	**250** ^oC	**315** ^oC
Non-hybrid	2	2	2	2
Ti_PEI_1-hour	2	2	1	N/A
Ti_PEI_16-hour	2	2	3	1
NiTi_PEI_16-hour	2	2	N/A	N/A

The DCB tests in this work were performed at 25 ^oC, 150 ^oC, 250 ^oC, and 315 ^oC. For high temperature tests, the environmental chamber was pre-heated to the test temperature and allowed to stabilized for 1 hour. Each specimen tested at high temperature were loaded onto the test fixture once the test temperature was stabilized. The specimen remained in the oven for an additional 1 hour before any loading was applied. This was done to ensure that the specimen was subjected to the test temperature and the temperature profile in the specimen is uniform. Table 6.1 presents the test matrix for the characterization of mode I fracture toughness as a function of temperature of the non-hybrid and hybrid interfaces performed in this section.

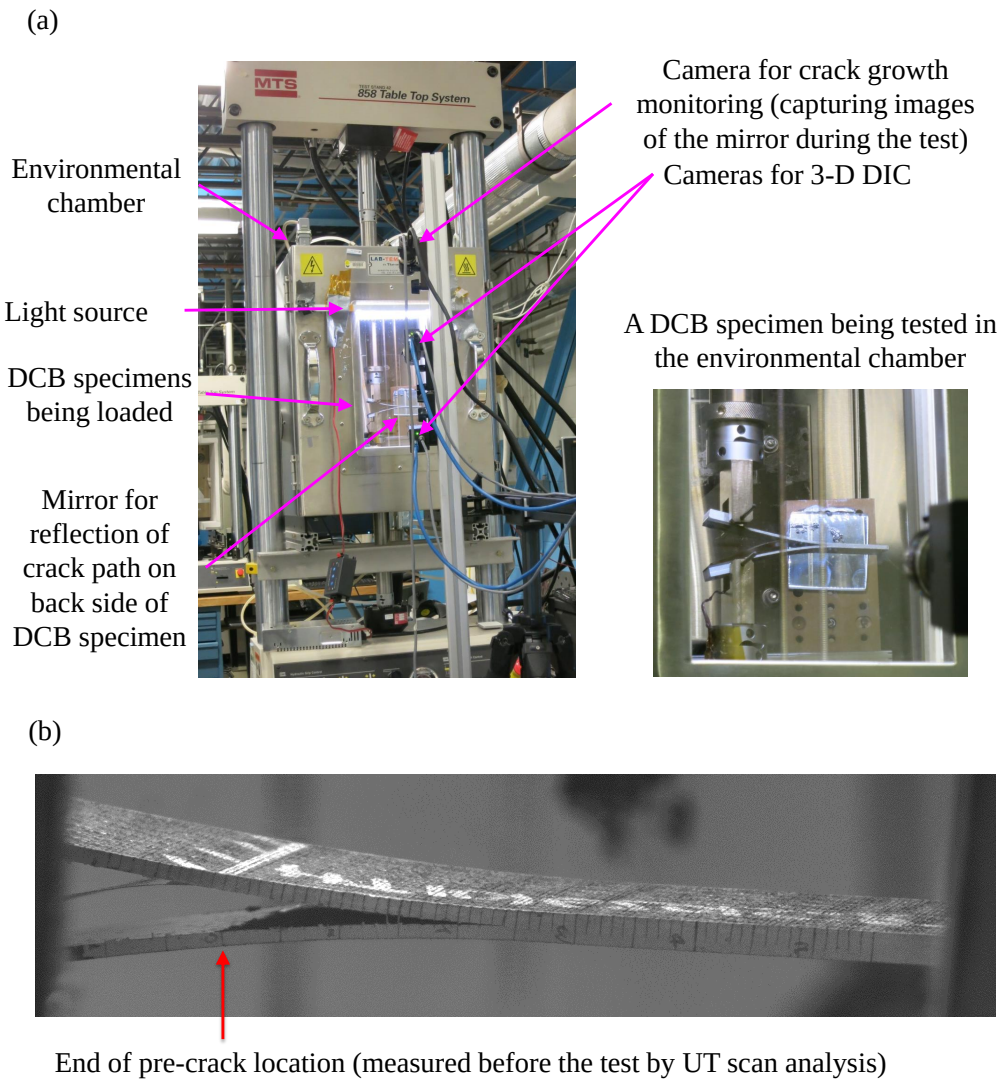

Figure 6.2: (a) The double cantilever beam test setup that facilitates testing at room and elevated temperature and in-situ digital image correlation measurement. (b) Monitoring crack growth visually on one side of the DCB specimen.

6.1.3 Non-destructive Evaluation of the DCB Specimens

Non-destructive evaluation of the DCB specimens was performed before and after each test using ultrasonic transducer scanning. A table-top system where a contact

probe was used to transmit UT signal to the specimen and obtain reflective signals. A transducer of 10 MHz was employed. UT signal frequency was not able to penetrate through the Ti layer, thus no reflection signal was obtained beyond the Ti-PMC interface. As a result, UT scans were performed on both sides of each specimen. This was done before and after each test to identify the initial crack front and monitor the crack propagation.

6.1.4 Data Reduction

The modified beam theory method for interlaminar fracture toughness calculations as described in ASTM Standard 5528 [75] is adopted. Load-displacement values corresponding to each crack length measured were obtained from the analog output from DIC system.

$$G_{IC} = \frac{3P\delta}{2b(a + |\Delta|)} \tag{6.1}$$

where:

P is the load recorded by the MTS load frame,

δ is the applied opening displacement,

b is the width of the specimen, and

a is the crack length (measured from the applied load point to the crack tip).

$|\Delta|$ is the correction factor that is used to avoid overestimating the G_I values due to the fact that rotation may occur at the crack front and thus, it should be assumed that the DCB beam has a crack length is slightly longer than its actual crack length. Δ can be evaluated experimentally by creating a leasts square plot of the cubic root of the compliance as a function of crack length. The absolute value of a where this $C^{1/3}(a)$ curve intercepts the a-axis is $|\Delta|$. This process of $|\Delta|$ value evaluation is illustrated in Figure 6.3.

The expression for compliance of a DCB based on beam theory is as follows.

$$C(a) = C^3 a + C_o \tag{6.2}$$

where:

$$C = \frac{\delta}{P} \tag{6.3}$$

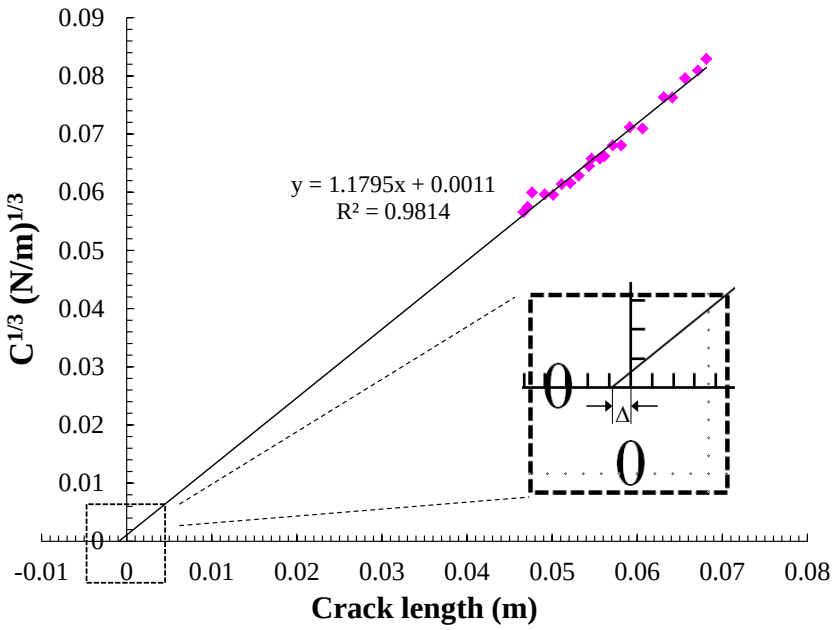

Figure 6.3: An example of the compliance calibration for DCB data reduction using the modified beam theory method. The data set illustrated in this figure is from specimen 7 from panel Ti_PEI_16-hour, tested at 250 ^{o}C.

6.2 Results and Discussion

The load-displacement and fracture toughness results with detailed investigation of the room and elevated DCB tests for the non-hybrid, Ti_PEI_1-hour, Ti_PEI_1-hour, and NiTi_PEI_16-hour interfaces are presented in this section.

6.2.1 Mode I Fracture Toughness of Non-hybrid T650-8HS/AFR-PE-4 Laminate

There is limited reference on the mode I interlaminar fracture toughness of non-hybrid T650-8HS/AFR-PE-4 laminate (or similar woven carbon fabric polyimide matrix composite systems) published in the literature [87]. Thus, the non-hybrid laminate fracture toughness was first carefully studied in this work to establish an understanding of the composite interlaminar delamination behavior before proceeding to investigating that of the hybrid interfaces. A total of eight DCB specimens from the non-hybrid T650-8HS/AFR-PE-4 panel (16 layers of prepreg) was tested, where two specimens were used for each temperature at which the DCB tests were carried out. Except for specimen 2 and specimen 5 tested at 25 ^oC and 315 ^oC, respectively, all other specimens were subjected to one loading cycle and tested until the specimens failed before an opening displacement of 25 mm was reached. Specimen 2 was subject to two loading and unloading cycles at room temperature. During the first cycle, opening displacement was applied on specimen 2 until a large, sudden load drop was observed on the load-displacement curve followed by the appearance of a real crack on the specimen edges. This is an indication that the crack propagated from the pre-crack front created by the Kapton film layers. After this sudden load drop, specimen 2 was unloaded to zero displacement. During the second loading-unloading cycle, specimen 2 was unloaded when a maximum displacement of 12.7 mm was reached. After each cycle, the specimen was UT scanned. The crack length after each test was obtained from UT analysis and compared with the value mea-

sured visually during the test. It was found that the crack length measurements using both methods are consistent. In addition, the crack front remained relatively straight implying that the assumption of straight crack front for the calculation of fracture toughness is reasonable. Hence, it is accepted that the visual crack extension measurement method presented in Section 6.1.2 is reliable. For specimen 5, since it did not fully delaminated when an opening displacement of 25.4 mm was applied, the applied displacement was removed at a rate of 5.08 mm/min until the specimen was subjected to zero load.

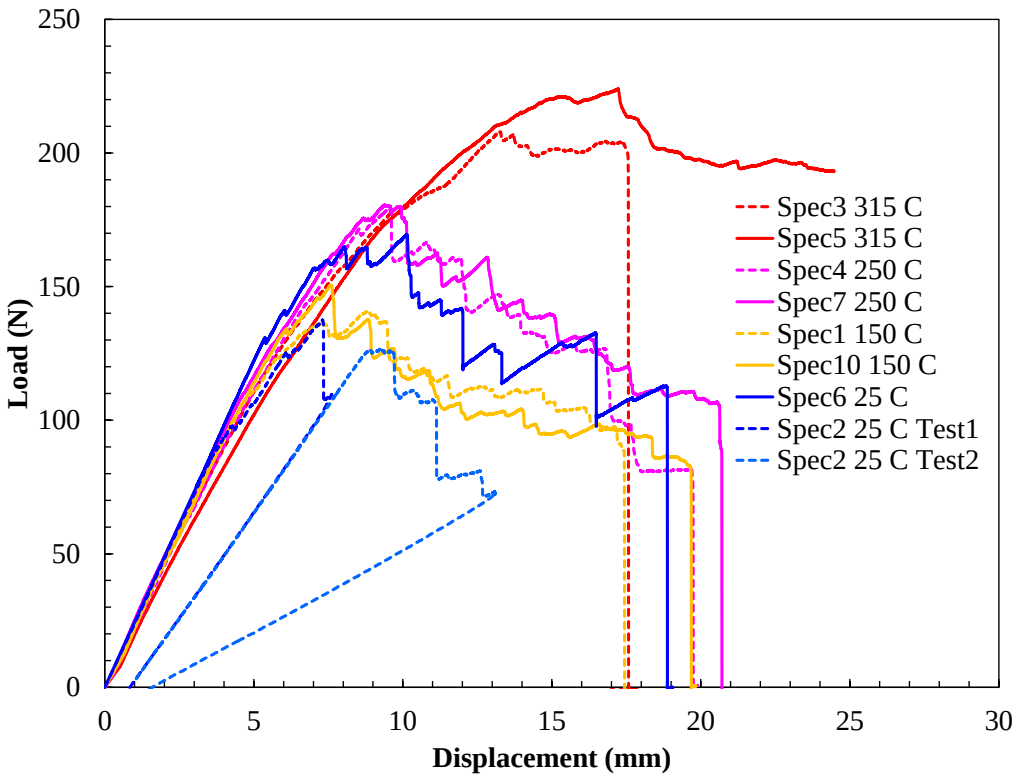

Figure 6.4: Load-displacement curves for non-hybrid T650-8HS/AFR-PE-4 DCB specimens (16 layers) tested at 25 ^oC, 150 ^oC, 250 ^oC, and 315 ^oC. *Unloading curve from the specimen 5 test was not plotted for clarity.*

The load-displacement curves for all tested specimens from the non-hybrid laminate are presented in Figure 6.4. It is observed that all load-displacement curves presented in Figure 6.4 exhibited the saw-tooth behavior where the softening portions of the curves had sudden load-drops followed by increases in load as the displacement continued to apply on the specimens. These saw-tooth features are associated with unstable crack growth where the crack propagates instantaneously when a local critical load (the tip of each saw-tooth) is reached, and the crack arrests at the new delamination front location until another critical load is attained. Observations of the crack growth-arrest behavior and saw-tooth features on DCB load-displacement curves of woven fabric composites have been reported by a number of authors [88, 89, 90]. In Figure 6.4, the load-displacement curves for the DCB tests performed at room temperature exhibit clearer and larger saw-tooths comparing to those obtained from the tests carried out at elevated temperature. The higher the test temperature was, the smaller saw-tooths were observed. That is, the sudden load-drops became less pronounced, leading to more stable crack growth at higher temperature.

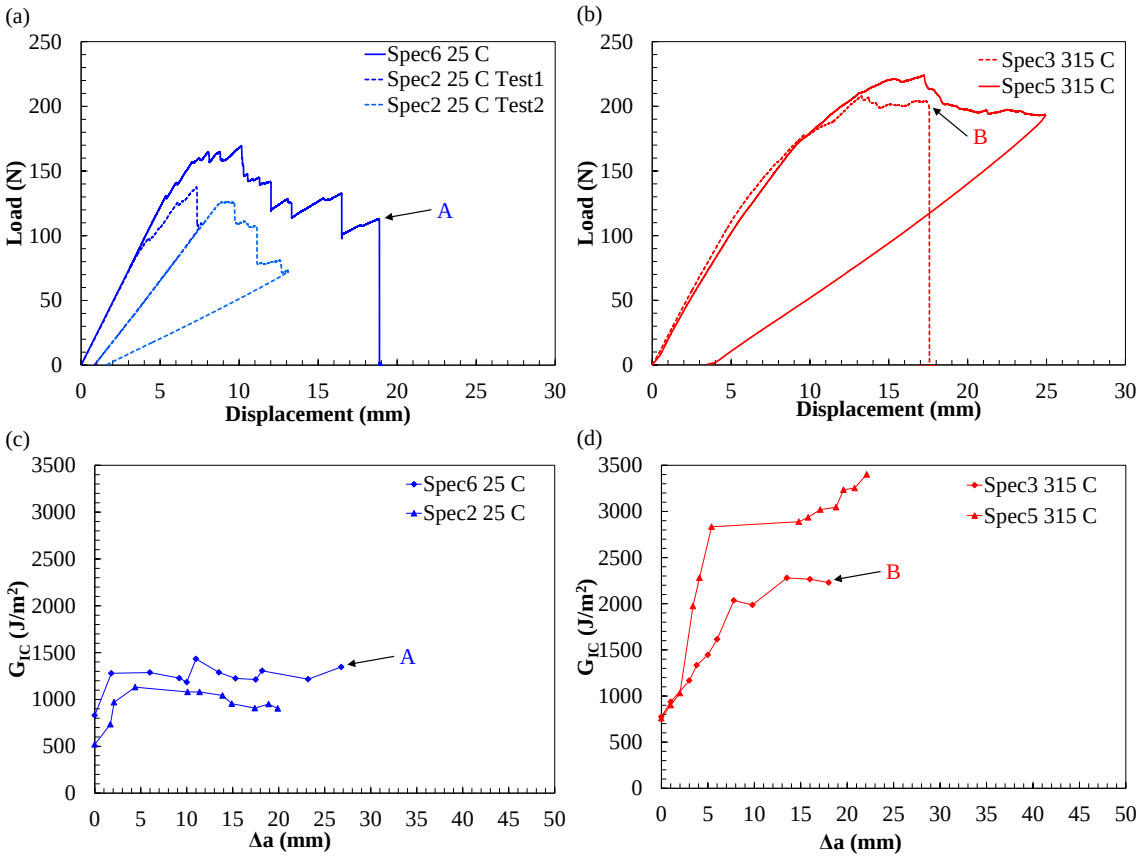

Figure 6.5: (a) Load-displacement curves from non-hybrid DCB specimens tested at 25 ^oC. (b) Load-displacement curves from non-hybrid DCB specimens tested at 315 ^oC. (c) Resistance curves from non-hybrid DCB specimens tested at 25 ^oC. (d) Resistance curves from non-hybrid DCB specimens tested at 315 ^oC. Specimens 6 (25 ^oC test) and 3 (315 ^oC test) fully delaminated when the load-displacement A and B, respectively, was reached. The corresponding fracture toughness values before final failure is shown in Figure (c) and (d).

The load-displacement curves presented in Figure 6.5(a) and (b) demonstrate the clear differences between the 25 ^oC and 315 ^oC tests. At 25 ^oC, the loading portion before any crack propagation occured, and the unloading portion are linear. Together with the large saw-tooth features, this indicates the non-hybrid laminate exhibits elastic and brittle behavior, governed by the elastic behavior of the polyimide matrix at room temperature. Observations from the tests done on specimen 2 show slight nonlinear response. After specimen 2 underwent two loading and unloading cycles, the test result shows non-zero displacement at zero load upon unloading the second time. The residual opening displacement on specimen 2 after the tests is demonstrated in Figure 6.6. This minor nonlinearity the specimen exhibits at room temperature could be attributed to the rough fracture surfaces formed during the tests due to the local fracture mechanisms and fiber/tow breakage, etc. causing the crack to be unable to fully close upon unloading. Observations of the specimen's edge shows formation of micro-cracks and crack branching (crack advancing around the tows) in the crack tip vicinity during the delamination growth process. Visual inspection of the fracture surfaces, presented in Figure 6.7, reveals multiple local fracture mechanisms during crack progation, evidenced by the observation of intra-ply and intra-tow cracking and crack changing interfaces.

In contrast to that presented for the room temperature tests, the load-displacement curves obtained from the tests at 315 ^oC exhibit significant nonlinearity and relatively smooth softening portions. The large nonlinearity is due to the permanent deformation in the matrix as the material underwent a secondary transition at 150 ^oC and approaching the onset of glass transition near 400 ^oC. The significant nonlinearity was represented by a large residual displacement observed on the tested specimen 5, in comparison to that of specimen 2, as shown in Figure 6.6. The relatively smooth portion of the load-displacement curve, corresponding to the crack

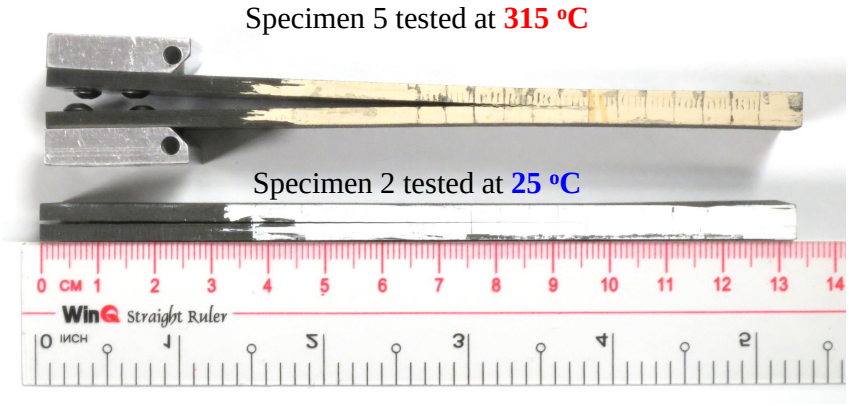

Figure 6.6: Non-hybrid DCB specimens exhibit permanent deformation after unloaded. Specimen 5 tested at 315 ^oC exhibits significant nonlinearity.

propagation stage, depicts a fairly stable crack growth behavior.

The mode I fracture toughness for non-hybrid interface tested at 25 ^oC and 315 ^oC are presented in Figure 6.5(c) and (d), respectively. It is perspicuously seen from those figures that a large variation in the resistance curves is found among the two specimens tested at each temperature. This scatter in fracture toughness could be attributed to the differences in the local fracture mechanisms. It has been observed on the fracture surfaces shown in Figure 6.7 that the crack may not always grow at the mid-plane of the specimen but can change interfaces as it propagates. In other words, upon crack propagation, the crack front may not remain in between the two fabric layers adjacent to the initial crack plane, but can slightly change direction and partially migrate into one of them. This could be due to local crack bifurcation caused by the weave undulation and presence of the resin rich pockets and interstitial sites at the intersections of the warp and fill yarns. Nevertheless, further microscopic and fractographic investigation is required to identify the local

failure modes that contribute to the scatter. Figure 6.8 illustrates the possible crack growth paths when the described crack changing interfaces occurs. Two 8-harness satin weave fabric layers that are adjacent to the initial crack front are shown. That is, only the 8^{th} and 9^{th} layers of a 16-layer laminate are demonstrated.

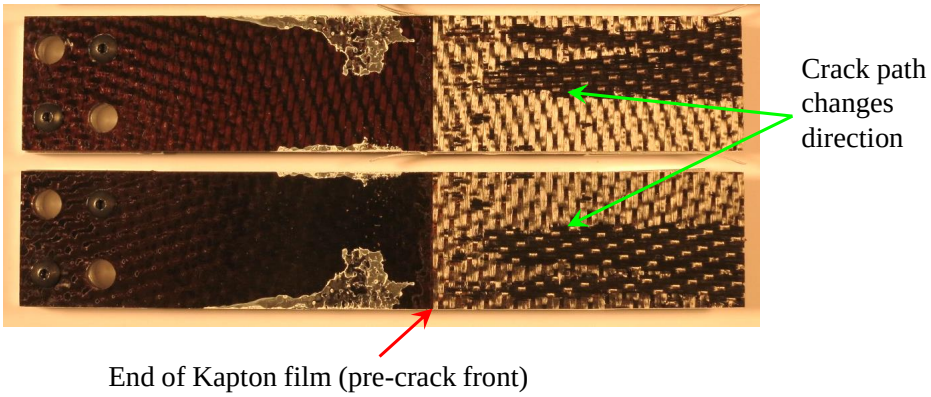

Figure 6.7: Example of crack front changing interface in the non-hybrid DCB specimens. Fracture surfaces of specimen 6 tested at 25 ^oC are shown in this figure.

Regardless of the scatter, the G_{Ic} values presented in Figure 6.5 for non-hybrid T650-8HS/AFR-PE-4 interface tested at 25 ^oC and 315 ^oC are comparable with those reported by Czabaj and Davidson [87] for a similar material system. The mode I fracture toughness of the non-hybrid T650-8HS/AFR-PE-4 interface as a function of temperature is presented in Figure 6.9. That is, R curves from all DCB tests performed at 25 ^oC, 150 ^oC, 250 ^oC and 315 ^oC for this interface are plotted. In all cases, it was found that the fracture toughness first increased for a delamination extension of approximately 5 to 7 mm. Then, the resistance curve reached a plateau representing by a steady-state value around which the fracture toughness oscilated.

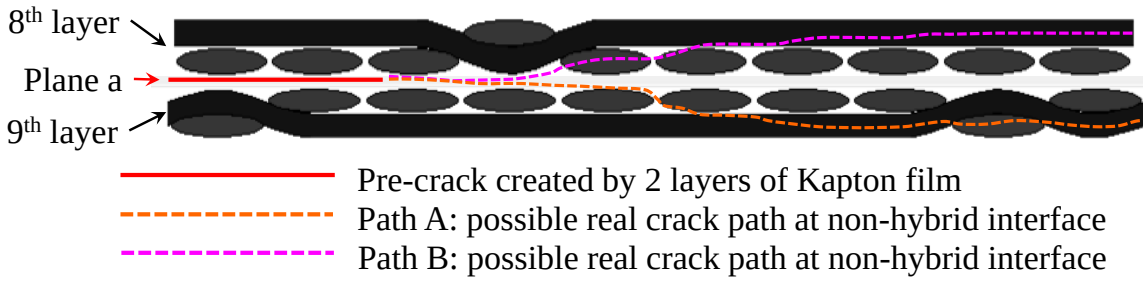

Figure 6.8: Schematic showing possible crack propagation paths in the non-hybrid DCB specimens. Only the two 8-harness satin weave fabric layers (8^{th} and 9^{th} layers in the 16-ply panel) adjacent to the crack plane are shown. The crack does not always propagate in between the 8^{th} and 9^{th} layers (along plane a) but can follow either path A or path B.

This is consistent with the observations published in the literature for interlaminar fracture toughness of woven fabric composites [91, 88, 92, 89].

It is generally accepted that the mode I fracture toughness of thermosetting polymer matrix composite, both non-hybrid [93, 90] and hybrid [94, 95, 3] interfaces, is increased as temperature increases. This is attributed to the large plastic zone near the crack tip caused by the increase in matrix ductility at elevated temperature [93]. It should be noted that most of these investigations were performed on epoxy matrix composites. This postulation, however, is not applicable for the polyimide composite system investigated in this study. It is herein observed that the mode I fracture toughness of T650-8HS/AFR-PE-4 does not always increase with increasing temperature (below glass transition temperature). The results presented in Figure 6.5 reveal a decrease in fracture toughness as temperature increased from 25 ^oC to 150 ^oC. This behavior could be explained by the β transition in T650-8HS/AFR-PE-4 composite that occurs at 150 ^oC where a large amount of local polymer chain motion occurs, as discussed in Section 5.5.1. This behavior does not exhibit in the published

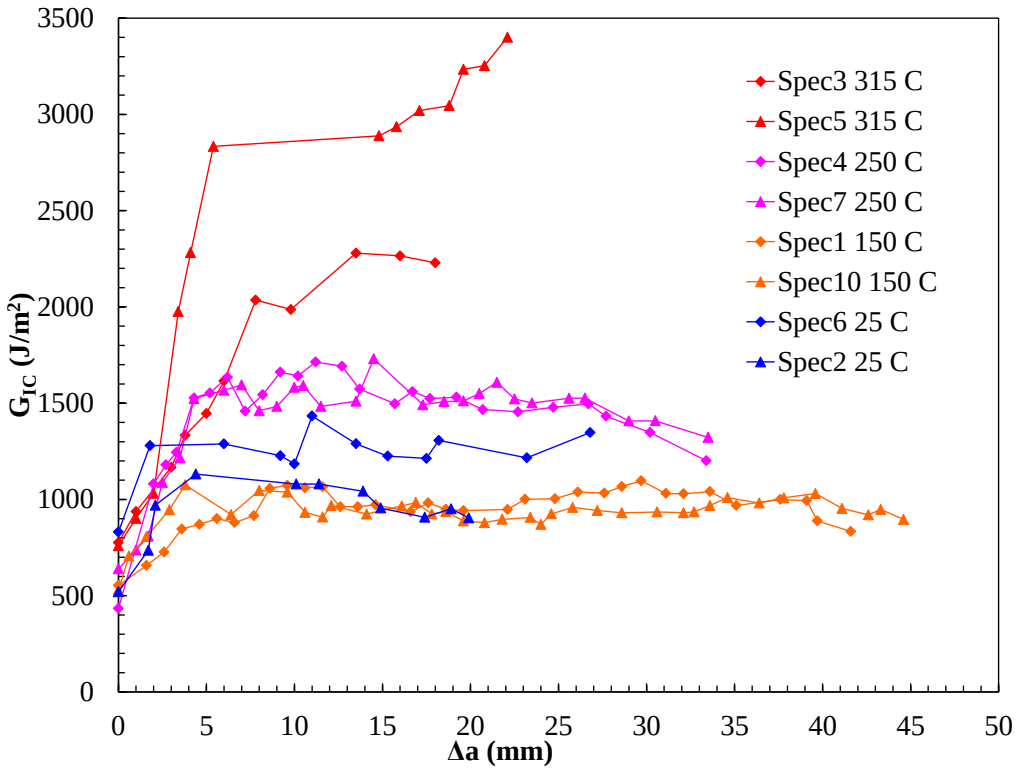

Figure 6.9: Delamination resistance curves (R curves) for non-hybrid T650-8HS/ AFR -PE-4 DCB specimens (16 layers) tested at 25 ^oC, 150 ^oC, 250 ^oC, and 315 ^oC. R curves from 25 ^oC and 315 ^oC DCB tests show a large scatter between the two specimens tested at each temperature. Consistency in the R curves from 150 ^oC and 250 ^oC DCB tests is found among the two tested specimens in each case.

studies on the non-hybrid [93, 90] interfaces with epoxy matrix composites and hybrid interfaces investigated in section 4 because T_β transition for epoxy typically occurs at temperatures range from -80 ^oC to -30 ^oC [70], which are well below the selected temperatures for testing (room temperature and above).

At temperature above 150 ^oC, an increase in temperature indeed caused the fracture toughness to increase. Once β transition is complete, as the temperature increases, the R-curves become shorter while the initiation and steady-state fracture toughness values become higher. This is because of matrix softening as temperature

approaches T_g causing the composite to exhibit ductile-like behavior. Thus, at higher temperature (above T_β and below T_g) the strain energy induced by the applied loading would cause the arm to plastically deform more than causing the crack to grow. This explains why more energy is required to propagate the crack and the crack extension is less at higher temperature. Consistency in the resistance curves presented in Figure 6.9 is found among each pair of specimens tested at 150 ^oC and 250 ^oC. This observation is supported by the similarity on the fracture surfaces of the two specimens tested at each temperature as visually inspected. Crack changing interface is also observed on these fracture surfaces. Further fractographic investigation using OM and SEM is needed to provide more understanding and better explain the temperature-dependent fracture toughness behavior speculated.

6.2.2 Ti-PMC Hybrid Interfaces

It was presented in section 5 that three different sol-gel chemistries were utilized to prepare the Ti surfaces before fabrication of the hybrid laminates. Cross-section investigations on the hybrid interfaces of all three panels suggested that reasonable adhesion was achieved. However, preliminary DCB testing at room temperature for one specimen from panel Ti_AP and two specimens from panel Ti_EPII revealed that these specimens exhibited 100% adhesive failure mode. Figure C.2 in Appendix C shows the fracture surfaces of these specimens. Bare Ti surfaces were exposed after these specimens were fully delaminated. No evidence of residual resin from the PMC that adhered to the Ti foil and remained on the Ti fracture surface was observed. This is an indication that the Ti_AP and Ti_EPII are weak interfaces. Hybrid interfacial adhesion was mainly achieved by mechanical interlocking with few covalent bonds formation at these interfaces. Thus, no further investigation on the mode I fracture toughness of these panels was carried out in this work. The

results and discussion presented in this section reflect the detailed investigation on the Ti_PEI_1-hour, Ti_PEI_16-hour and NiTi_PEI_16-hour interfaces.

A total of five DCB specimens cut from panel Ti_PEI_1-hour were tested while the DCB tests were performed on eight specimens prepared from the Ti_PEI_16-hour panel. Among the five Ti_PEI_1-hour DCB specimens, two were tested at 25 ^oC, one was tested at 150 ^oC, and the other two specimens were tested 250 ^oC. No DCB test at 315 ^oC was carried out for this panel because one of the two DCB tests performed at 250 ^oC revealed a predominance of adhesive failure mode. The second specimen tested at 250 ^oC exhibited multiple delamination at both the tested and non-tested hybrid interface, i.e., delamination was also initiated and propagated at the Ti-PMC interface that did not contain the Kapton pre-crack. This is indicative of weak interfacial adhesion at temperatures near 250 ^{o}C exhibited by the Ti_PEI_1-hour hybrid interface. In contrast, the dominant mode of failure observed from the three specimens tested at 250 ^oC was cohesive. As a result, the mode I fracture toughness of the Ti_PEI_16-hour hybrid interface was investigated at a temperature above 250 ^{o}C, where one specimen was tested at 315 ^oC. At 25 ^oC and 150 ^oC, two Ti_PEI_16-hour specimens were tested in each case.

For any particular testing condition, the selected specimens were obtained from various locations across the panels. For example, from panel Ti_PEI_16-hour, specimens 1 and 6 were tested at 25 ^oC whereas specimens 5 and 10 were used for the tests performed at 150 ^oC. Note that the specimens were numbered consecutively in the order they were cut from each panel, i.e. specimen 2 was adjacent to specimen 1 and so on. With the exception of specimen 4 from panel Ti_PEI_1-hour that was tested at 250 ^oC, a maximum displacement of 25.4 mm was applied on all DCB specimens. The maximum displacement applied to specimen Ti_PEI_1-hour numbered 4 was 18 mm. Except for specimens 1 from both panels, all DCB specimens tested

were subjected to one single loading followed by unloading to zero displacement. Due to the limited number of specimens, to provide initial insights into the behavior of the hybrid interfaces, specimens numbered 1 from panel Ti_PEI_1-hour and panel Ti_PEI_16-hour were tested in multiple steps followed by careful visual and nondestructive inspections after each step. They were subjected to three loading-unloading cycles. During the first two cycles, displacement was applied until a visual crack extension of 2 to 5 mm was observed on the specimen edges. Then, the specimens were unloaded and removed from the test fixture for inspections. During the last cycle, the crack was allowed to propagate as the displacement was continuously applied until a value of 25.4 mm was reached. To ensure the validity of the crack length measurement method, the uniformity of the crack front after each DCB test as well as to investigate the failure modes, nondestructive evaluation using ultrasonic transducer scanning was performed after each load-unloading cycles performed on specimens 1 and after each of the other specimens were tested. It was observed that no specimen fully delaminated when the applied displacement reached its maximum value. The load-displacement response and mode I fracture toughness results of the Ti_PEI_1-hour and Ti_PEI_16-hour specimens are presented in sections 6.2.2.1 and 6.2.2.2. Sections 6.2.2.3 and 6.2.2.4 present further discussion on the modes of failure observed visually on the fracture surfaces and via nondestructive evaluation using UT scan analysis.

6.2.2.1 Load-Displacement Response

The load-displacement responses from the Ti_PEI_1-hour tested specimens are presented in Figure 6.10. Although two specimens from this panel were tested at 250 ^oC, due to multiple delamination occuring at both Ti-PMC interfaces observed during the DCB test for one of them, the results from testing this specimen is considered

invalid. Thus, the load-displacement and fracture toughness response for this specimen is not reported herein. Representative load-displacement curves from the DCB tests performed for the Ti_PEI_16-hour specimens are presented in Figure 6.11. For each test temperature, one load-displacement curve is plotted in this figure. This was done for visual clarity and ease of discussion purpose. The full load-displacement plots for all tested specimens are shown in Figure C.1 in Appendix C.

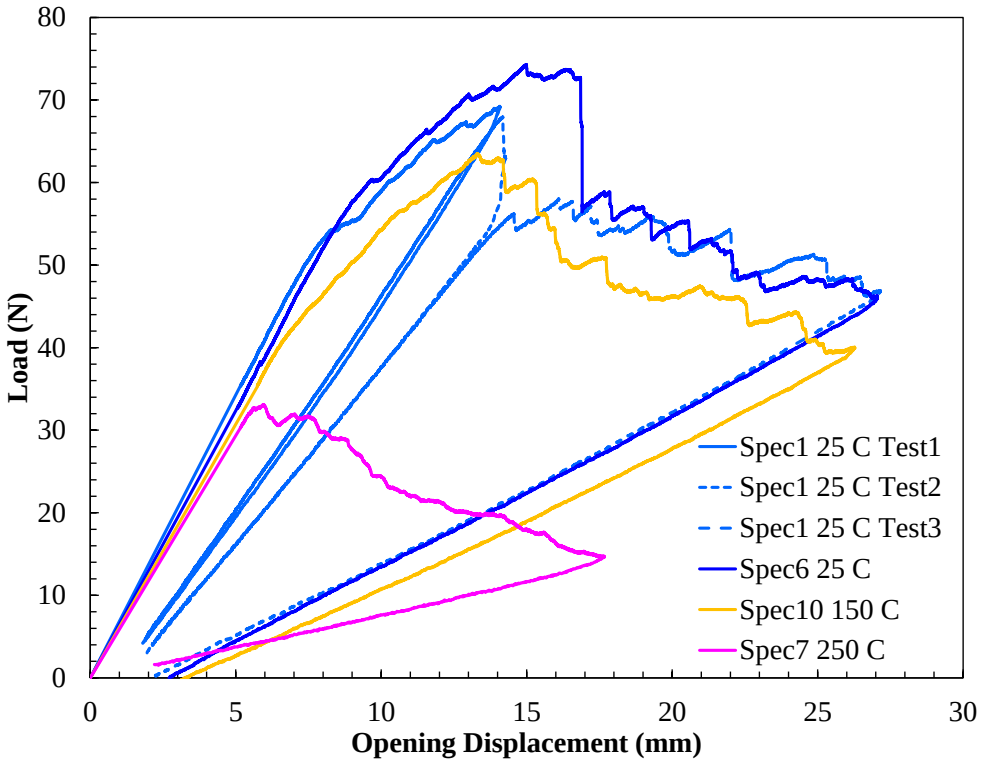

Figure 6.10: Load-displacement curves for Ti_PEI_1-hour DCB specimens tested at 25 ^{o}C, 150 ^{o}C, and 250 ^{o}C. The relatively low and smooth load-displacement curve from the test at 250 ^{o}C indicates adhesive failure mode.

The following discussion is applicable for all tested hybrid Ti-PMC specimens that contain Ti_PEI interfaces, except for the Ti_PEI_1-hour specimen 7 tested

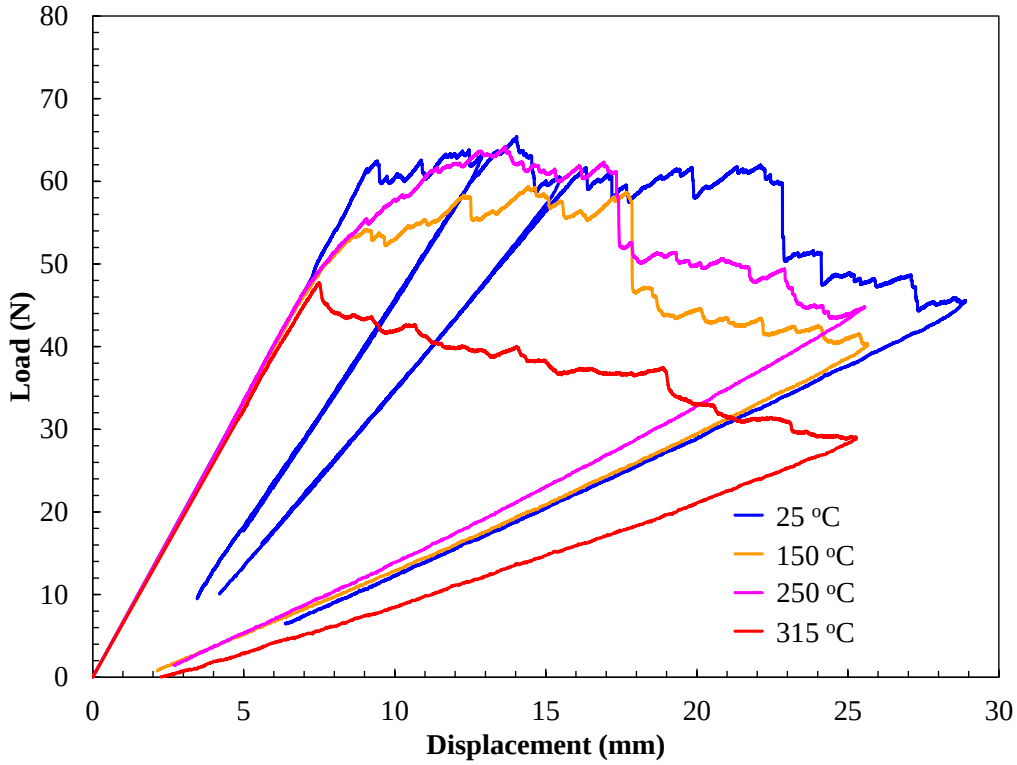

Figure 6.11: Representative load-displacement curves for Ti_PEI_16-hour DCB specimens tested at 25 ^{o}C, 150 ^{o}C, 250 ^{o}C, and 315 ^{o}C. The load-displacement response from DCB tests at 25 ^{o}C, 150 ^{o}C, 250 ^{o}C exhibits saw-tooth behavior, suggesting that the crack path is toward or inside the composite, which indicates cohesive failure. The relatively low and smooth load-displacement curve is observed from the test at 315 ^{o}C, indicating adhesive failure mode.

at 250 ^{o}C and Ti_PEI_16-hour specimen 4 tested at 315 ^{o}C. With the exception of the two mentioned specimens, each of the load-displacement curves in Figures 6.10 and 6.11 exhibited an initial linear loading response, followed by a toughening portion, then continued with a softening portion, and finally ended with a linear unloading response. The toughening portion is described as the nonlinear increase in load that succeeded the initial linear response. This nonlinear load increase was carried on from the deviation from the initial linearity until a global peak load was

achieved and slightly plateaued at or oscilated around that peak load level. The softening portion of the load-displacement response followed the toughening portion and is characterized as the response that showed a decreasing trend in load as the displacement continued to increase at a constant rate.

The nonlinear portions, i.e. both toughening and softening, on each DCB load-displacement response presented herein exhibits a combination of sharp and blunt saw-tooth features. These features are presented in the load-displacement response portions that are associated with the crack propagation stage. As discussed previously, the sharp saw-tooths are depicted as features in which a large, sudden load drop was exhibited after the load was linearly increased to a local peak, followed by an instantaneous release of the crack tip. The blunt saw-tooths are described as the portions of the load-displacement curve where the load was gradually decreased after it reached a local peak, representing a slow, steady crack propagation. The presence of the sharp and blunt saw-tooths on the load-displacement response indicates a combination of unstable and stable crack growth. This is a typical delamination behavior exhibited by both unidirectional and woven composites as discussed in Section 6.2.1 and reported in the literature [88, 89, 96]. This is also an indication of crack growth inside the composite rather than adjacent to the Ti surface at the Ti-PMC interface. Based on the assessment of the load-displacement curves and observations discussed above, it can be postulated that the hybrid Ti-PMC specimens exhitbiting such load-displacement response delaminated in cohesive failure mode. This postulation is supported by the features observed on the fracture surfaces as well as non-destructive evaluation using UT scanning of the tested specimens. The details of these observations are presented in sections 6.2.2.3 and 6.2.2.4.

For the hybrid DCB specimens tested in this work, the transition between the toughening and softening portions observed on the load-displacement response is

abrupt and presented as a sudden and large load-drop followed by an unstable crack growth. It was observed from Figures 6.10 and 6.11 that the transition between the toughening and softening portions in the DCB load-displacement response of hybrid Ti-PMC interface typically occured when the applied displacement reached 15 mm or above. This transition was also found in the load-displacement response for non-hybrid specimens, i.e. T650-8HS/AFR-PE-4 composite without any metallic foil constituent, as presented in Figure 6.4. However, for the non-hybrid specimens tested at 25 ^oC, 150 ^oC, and 250 ^oC, this transition occured at a much earlier stage in the load-displacement response when the peak load was obtained when the opening displacement reached a value between 5 and 10 mm. This observation is consistent with that from the previously reported DCB load-displacement reponse for woven fabric composites [96, 97, 98, 99].

For the non-hybrid interface case, the toughening-softening transition represents crack initiation from the end of the Kapton crack-starter and formation of a real crack front occured inside the composite. Once initiated, the crack propagated into the composite and the crack front either located at the interlaminar interface between two fabric layers, or slightly deflected into one of the fabric plies that were adjacent to the mid-plane where the pre-crack film was placed. During this stage, significant bridging mechanisms that occured in the vicinity of the crack tip caused the toughening response. These mechanisms can be either fiber bridging, tow bridging, ply bridging, or any combination of the above [96]. This initial stage of the crack propagation, as observed and discussed in Section 6.2.1, however, is relatively brief as the crack quickly reached a steady-state growth behavior once it resided inside the composite. This steady-state crack growth is associated with the softening response portion on the load-displacement curve.

For the hybrid interfaces exhibiting cohesive failure modes, there is a delay in the

toughening-softening transition, i.e. a larger opening displacement is required for the transition to occur, in comparison to that needed for the non-hybrid interface. Our hypothesis is that this delay could be attributed to the location where the crack tip was initiated, the crack migration and propagation paths. At the tested hybrid Ti-PMC interfaces, two layers of pre-crack film were placed between the Ti surface and a carbon fabric prepreg layer. As such, the crack could initiate either adjacent to the Ti foil or slightly toward the composite side, depending on the adhesion quality between the Ti surface and composite. In this case, the crack no longer immidiately grew in between two fabric layers like the crack growth behavior at the non-hybrid interface. Rather, it propagated at the interfacial region between the Ti foil and the carbon fabric, where carbon fabric was presented on one side and the other side could be either bare Ti surface or a thin layer of resin and/or imprint of fiber tows from the composite.

The relatively long toughening portion that exhibited saw-tooth features on the load-displacement response suggested that the crack migrated into the composite after initiation by the Kapton film. The relatively smooth toughening portions are exhibited by the Ti_PEI_1-hour specimens tested at 25 ^oC and 150 ^oC presented as compared to that of the specimens from panel Ti_PEI_16-hour tested at the same conditions, as shown in Figures 6.10 and 6.11. This implies a gradual crack migration from the Ti-matrix interface into the composite that occured during the initial crack propagation in the Ti_PEI_1-hour specimens. At the Ti_PEI_16-hour interface, the rough toughening portion on the load-displacement response is indicative of a crack initiation more toward the composite. These hypotheses are supported by observations of the fracture surfaces presented in the following section. Nevertheless, for both Ti_PEI_1-hour and Ti_PEI_16-hour interfaces, it takes more opening displacement, as compared to that needed for the non-hybrid interface, to drive the crack

into the composite before any bridging mechanism could occur. Therefore, it takes longer for the crack at the hybrid interfaces to reach steady-state crack growth. This delay, compared to the non-hybrid interface, is also reflected on the resistance curve response and evidenced on the fracture surface as well as UT images of the interface. These evidences are presented and discussed in sections 6.2.2.2 and 6.2.2.4. The primary toughening mechanism at the hybrid Ti-PMC interfaces in this early stage of crack propagation could be due to energy dissipated during the crack migration process, i.e. the energy to drive the crack into the composite by breaking resin and fiber tows. Furthermore, it should be noted that the laser ablation pattern presented on the Ti surface provide stress concentration sites, causing microcracks to form in the resin region that adhered to the ablated Ti surface. The energy dissipated due to the formation of these microcracks could also be a toughening mechanism. In addition, the fiber and tow bridging mechanisms could play an important role once the crack has fully migrated into the carbon fabric layer in the composite side adjacent to the Ti foil.

For both Ti_PEI_1-hour and Ti_PEI_16-hour panels, both the toughening and softening portions on the load-displacement curve of specimens tested at 150 ^oC occured at a lower load level in comparison to that of the 25 ^oC tests. This is attributed to the effect of β transition occuring at temperature near 150 ^oC as discussed in sections 5.5.1 and 6.2.1. At 250 ^oC, the response from Ti_PEI_16-hour interface shows higher load level compared to the 150 ^oC response, however, still lower than that obtained from specimens tested at 25 ^oC. This could be due to the combined influence of hybrid interface degradation and matrix softening at temperature near glass transition. The relatively less quantity and smaller saw-tooth features observed at higher temperatures indicate the influence of matrix softening and more stable crack growth. This is also evidenced on the fracture surface and

will be further discussed in the following section.

Similarity is observed on the load-displacement response for the Ti_PEI_1-hour specimen 7 (tested at 250 ^oC) and Ti_PEI_16-hour specimen 4 (tested at 315 ^oC). The load-displacement curves for these specimens did not exhibit a toughening portion but immediately transitioned to the softening stage once the critical load was reached from the initial linear loading. The relatively smooth softening curve implies that the crack growth occured at a relatively smooth surface. This is an indication that the crack had minimal or no interaction with fiber and tows from the composite during the crack propagation process. Rather, it propagated adjacent to the Ti surface. In addition, the softening portions of these specimens occured at a distinctively lower load level in comparison to those from the same panel that exhibited the saw-tooth features. It can be postulated that the Ti_PEI_1-hour and Ti_PEI_16-hour interfaces are weak at 250 ^oC and 315 ^oC, respectively.

6.2.2.2 Mode I Resistance Curves

Figures 6.12 and 6.13 respectively present the mode I resistance curves for hybrid Ti_PEI_1-hour and Ti_PEI_16-hour interfaces tested at temperature up to 315 ^oC. Except for the Ti_PEI_1-hour specimen tested at 250 ^oC, and Ti_PEI_16-hour specimen tested at 315 ^oC which exhibit adhesive failure mode, as implied by the load-displacement response, all the other tested specimens exhibited composite-like resistance curve behavior, indicating cohesive failure mode. These composite-like R curves contained a toughening portion and a plateau-like portion. They started with a relatively low G value, then rapidly increased with crack extension, and resulted in a toughening curve with a steep slope. The R curves then reached a maximum G_{IC} then slightly decreased and plateaued out.

As seen in Figure 6.12, the R curves for the two specimens tested at 25 ^oC had

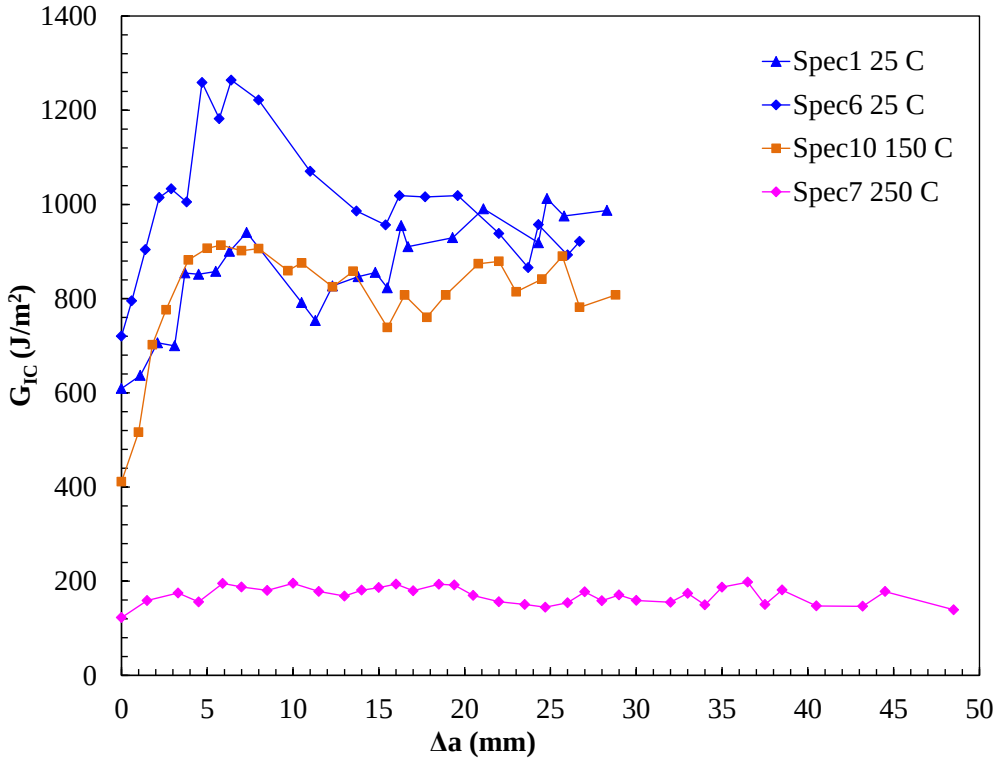

Figure 6.12: G_{IC} versus crack extension Δa (resistance curve) plot for DCB specimens from the Ti_PEI_1-hour panel. Composite-like R-curve behavior is observed at 25 ^oC and 150 ^oC, indicating cohesive failure. The relatively flat and low R curve from the test at 250 ^oC suggested adhesive failure.

the toughening portion spanned from the end of the pre-crack film to an extension of 7-8 mm while the R curve from the specimen tested at 150 ^oC reached plateau at 5 mm crack extension. Similarly, observation from Figure 6.13 shows that the G values on the R curves for Ti_PEI_16-hour interface (at testing conditions where cohesive failure mode was revealed) increased to a crack extension of approximately 12 to 15 mm, then slightly decreased once the peak values was reached, and finally approached the steady-state values. The peak G values on the R curves marked the transition from toughening stage to steady-state during crack propagation. This transition as

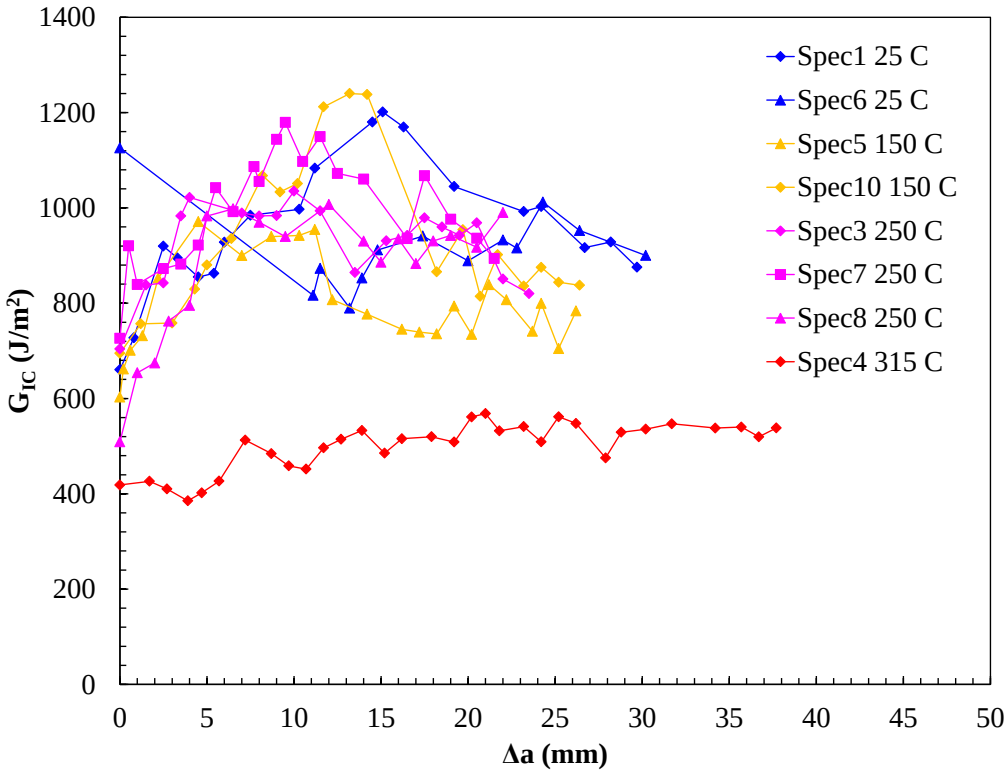

Figure 6.13: G_{IC} versus crack extension Δa (resistance curve) plot for DCB specimens from the Ti_PEI_16-hour panel. Composite-like R-curve behavior is observed at 25 ^oC, 150 ^oC, and 250 ^oC, indicating cohesive failure. The relatively flat and low R curve from the test at 315 ^oC suggested adhesive failure at this temperature.

displayed on the R curves corresponds to the transition from toughening to softening as seen previously in the load-displacement response. That is, the measured crack extension at which the transition between toughening and softening on the load-diplacement response occured correlates with the crack extension where the G value on the corresponding R curve slightly decreased from its peak. This proved the hypothesis that the softening portion on the load-displacement curve associated with steady-crack growth.

The toughening portions on the R curves for Ti_PEI_16-hour interface are not

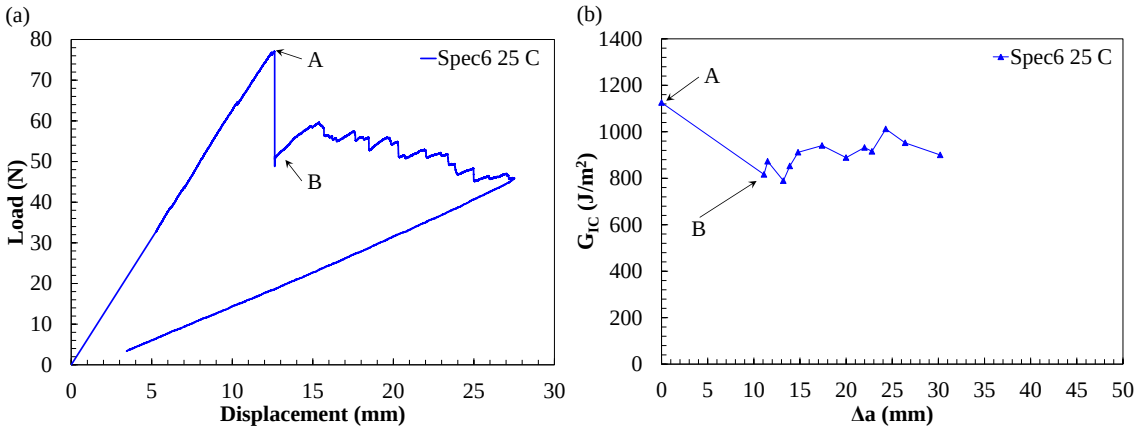

Figure 6.14: Load-displacement and corresponding R-curve plot for specimen 6 from the Ti_PEI_16-hour panel that was tested at 25 ^oC. The large-sudden load drop followed by an unstable initial crack propagation from the pre-crack (point A to point B on both plots) is attributed to a resin-rich pocket at the pre-crack front.

as steep as that of the Ti_PEI_1-hour interface. The delay in reaching the peak G values on the R curves for the Ti_PEI_16-hour interface correllates precisely to the delay in reaching the peak of the R curve. This delay could be attributed to the effect of fiber and tow bridging as well as other toughening mechanisms as previously discussed. Figure 6.9 crack extension 5 to 8 mm reach plateau. Crack changing interface also has a toughening effect. This observation was reported by Truong *et al.* [94]. The crack propagation is slighly shorter at higher temperature, considering cohesive failure mode. This is the influence of the AFR-PE-4 as observed for the non-hybrid interface and discussed in section 6.2.1. This will be further discussed in section fractography and UT analysis.

Figure 6.14 show the load-displacement and R curve response for a specimen form the Ti_PEI_16-hour panel tested at room temperature. The initial crack propagation of this specimen is an outlier since the crack initiate and propagate unstably from the precrack to the composite with an initial extension of 11.1 mm. At this crack

extension, the crack front located far enough away from the pre-crack tip and into the composite to propagate steadily. Thus, there is no toughening portion displayed on both the load-displacement and the R curve of this specimen.

The influence of temperature on fracture toughness is revealed on the resistance curve plot. The slightly lower G values at 150 ^oC for Ti_PEI_1-hour interface could be the combined influence of beta transition in AFR-PE-4 matrix composite and thermal degradation of the hybrid interface. The Ti_PEI_1-hour specimen tested at 250 ^oC, and Ti_PEI_16-hour specimen tested at 315 ^oC which exhibit adhesive failure mode show relatively flat R-curves. For hybrid interface, the metal-PMC interface governs the behavior. The R curve for the adhesive failure case remains relatively flat indicating no toughening mechanism from the PMC side. For panel Ti_PEI_1-hour (one specimen was tested, the other specimen has multiple interface delamination (crack initiated on the non-tested Ti-PMC interface). This suggests that the sol-gel product degrades at temperature close to 250 ^{o}C in this case. Initiation value of Ti_PEI_1-hour are lower comparing to that of the Ti_PEI_16-hour at all testing condition. When the adhesive failure is revealed, the Ti_PEI_16-hour interface shows more resistance to crack propagation comparing to Ti_PEI_1-hour interface. This is evidenced by the higher fracture toughness (280 % or 2.8 times higher) and shorter crack extension given the same applied displacement as shown in Figure 6.15(b). The Ti_PEI_1-hour interface exhibited adhesive failure at 250 ^{o}C while the mode of failure revealed from three tests of the Ti_PEI_16-hour interface at that same temperature was cohesive. This could be because the longer hydrolysis time allowed more -COOH groups to form and available for bonding with the Ti surfaces. As a results, more covalent bonds were formed at the Ti_PEI_16-hour interface causing it to be stronger and it takes more energy to break all these covalent bonds to yield adhesive failure.

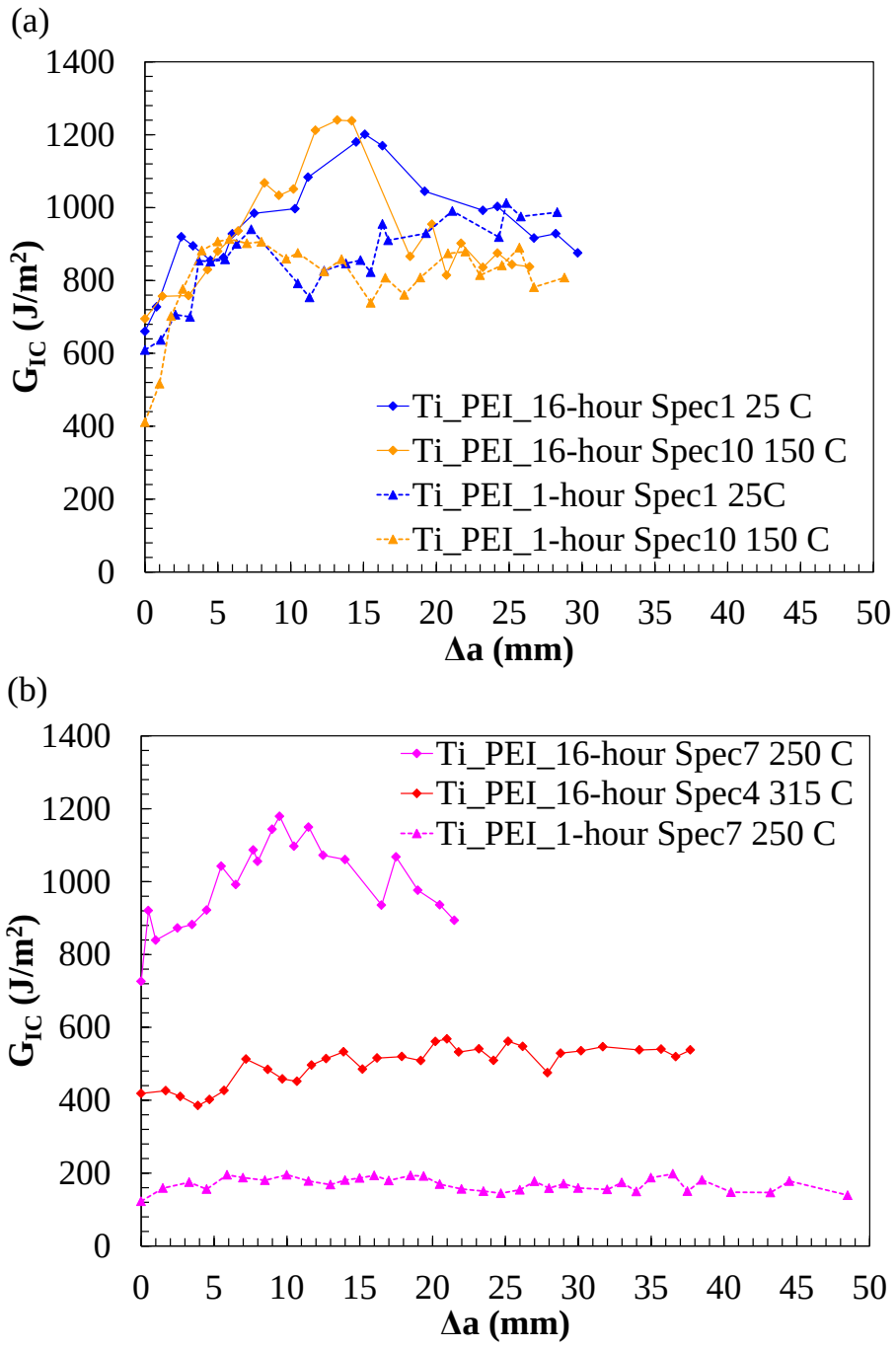

Figure 6.15: Comparison of R curves for DCB specimens from the Ti_PEI_1-hour and Ti_PEI_16-hour panels (a) results at 25 ^{o}C and 150 ^{o}C (b) results at 250 ^{o}C and 315 ^{o}C.

6.2.2.3 Fractography

Fracture surfaces of Ti_PEI_1-hour and Ti_PEI_16-hour interfaces tested at various temperatures are presented in Figures 6.16 and 6.17. For the Ti_PEI_1-hour interface, cohesive failure is revealed at 25 ^{o}C and 150 ^{o}C. For the Ti_PEI_16-hour interface, cohesive failure is revealed at 25 ^{o}C, 150 ^{o}C and 250 ^{o}C. Adhesive failure is clearly observed on the Ti_PEI_1-hour specimen tested at 250 ^{o}C and Ti_PEI_16-hour tested at 315 ^{o}C, although on the latter specimen's fracture surfaces, some residual from the PMC remained on the Ti surface was seen. All the evidence presented on the fracture surface support the observations and conclusions from the analysis of load-displacement response and resistance curves made in the previous sections.

It is observed on the fracture surfaces shown in Figures 6.16 that in the case of cohesive failure, the crack at initiated adjacent to the Ti surface. At a crack extension of 5-7 mm, the crack migrated into the composite side and remained there until the test completion. In Figure 6.17, it is observed that the crack first started in the resin rich region inside the PMC and continued to propagate in the PMC without any sign of crack migration towards the Ti surface. This observation further support the postulations about toughening behavior seen on the load-displacement and R curves. This is also an indication that the NiTi_PEI_16-hour interface is stronger than the NiTi_PEI_1-hour interface. The crack paths associated with the above observations are illustrated in Figure 6.18.

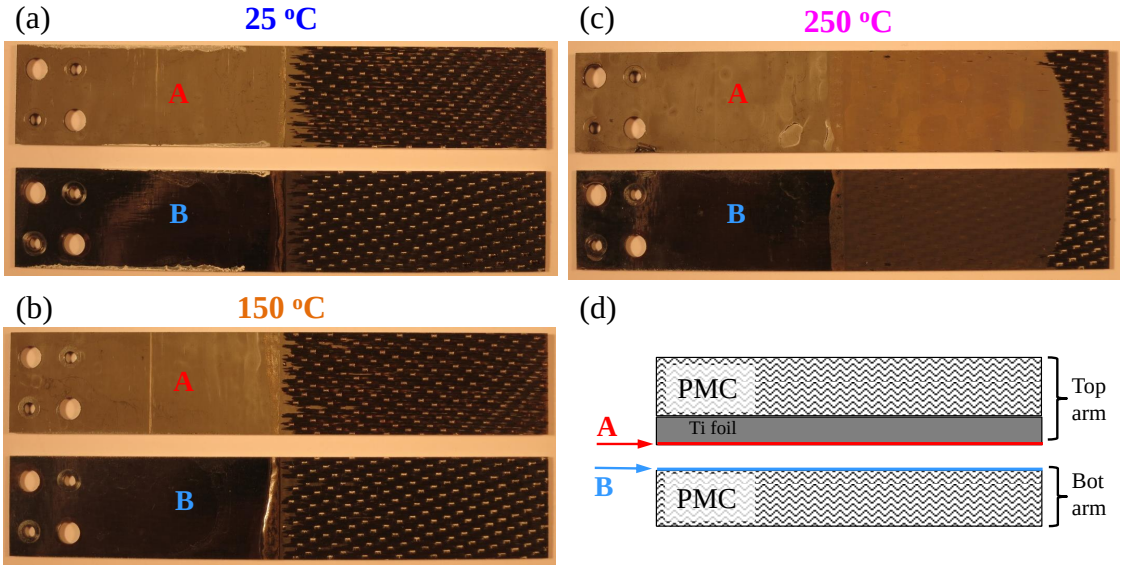

Figure 6.16: Fracture surfaces from tested DCB specimen from panel Ti_PEI_1-hour (a) 25 ^{o}C. (b) 150 ^{o}C. (c) 250 ^{o}C. (d) Schematic of a tested DCB specimen illustrating the locations of surface A and surface B showing in Figures 6.16 (a-c) and 6.17 (a-d).

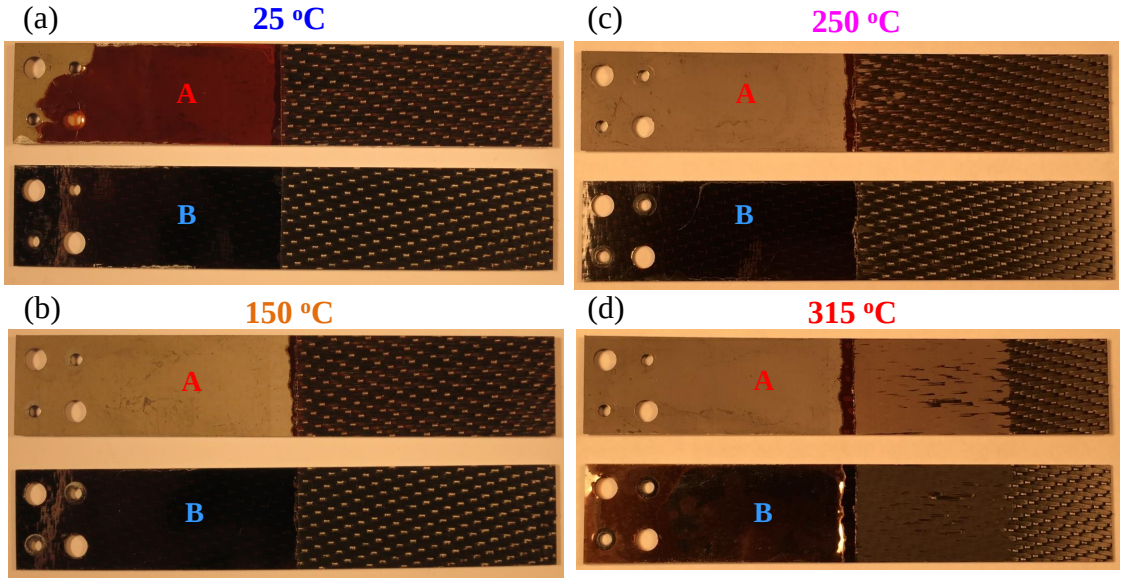

Figure 6.17: Fracture surfaces of DCB specimens from the Ti_PEI_16-hour panel tested at (a) 25 ^{o}C. (b) 150 ^{o}C. (c) 250 ^{o}C. (d) 315 ^{o}C. Except for the specimen tested at 315 ^{o}C, the dominant mode of failure for DCB specimens tested at temperature up to 250 ^{o}C is cohesive.

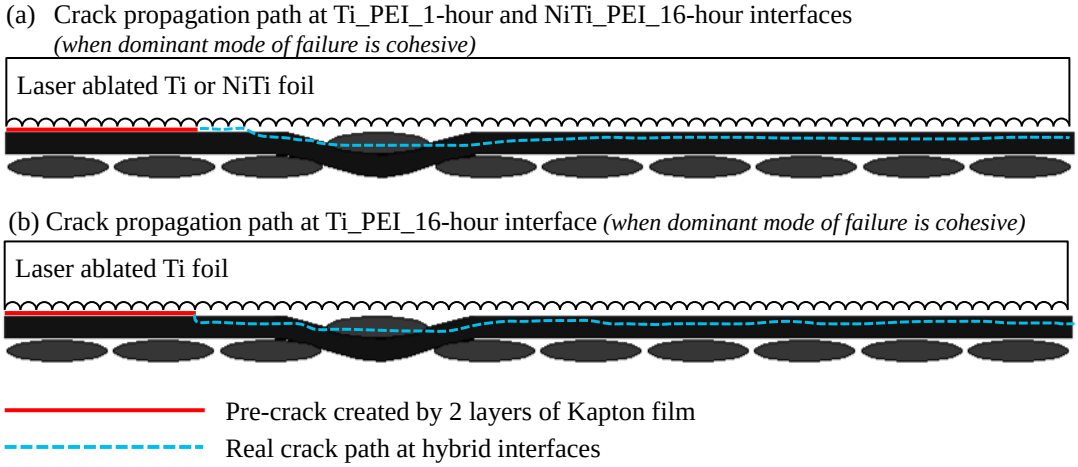

Figure 6.18: Schematics of crack propagation path at the (a) Ti_PEI_1-hour interface (applicable for DCB specimens tested at 25 ^{o}C and 150 ^{o}C) and NiTi_PEI_16-hour interface (DCB specimens tested at 25 ^{o}C). (b) Ti_PEI_16-hour interface (applicable for DCB specimens tested at 25 ^{o}C, 150 ^{o}C, and 250 ^{o}C). *The weave pattern in this figure was generated using TexGen [2].*

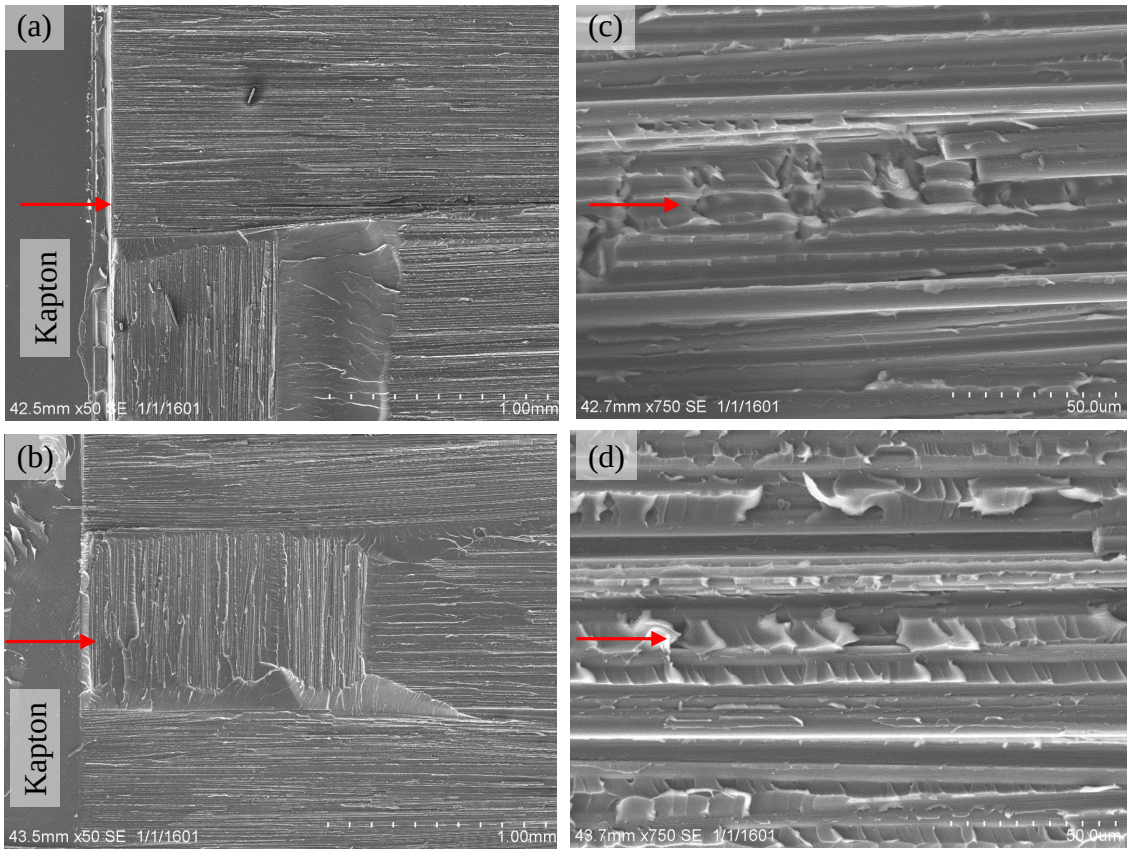

Figure 6.19: SEM fracture surfaces from tested DCB specimen from panel Ti_PEI_16-hour (a) Low-mag image near the Kapton film - specimen tested at 25 ^{o}C. (b) High-mag image near the Kapton film - specimen tested at 25 ^{o}C. (c) Low-mag image near the Kapton film - specimen tested at 150 ^{o}C. (d) High-mag image near the Kapton film - specimen tested at 150 ^{o}C. Formation of micro-crack due to stress concentrated created by laser ablation pattern is observed on the high-mag images, showing an additional toughening mechanism. More cusp features observed on the fracture surface from the specimen tested at higher temperature indicate the softening of matrix and its influence on the fracture behavior of the hybrid interface.

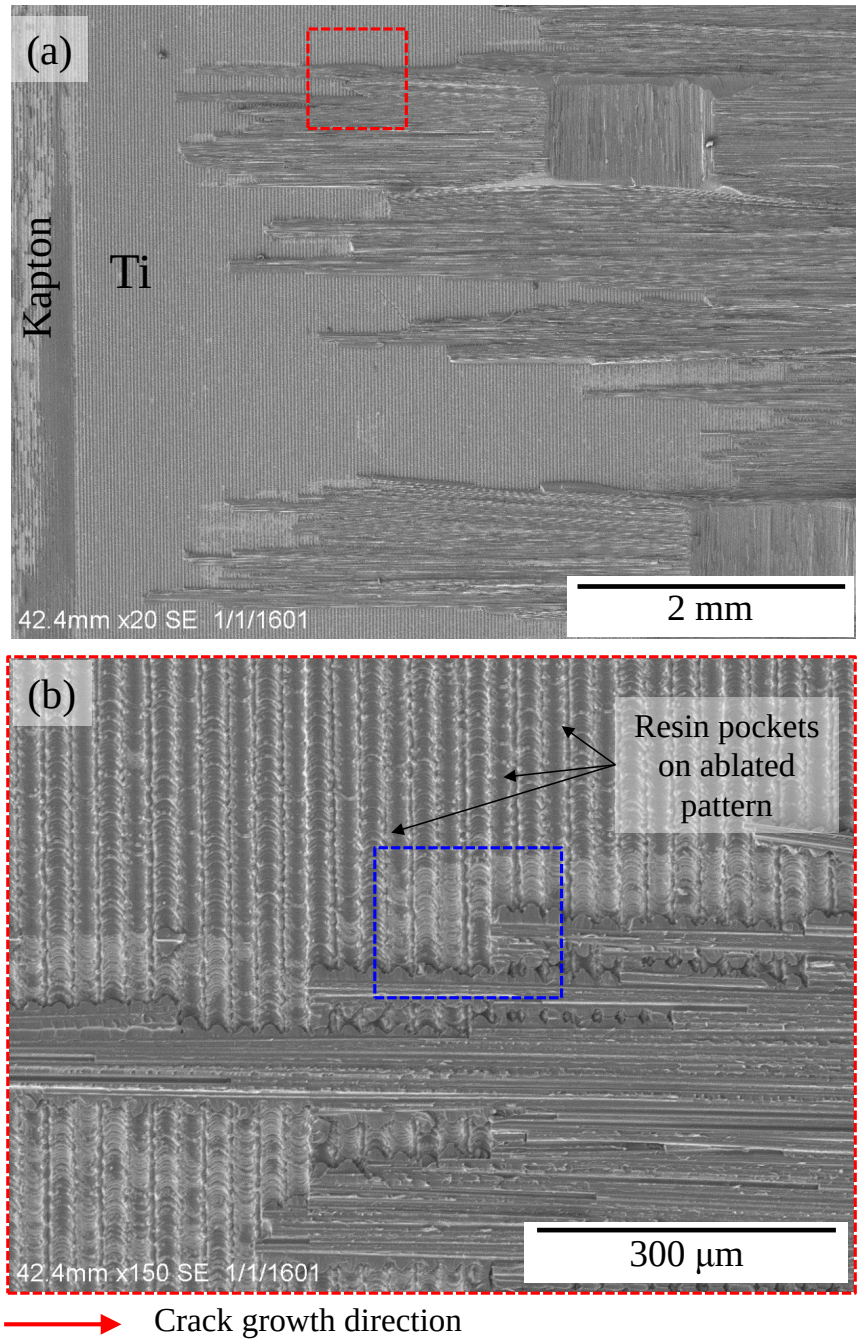

Figure 6.20: SEM fracture surfaces of a DCB specimen from Ti_PEI_1-hour panel tested at 25 ^{o}C (a) near the Kapton insert. (b) close-up view of region indicated by the red box in image (a). The dashed blue box on image (b) indicates the area subjected to EDS analysis presented in Figure 6.21. The images in this figure show crack migration from area next to Ti surface into the composite, evidenced by fracture of fibers and fiber imprints. In the area where adhesive failure was revealed by macroscopic inspection, resin pockets remained on the ablated pattern were observed.

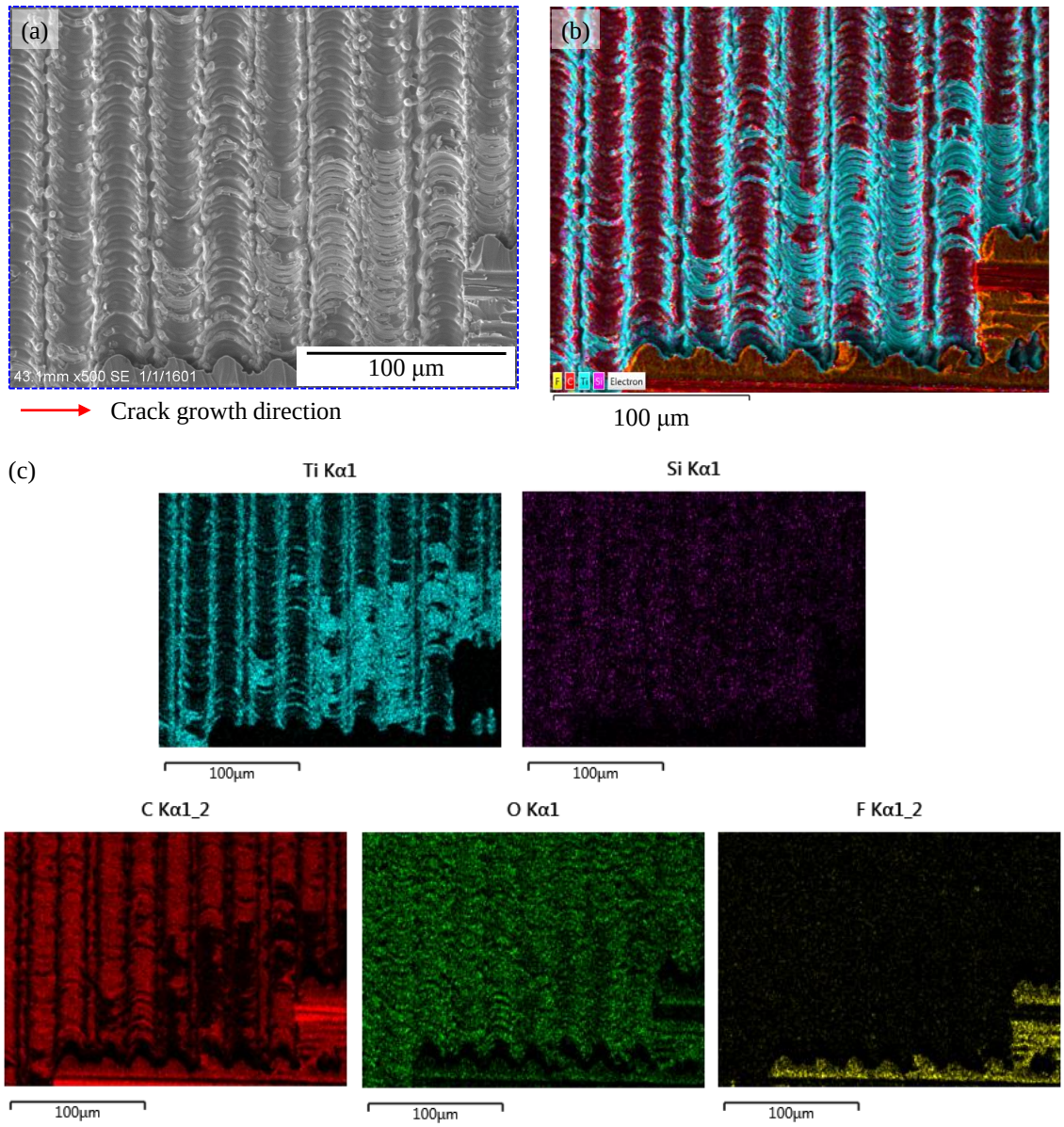

Figure 6.21: (a)Fracture surfaces of a DCB specimen from Ti_PEI_1-hour panel tested at 25 ^{o}C, a close-up view of region indicated by the blue box in Figure 6.20(b). (b) Layered EDS map. (c) Individual elemental map.

6.2.2.4 Nondestructive Evaluation using Ultrasonic Transducer

After each tests where opening displacement of 25 mm was applied and the crack were allowed to propagate, the specimens were unloaded and removed from the test frames. They were subsequently UT scanned and crack front profiles were analyzed. Figure 6.22 shows UT images reflecting the tested interface. UT images of interface tested at 25 ^{o}C, 150 ^{o}C, 250 ^{o}C revealed cohesive failure mode. In addition, at higher test temperature, the crack extension decreases. This is due to the influence of matrix softening as temperature increases, causing the composite to plastically deform more than causing the crack to propagate. Adhesive failure is observed on specimen tested at 315 ^{o}C. The crack propagrated to a further extension comparing to the crack propagation at lower temperatures.

Figures 6.23 and 6.24 shows UT analysis of a Ti_PEI_16-hour specimen before and after DCB test at 25 ^{o}C. The warped portion of the beam correlate to the delaminated portion. Images of the real specimen before and after the test are shown in Figure 6.25.

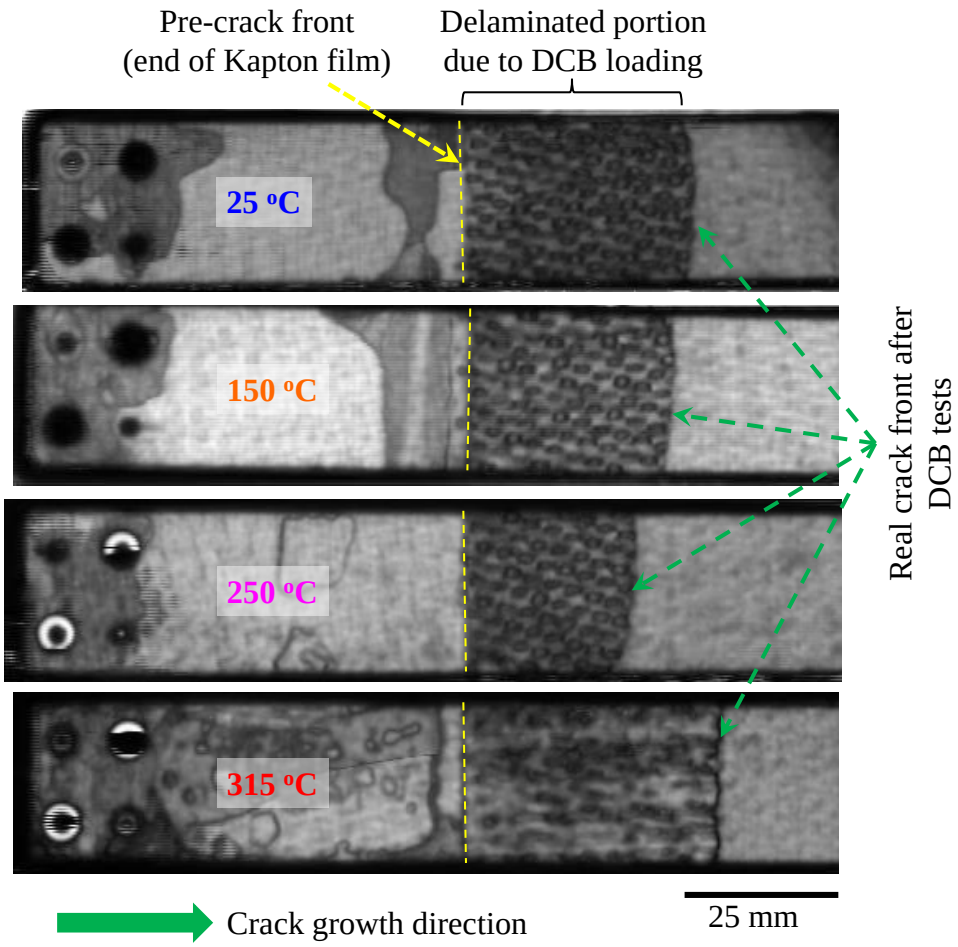

Figure 6.22: UT scan analysis of tested DCB specimens from panel Ti_PEI_16-hour. For specimens exhibiting cohesive mode of failure, i.e. specimens tested at 25 ^{o}C, 150 ^{o}C, 250 ^{o}C, and the same maximum displacement applied to the specimens (25.4 mm in this work), the delamination extension decreases as test temperature increases.

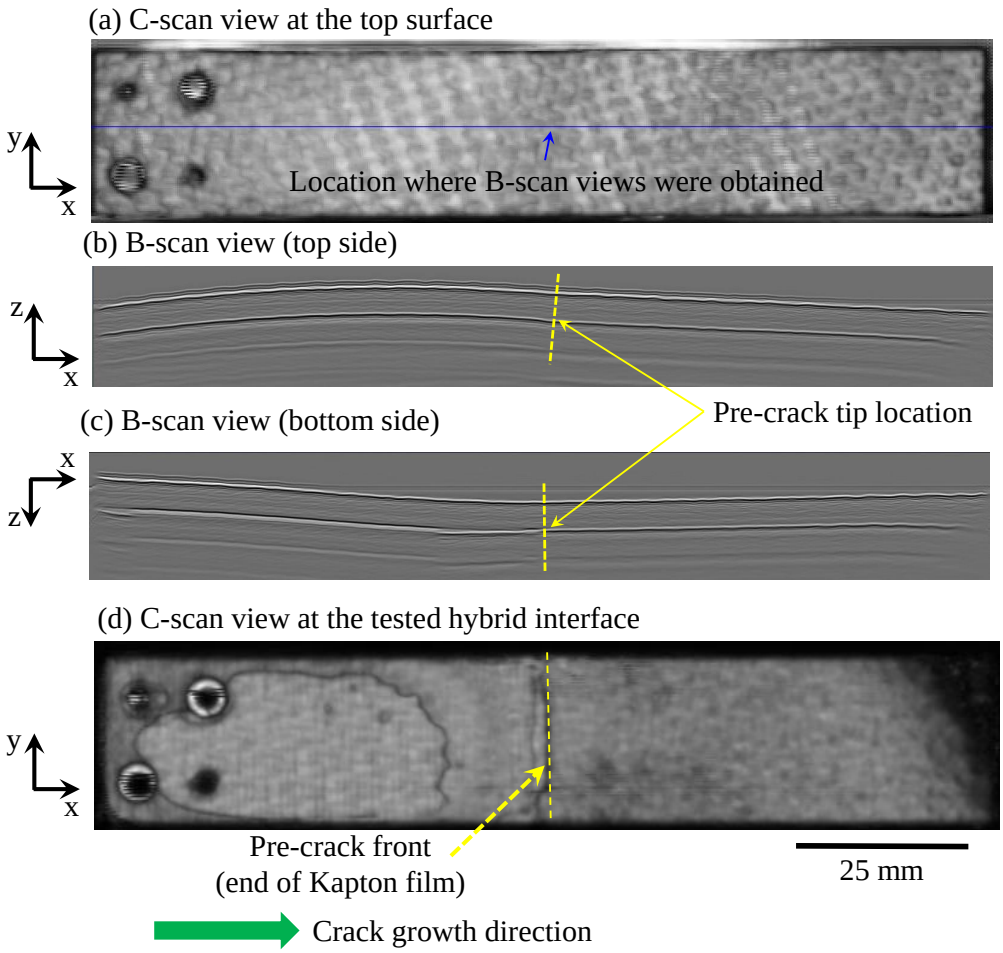

Figure 6.23: UT scan analysis of specimen 1 from panel Ti_PEI_16-hour before DCB test.

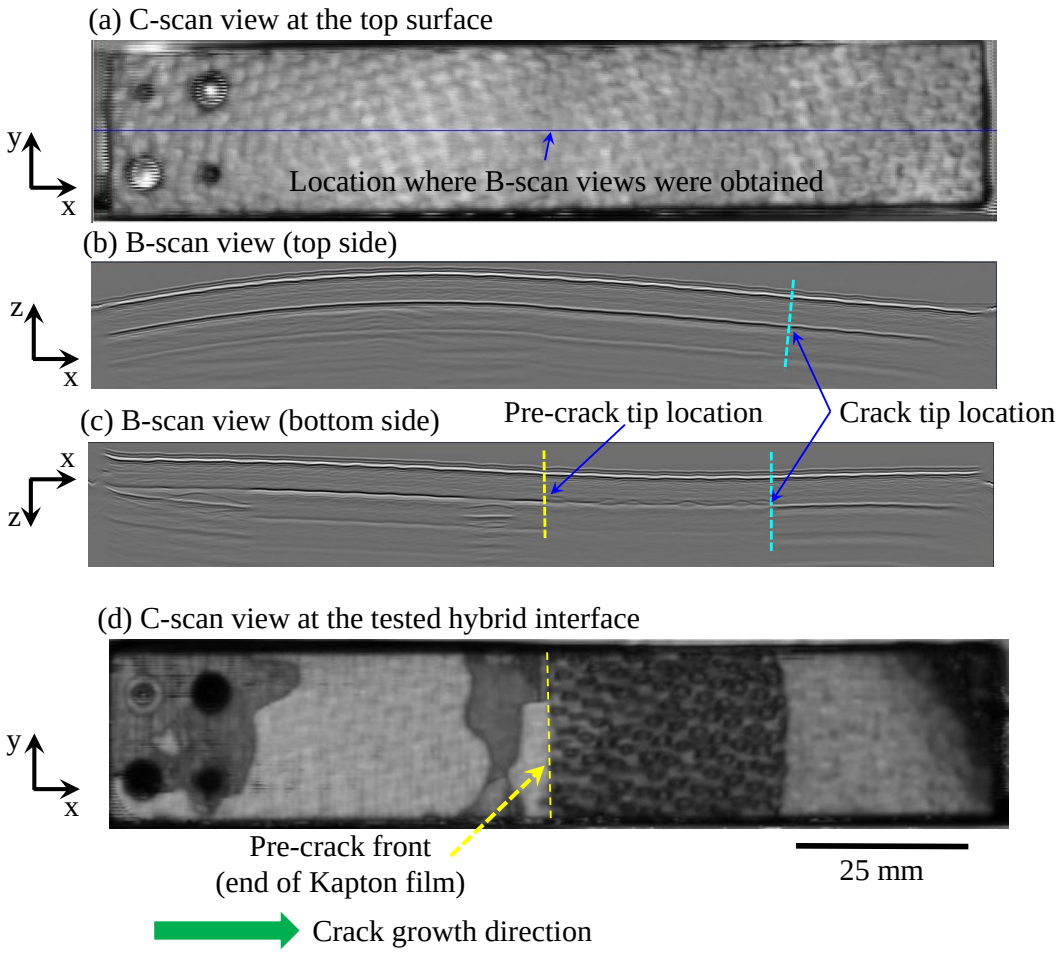

Figure 6.24: UT scan analysis of specimen 1 from panel Ti_PEI_16-hour after DCB test.

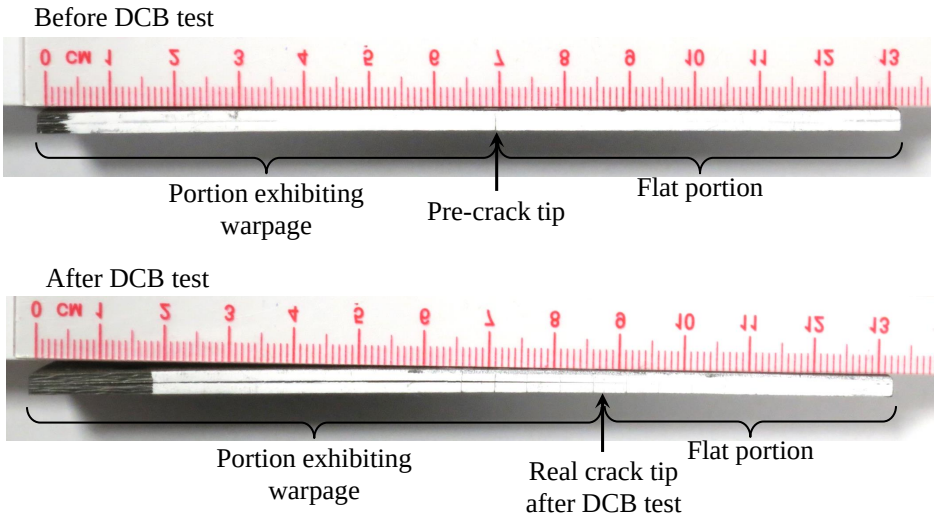

Figure 6.25: Partial warpage due to thermal cooling from curing temperature: observation on a real DCB specimen before and after being tested.

6.2.3 NiTi-PMC Hybrid Interface

The mode I fracture toughness behavior of the NiTi-polyimide matrix composite interface was investigated via the DCB tests. The temperatures selected for testing hybrid DCB specimens containing NiTi foil were 25 ^oC and 150 ^oC. It should be noted that the phase transformation temperatures M_s, M_f, A_s, and A_f of the NiTi foil presented in the fabricated hybrid panel are 4 ^oC, 19 ^oC, 47 ^oC, and 62 ^oC respectively, according to the DSC analysis shown in Figure B.3. During fabrication of the hybrid composite panel, the entire panel was cooled to RT from the curing temperature of 371 ^oC. In addition, no further thermal and mechanical processing was performed on the panel except for specimen cutting by a waterjet. Thus, the DSC curve in Figure B.3 suggested that at room temperature, the NiTi foil exhibited the austenitic phase. However, there could be stress-induced phase transformation occuring the NiTi during cooling due to thermal residual stresses developed in the panel as the panel was subjected to a thermal load ΔT of -346 ^oC. The effect of thermal residual stresses on SMA phase transformation and crack propagation behavior at the hybrid NiTi-PMC interface will be discussed in section 8.

For the tests performed at 25 ^oC, which is above M_s (19 ^oC) and below A_s (62 ^oC) of the NiTi foil, it is expected that the NiTi exhibited pseudoelastic behavior where the stress-induced phase transformation from austenite to detwinned martensite occurs during the tests. During the test at 150 ^oC, which is 88 ^oC above A_f, when the material was fully in austenitic phase and presumably would behave like a linear elastic monolithic metal where no transformation occured unless a high stress level is reached. Figure 6.26(a) shows the schematic of the stress-temperature phase diagram of a shape memory alloy, illustrating the loading paths A and B, which represent the loading paths associated with testing at 25 ^oC and 150 ^oC, respectively.

The stress-strain responses correlated to isothermal mechanical testing at 25 ^oC and 150 ^oC are illustrated in Figure 6.26(b) and (c) respectively.

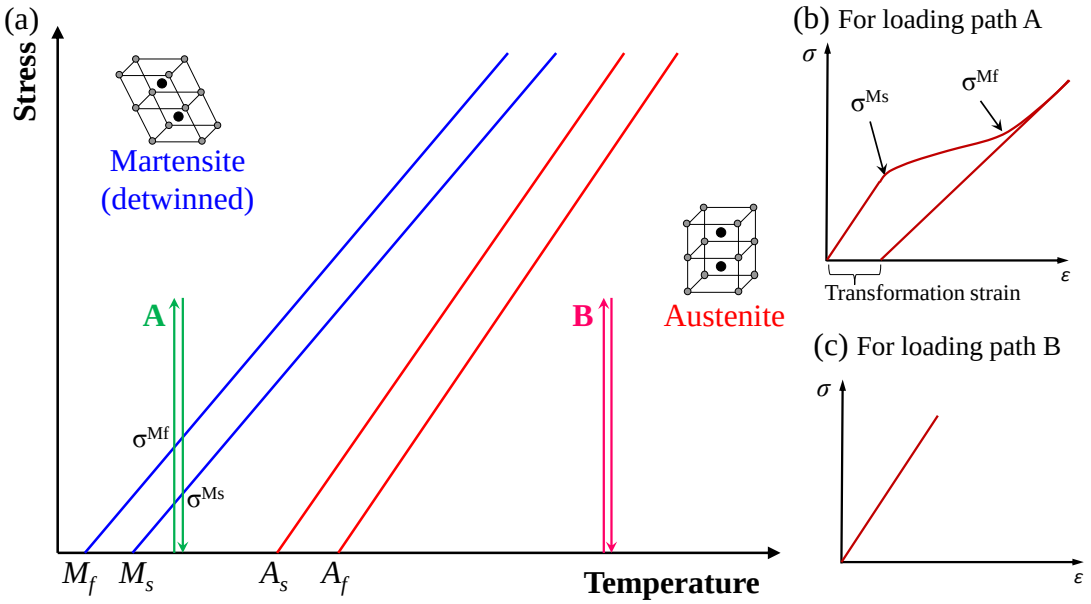

Figure 6.26: (a) Schematic of a stress-temperature phase diagram for a shape memory alloy. (b) Schematic of the stress-strain response from loading path A: isothermal loading at temperature above M_s and below A_s. (c) Schematic of the stress-strain response from loading path B: isothermal loading at temperature above A_f.

At each of the selected testing temperature, two DCB specimens were tested. However, during one of the tests carried out at 150 ^oC, after the specimen was allowed to stabilize at that temperature, one of the aluminum tabs debonded before any load or displacement was applied to the specimen. Thus, no DCB results was obtained from that specimen. During the second test at 150 ^oC, failed before testing or during the test. The results from the incomplete test at 150 ^oC is presented herein together with those obtained from the two DCB tests performed at room temper-

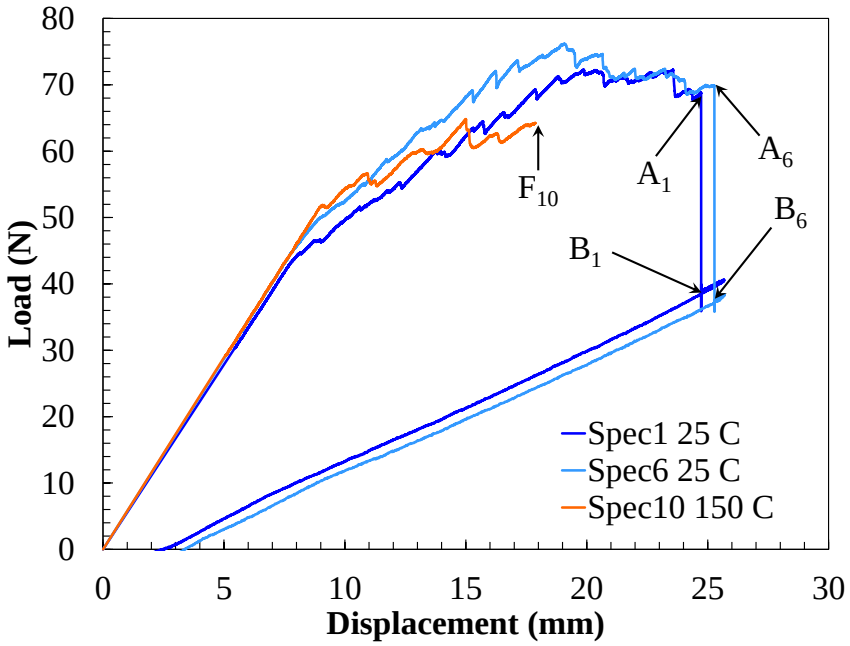

Figure 6.27: Load-displacement plot for DCB specimens from the NiTi_PEI_16-hour panel

ature. The load-displacement response for the tested NiTi_PEI_1-hour specimens is presented in Figure 6.27. It is observed from the two curves associated with the tests performed at 25 ^oC that the load-displacement response exhitbit four main portions: an initial linear response followed by a toughening portion, then a sudden and large load-drop when opening displacement reached 25 mm, and finally a linear unloading response. Different from the non-hybrid, Ti_PEI_1-hour, Ti_PEI_16-hour interfaces, the load-displacement response for NiTi_PEI_16-hour interface at 25 ^oC does not exhibit a softening portion. On the toughening portion, there is a slight decrease in load after a peak load was achieved. However this slightly decreasing trend in load is not significant enough to represent softening load-displacement response and steady-state crack growth. The fact that a large, sudden load-drop occured at an opening displacement of 25 mm followed by an unstable crack growth suggested

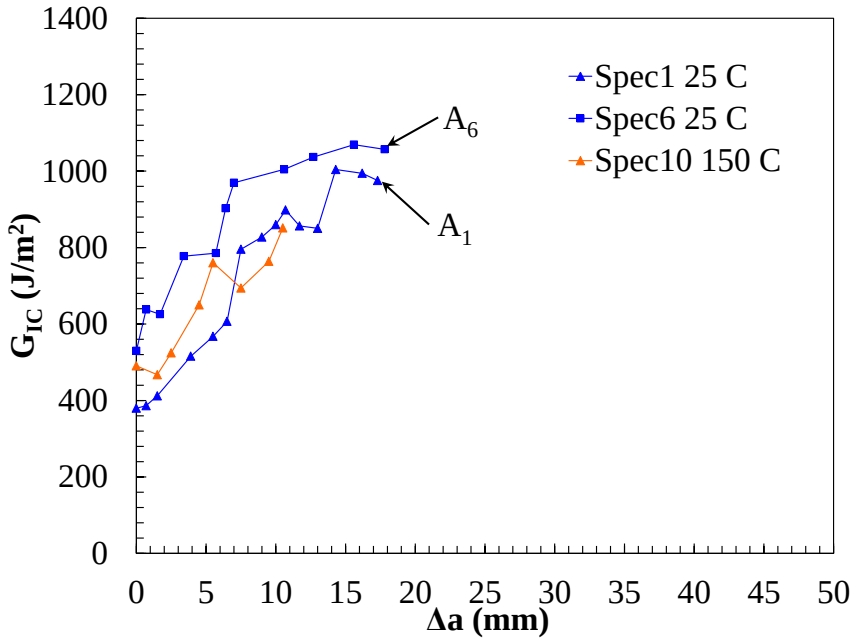

Figure 6.28: Mode I resistance curves for NiTi_PEI_16-hour DCB specimens tested at 25 ^oC and 150 ^oC. The G_{IC} values indicated by points A1 and A6 are associated with points A1 and A6 on the load-displacement response presented in Figure 6.27, i.e. the strain energy release rates associated with the unstable crack growth with crack extension of 10.8 ± 0.6 mm.

that steady-state crack growth stage was not achieved yet. Based on the discussion presented in the previous section, it could be articulated that the transition between the toughening and softening stages on the load-displacement response for this particular NiTi-PMC interface is delayed further compared to that of the non-hybrid and hybrid Ti-PMC interfaces.

The crack extensions associated with the large drop in load from point A1 to B1 and from point A6 to B6 illustrated in Figure 6.27 are 10.2 mm and 11.4 mm, respectively. This significant load-drop associated with the unstable crack growth are due to fracture instability occuring when certain load and displacement levels are reached simutaneously [100, 101]. It should be noted that the in-plane dimensions

of each 8-harness satin weave unit cell are approximately 8 mm x 8 mm. The fact that the crack arrested after an extension of 10.8 ± 0.6 mm due to the large drop in load at 25 mm opening displacement could be ascribed to influence of the woven fabric architecture.

The mode I resistance curves for the NiTi_PEI_16-hour specimens are presented in Figure6.28. The low initial G values together with the relatively smooth initial toughening load-displacement response suggested that the crack initiated near the NiTi face. The R curves show toughening behavior as the G_I values monotonically increased with a small increase in crack extension. No plateau was observed on these R curves, indicating that the crack propagation did not reach steady state at this hybrid interface. This increase in G values is also an indication of crack migration into the composite side. It is observed that before the sudden load-drop occur, the crack only propagated with an extension of 18 mm at the NiTi_PEI_16-hour interface. This is only 60 % the crack extension at the Ti_PEI_16-hour (30 mm) at the same applied displacement level. Note that for both interfaces, the maximum applied opening displacement during the DCB tests was 25.4 mm. This resistance to crack propagation, i.e. shorter crack extension, could be explained by the crack shielding effect caused by stress-induced phase transformation occuring in the NiTi due to high stress concentration at the crack tip. It has been studied and proved numerically that SMA phase transformation occuring behind the crack tip, i.e. in the delaminated portion of the beam, could cause the crack to shield [102]. The results from finite element analysis presented in section 8 demonstrate the region in the NiTi foil that transformed during the DCB test.

The reason for the toughening portion on the load-displacement to span over a long range of opening displacement, i.e. from the deviation from linearity at displacement of 10-11 mm to the sudden load drop at 25 mm displacement, could

be attributed to crack shielding effect caused by stress-induced phase transformation exhibited in the SMA constituent. The crack has not propagated into the composite far enough to reach steady-state growth, which results in softening portion on the load-displacement response. It is hypothesized that if the opening displacement continued to apply on the specimen at the same constant rate, the crack could reach stead-state growth and softening load-displacemnet response could be observed. However, due to the limitation of the testing equipment that only allowed a maximum displacement of 25.4 mm, the test was not carried out further.

The UT scan analysis before and after the DCB test at 25 ^oC is presented in Figures 6.29 and 6.30. Different from the hybrid Ti-PMC specimens, the B-scan images from UT scans for both the top and bottom sides shown in Figure 6.29 display relatively flat top and bottom surfaces. This suggests that the specimen exhibited minimal thermal warpage before the test. However, the residual opening displacement observed visually on the tested specimen is captured by the UT scans on both sides, as presented in Figure 6.30(b) and (c). It should be noted that only the part of the specimen that was not bonded to the aluminum tabs was UT scanned after the DCB test. The UT image of the tested hybrid interface after the test as shown in Figure 6.30(d) reveals a relatively smooth fracture surface morphology in the region adjacent to the end of Kapton film followed by a rough fracture morphology. The smooth portion of span a distance of approximately 5 mm from the Kapton precrack film. This observation suggested that this interface exhibited adhesive failure mode at crack initiation. Then, the crack migrated into the composite and remained there till the end of the DCB test. It is also observed that the crack front remained relatively straight and fracture surfaces were relatively uniform after the test. This implies the fact that after the crack migrated into the composite, it did not deflect more into the composite to the next ply but stayed in the first fabric layer that was adjacent

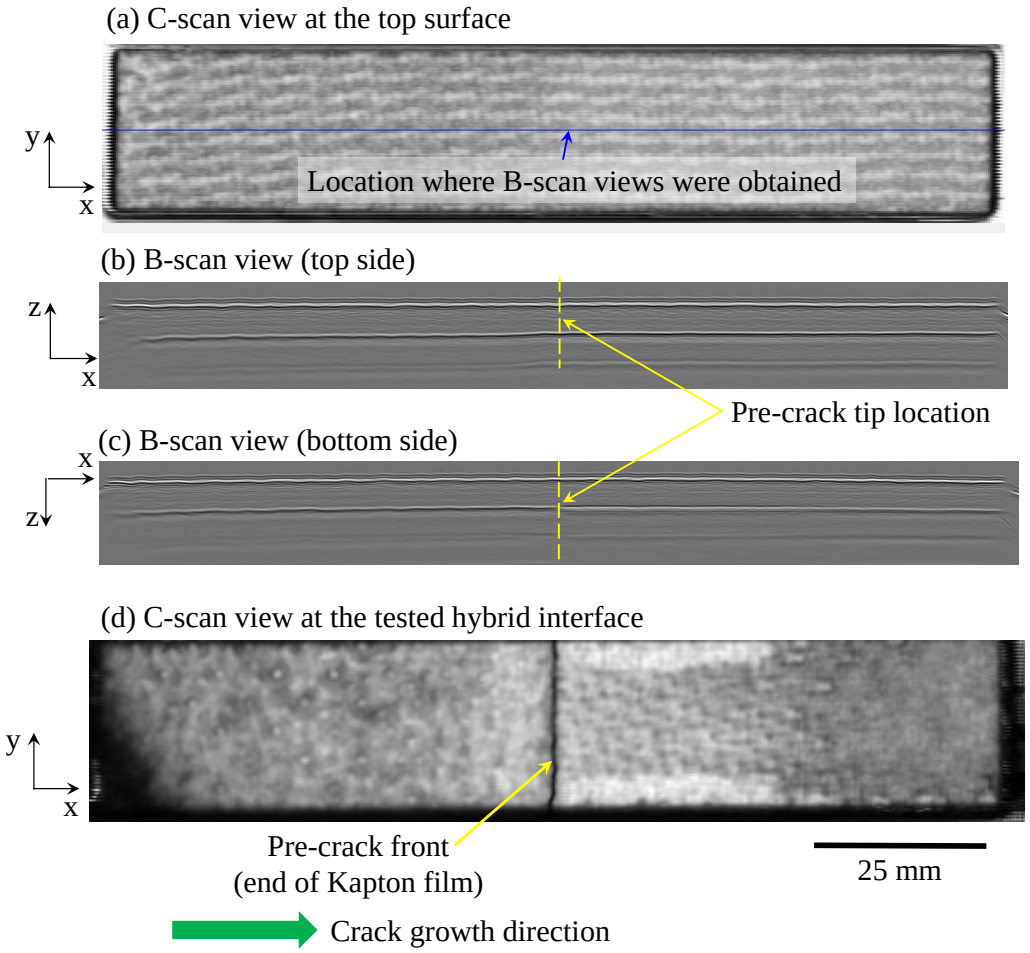

Figure 6.29: UT scan analysis of specimen 1 from panel NiTi_PEI_16-hour before DCB test.

to the NiTi foil. The UT scan results suggest a dominant cohesive failure mode and further support the postulations based on the analysis of load-displacement and R-curve response of the hybrid NiTi-interface.

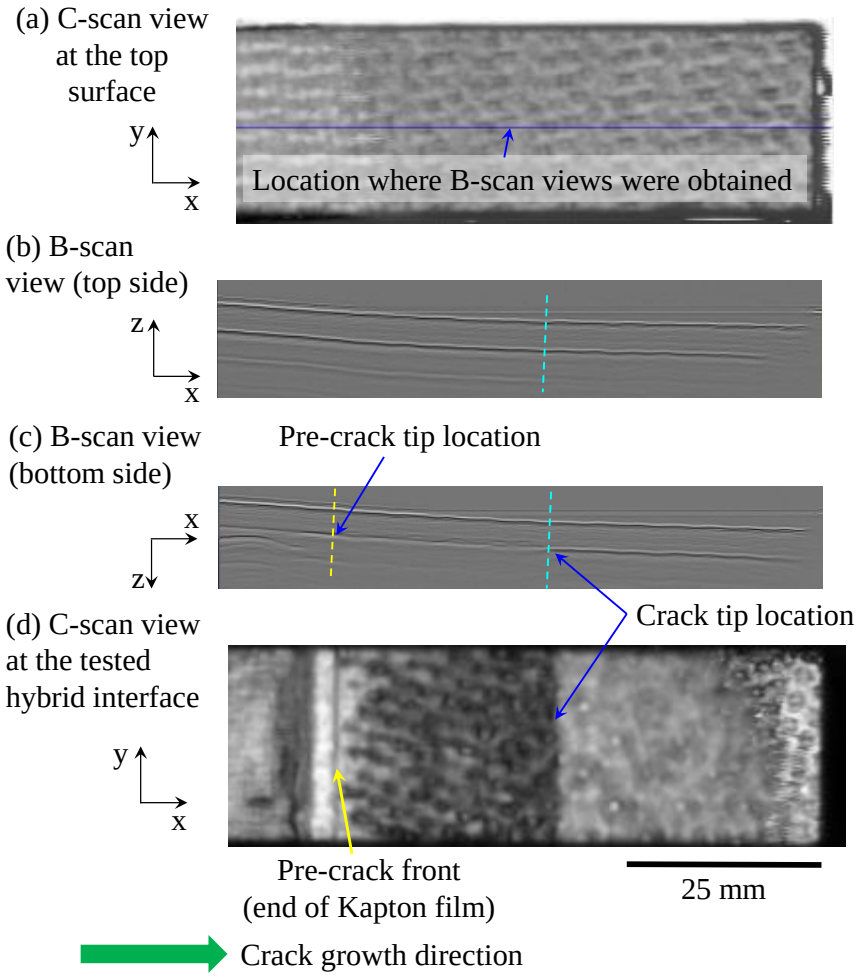

Figure 6.30: UT scan analysis of specimen 1 from panel NiTi_PEI_16-hour after DCB test at 25 ^oC.

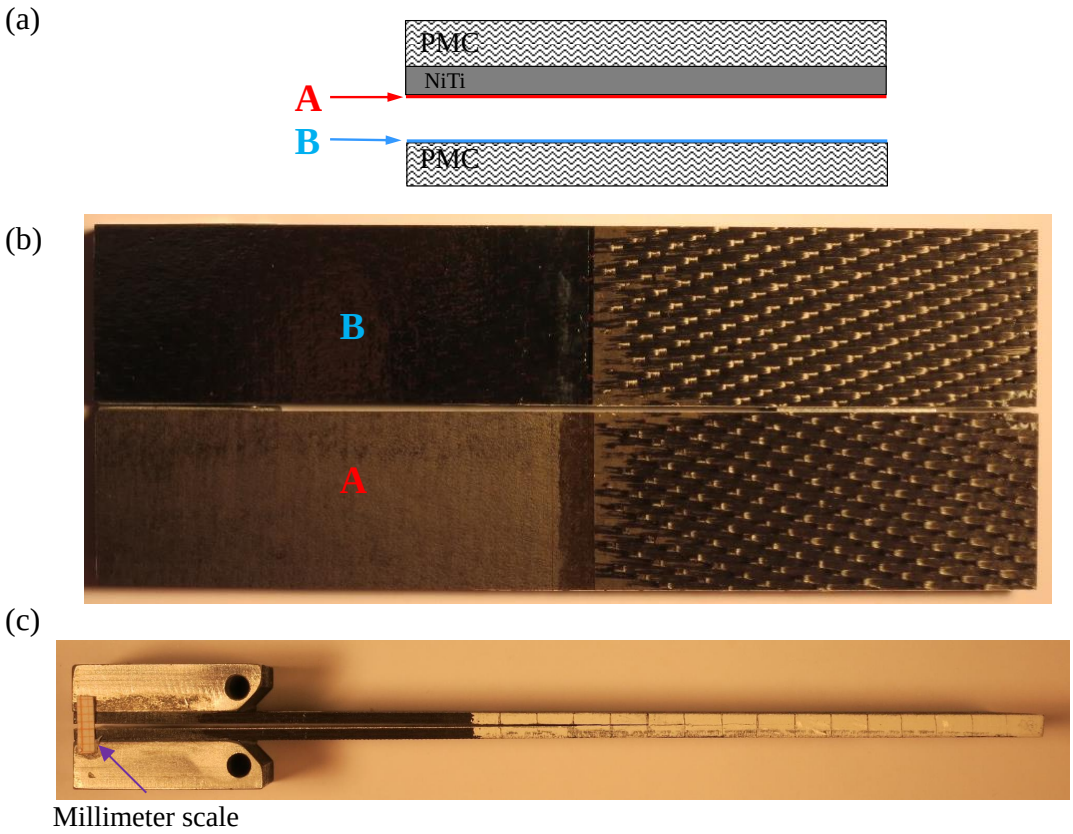

Figure 6.31: (a) Schematic of a tested specimen for fracture surfaces observation. (b) Fracture surfaces of a NiTi_PEI_16-hour specimen tested at 25 ^oC revealing a dominant cohesive failure mode. (c) Side-view of a specimen showing residual opening displacement of approximately 1 mm after the DCB test at 25 ^oC. This is an indication of phase transformation occured in the NiTi foil during the DCB test.

The fracture surfaces of a NiTi_PEI_16-hour specimen tested at 25 ^{o}C as shown in Figure 6.31 revealed a dominant cohesive failure mode. It is clearly seen in Figure 6.31(b) that the region adjacent to the Kapton film (spans a crack extension of approximately 5 mm) in the delaminated side exhibited adhesive failure mode. Thus, it is confirmed that the crack at the NiTi_PEI_16-hour hybrid interface initiated adjacent to the NiTi foil, then gradually migrated to the composite side and continued

propagating at the new interface. The fracture surfaces shown in this figure proved the postulations discussed earlier from examination of the load-displacement and resistance curves as well as observations from UT scan analysis. Figure 6.31(c) shows the side-view of a DCB specimen tested at 25 ^oC, revealing a residual opening displacement of approximately 1 mm after the test. This is an evidence of phase transformation occured in the NiTi foil during the DCB test, further supporting the crack shielding effect hypothesis as discussed earlier.

6.2.4 Strain Energy Release Rates due to Thermal Warpage

The contribution of thermal loading on the strain energy release rate is investigated in this section. It was observed from UT analysis that only the delaminated portion of the DCB exhibits curvature or warpage, both before and after the test. Only the delaminated portion of the beam is subjected to curvature due to the asymmetric layup. Adopting the approach presented in [103, 104], a formula was derived to calculate the contribution of thermal warpage to the strain energy release rates using the strain energy method.

The strain energy stored in a beam due to an axial load N and bending moment M is $\int \frac{N^2}{2EA}dx$ and $\int \frac{M^2}{2EI}dx$, respectively.
The strain energy stored due to thermal warpage (U_{tw}) in the warped DCB portion illustrated in Figure 6.33 can be calculated as.

$$U_{tw} = \frac{N^2 a}{2Bt_1E_1} + \frac{N^2 a}{2Bt_2E_2} + \frac{M_1^2 a}{2E_1I_1} + \frac{M_2^2 a}{2E_2I_2} \tag{6.4}$$

where B is the width of the specimen, a is the crack length, and E_1, I_1, t_1, E_2, I_2, t_2 are respectively the elastic modulus, second moment of inertia, and thickness of the PMC and Ti layers.

Thus, by definition, the strain energy release rate due to thermal warpage is cal-

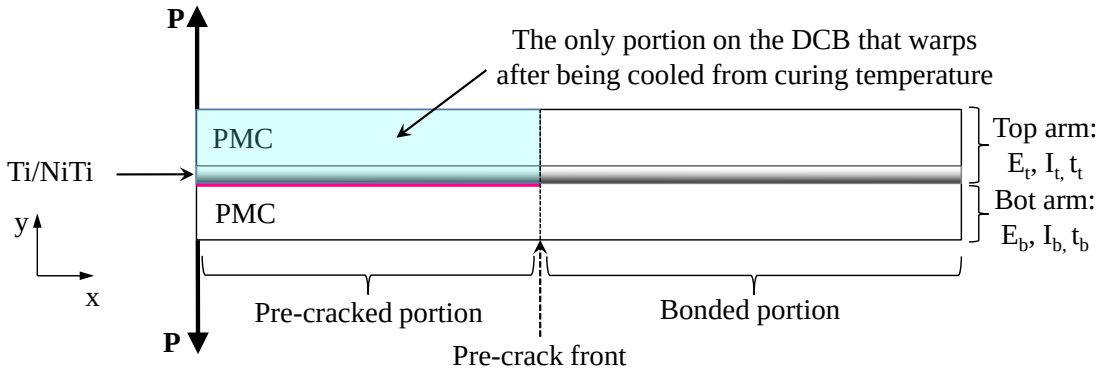

Figure 6.32: Schematic of a DCB subjected to mechanical loading and thermal cooling. The only portion on the DCB that warps due to thermal cooling from the curing temperature is highlighted.

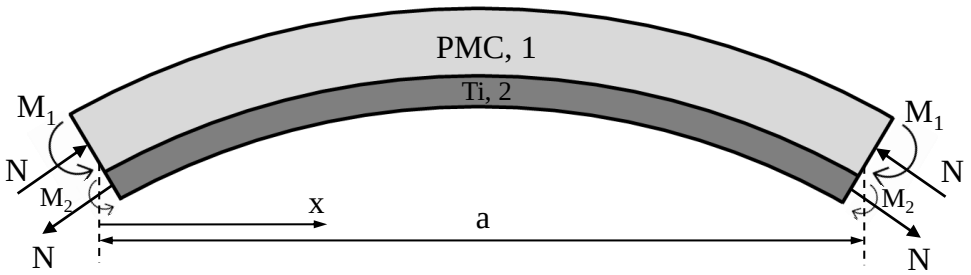

Figure 6.33: Schematic of the warped portion of the DCB subjected to a thermal load $\Delta T < 0$.

culated as follows.

$$G_{tw} = -\frac{1}{B}\frac{\partial U_{tw}}{\partial a} = -\left(\frac{N^2}{2Bt_1E_1} + \frac{N^2}{2Bt_2E_2} + \frac{M_1^2}{2E_1I_1} + \frac{M_2^2}{2E_2I_2}\right) \tag{6.5}$$

where:

$M_1 = \dfrac{E_1I_1}{\rho}$, $M_2 = \dfrac{E_2I_2}{\rho}$ and $N = \dfrac{2}{\rho}\left(\dfrac{E_1I_1 + E_2I_1}{t_1 + t_2}\right)$ according to Timoshenko's

derivation for bimaterial thermostat strips.

It can be seen from Equation 6.5 that the strain energy release rate due to thermal warpage G_{tw} is independent of the crack length.

The radius of curvature for the asymmetric Ti-PMC beam at room temperature was determined experimentally by measuring L and δ (add sketch), ρ was calculated as. Measurements for ρ determination was performed on the top arms of several fully delaminated hybrid DCB specimens. It was found that the G_{tw} is a constant which only depends on the elastic and independent of crack length.

The radius of curvature can also be calculated using classical laminated plate theory. This method allowed for ρ calculation at any test temperature given the known thermal-mechanical properties (elastic moduli and thermal expansion coefficient) and curing temperature. It was assumed that the arms are linear elastic in all cases (even at 315 ^oC). The effect of thermal curing stresses since the NiTi undergoes phase transformation upon cooling and stressed induced transformation, the calculation is more involved. The effect of curing and thermal stresses will be further addressed in FEA section.

6.2.5 Discussion

Figure 6.34(a) shows comparison of R curves for DCB specimens from the non-hybrid and Ti_PEI_16-hour panels that were tested at 25 ^oC and 150 ^oC. Initiation fracture toughness at both 25 ^oC and 150 ^oC for the non-hybrid interface is lower than that of the Ti_PEI_16-hour interface. Toughening and steady-state toughness for these interfaces are comparable, indicating strong adhesion between the Ti and PMC at the Ti_PEI_16-hour interface. Non-hybrid interface toughness reached steady-state (R curves plateau) at around 5-7 mm crack extension while the Ti_PEI_16-hour interface R curves show toughening behavior up to crack extension at around 12 to

Table 6.2: Summary of strain energy release rates due to thermal loading. Radius of curvature was calculated using CLPT.

Temperature	**Radius of Curvature (m)**	$\mathbf{G}_{tw}$ (J/m^2)
25 ^oC	1.213	199.38
25 ^oC *(curvature experimentally measured)*	1.350	160.93
150 ^oC	1.899	81.36
250 ^oC	3.467	24.41
315 ^oC	7.496	5.22

15 mm. In the case of non-hybrid, once the crack initiated/propagated from the end of the Kapton film, it resided in the PMC, initial toughening is due to bridging effects in fiber, tow and ply or any combination of these bridging mechanisms. Thus, the non-hybrid reached plateau or steady state faster than the hybrid interface. In the hybrid, since the crack initiated at an interface where only one fabric layer presented on one side, once the crack propagated from the initiation site, it needs to reach a longer extension before it can find a stable path in the PMC side.

Figure 6.34(b) shows comparison of R curves for DCB specimens from the Ti_PEI_16-hour and NiTi_PEI_16-hour panels that were tested at 25 ^oC and 150 ^oC. The fracture toughness values of NiTi_PEI_16-hour interface are lower than that of the Ti_PEI_16-hour interface at both 25 ^oC and 150 ^oC. In contrast, the crack extension at the NiTi_PEI_16-hour interface is less comparing the Ti_PEI_16-hour interface, given the same maximum applied opening displacement level. This is attributed to the crack shielding effect caused by phase transformation of NiTi occuring in the vicinity of the crack tip at the NiTi_PEI_16-hour interface.

Figure 6.35 shows comparison of average initiation and propagation mode I fracture toughness values obtained at various temperature for all non-hybrid and hybrid T650-8HS/AFR-PE-4 panels tested in this work. In all interfaces tested and for both initiation and propagation, the fracture toughess at 150 ^oC is lower than that obtained at 25 ^oC. This is attributed to the β transition occuring at temperature near 150 ^oC. Beyond 150 ^oC, in the non-hybrid and hybrid interface exhibiting cohesive failure, the fracture toughness increases with increasing temperature.

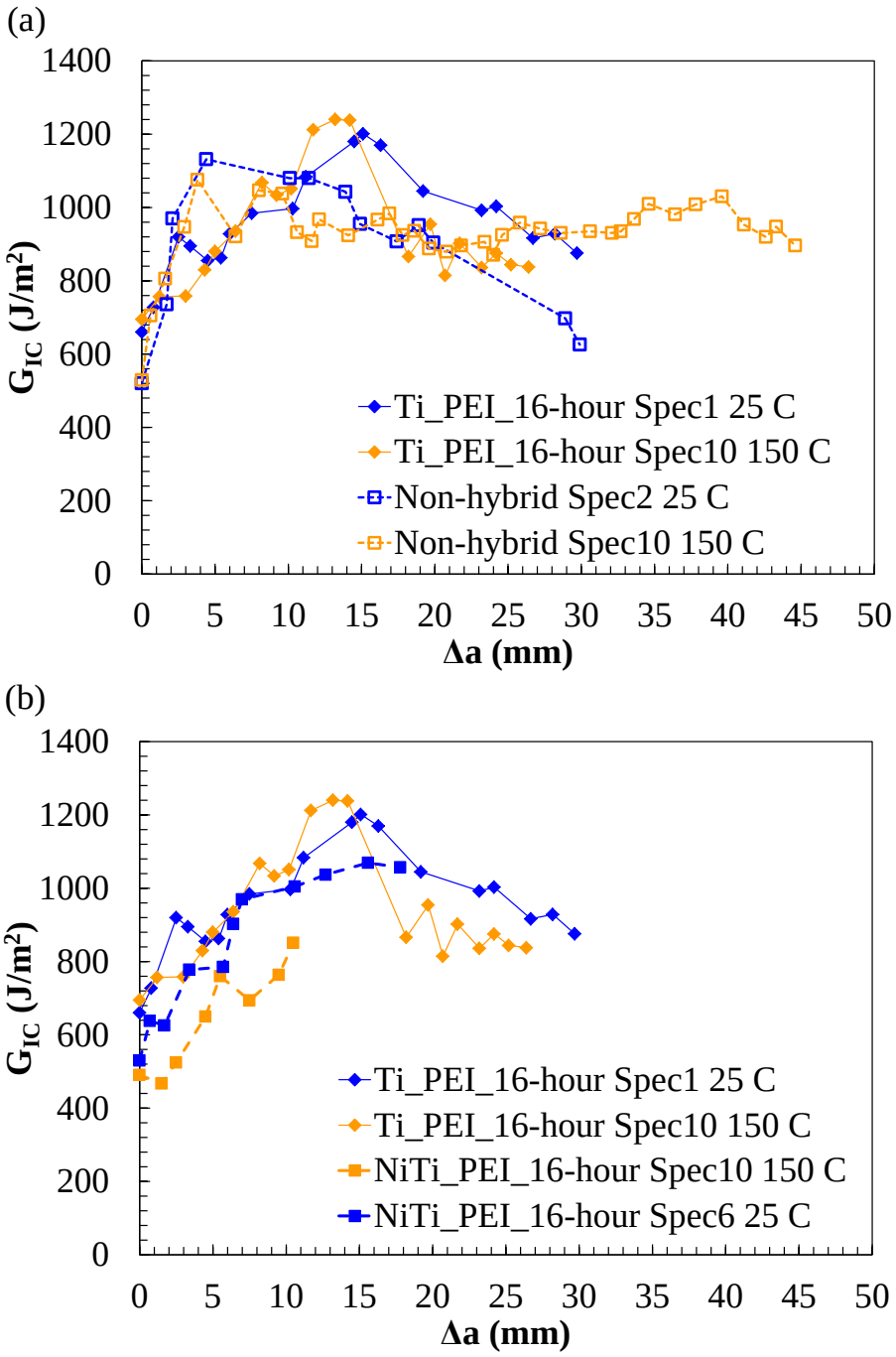

Figure 6.34: (a) Comparison of R curves for DCB specimens from the non-hybrid and Ti_PEI_16-hour panels that were tested at 25 ^oC and 150 ^oC. (b) Comparison of R curves for DCB specimens from the Ti_PEI_16-hour and NiTi_PEI_16-hour panels that were tested at 25 ^oC and 150 ^oC.

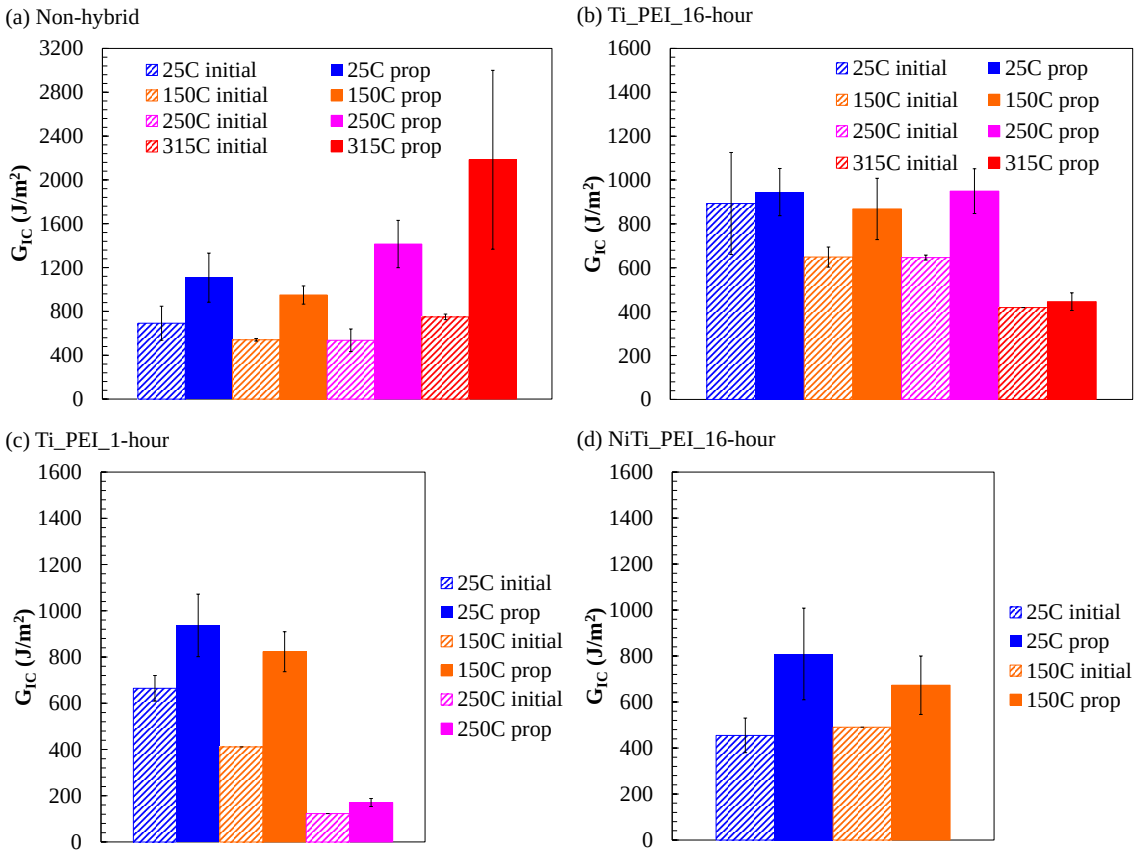

Figure 6.35: Comparison of average initiation and propagation mode I fracture toughness values obtained at various temperature for (a) non-hybrid T650-8HS/AFR-PE-4 interface. (b) Ti_PEI_16-hour interface. (c) Ti_PEI_1-hour interface. (d) NiTi_PEI_16-hour interface.

6.3 Summary

In this section, our approach to high temperature DCB testing were presented. In section 5 it was presented that we successfully created the high temperature hybrid laminate. This section proved that the hybrid laminates fabricated in this work could sustain temperature up to 250 ^oC. The time of hydrolysis during synthesis of the PEI sol-gel solution has a strong influence on the interfacial adhesion between the surface-treated Ti and the polyimide resin. The longer hydrolysis time allowed more hydroxyl (-OH) groups to form and be available for covalent bonding with the Ti substrate, leading to more covalent bonds formation at the hybrid interfaces. Consequently, the longer the sol-gel was hydrolyzed, the stronger the hybrid interface was and the higher temperature the interface could sustain. In this work it was shown that 16 hours provided stronger interfaces than 1-hour hydrolysis. However, future investigation is needed to optimize this processing parameter.

Fracture toughness of hybrid interfaces where Ti surfaces were treated with EPII and AP sol-gel solution were also investigated. However, it was revealed that these interfaces were weak and the fracture surfaces showed adhesive failure. It was observed that the interfacial bond strength or the mode of failure, i.e. whether the hybrid interface failed in adhesive or cohesive mode, governs the fracture toughness more than the deformation of the matrix/composite constituent.

It was observed in this work that during mode I fracture toughness tests at temperature slightly above M_s, in this case 25 ^oC, of specimens containing NiTi foil, the NiTi foil underwent shape memory alloy phase transformation. This transformation causes a crack shielding effect where the crack extended a shorter distance as compared to the crack propagation at the interface between composite and another linear elastic monolithic metal foil or Ti foil in this work, given the same applied

opening displacement.

Furthermore, the fracture toughness of non-hybrid and hybrid interfaces containing AFR-PE-4 matrix composite is influenced by the β transition exhibited when the testing or operating temperature approaches T_β. It was discovered in this work that near T_β, the mode I fracture toughness is lower comparing to that obtained at a lower ($25\ ^oC$) or higher ($250\ ^oC$) temperature. However, more testing should be performed at various temperature below and above T_β in order to study the actual effect of β transition on fracture toughness of the material systems investigated herein.

7. HYBRID TI-POLYIMIDE MATRIX COMPOSITE INTERFACE: MODE II FRACTURE TOUGHNESS CHARACTERIZATION[1]

The investigation on mode I fracture toughness of non-hybrid and hybrid metal-polyimide matrix composite interfaces was presented in the previous section. This section reports our study on mode II fracture toughness testing of the non-hybrid and Ti_PEI_1-hour interfaces. UT scanning analysis was performed before and after each fracture toughness test to monitor the crack growth and crack front shape as well as determine any additional damage initiated at the interface or in the composite. Post-fracture testing investigations carried out include fractography using SEM/EDS and FTIR analysis. The characterization approach and results are presented herein.

7.1 Mode II Fracture Toughness Testing: The 4-point End Notch Flexure Test

The mode II fracture toughness of the non-hybrid and hybrid interfaces was accessed via the 4-point end notch flexure (4-ENF) tests adopting the approach presented by Carlsson *et al.* [105]. The four-point end notch flexure test is selected over the 3-point ENF test because of the stable crack growth nature due to the constant moment presented over the loading span where the crack tip resides. Thus, Mode II resistance curves can be obtained from the 4ENF tests.

7.1.1 Specimen Preparation

After fabrication of the hybrid Ti_PEI_1-hour panel as presented in section 5, 4-ENF specimens were water-jet cut. Each specimen has nominal dimensions of 3.2 mm x 25.4 mm x 158.5 mm. The specimens were cut such that the prior to testing, the nominal initial crack length was 55.9 mm as measured from the pre-crack edge

[1]The experimental work presented in this section was performed at NASA Langley Research Center, Hampton, VA in collaboration with Drs. John Connell and Frank Palmieri.

to the crack tip. The longitudinal edges of each specimen were painted white using WiteOut liquid. The specimens were UT scanned before the 4-ENF tests. Initial crack length was measured and the location of the crack tip was marked on the white-painted edges. To facilitate viual crack length measurement during the tests, millimeter scales was either adhesively bonded to the specimen edges using double-sided tape or directly marked on using a sharp razor blade. The second approach was adopted for high temperature testing where the tape adhesive fails.

7.1.2 Test Setup and Procedure

The 4-ENF test setup for high temperature testing is shown in Figure 7.1. Similar to the setup for high temperature DCB tests, an environmental chamber was used to control the test temperature. The tests were performed using an MTS 858 table-top system with a 13.3 kN load cell and an MTS 458.20 MicroConsole analog controller. A ± 0.5 inches (± 12.7 mm) displacement cartridge and ± 300 lbf (± 1334 N) cartridge were used for the AC controller and DC controller, respectively. Besides the built-in thermocouples that were used to control the thermal chamber, an additional thermocouple was employed to monitor the temperature near the specimen before and during the tests. The fixture was placed in the MTS test frame with the loading span located on the top side. The loading and support spans were 50.8 mm and 101.6 mm, respectively.

It is worth noting that even though the hybrid specimens were symmetric with respect to the metal foil, it is asymmetric with respect to the crack plane since the pre-crack was placed on one side of the foil. The neutral axis of the hybrid beam lies in the mid-plane of the metal layer. Thus, under bending, the crack plane could locate in either the compression or tension side of the hybrid beam. To investigate the effect of loading configuration on the mode II fracture behavior of the hybrid interface, the

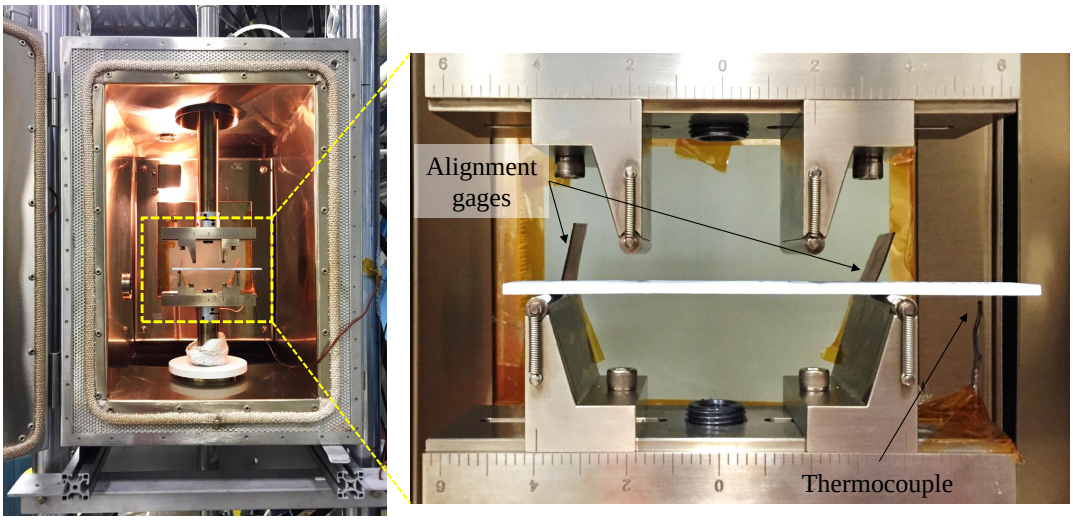

Figure 7.1: Four-point end notch flexure test setup for high temperature testing

specimens were position on the test fixture in two different orientations, where the pre-crack film located on either the top (compression) side or the bottom (tension) side reference to the metal foil. Schematics of the 4-ENF test configurations are shown in Figure 7.2. The overhanging length on the pre-crack side was 19.1 mm as measured from the edge of the pre-crack side to the nearest support pin (on the left). As a result, the crack tip located 11.4 mm inside the left loading pin. Table 7.1 presents the test matrix for the characterization of mode II fracture toughness non-hybrid and hybrid Ti_PEI_1-hour interfaces performed in this section.

Multiple 4-ENF tests were performed on each specimen where the specimen was loaded until a crack extension of approximately 2 to 3 mm was observed, then it was fully unloaded. Once the specimen was unloaded, it was removed from the test fixture and UT scanned. After the scanning step completed, the specimen was loaded

Table 7.1: Test matrix for mode II fracture toughness characterization of non-hybrid and hybrid Ti−T650-8HS/AFR-PE-4 interfaces. Except for the first column, the numbers in each column show the number of specimens tested at various configurations where the initial crack located at either the mid-plane or on compression or tension side of the 4-ENF beam. All tests were performed at 25 ^oC.

Panel name	**Mid-plane**	**Tension side**	**Compression side**
Non-hybrid	1	N/A	N/A
Ti_PEI_1-hour	N/A	2	2

into the fixture and tested again. Alignment gages were mounted on the test fixture to ensure consistency among the tests. Each specimen was tested until the crack tip reached within 10 mm inside the right loading pin. During each 4-ENF test, displacement-control loading was applied to the top pins at a loading and unloading rate of 0.508 mm/min and 2.54 mm, respectively.

As described in section 6, UT scan experiment was performed using a table-top system with a 10 MHz transducer. Each specimen was scanned both on the top and bottom sides since the UT signal could not penetrate through the metal layer. UT analysis was used to measure the crack length after each test. Note that the crack length a used for fracture toughness determination is measured from the left support pin to the end of the crack tip.

7.1.3 Data Reduction

Since there is no ASTM Standard for 4-ENF test, the data reduction scheme presented below was adopted from Carlsson *et al.* [105]. Based on fracture mechanics and beam theory, strain energy release rate is

$$G = \frac{P^2}{2b}\frac{dC}{da} \tag{7.1}$$

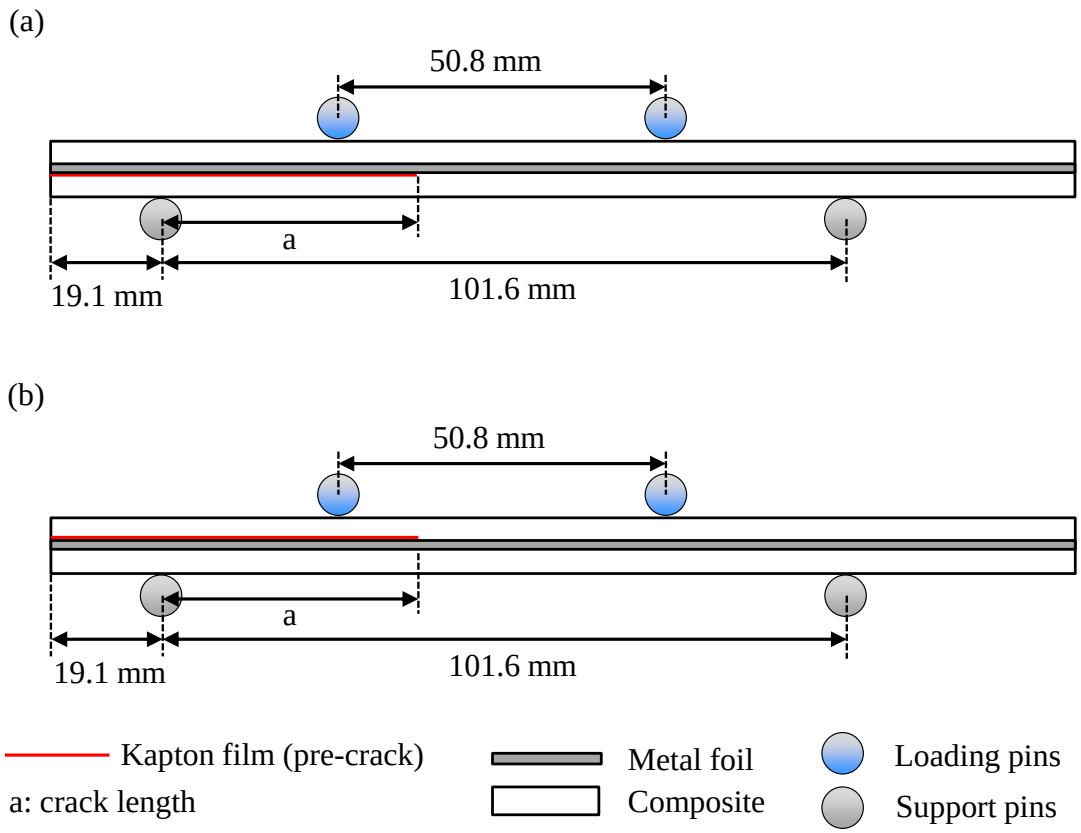

Figure 7.2: Schematic of 4-ENF test with (a) Crack growth on tension side (Kapton film is on the bottom of Ti foil). (b) Crack growth on compression side (Kapton film is on the bottom of Ti foil).

where:

P is the load recorded by the MTS load frame,

b is the width of the specimen,

C is the compliance of the beam, and

a is the crack length (measured from the left support point to the crack tip).

For a 4-ENF beam, the compliance is a linear function of the crack length [105].

The expression for compliance of a 4-ENF beam is as follows.

$$C(a) = C_1 a + C_o \tag{7.2}$$

where compliance $C = \dfrac{\delta}{P}$ is calculated as the inverse of the linear slope of the experimentally measured load-displacement curve.

Thus, mode II strain energy release rates measured from 4-ENF configuration can be calculated as

$$G_{II} = \frac{P^2 C_1}{2b} \tag{7.3}$$

At fracture, $P = P_c$ and $G_{II} = G_{IIC} = \dfrac{P_c^2 C_1}{2b}$. In this work, the value of critical load P_c used for fracture toughness specimen was the maximum load measured from each test.

7.2 Results and Discussion

In this section, the mode II fracture toughness results from four Ti_PEI_1-hour specimens tested at 25 ^oC are presented. Three 4-ENF specimens from this panel was tested at 315 ^oC. However, because multiple delaminations occured at both Ti-PMC interfaces due to degradation of the interfacial adhesion at this temperature, only UT analysis results are shown for these specimens.

Typical load-displacement curves from all the tests performed on Ti_PEI_1-hour specimens tested at 25 ^oC are presented in Figure 7.3. During the first test, i.e. Test 1, a sudden and sharp load drop was observed. This is attributed to unstable crack growth from the Kapton pre-crack. As expected, the 4-ENF test configuration caused the crack to grow in a stable manner in the subsequent tests as long as the crack tip located inside the inner loading span. This is evidenced by the smooth transition between the loading and unloading curves for tests 2 to 8 as shown in this

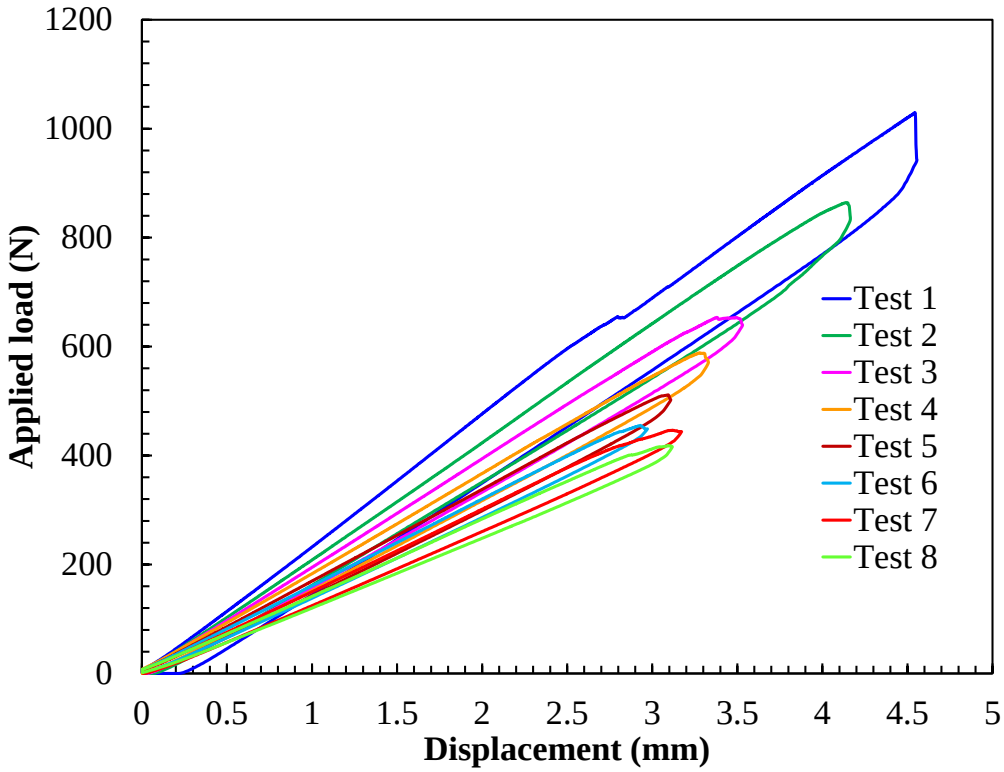

Figure 7.3: Typical load-displacement curves from Ti_PEI_1-hour tests at 25 ^oC with the crack located on the compression side. The results presented in this figure was obtained from the tests performed on specimen 11.

figure.

Figure 7.4 demonstrates the compliance calibration for the specimen whose load-displacement response was presented in Figure 7.3. The compliance C_1 used in Equation 7.3 to calculate the mode II fracture toughness values is determined as the linear slope of the compliance versus crack length a curve. Since unstable crack growth was observed from test 1, compliance calibration for this test was carried out separately, and demonstrated in Figure 7.4(a). In order to have a linear slope, at least two data points on the compliance vs. crack length a plot is required for this test. The two crack length values associated with Test 1 are the initial crack

(a) Compliance Calibration for Test 1

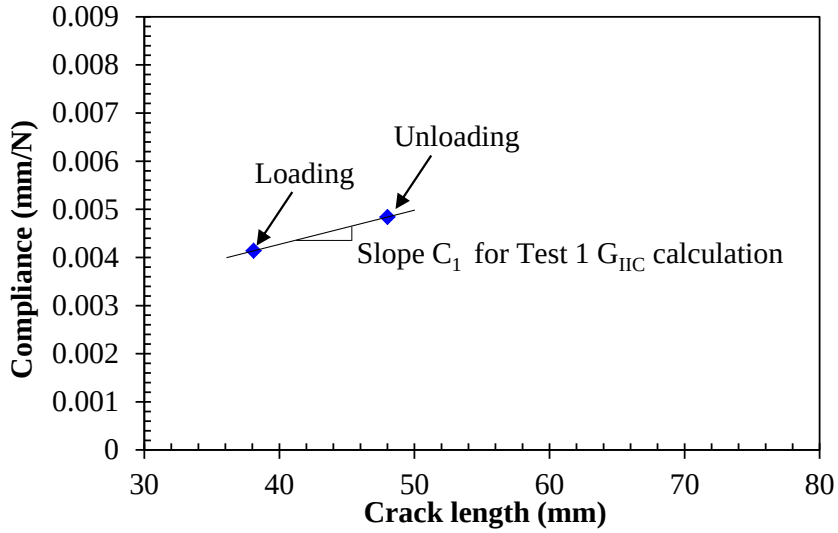

(b) Compliance Calibration for Test 2-9 (excluding Test 1)

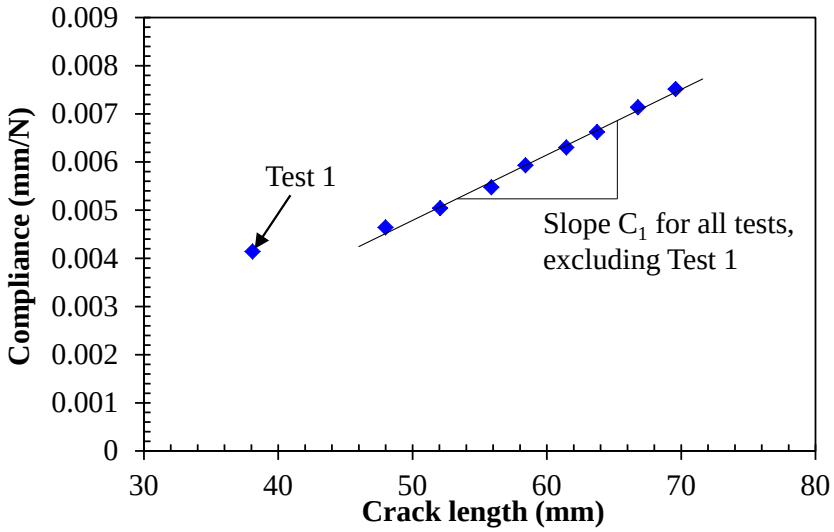

Figure 7.4: Compliance calibration of the specimen whose load-displacement curve were shown in Figure 7.3 for (a) Test 1, where the crack propagated unstably from the Kapton pre-crack film. (b) all subsequent tests (excluding Test 1).

length, i,e. before the test, and the crack length measured after the test. The two corresponding compliance C values used for the plot in Figure 7.4(a) are the inverses of the linear slopes of the loading and unloading curves. Compliance calibration

for all subsequent tests for this specimen is demonstrated in Figure 7.4(a). Linear relationship between the compliance and crack length is revealed in this figure. Each compliance C value used for the plot in Figure 7.4(b) is the inverse of the linear slope of the loading curve obtained from each test performed. The crack length a associated with each of these compliance C is the initial crack length the specimen exhibited in each test. For example, for test 2, the crack length a correllated to the compliance calculated from the linear slope of the loading curve of this test is the crack length presented in the specimen before the test was carried out, i.e. the crack length measured after the completion of test 1.

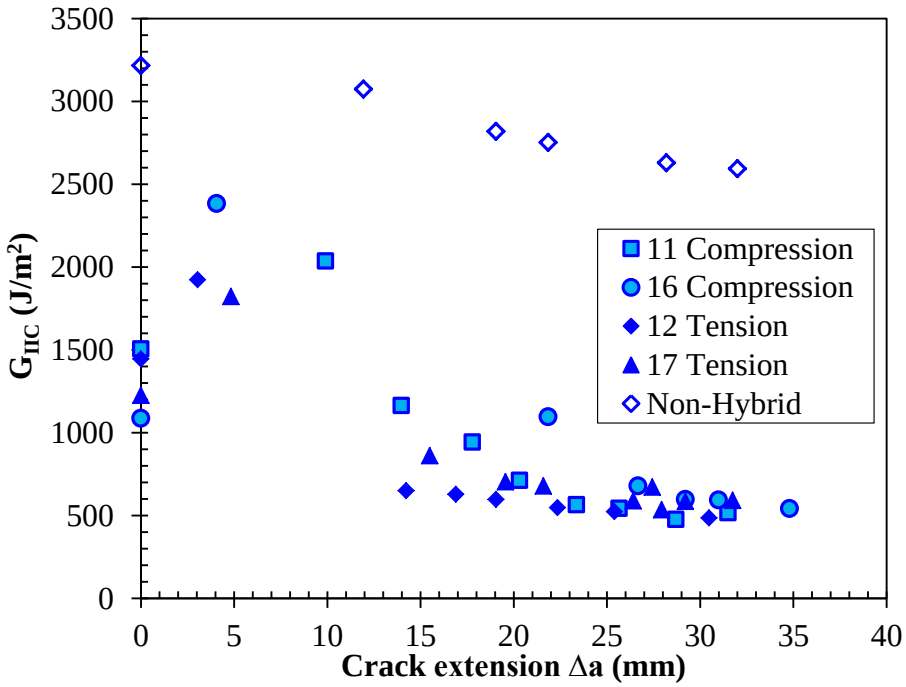

Figure 7.5: Mode II resistance curves for 25 ^oC Ti_PEI_1-hour specimens in comparison to one non-hybrid (16 layers T650-8HS/AFR-PE-4 without metal foil) specimen. Specimens 11 and 16 were tested when the crack was located on the compression side of the 4-ENF beam. The crack in specimens 12 and 17 located on the tension side of the 4-ENF beam during the tests.

Figure 7.5 shows the mode II resistance curves for four Ti_PEI_1-hour specimens and one non-hybrid (16 layers T650-8HS/AFR-PE-4 without metal foil) specimen. All of these specimens were tested at 25 ^oC. The mode II R curve for the non-hybrid exhibits the typical mode II resistance curve behavior of composite materials determined by 4-ENF tests [106, 107]. In contrast to the typical mode I R curve, on the mode II R curve for teh non-hybrid specimen shown in Figure 7.5, the initial fracture toughness was the highest value, then as the crack extension increased, the R curve exhibited a decreasing trend until a plateau or steady-state fracture toughness value was reached. Czabaj and Davidson reported a room temperature G_{IIC} of 2280.61 $\pm$ 108.28 J/m^2 for a similar material system that was composed of T650-8HS fabric and a phenylethynyl end-capped polyimide matrix [87]. This referenced value is relatively lower than that reported in Figure 7.5. It should be noted that the mode II fracture toughness reported by Czabaj and Davidson was determined via the three-point end notch flexure test (3-ENF) [87]. The influence of test configuration 3-ENF versus 4-ENF on the measurement of mode II fracture toughness was studied by Schuecker and Davidson [108]. They concluded that typically the values measured by the 4-ENF tests are 10 to 20 % higher than that measured by the 3-ENF tests. This is attributed to the more severe sliding friction between the crack surfaces experienced by the 4-ENF beam compared to the 3-ENF beam [108].

As shown in Figure 7.5, regardless of the test configuration, i.e. whether the crack plane is on the compression or tension side of the beam, the mode II resistance curves of the Ti_PEI_1-hour specimens exhibit a relatively low initiation fracture toughness followed by an unstable crack growth. The fracture toughness is higher at the new crack tip location then the R curve followed a decreasing trend and reached a plateau. The initial unstable crack growth and relatively low fracture toughness is attributed to the nature of crack propagation from pre-crack tip created by Kapton

film. It is observed that after crack initiation from the pre-crack tip, at the beginning stage of crack propagation, the fracture toughness measured from the tests where the crack located in the compression side was higher than that measured when the crack laid on the tension side. As the R curves reached their plateau, they converged to a fracture toughness value of 500 J/m^2. The convergence of these R curves occured when the crack propagated approximately 22 mm away from the pre-crack tip.

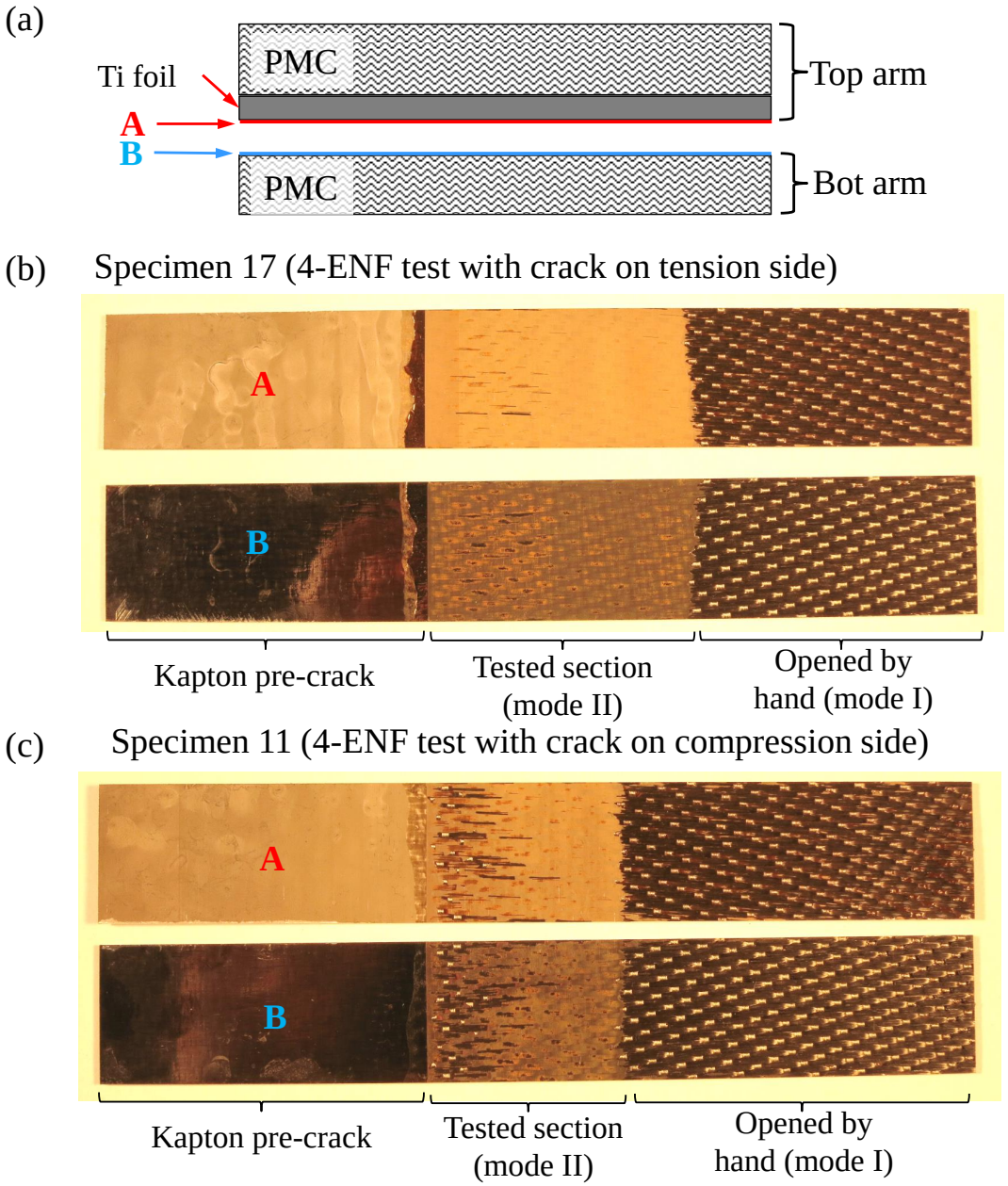

Figure 7.6: (a) Schematic of cross-section view of tested 4-ENF hybrid specimens and locations of the crack faces presented in Figure (b) and (c). (b) Macroscopic view of fracture surfaces from a Ti_PEI_1-hour specimen tested when crack propagation occured on the tension side of the beam. (c) Macroscopic view of fracture surfaces from a Ti_PEI_1-hour specimen tested when crack propagation occured on the compression side of the beam.

After the specimens were fully tested, i.e. when the crack tip reached within 5 to 10 mm inside of the right loading span, they were splitted by hand and cracked open completely and their fracture surfaces were revealed. Figure 7.6 shows the fracture surfaces of Ti_PEI_1-hour specimens tested when the crack propagated on the compression and tension side of the beam. It should be noted that the portions that exhibit cohesive failure mode as observed in this figure are associated to the untested portion of the beam after the 4-ENF tests were completed for each specimen. That is, those portions experienced mode I loading during the splitting-opening process and revealed cohesive failure mode. This is consistent with the observation of cohesive mode of failure for this interface under DCB loading condition as presented and discussed in section 6.

The fracture surface portions associated with 4-ENF fracture test exhibited dominantly adhesive failure. For the specimens exhibited crack growth on the compression side, at the location 5 mm away from the pre-crack tip, a region of cohesive failure is observed. This supports the observation of higher fracture toughness measured after crack initiation from the crack tip. Comparing the fracture surfaces of the compression versus the tension case, more imprints of the composite remained on the Ti surface of the compression case, compared to that of the tension case, are seen. This also explains why fracture toughness from the compression configuration is slightly higher than that obtained from the tension test configuration before the R curves reached steady-state. As the crack propagation reached steady-state, in both tension and compression configuration, the crack grew stably right adjacent to the Ti surface, resulted in macroscopically-viewed adhesive failure mode observed on the fracture surfaces.

Investigations were performed on the nature of microcrack formation in composite materials during mode-II fracture toughness tests. It was found that these microc-

racks orient approximately 45 degrees upward, i.e. toward the compression side of the beam [109]. Thus, in this study, when the crack laid on the tension side of the beam, the microcracks formed during the test tends to point toward the interface. In contrast, in the test configuration where the crack propagateed on the compression side, the crack tend to grow away from the hybrid Ti-PMC interface.

Figure 7.7 shows UT analysis images at the hybrid interface of a Ti_PEI_1-hour specimen tested when the crack propagated on the compression side of the beam. Patterns from the T650-8HS carbon fabric, which belonged to the PMC side before the test, bonded on Ti foil surface. These images revealed some cohesive failure occured near the pre-crack tip.

Figure 7.8 shows UT analysis images at the hybrid interface of a Ti_PEI_1-hour specimen tested when the crack propagated on the tension side of the beam. Relatively flat and clean fracture surfaces were revealed, indicating dominantly adhesive failure.

Two Ti_PEI_1-hour specimens were tested at 315 ^oC, one in comppression configuration and the other in tension. UT scan was performed after each test of these specimens. The UT images presented in Figures 7.9 and 7.10 show irregular crack fronts after each tests. Multiple delaminations at the two hybrid interfaces present in each specimen are observed. It should be noted that the delamination occured at the non-tested hybrid interface initiated at the location near the crack tip. This could be attributed to the high stress concentration present in the vicinity of the crack tip.

7.2.1 Fractography using OM, SEM/EDS

Figures 7.11 and 7.12 show the SEM fracture surfaces on the Ti side of a 4-ENF Ti_PEI_1-hour specimen tested when the crack propagated on the compression and

tension side, respectively. It is observed that when the specimen was tested with the crack on the compression side, the fracture surface on Ti side exhibits more and larger cusps features. When the crack located on the tensile side, the fracture surface on Ti side exhibits less cusps and less dense and smaller cusp features. Figure 7.13 shows that microcracks were formed on the fracture surface due to stress concentration on the troughs of the laser ablation patterns. This indicates additional fracture mechanims and more energy was released during the fracture tests.

7.2.2 FTIR Analysis on Fracture Surfaces

FTIR was performed on the Ti side fracture surface of a Ti_PEI_1-hour specimen. The results are presented in Figure 7.18.

Figure 7.19 shows comparison of FTIR data obtained herein with nanoIR results presented in section 4 for the Ti_PEI_1-hour interface. Consistency between the two methods is found. It is worth noting that the sampling size where the FTIR spectra were obtained in this work was 3.4 mm, i.e. macroscale.

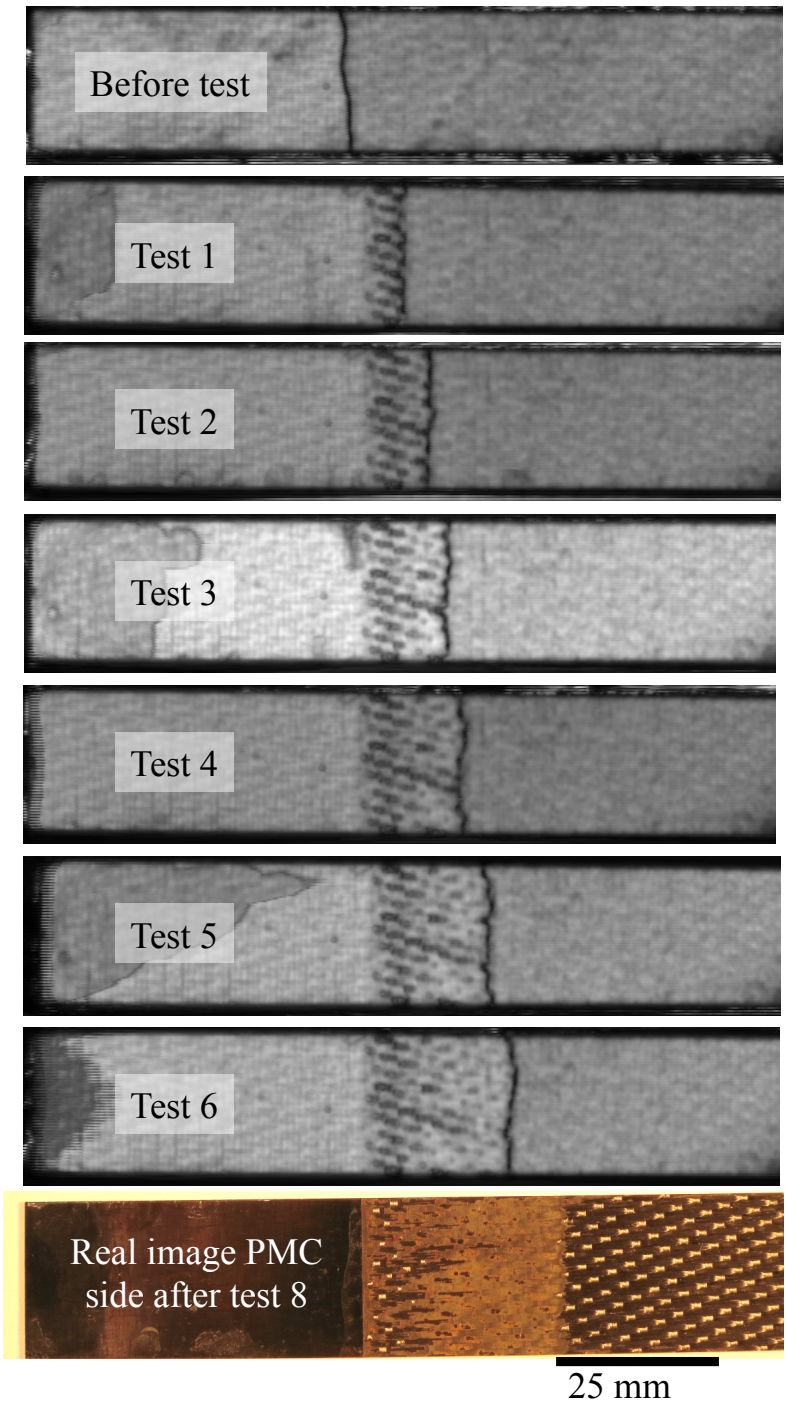

Figure 7.7: UT scan analysis showing crack progression and the crack front profiles after the 4-ENF tests performed on a Ti_PEI_1-hour specimen tested when the crack propagated on the compression side of the beam. This specimen underwent 4-ENF tests at 25 ^oC.

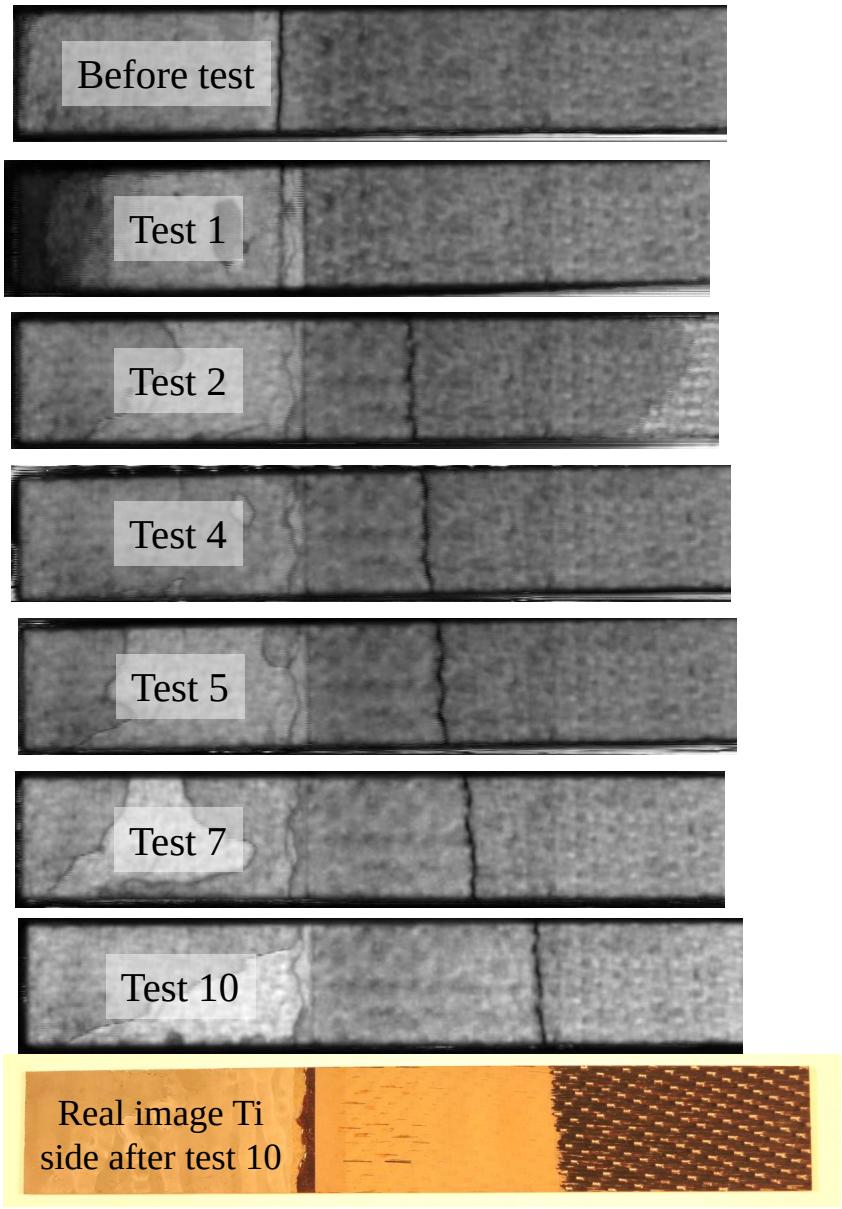

Figure 7.8: UT scan analysis showing crack progression and the crack front profiles after the 4-ENF tests performed on a Ti_PEI_1-hour specimen tested when the crack propagated on the tension side of the beam. This specimen underwent 4-ENF tests at 25 ^oC.

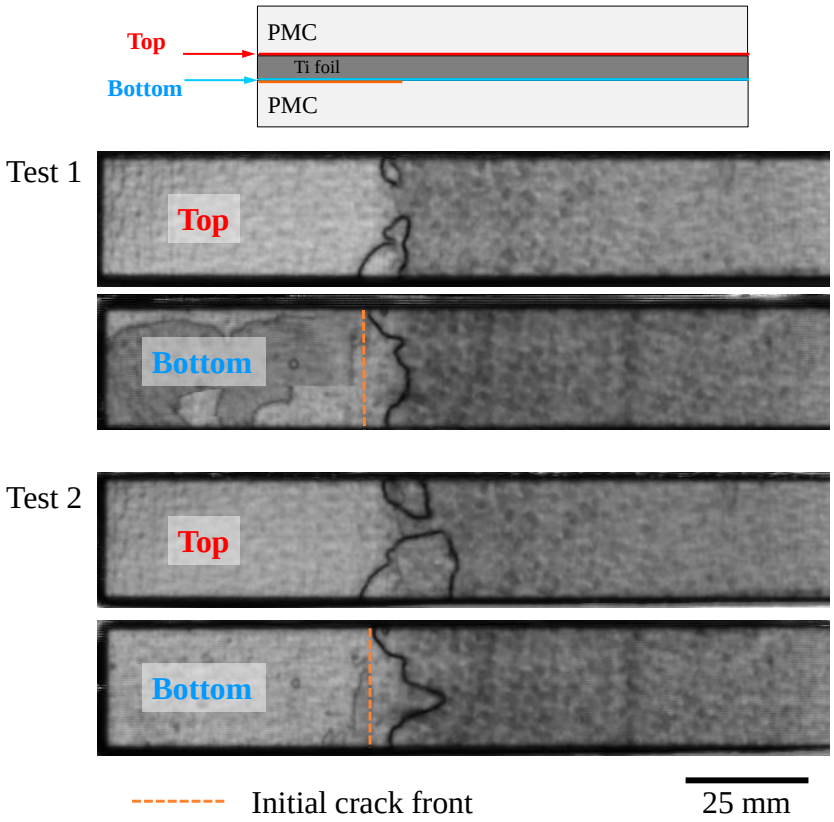

Figure 7.9: UT scan analysis showing irregular crack front and multiple delamination at the two hybrid Ti-PMC interfaces after the 4-ENF tests performed at 315 ^oC. These tests were performed on a Ti_PEI_1-hour specimen tested when the crack propagated on the tension side of the beam.

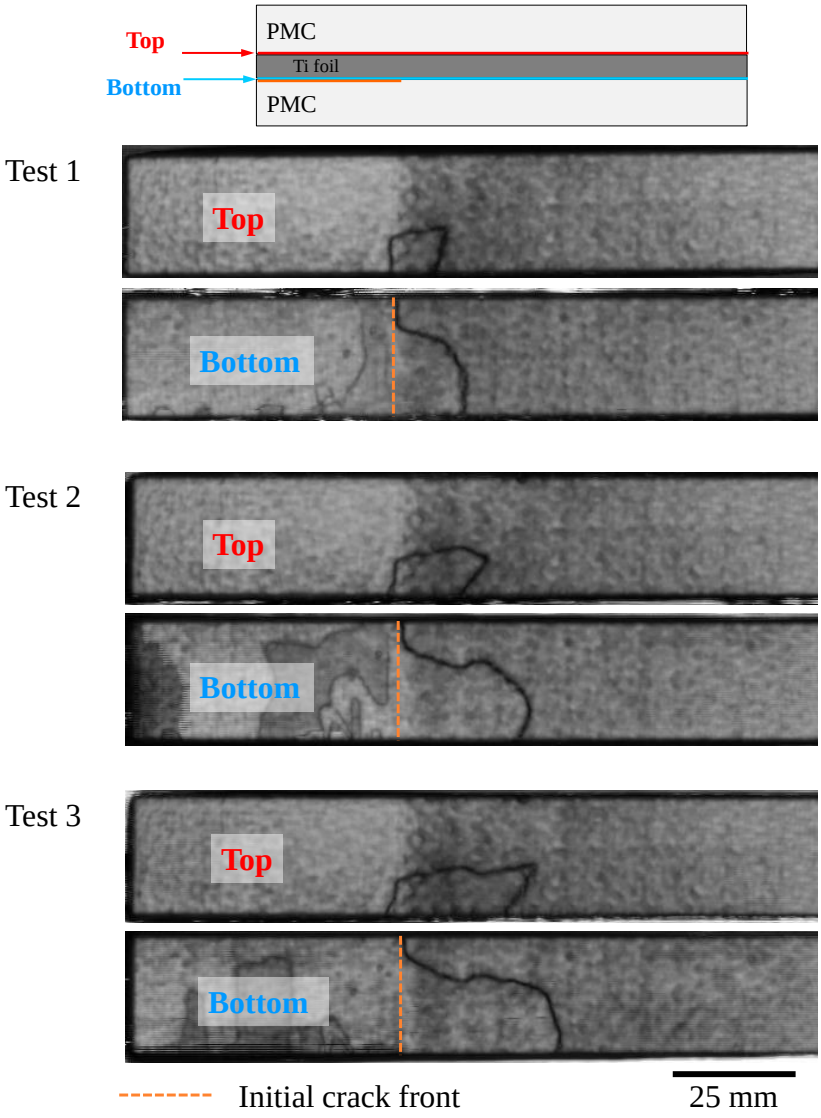

Figure 7.10: UT scan analysis showing irregular crack front and multiple delamination at the two hybrid Ti-PMC interfaces after the 4-ENF tests performed at 315 ^oC. These tests were performed on a Ti_PEI_1-hour specimen tested when the crack propagated on the compression side of the beam.

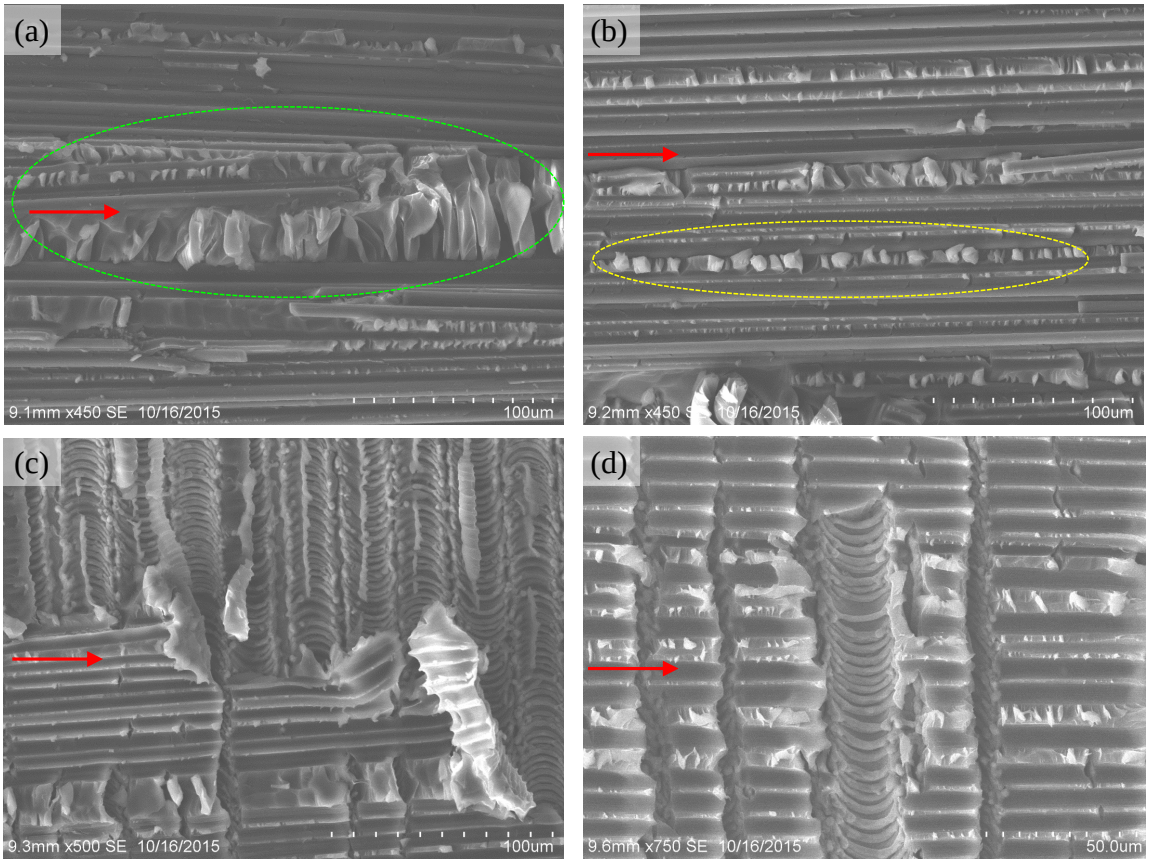

Figure 7.11: SEM fracture surfaces on the Ti side of a 4-ENF Ti_PEI_1-hour specimen tested at 25 ^oC when the crack propagated on the compression side of the beam. The red arrows indicate the crack growth direction.

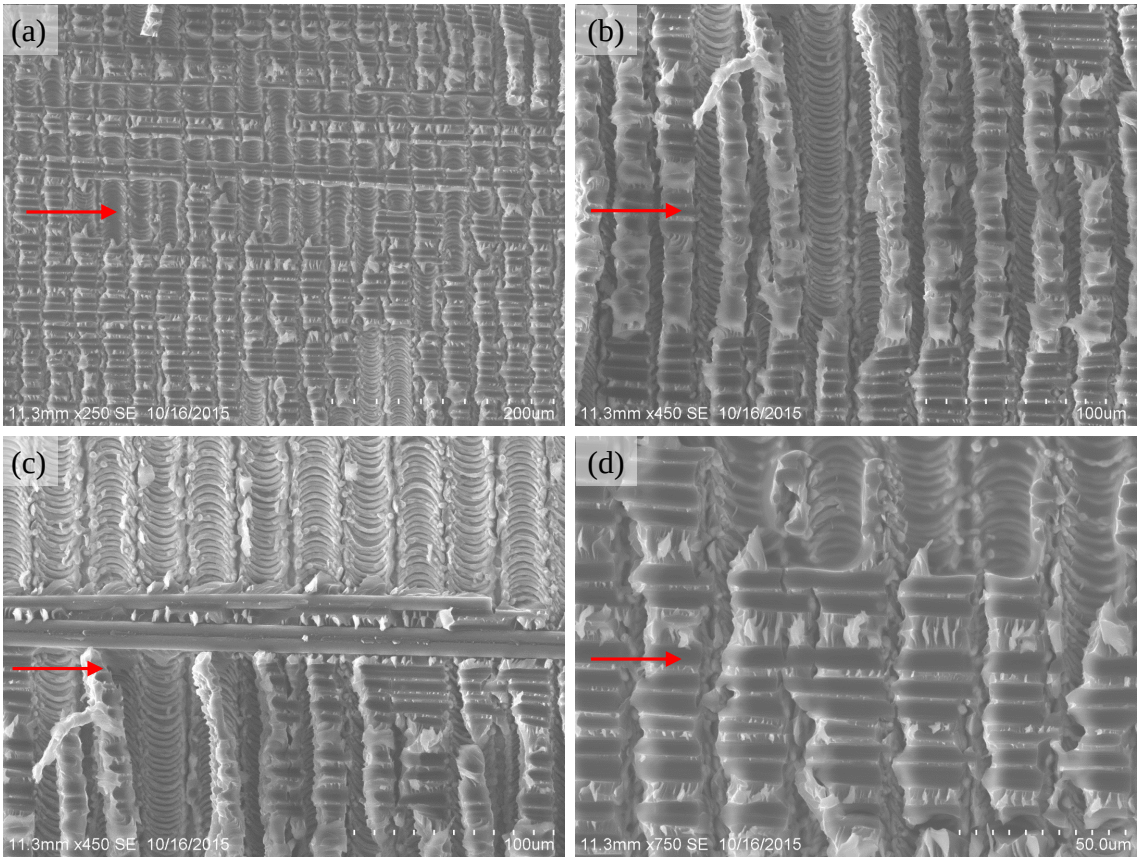

Figure 7.12: SEM fracture surfaces on the Ti side of a 4-ENF Ti_PEI_1-hour specimen tested at 25 ^oC when the crack propagated on the tension side of the beam. The red arrows indicate the crack growth direction.

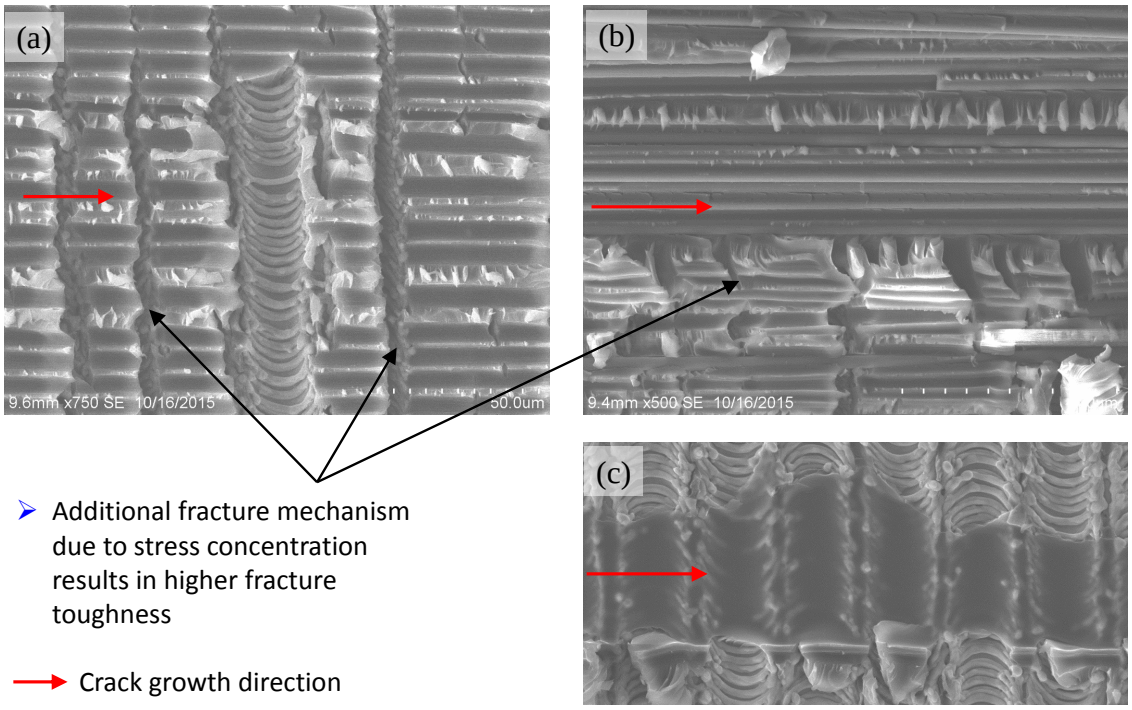

Figure 7.13: SEM fracture surfaces on the Ti side of a 4-ENF Ti_PEI_1-hour specimen tested at 25 ^oC when the crack propagated on the compression side of the beam. Microcracks formation due to stress concentration on the troughs of the laser ablation patterns indicate additional fracture mechanims and more energy released during the fracture tests.

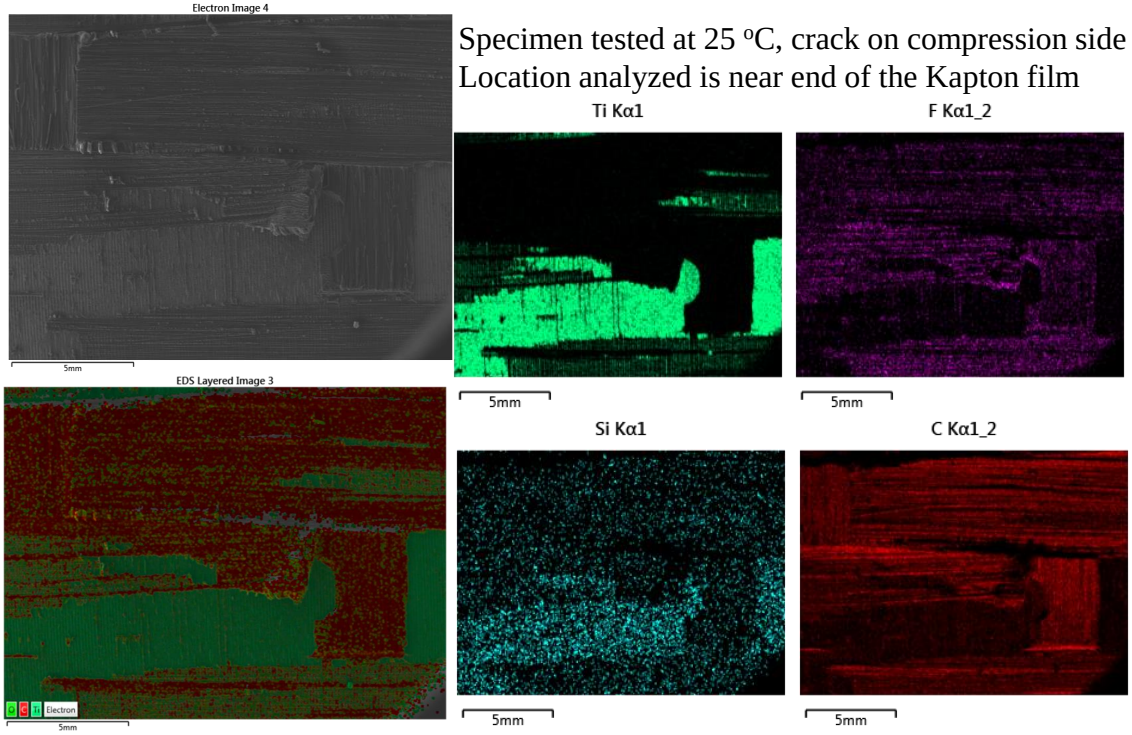

Figure 7.14: EDS analysis performed on SEM fracture surfaces on the Ti side of a 4-ENF Ti_PEI_1-hour specimen tested at 25 ^oC when the crack propagated on the compression side of the beam. The location analyzed is near the Kapton pre-crack where cohesive failure mode was revealed.

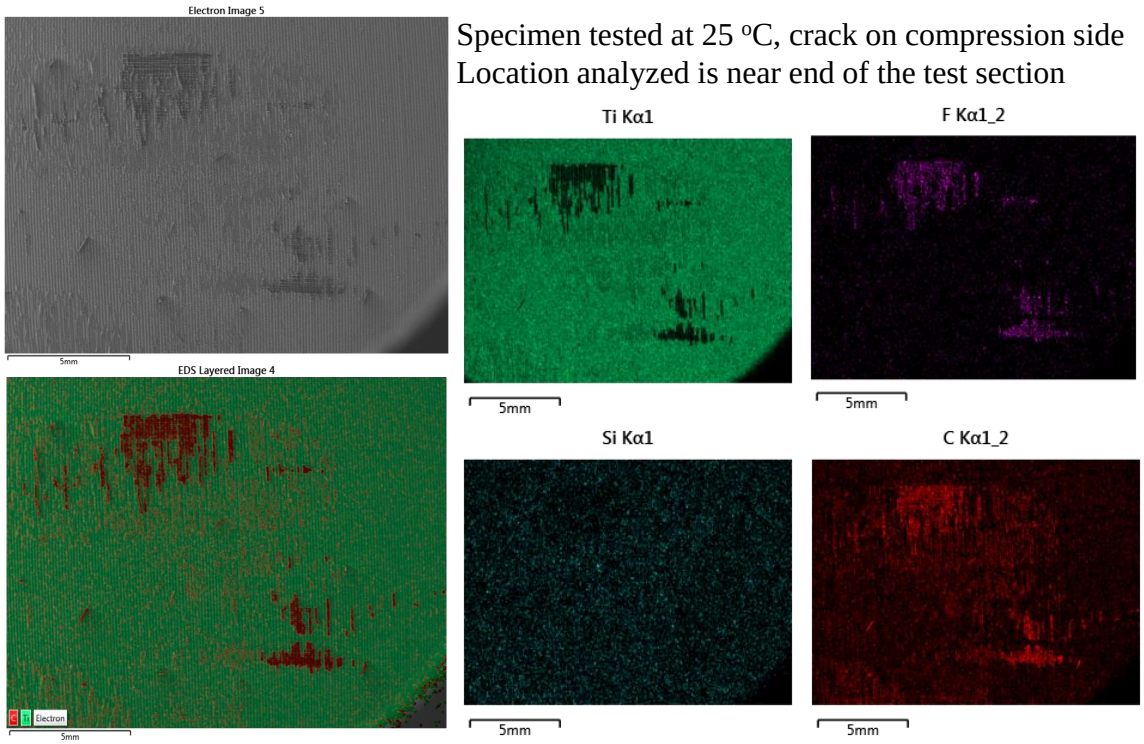

Figure 7.15: EDS analysis performed on SEM fracture surfaces on the Ti side of a 4-ENF Ti_PEI_1-hour specimen tested at 25 ^oC when the crack propagated on the compression side of the beam. The location analyzed is near the end of the test section. Some cohesive failure was observed.

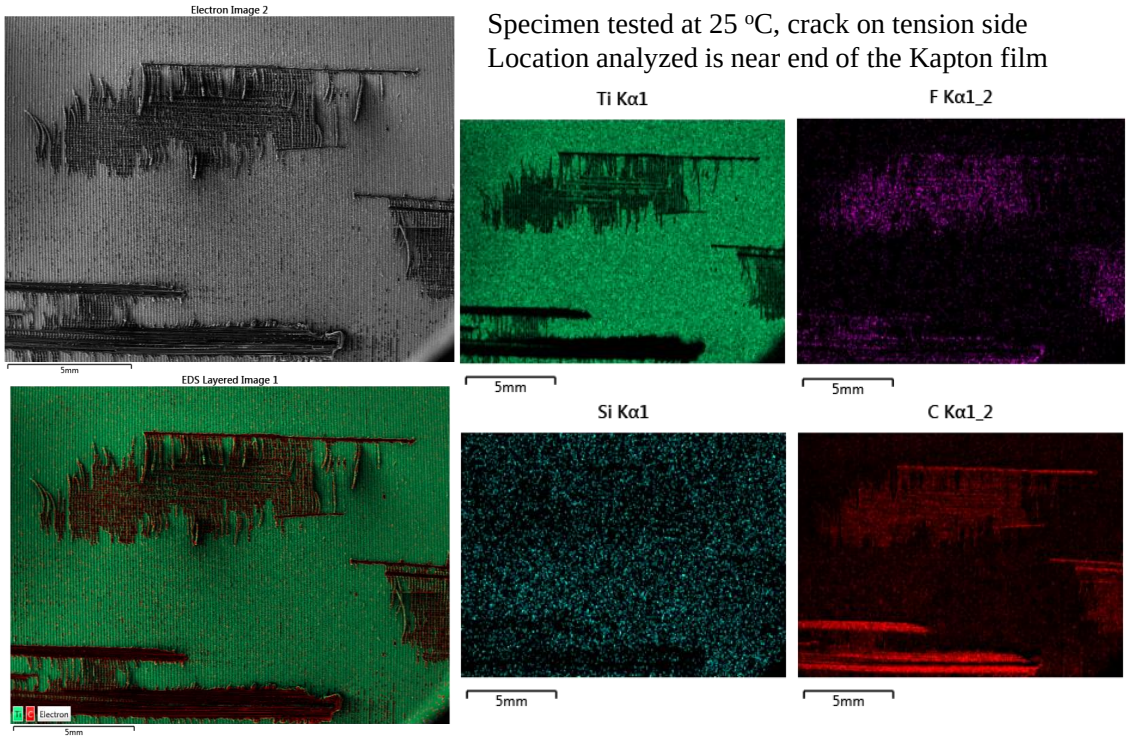

Figure 7.16: EDS analysis performed on SEM fracture surfaces on the Ti side of a 4-ENF Ti_PEI_1-hour specimen tested at 25 ^oC when the crack propagated on the tension side of the beam. The location analyzed is near the Kapton pre-crack. Some cohesive failure mode was observed.

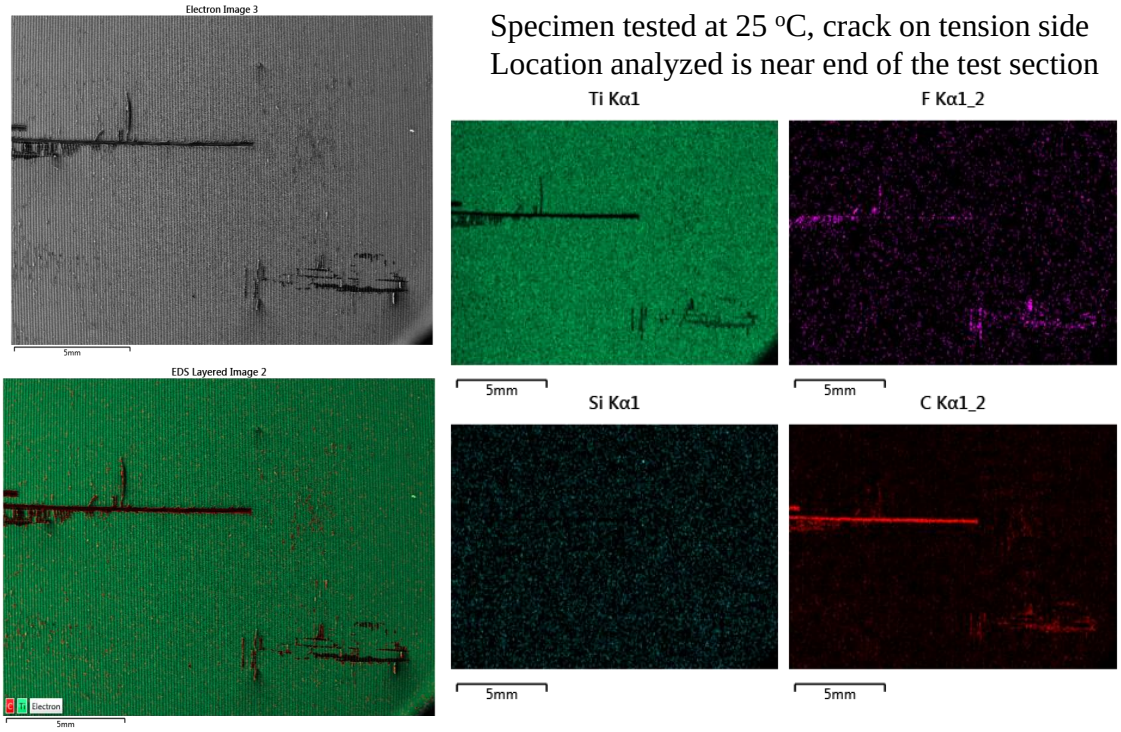

Figure 7.17: EDS analysis performed on SEM fracture surfaces on the Ti side of a 4-ENF Ti_PEI_1-hour specimen tested when the crack propagated on the tensionsion side of the beam. The location analyzed is near the end of test section.

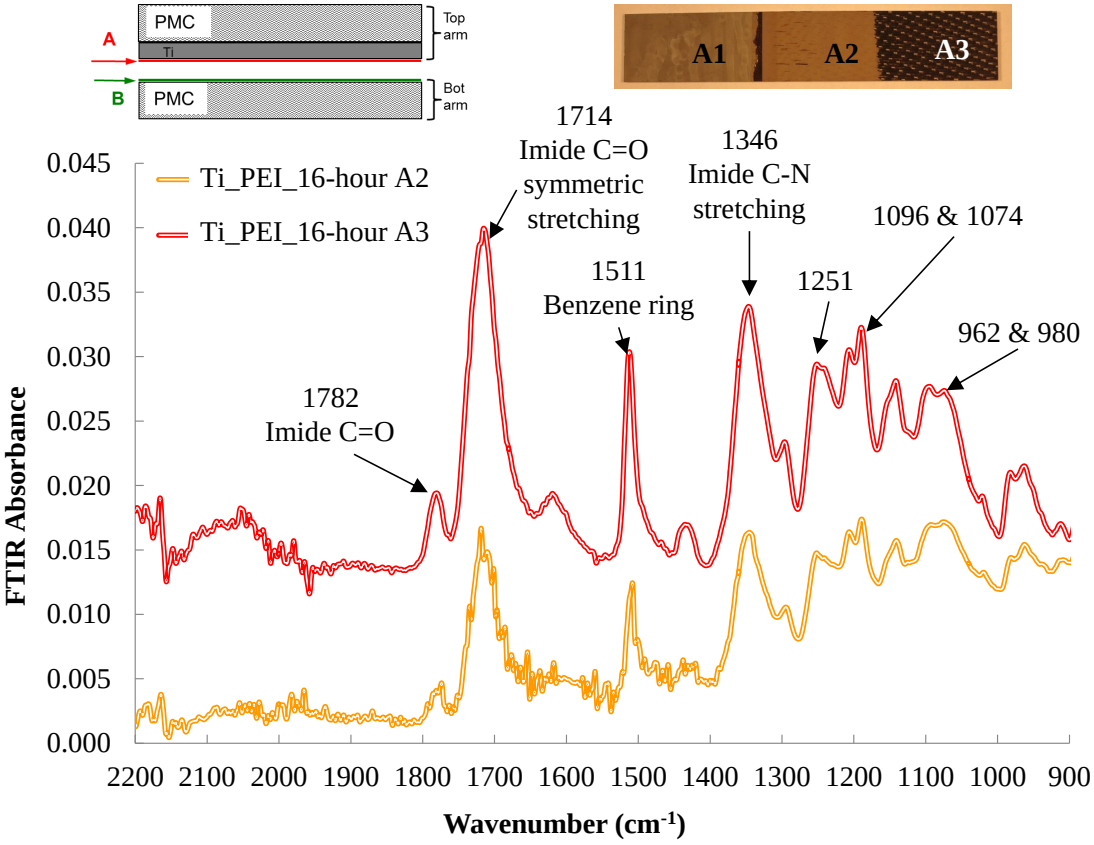

Figure 7.18: ATR-FTIR results for specimens from Ti_PEI_1-hour panel

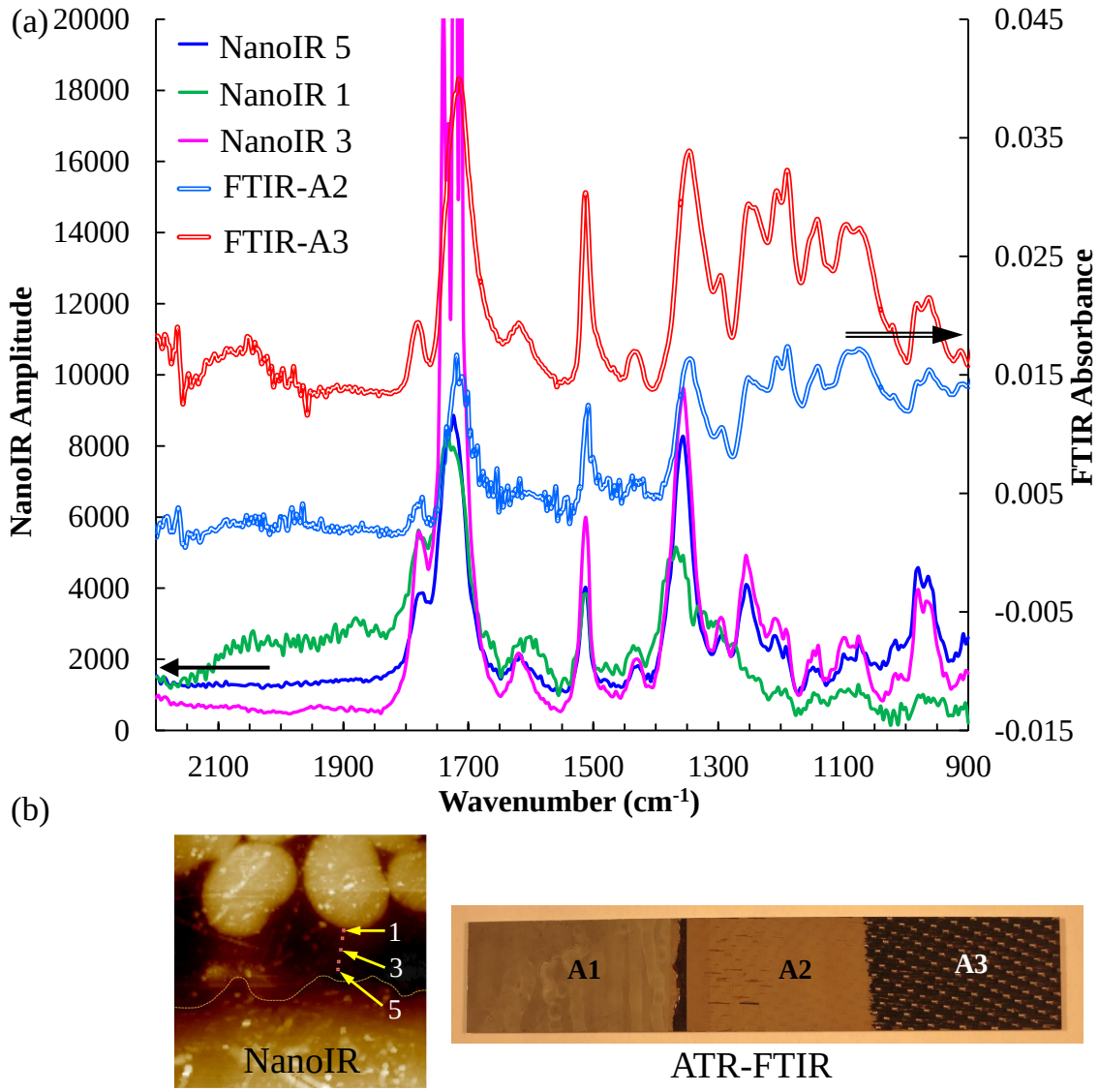

Figure 7.19: (a) NanoIR and ATR-FTIR result comparison for specimens from Ti_PEI_1-hour panel. (b) The locations where NanoIR and ATR-FTIR results are shown in Figure (a).

8. FINITE ELEMENT ANALYSES OF THE DOUBLE CANTILEVER BEAM CONTAINING HYBRID METAL−COMPOSITE INTERFACES

The finite element analyses presented in this section were carried out to further investigate the crack propagation behavior of the hybrid double cantilever beams containing Al−T300-PW/Epoxy 04908, Ti−T650-8HS/AFR-PE-4, and NiTi−T650-8HS/AFR-PE-4 interfaces. Strain profiles along the length of the specimen obtained from FE analysis presented in Section 8.1 of the DCB containing Al−T300-PW/Epoxy 04908 interface were compared with the distributed strain profiles obtained from the fiber optic measurements presented in section 4. For the DCB containing Ti−T650-8HS/AFR-PE-4 interface, FE analyses presented in Section 8.2 were carried out with and without consideration of thermal residual stresses due to curing. The thermal warping exhibited on the hybrid DCB specimens as observed and presented in section 6 was further investigated and explained in this section via the FE analysis. Finally, as discussed in section 6, during crack propagation, the DCB specimen containing NiTi−T650-8HS/AFR-PE-4 hybrid interface experienced stress-induced phase transformation in the NiTi foil layer. This phase transformation was captured in the DCB analysis for NiTi−T650-8HS/AFR-PE-4 interface presented in Section 8.3.

The commercial finite element software ABAQUS was used to perform the finite element analyses presented in this section. The virtual crack closure technique (VCCT) with Benzeggagh-Kenane (B-K) mixed mode fracture criterion [110] was used to study crack propagation at the hybrid interfaces. All analyses were carried out with the ABAQUS built-in nonlinear geometric option activated.

8.1 Analysis of Double Cantilever Beam Containing Al−T300-PW/Epoxy 04908 Interface: Comparison of Strain Profiles from FEA and Experimental Fiber Optics Measurements

8.1.1 Model Descriptions and Boundary Conditions

Two- and three-dimensional finite element analyses of the DCB specimen containing the Al−T300-PW/Epoxy 04908 interface were carried out to study the mode-I delamination behavior at this hybrid interface. In the two-dimensional analysis, linear incompatible plane strain elements (CPE4I) were used, while the linear incompatible solid elements (C3D8I) were used ins the three-dimensional analyses. A schematic of the DCB specimen with boundary conditions is illustrated on Figure 8.1.

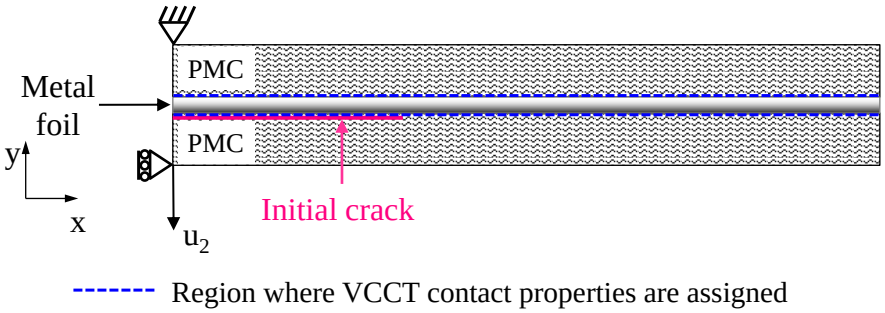

Figure 8.1: Schematic of DCB specimen and boundary conditions

The DCB model has dimensions of 4.4 mm x 25.4 mm x 125 mm. Each of the PMC arms has a thickness of 2 mm. The thickness of the Al layer was 0.4 mm. The initial crack length was 50 mm. In the two-dimensional analysis, two elements were used through-the-thickness of the Al foil layer, while the thickness of each PMC arm was discretized into eight elements. The PMC and Al layers were meshed such that

the aspect ratio of each element was kept at 1:2 and 1:2.5, respectively. That is, the elements size in the PMC layers was 0.25 mm x 0.5 mm and that of the Al layer was 0.2 mm x 0.5 mm. An example of the two-dimensional mesh of the DCB containing Al−T300-PW/Epoxy 04908 interface is illustrated in Figure 8.2.

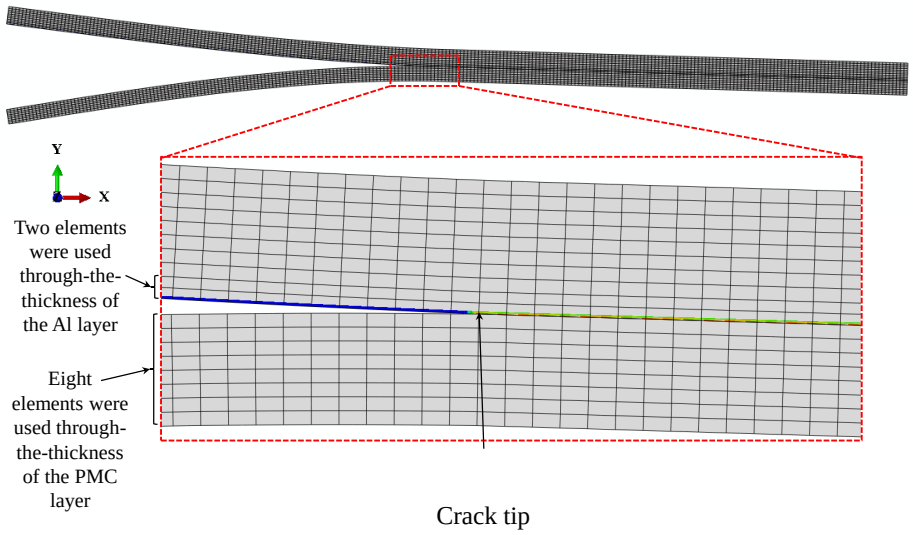

Figure 8.2: Example of the two-dimensional FEA mesh of the DCB containing Al−T300-PW/Epoxy 04908 interface.

In the three-dimensional analysis, each element had in-plane dimensions of either 1 mm x 1 mm or 5 mm x 5 mm. The coarse mesh size was selected to investigate the effect of the plain weave unit cell size, which is approximately 4.5 to 5.0 mm, on the crack propagation behavior at the hybrid interface. An example of the coarse three-dimensional mesh is shown in Figure 8.3.

Transversely isotropic linear elastic material properties were used for the PMC. These properties were obtained from finite element homogenization analyses performed at the micro-scale for the tow (hexagonal packing array) and the meso-scale

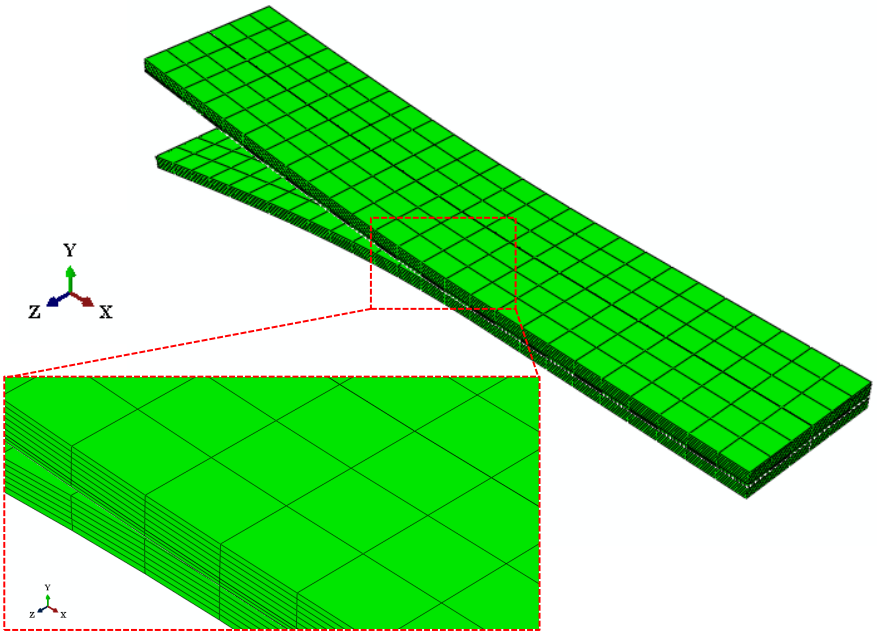

Figure 8.3: Example of a coarse three-dimensional FEA mesh of the DCB containing Al−T300-PW/Epoxy 04908 interface.

Table 8.1: Homogenized thermal-mechanical properties of T300-PW/Epoxy 04908 composite laminate [3]

$E_{11} = E_{22}$ (GPa)	56.5
E_{33} (GPa)	10.6
G_{12} (GPa)	4.13
$G_{23} = G_{13}$ (GPa)	3.13
ν_{12}	0.148
$\nu_{23} = \nu_{13}$	0.392
$\alpha_{11} = \alpha_{22}$ ($1/^oC$)	2.17 x 10^{-5}
α_{33} ($1/^oC$)	3.62 x 10^{-7}

for the woven lamina (plain weave). An overall fiber volume fraction of 66% as obtained from thermal gravimetric analysis (TGA) measurement was used for the homogenization analyses. The homogenized properties of PMC used in the DCB

analyses are summarized in Table 8.1. Linear isotropic properties were used for the Al layer. The material properties of Al is summarized in Table 8.2.

Table 8.2: Thermal-mechanical properties of Al foil in FEA of DCB containing Al−T300-PW/Epoxy 04908 interface [4].

E (GPa)	68.9
ν	0.33
α ($1/^oC$)	25.2 x 10^{-6}

8.1.2 Results and Discussion

The results from finite element analyses in both two- and three-dimension are in good agreement with the experimental results. Figure 8.4 shows load-opening displacement response for results from two- and three-dimensional FEA in comparison with experimental result for DCB containing Al−T300-PW/Epoxy 04908 interface that was presented in section 4. The load-displacement response from both the two- and three-dimensional FEA closely captured the experimental initial linear slope as well as the load and displacement values at final failure, i.e. before the specimen was fully delaminated as the crack reached the end of the specimen.

The softening portions of the FEA load-displacement curves that were associated with crack propagation followed the trend exhibited on the experimental curve. The two-dimensional FEA curve possessed a smooth softening curve indicating stable crack propagation was observed in this analysis. From the load-displacement results of the three-dimensional analysis, saw-tooth and crack growth-arresting behaviors were observed. The size of these saw-tooth features are in good agreement with those exhibited on the experimental load-displacement curve. However, it should be noted that the saw-tooth pattern size from the FEA was due to the size of the elements

used in the three-dimensional mesh while the experimentally observed patterns were due to the weave architecture of the PMC reinforcement.

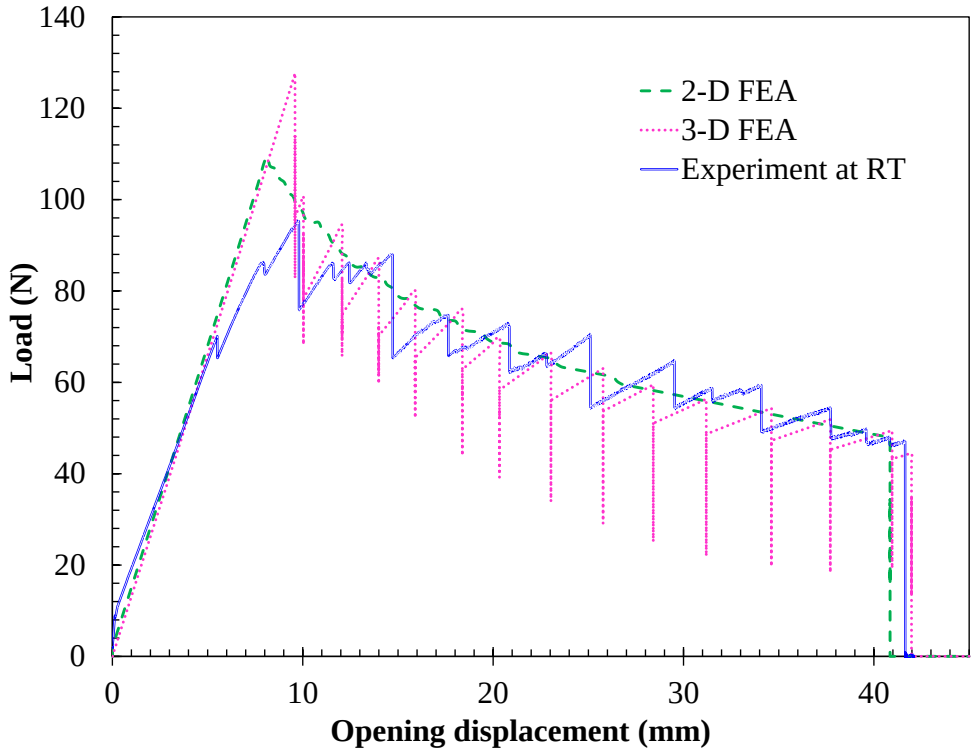

Figure 8.4: Comparison of load-displacement response obtained from experiment and two- and three-dimensional FEA of a DCB containing Al−T300-PW/Epoxy 04908 interface.

Figure 8.5 shows comparison of strain ϵ_{11} profiles along the top edge of the DCB specimen obtained from the experiment with Rayleigh back-scattered fiber optics presented in section 4 and the two- and three-dimensional FEA. The paths in the two- and three-dimensional FE models along which the strain ϵ_{11} profiles were obtained are highlighted on the schematic images in this figure. The strain ϵ_{11} profiles presented in Figure 8.5 were obtained at the instance immediately before the crack propagated

from the initial crack tip.

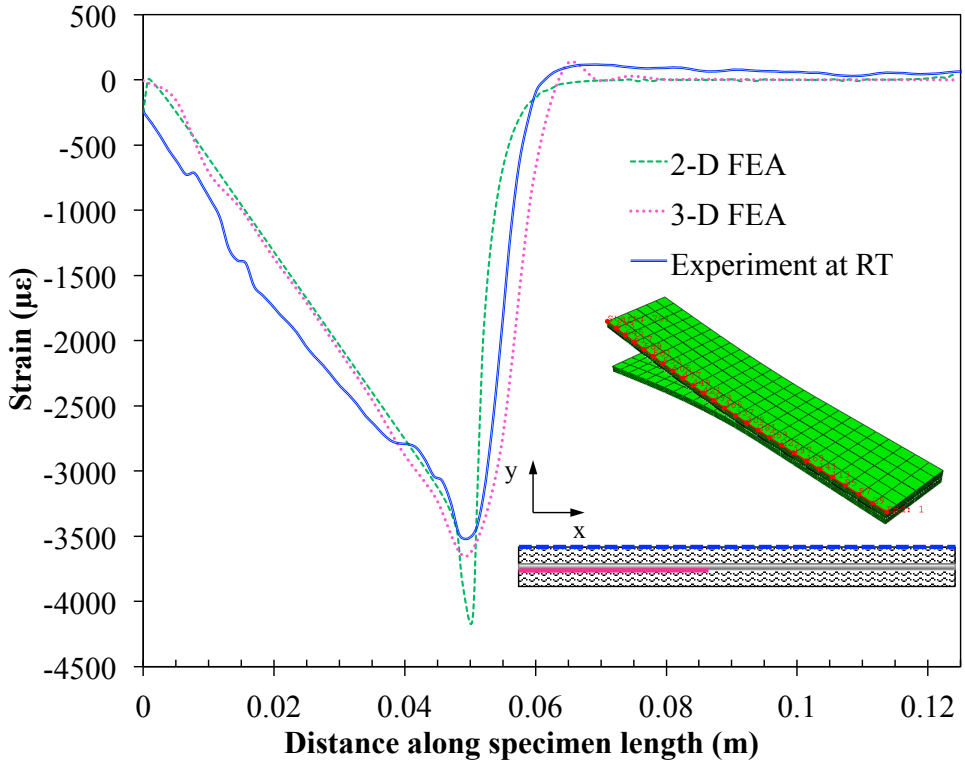

Figure 8.5: Comparison of strain ϵ_{11} profiles obtained from fiber optics distributed strain measurement and two- and three-dimensional FEA of DCB containing Al−T300-PW/Epoxy 04908 interface. These strain profiles were obtained at the instance immediately prior to the crack propagated from the initial crack tip.

The strain ϵ_{11} results from both the two- and three-dimensional FEA are in good agreement with the distributed strain profiles measured experimentally. As discussed previously in section 4, as opening displacement was applied at the delaminated end of the specimen, the top and bottom sides of the loaded DCB specimen were under compression. Thus, negative strain values were obtained. Along the specimen's length, the compression strain magnitude increased from the delaminated end of the beam, or the loading pin, to the vicinity of the crack tip, where the maximum

compression strain value was measured, and then immediately decayed to zero strain. This is because no loads or constraints were applied on the undelaminated segment of the DCB beam. Under no load, that segment of the DCB specimen exhibited zero strain.

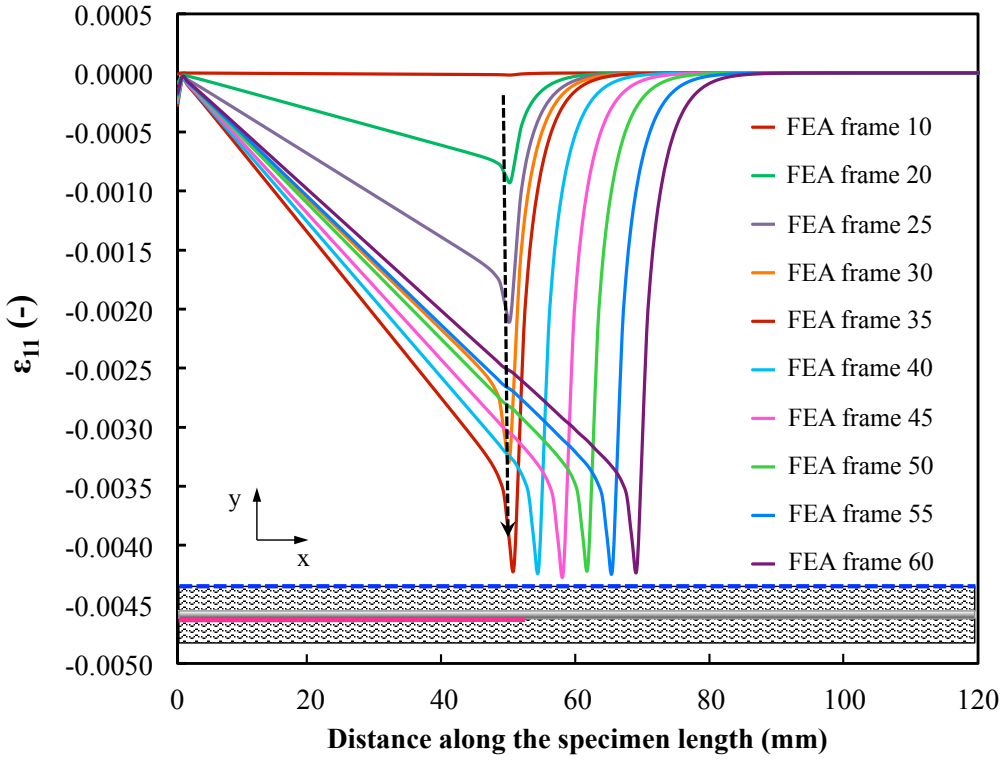

Figure 8.6: Evolution of strain profiles obtained on the topside of the DCB specimen (Al−T300-PW/Epoxy 04908 interface) in the two-dimensional FE analysis. The location where the strain profiles were obtained is highlighted by the dashed blue line in the schematic in this figure.

ϵ_{11} strain profiles obtained from the two-dimensional FEA on the topside of the DCB specimen at different time frames in the analysis are shown in Figure 8.6. The dashed arrow in Figure 8.6 shows the evolution of strain profiles when the crack tip is at the initial location. Similar to what was observed in the experiment with fiber

optics presented in section 4, the compressive strain values gradually decreased as the opening displacement was applied to the specimen. Once the critical value was reached, the delamination started to grow. However, the crack propagation observed in the two-dimensional analysis did not exhibit the growing-resetting behavior as seen in the experiment presented in section 4. The critical strain values remained almost constant as the crack propagates following the trend indicated by the solid arrow in Figure 8.6. The crack progression demonstrated in the two-dimensional analysis was smooth, and thus, representing a stable crack growth. This further confirmed the stable crack growth behavior observed on the load-displacement plot shown earlier in Figure 8.4. This is because in the FEA, the delamination occured on a straight and smooth interface predefined between the Al and PMC layers, while in reality, the weave architecture played an important role on crack propagation behavior. The influence of the weave unit cell size on crack propagation behavior was investigated by the three-dimensional analysis presented herein.

Load-displacement response from the three-dimensional FEA of the DCB containing Al−T300-PW/Epoxy 04908 interface is presented in Figure 8.7. Figure 8.8(a) shows the evolution of strain ϵ_{11} profiles prior to and immediately after the crack propagated from the initial crack front. These strain ϵ_{11} profiles were obtained along the top edge of the specimen, as highlighted by the path shown on the mesh image in this figure. The ϵ_{11} profiles evolving along the dashed arrow presented in Figure 8.8(a) correspond to the initial loading from A to B as demonstrated in Figure 8.7. As the load dropped from B to C in Figure 8.7, the crack propagated an extension of 5 mm and the absolute of maximum compressive strain ϵ_{11} value dropped an amount of approximately 500 microstrain, as illustrated by the solid arrow from B to C in Figure 8.8(a). This is in good agreement with observation on the distributed strain profiles measured and presented in section 4.

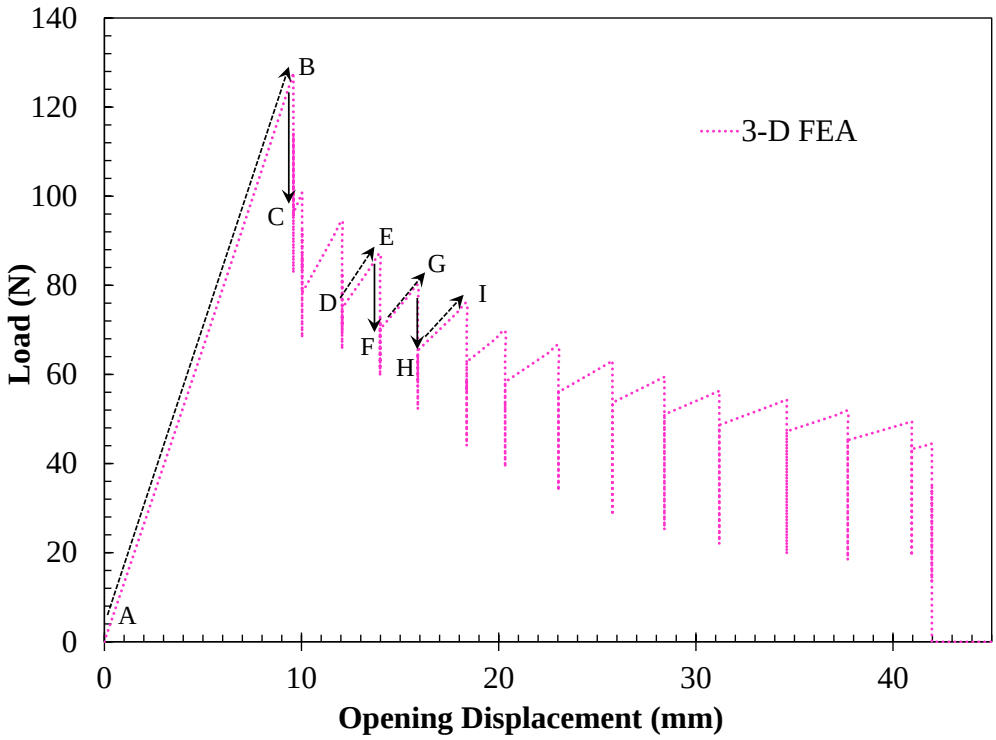

Figure 8.7: Load-displacement response obtained from three-dimensional FEA of the DCB containing Al−T300-PW/Epoxy 04908 interface.

Figure 8.8(b) shows examples of strain evolution during subsequent crack propagations following the saw-tooth pattern on the load-displacement curve in Figure 8.7. As the specimen exhibited a linear increase in load with applied displacement from D to E, F to G and H to I, the strain values decreased while the crack tip location remained constant, indicated by the unchanged location of the crack tip, or the location along the specimen's length at which the absolute compressive strain value was maximum on each strain ϵ_{11} profile. As the peak loads were reached at E, G and I, this maximum absolute strain reached its critical value and the crack propagated.

Following the peak loads at E and G are instantaneous load drops from E to F

and G to H as shown by the solid arrows in Figure 8.7. Accordingly, the maximum absolute strain value dropped an amount of 500 microstrain as discussed previously. This new maximum absolute strain value occurred at a new location along the specimen length, indicating the crack propagated to a new location. The solid arrows from E to F and G to H in Figure 8.8(b) show this strain resetting behavior as the crack propagated. The strain energy release during crack propagation previously captured via fiber optics measurements is now captured by the three-dimensional FEA.

It should be noted that in the three-dimensional FEA, each crack extension according each load-drop on the saw-tooth pattern in Figure 8.7 was 5 mm. The amount the crack advanced each time is demonstrated in Figure 8.8. The crack extension in the three-dimensional FEA is dictated by the element size used, in this case it was 5 mm. This is because energy-based VCCT criterion was used to model crack propagation. At each crack growth, one set of nodes across the specimen width was release and the crack front arrested at the set of node adjacent to it. Since linear elements were used, the crack propagated from one end to the other end of each element.

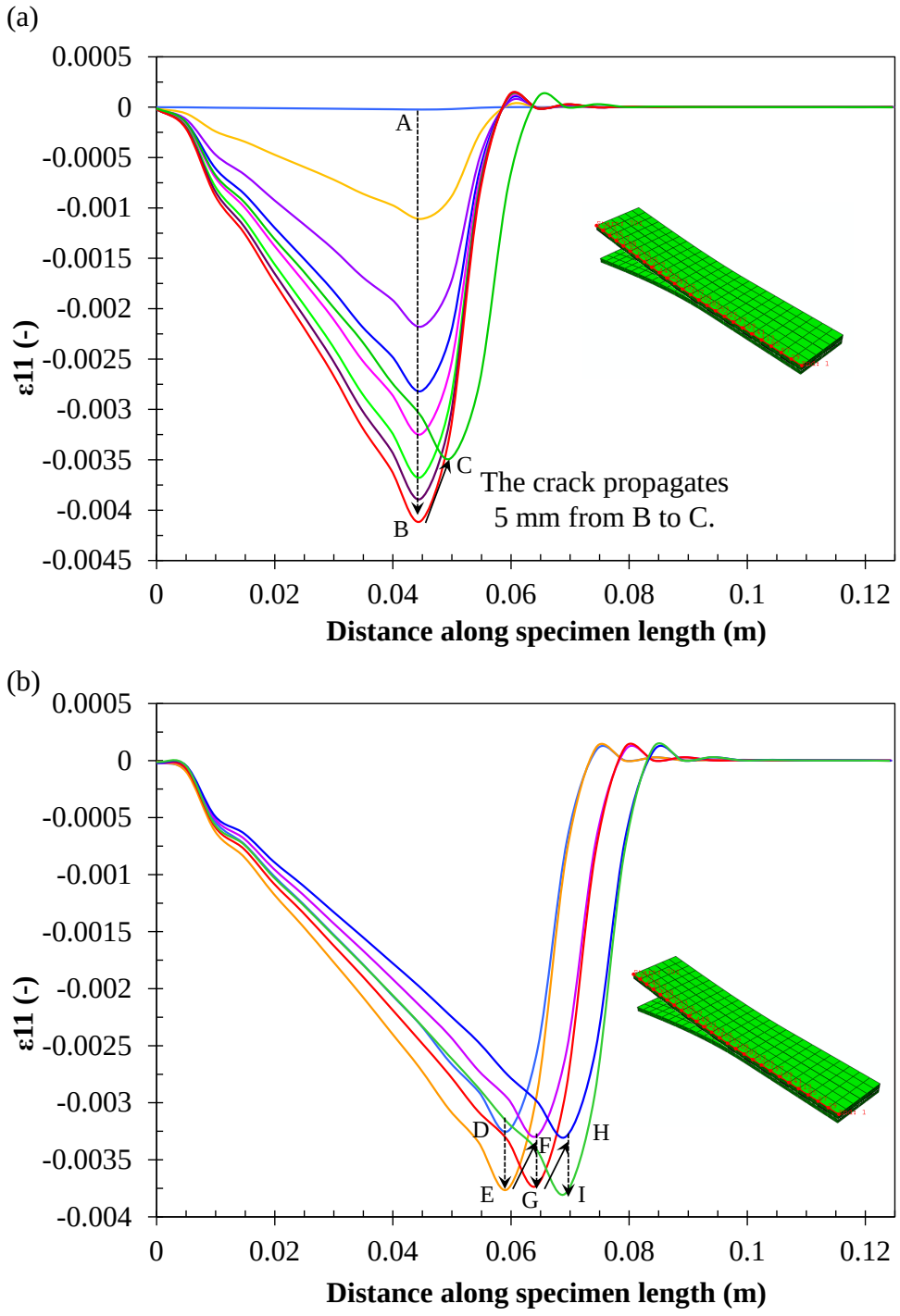

Figure 8.8: Strain ϵ_{11} profiles obtained from three-dimensional FEA along the path highlighted on the mesh image (a) prior to and after the crack propagated from the initial crack front. (b) before and after the subsequent crack advances during the propagation process. The DCB specimen analyzed contained Al−T300-PW/Epoxy 04908 interface.

It is also noted from the three-dimensional analysis results that the crack front across the specimen's width first propagates from the center and then advances outward to the free edges. Figure 8.9 shows the bond state across the with of the DCB specimen during crack propagation. The images in Figure Figure 8.9 was obtained from the fine mesh (1 mm x 1 mm element size) three-dimensional FEA. This observation from the FEA results supports the crack propagation behavior characterized by ultrasonic C-scan presented in sections 6 and 7.

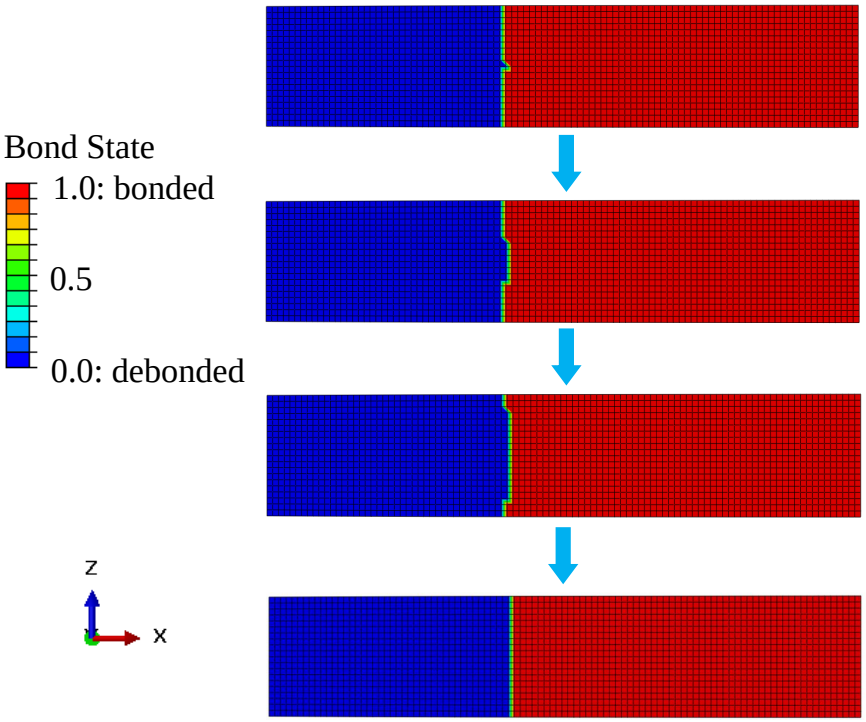

Figure 8.9: Bond state as the crack propagates.

8.2 Analysis of Double Cantilever Beam containing Ti−T650-8HS/AFR-PE-4 Interface: Consideration of Thermal Residual Stresses due to Curing

8.2.1 Model Descriptions and Boundary Conditions

In this section, two-dimensional finite element analyses were carried out to model the DCB containing Ti−T650-8HS/AFR-PE-4 interface. These FEA were performed with and without the consideration of thermal residual stress due to curing. All analyses in this section were carried out following the same procedure but different temperature inputs were used for the cases where residual stress due to cooling from the curing temperature was and was not considered. The effect of critical strain energy release rate inputs was also investigated.

The analysis steps performed for computational models that take into account thermal residual stress in the DCB can be summarized as follows.

- Initial step: The entire DCB was subjected to an initial temperature field of T_i. For the analysis with and without consideration of thermal residual stress due to curing, T_i value is 644 K and 298 K, respectively.

- Constrained cooling step: The temperature field of T = 298 K was applied. As a result, the entire DCB was subjected to a temperature change $\Delta T = T_i$ - T. A pressure load of 1.4 MPa was applied to the top longitudinal edge of the specimen. The bottom longitudinal edge of the specimen was subjected to a boundary condition of $u_2 = 0$ or displacement in the thickness-direction was restricted to 0.

- Cooling constraints removal step: The applied load and boundary condition for the constrained cooling step were removed while temperature field was kept constant.

- DCB loading step: Displacement boundary conditions were applied to facilitate DCB displacement controlled loading to an opening displacement of 25.4 mm. These boundary conditions are illustrated in the schematic in Figure 8.1.

- DCB unloading step: The opening displacement boundary condition applied in the previous step was reset to zero, $u_2 = 0$, to simulate the unloading step or closing of the DCB.

Similar to the DCB analysis performed in the previous section, the VCCT criterion was used to model the crack propagation. The B-K fracture criterion was used. The critical mode I and mode II strain energy release rates used in this section are values measured experimentally as reported in sections 6 and 7. As reported in Figure 6.35, the critical mode I strain energy release rate used as input for the VCCT model in this section is either the initiation toughness (893 J/m^2) or propagation toughness (945 J/m^2). The material properties for the T650-8HS/AFR-PE-4 composite and Ti layers are summarized in Tables 8.3.1 and 8.4, respectively. Similar to the previous section, linear plane strain incompatible (CPE4I) elements were used in the FEA presented in this section.

Table 8.3: Homogenized thermal-mechanical properties of the PMC in FEA of DCB containing Ti−T650-8HS/AFR-PE-4 interface [5].

$E_{11} = E_{33}$ (GPa)	62.5
E_{22} (GPa)	12.8
G_{13} (GPa)	5.5
$G_{12} = G_{23}$ (GPa)	4.3
ν_{13}	0.08
$\nu_{12} = \nu_{23}$	0.164
$\alpha_{11} = \alpha_{33}$ ($1/^oC$)	3.735 x 10^{-6}
α_{22} ($1/^oC$)	57.42 x 10^{-6}

Table 8.4: Thermal-mechanical properties of Ti foil in FEA of DCB containing Ti−T650-8HS/AFR-PE-4 interface [6].

E (GPa)	102.0
ν	0.34
α ($1/^oC$)	9.2 x 10^{-6}

8.2.2 Results and Discussion

8.2.2.1 Effect of Thermal Residual Stress

The load-displacement responses of the DCB containing Ti−T650-8HS/AFR-PE-4 interface from the FEA with and without consideration of thermal residual stress in comparison with experimental result are presented in Figure 8.10. It should be noted that the numerical results presented in Figure 8.10 were obtained from the analysis where $G_{IC} = 945\ J/m^2$ was used as the critical mode I strain energy release rate input for the VCCT criterion. From the FEA without consideration of thermal stress due to curing, the load-displacement curve started at the origin on the graph, that is zero load at zero applied opening displacement. The initial slope of this curve is slightly higher than the initial slope of the experimental load-displacement curve. The critical load at which the crack started to propagate from the initial crack front obtained from this FEA is in good agreement with the experimental result. The softening segment of FEA load-displacement curve (without residual stress consideration) that corresponded to crack propagation upon opening of the DCB, was higher than that of the experimental curve. After being unloaded, the load-displacement from this analysis returned to the origin, which is not the behavior observed from the experimental result shown in Figure 8.10.

In the FE analysis where thermal residual stress due to curing was taken into account, the DCB specimen was subjected to a load of 10 N before any opening

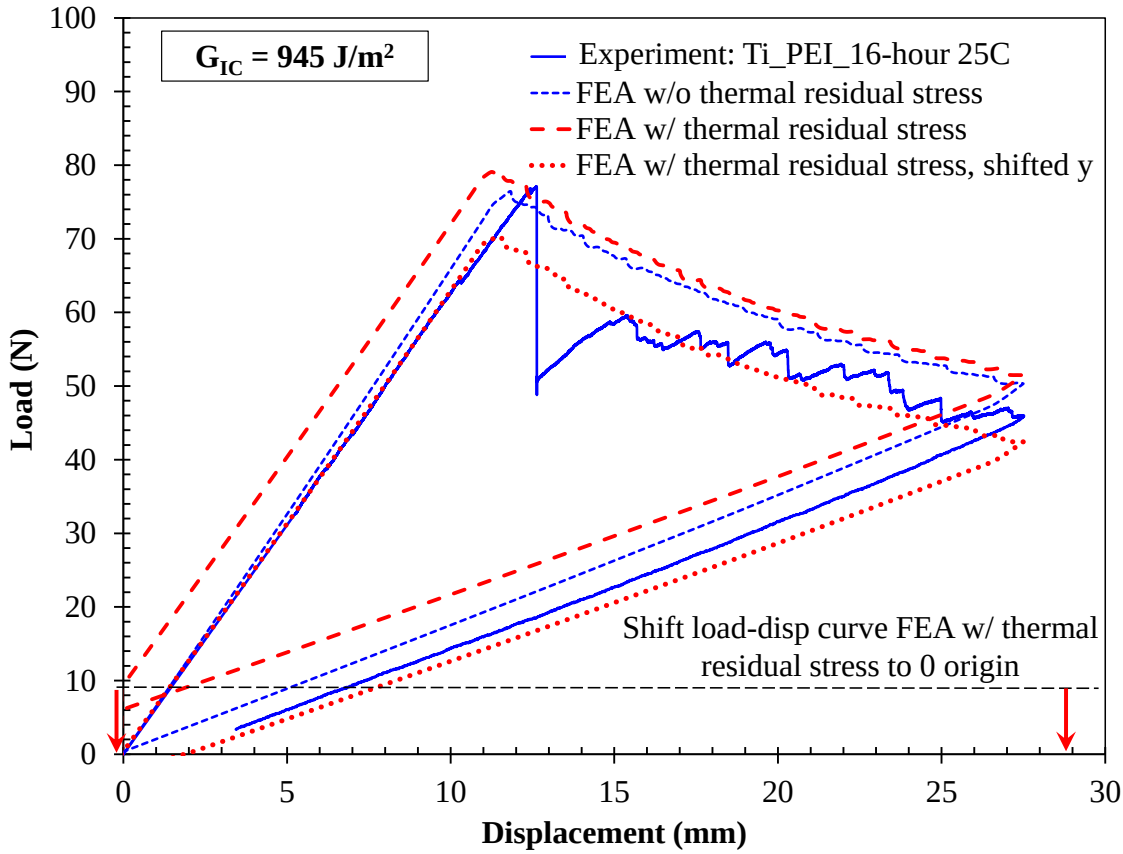

Figure 8.10: Load-displacement response from FE analysis of the hybrid DCB with and without consideration of thermal residual stress due to curing.

displacement was applied to it. This 10 N load is the reaction force due to cooling from the curing temperature of 644 K. In order to compare this load-displacement response with that obtained from the experiment and the FEA without residual stress consideration, the load-displacement curve from the FEA with residual stress effect was shifted along the y-axis (load axis) such that at zero opening displacement, the specimen as subjected to zero load. After undergoing this shifting, the load-displacement curve from the FEA with residual stress consideration exhibits an initial linear slope that is in better agreement with the experimental results, as compared to the load-displacement response obtained from the FEA without consideration of

thermal residual stress. In addition, after shifted, the softening segment of the load-displacement curve that corresponded to crack propagation occurred at the load level slightly below the average load level exhibited by corresponding segment on the experimental curve. The unloading segment of the shifted FEA load-displacement curve exhibited a non-zero displacement at zero load. This behavior agrees with what observed experimentally as shown in Figure 8.10.

The effect of thermal residual stress on the DCB before and during crack propagation as well as after unloading is also demonstrated on the stress contours obtained from the FEA. All stress σ_{11} contours presented in this section were obtained from the FE analyses with $G_{IC} = 945\ J/m^2$. Figure 8.11 shows σ_{11} contours on the DCB from the FEA without consideration of residual stress when an opening displacement of 25.4 mm was applied. As the DCB was opened, the top and bottom sides of the DCB exhibited compressive stress. Toward the crack plane, the DCB exhibited tensile stress. Stress concentration in the vicinity of the crack tip was observed. The stress (tensile) is highest in the Ti foil at the crack tip. Away from the crack tip region, the undelaminated segment of the DCB experienced zero stress σ_{11}. This is in agreement with the strain ϵ_{11} profiles along the DCB specimen length presented in Section 8.1.

The σ_{11} contours on the DCB specimen after it was fully unloaded are presented in Figure 8.12. The specimen exhibited zero stress except for residual stress contours exhibited in the region between the initial and final crack tip locations. This residual stress was resulted from crack propagation from the initial crack tip to the final crack tip location when maximum opening displacement of 25.4 mm was applied. However, the values of this residual stress were insignificant and ranged between -3.25 MPa and 3.0 MPa, except for the segment of the bottom PMC arm that located adjacent to the crack plane. σ_{11} at this location reached 21.1 MPa as shown in Figure 8.12.

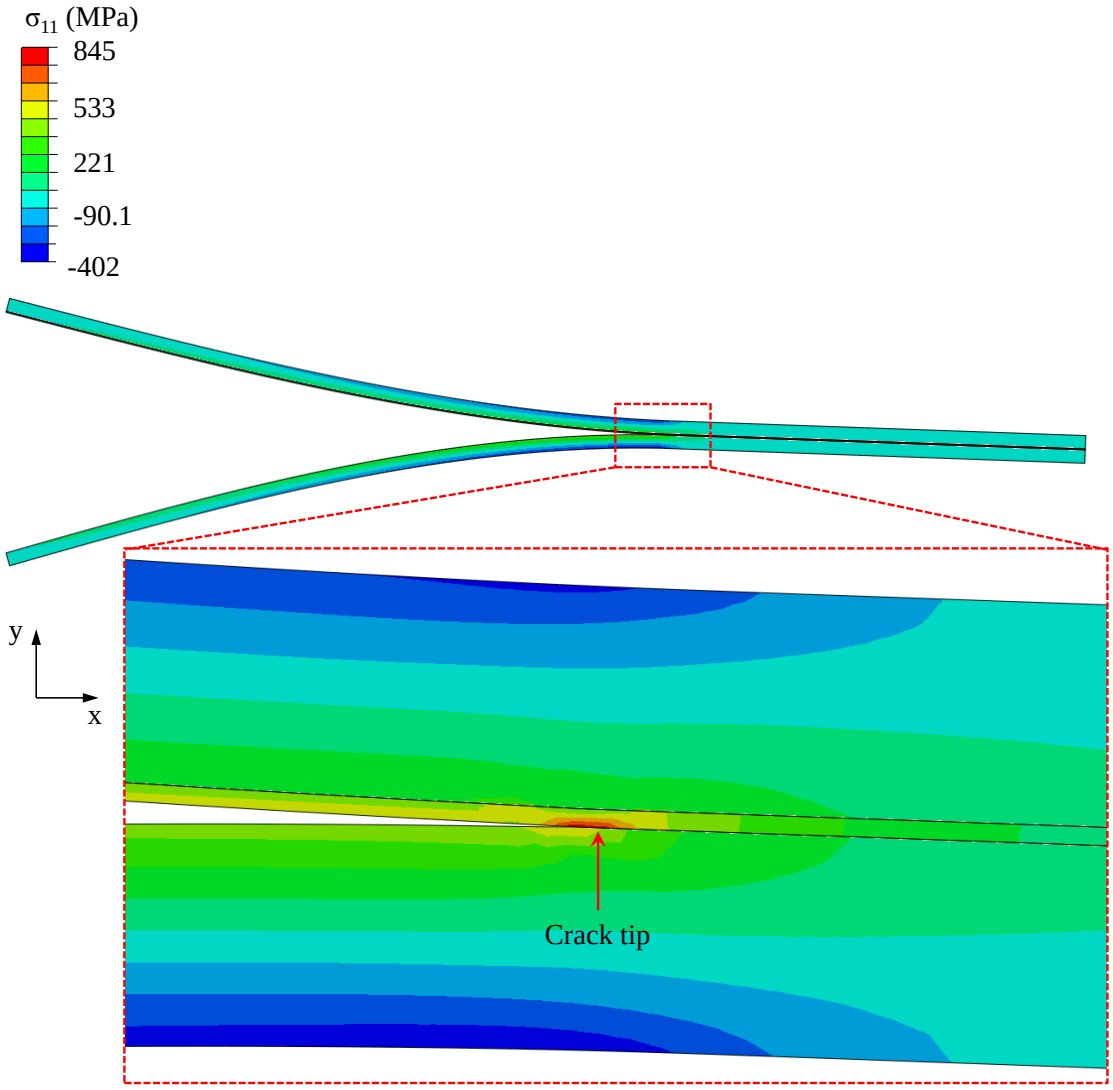

Figure 8.11: σ_{11} from the FEA without thermal residual stress before unloading (when maximum displacement was applied).

Besides what was observed from the load-displacement response, the effect of thermal residual stress due to curing are evidenced from the observations of the displacement and stress contours. Figure 8.13 shows displacement contour images obtained from the FEA with consideration of thermal residual stress that are in

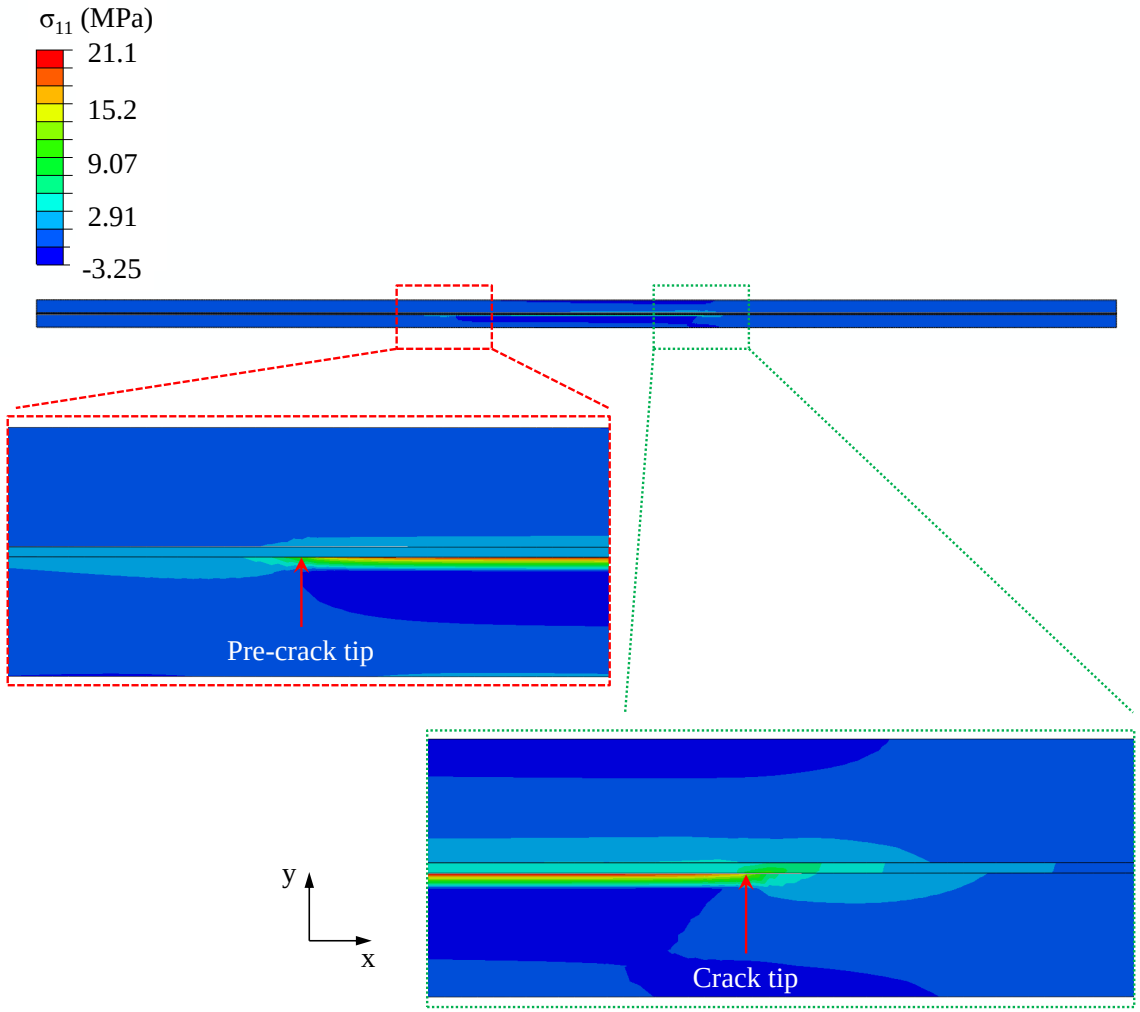

Figure 8.12: σ_{11} from the FEA without thermal residual stress after the specimen was fully unloaded.

agreement with the observation of the real DCB specimen. After cooling from the curing temperature, the specimen exhibited thermal warping in the delaminated segment due to asymmetry in the layup. The warped DCB before any external load was applied is shown in Figure 8.13(a). It should be noted that the DCB

specimen analyzed herein was PMC-Ti-PMC. As a result, it was symmetric about the mid-plane of the specimen, which is the mid-plane of the Ti foil layer. This symmetry, however, was exhibited only in the undelaminated segment of the DCB. In the delaminated segment, due to the free surface at the crack plane, the top arm that contained the Ti foil and PMC layers was in asymmetric configuration. Consequently, after this asymmetric segment underwent thermal cooling, it exhibited thermal warping.

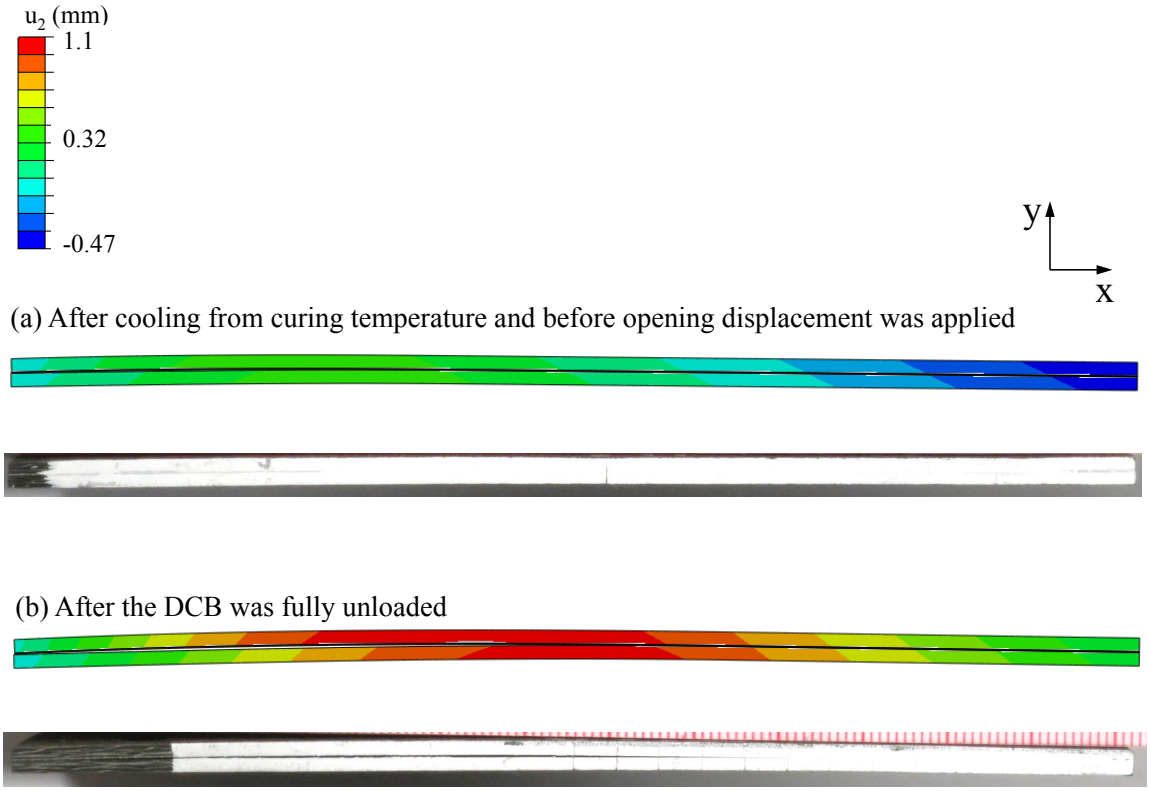

Figure 8.13: Effect of thermal residual stress on DCB beam warping.

The warping in the DCB became more pronounced after an opening displace-

ment of 25.4 mm was applied to the specimen followed by fully unloading to zero displacement. This warping is demonstrated in Figure 8.13(b). At this instant, the crack had propagated and the crack tip located 30 mm away from the initial crack tip. Because of that, the delaminated segment of the DCB shown in Figure 8.13(b) was longer than that presented in Figure 8.13(a). As a result, the warped segment of the DCB in Figure 8.13(b) was longer, hence, the curvature was more visual. This is in agreement with ultrasonic B-scan analysis results presented in section 6. In addition, the gap between the arms where the crack located in the DCB was higher in Figure 8.13(b) as observed from both the FEA displacement contour and image of the real specimen.

σ_{11} contours on the DCB in the FEA with consideration of thermal residual stress due to curing are presented in Figure 8.14. After undergoing constrained cooling from the curing temperature at 644 K, the specimen exhibited thermal residual stress due to cooling. The σ_{11} contours developed in the DCB due to cooling are presented in Figure 8.14(a) where the specimen was in a straight and flat configuration because of the applied constraints. As soon as these constraints were removed, the specimen became warped but the stress profiles remained the same. This is demonstrated in Figure 8.14(b).

It is observed that the PMC parts of the DCB exhibited compressive σ_{11} stress while σ_{11} in the Ti foil was tensile. The delaminated segment of the DCB exhibited inhomogeneous stress field due to thermal warping caused by asymmetric layup and the free surface in between the Ti foil and the bottom PMC part. The zoomed-in image in Figure 8.14(b) shows the σ_{11} field in the vicinity of the crack tip. Before any opening displacement was applied to the DCB, the Ti foil in the undelaminated segment exhibited σ_{11} of 340 MPa. This stress was developed during cooling due to the thermal coefficient mismatch between the Ti foil and PMC parts. Symmetric

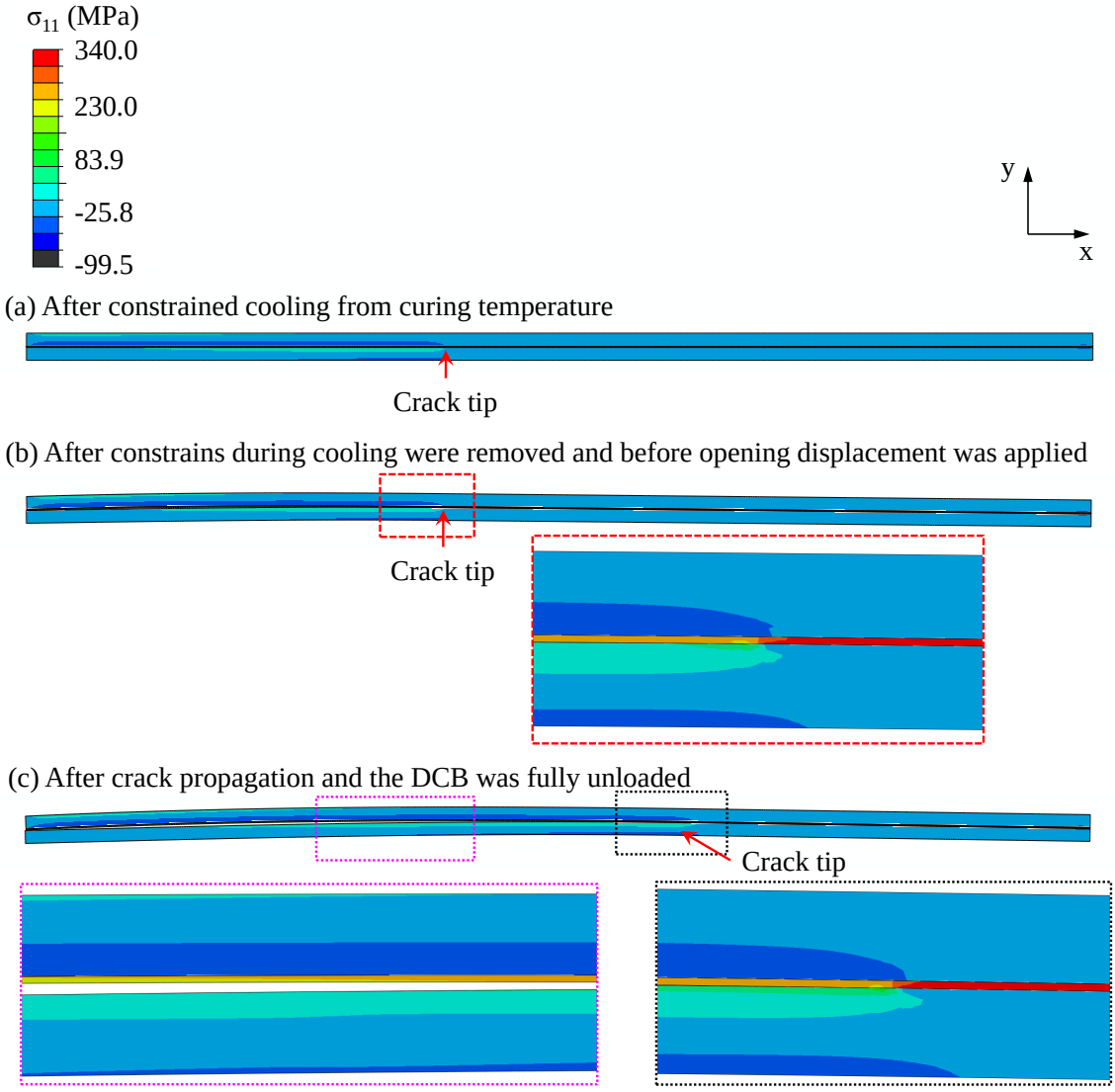

Figure 8.14: σ_{11} contours on the DCB (a) after the DCB underwent constrained cooling from the curing temperature at 644 K. (b) after removal of the constraints that were applied to the specimen during cooling and before opening displacement was applied to the DCB. (c) after an opening displacement of 25.4 mm was applied to the specimen followed by fully unloading to zero displacement.

stress profile with respect to the Ti foil neutral axis was observed on the undelaminated segment of the beam. As previously mentioned, the zoomed-in image in Figure

8.14(b) clearly shows inhomogeneous stress field in the delaminated segment of the DCB. The Ti foil in this segment exhibited a tensile σ_{11} value of 250 MPa. The PMC part bonded to the Ti foil, i.e. the top PMC part, displayed compressive stress in general. The magnitude of compressive σ_{11} on this top PMC part was higher at the location adjacent to the Ti foil. Near the free surface of this PMC part, i.e. vertically away from the Ti foil, tensile stress is observed because the curvature of this PMC segment was concave down. Similarly, in the bottom PMC part, due to thermal warping, the stress profile from the crack plane outward transitioned from tension to compression due to the concave-down curvature.

Figure 8.14(c) shows σ_{11} contours exhibited by the DCB after undergoing crack propagation as an opening displacement of 25.4 mm was applied followed by fully unloading. The stress profiles displayed on the DCB observed in this figure are similar to those presented and described in Figure 8.14(b). This similarity in stress field is dictated by the similar thermal warping curvature as discussed previously from observation of the displacement field presented in Figure 8.13.

Figure 8.15 shows the stress field at the analysis time when opening displacement of 25.4 mm was applied, i.e. immediately before the start of the unloading to zero displacement. The stress contours in Figure 8.15 is similar to what observed in Figure 8.11 that was obtained from the FEA without consideration of thermal residual stress. However, the magnitude of stress exhibited by the DCB in the FEA with thermal stress consideration shown in Figure 8.15 was higher. This is because the DCB whose results are shown in Figure 8.11 exhibited non-zero residual stress field prior to the application of opening displacement. The initial stress field at the start of the DCB loading step was presented in Figure 8.14(b). In contrast, in the FEA without thermal residual stress consideration whose stress contours were shown in Figure 8.11, before any opening displacement was applied, the DCB specimen exhibited

zero stress.

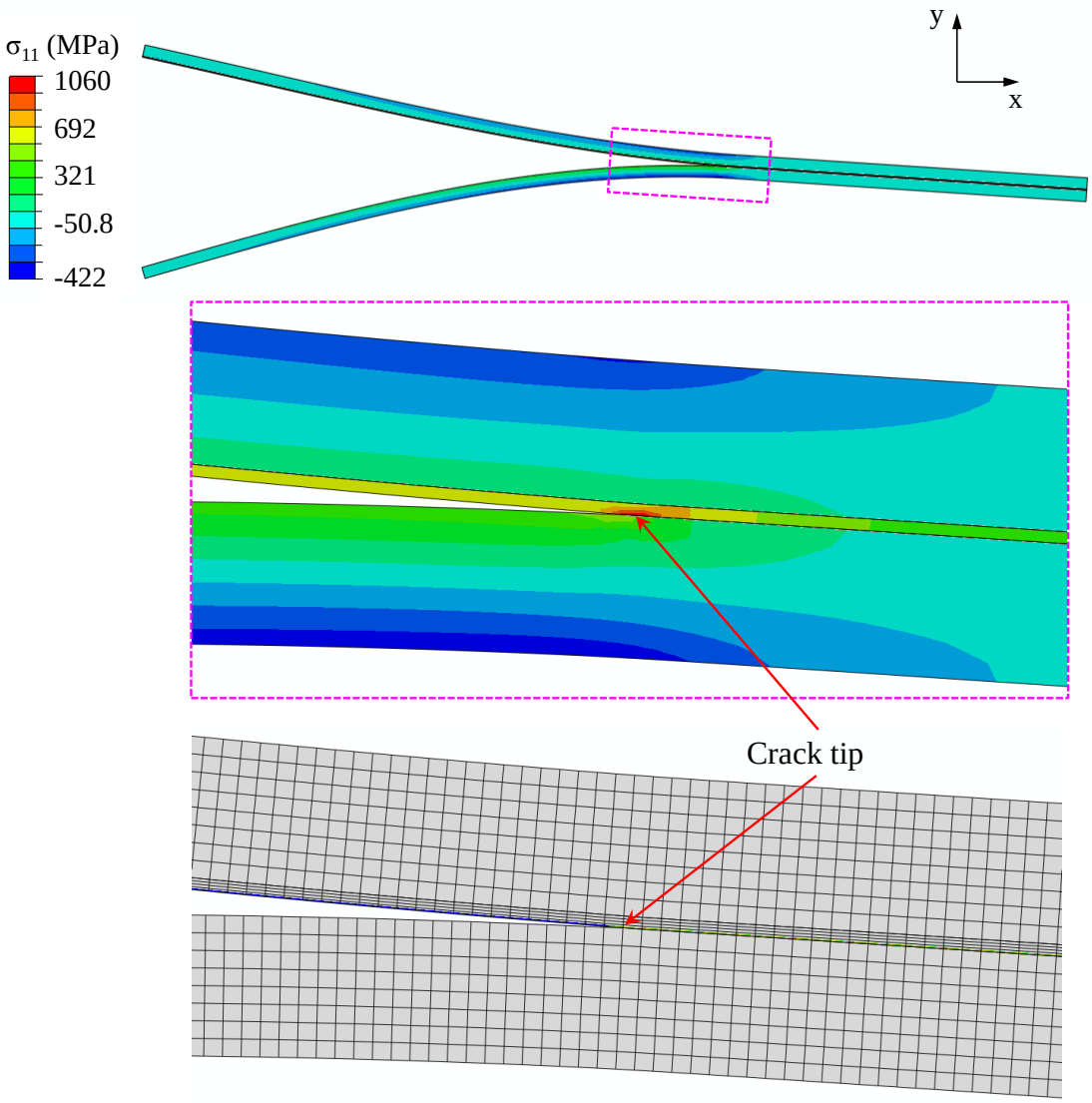

Figure 8.15: σ_{11} at analysis step when maximum opening displacement was applied. The stress field in this figure was obtained from the FEA with consideration of thermal residual stress due to curing.

8.2.2.2 Effect of Critical Mode I Strain Energy Release Rate Input

Figure 8.16 shows comparison of load-displacement response obtained from experiment and FEA with and without thermal residual stress consideration and with two different values of mode I critical strain energy release rate (G_{IC}). It should be noted from the FE analyses with residual stress consideration, before opening displacement was applied, the DCB specimen was subjected to a reaction force of approximately 10 N as a result of cooling from the curing temperature at 644 K. The load-displacement curves from FE analysis with residual stress shown in Figure 8.16 were shifted along the y-axis such that the specimen was subject to zero load at zero applied displacement.

For both cases where the analyses were carried out with and without residual stress, the use of two different G_{IC} input values resulted in load-displacement responses that had the same initial stiffness. When a higher G_{IC} was used, the softening segment of the load-displacement curve occurred at a higher load level compared to that of the load-displacement curve obtained from FEA in which a lower G_{IC} was use. This is because more energy was required to propagate the crack when a higher critical energy release rate was used as input for the VCCT criterion. The input G_{IC} values were obtained experimentally as presented in section 6 where the initiation and propagation fracture toughness was 893 J/m^2 and 945 J/m^2, respectively.

Comparing the shifted load-displacement curves obtained from FEA with residual stress to those obtained from FEA without residual stress, it is observed that the slopes of the former curves were in closer agreement with the experimental curves. In addition, the softening segments of the FEA without consideration of residual stress occurred at the upper bound of the experimental results. On the other hand, after being shifted to start at the origin, the softening segments of the curves obtained

from FEA with residual stress consideration occurred at the lower bound of the experimental curves. Furthermore, the shifted load-displacement curves from FEA with residual stress showed that upon unloading, the specimen was subjected to non-zero displacement at zero applied load. This is supported by the observation of the experimental load-displacement responses shown in Figure 8.16.

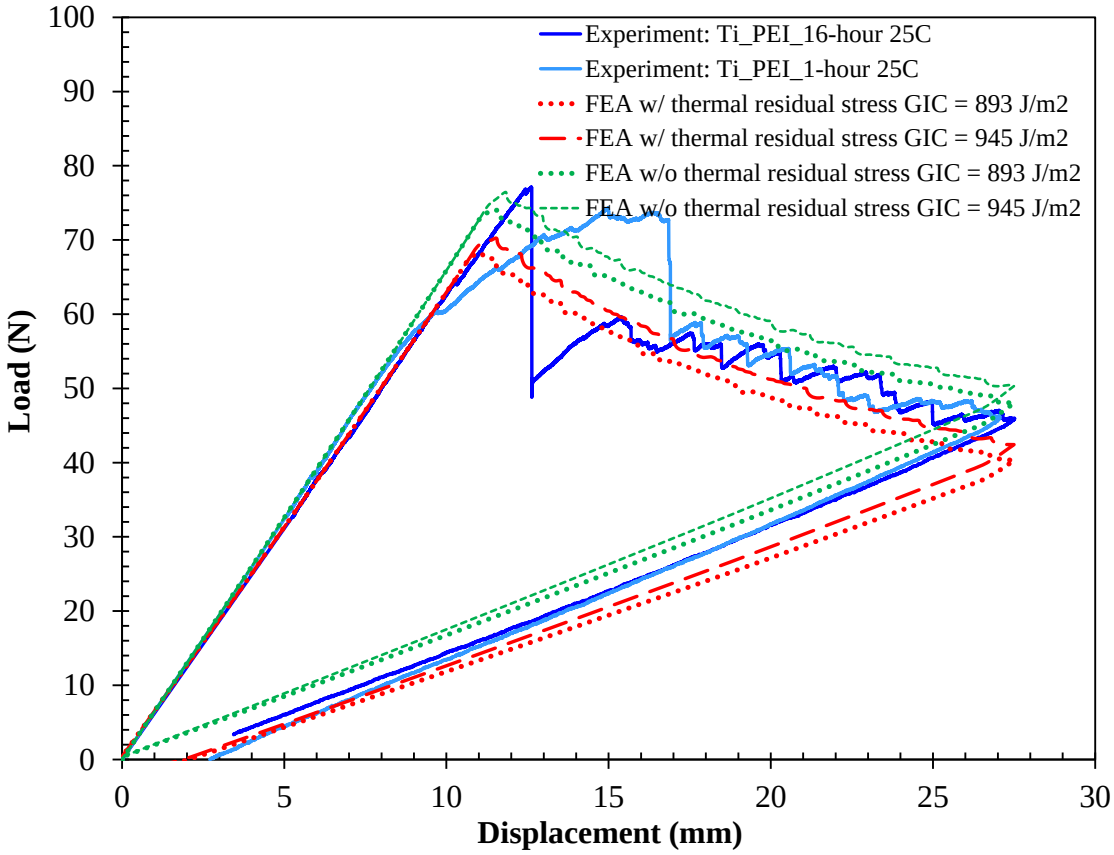

Figure 8.16: The effect of G_{IC} on load-displacement response from FE analysis of the hybrid DCB with and without consideration of thermal residual stress due to curing. Note that the load-displacement curves from FE analysis with residual stress were shifted along the y-axis such that the specimen was subject to zero load at zero applied displacement.

8.2.2.3 Summary and Discussions on FEA of DCB containing Ti−T650-8HS/AFR-PE-4 Interface

In this section, FEA were carried out to model the DCB containing Ti−T650-8HS/AFR-PE-4 interface. The effects of consideration of thermal residual stress due to curing on the load-displacement response, stress and displacement fields exhibited on the DCB specimen were investigated. In addition, the effect of using different values of mode I critical strain energy release rate (G_{IC}) as input for the VCCT criterion that modeled crack propagation was studied.

Table 8.5: Summary of Δa values from FE analysis with and without consideration of thermal residual stress sure to curing. Crack extension presented in this table was obtained at the end of the FE analysis, i.e. after the crack propagated from the initial crack as opening displacement of 25.4 mm was applied.

Critical mode I strain energy release rate	**Analysis case**	Δa (mm)
$G_{IC} = 945\ J/m^2$	with residual stress	29.56
	without residual stress	28.36
$G_{IC} = 893\ J/m^2$	with residual stress	30.76
	without residual stress	29.56

Regardless of the G_{IC} used in the analysis, it was observed that at the end of the analysis, when the DCB was fully unloaded from the maximum applied displacement of 25.4 mm to zero displacement, the FEA with consideration of residual stress shows that longer crack extension compared to that obtained from the FEA without residual

stress consideration. This is attributed to the initial strain energy stored in the DCB at the beginning of DCB loading step due to thermal warping in the FEA with residual stress. In addition, if a higher G_{IC} was used, the amount of crack extension at the same maximum applied displacement was less. This is because at the same applied load and displacement level, the use of a higher critical energy release rate value caused the crack to propagate less since higher energy is needed to overcome the critical value in order for the crack to grow. Summary of crack extension obtained from FEA where 893 J/m^2 or 945 J/m^2 were used as G_{IC} and FEA with and without residual stress consideration is presented in Table 8.5.

Table 8.6 shows summary of σ_{11} values in the Ti foil layer from the FEA with and without consideration of thermal residual stress sure to curing. Since similar trends were obtained from FEA where $G_{IC} = 893$ J/m^2 or 945 J/m^2 was used, the results reported in Table 8.6 were obtained from the analyses with $G_{IC} = 945$ J/m^2. The stress values presented in Table 8.6 were obtained from different analysis time steps as well as two locations with respect to the crack tip.

Table 8.6: Summary of σ_{11} values in the Ti foil layer from FE analysis with and without consideration of thermal residual stress sure to curing. The results reported in this table were obtained from analysis with $G_{IC} = 945\ J/m^2$.

Analysis case	**Analysis time**[1]	**Location with respect to crack tip**[2]	σ_{11} (MPa)
Without residual stress	before unload	ahead	410.0
		4 mm	60.4
	after unload	ahead	97.0
		4 mm	0.7
With residual stress	before load	ahead	304.0
		4 mm	308.4
	before unload	ahead	736.0
		4 mm	362.0
	after unload	ahead	288.0
		4 mm	310.0

[1]before load: at the beginning of DCB loading step (after the thermal cooling and removal of constraints during cooling),
before unload: at the beginning of the DCB unloading step,
after unload: at the end the DCB unloading step

[2]ahead: at location immediately ahead of crack tip,
4 mm: at location 4 mm away from the crack tip, in the undelaminated segment of the DCB

8.3 Analysis of Double Cantilever Beam containing NiTi−T650-8HS/AFR-PE-4 Interface: Observation of Phase Transformation in NiTi Foil upon Crack Propagation

8.3.1 Model Descriptions

It was observed experimentally and presented in section 6 that at room temperature, phase transformation occurred in the NiTi foil upon crack propagation at the hybrid NiTi−T650-8HS/AFR-PE-4 interface. In this section, finite element analyses of the DCB containing NiTi−T650-8HS/AFR-PE-4 interface were carried out to investigate the evolution of this phase transformation during crack growth. The model geometry, analysis steps, boundary conditions and meshing of the FEA carried out in this section were identical to that of the model described in Section 8.2. Material homogenized linear elastic properties of the PMC layers were presented in Table .

Nonlinear isotropic material properties were used for the NiTi foil. A user material subroutine (UMAT) defining the nonlinear behavior of SMA based on the constitutive relations developed by Lagoudas *et al.* was used [73]. The material properties of NiTi foil used in the FE analysis reported in this section are similar to those reported in Table 3.2 except for the transformation temperature values. These values were obtained via differential scanning calorimetry (DSC) measurement as reported in Section 5.3.2. The thermal-mechanical properties of NiTi foil used in the FEA in this section are summarized in Table 8.7.

During preliminary analysis, it was found that the use of incompatible linear plane strain (CPE4I) elements for the NiTi layer encountered convergent difficulties. As a result, the reduced integration linear plane strain (CPE4R) elements with hourglass stiffness control was used for the NiTi layer to facilitate numerical convergence. The hourglass stiffness value used in this work was identical to the austenitic modulus

(E^A) of the NiTi foil presented in Table 8.7. As reported in Figure 6.35, the critical mode I strain energy release rate used as input for the VCCT model of NiTi−T650-8HS/AFR-PE-4 interface in this section was either the initiation toughness (455 J/m^2) or propagation toughness (810 J/m^2).

Table 8.7: Thermal-mechanical properties of NiTi foil in FEA of DCB containing NiTi−T650-8HS/AFR-PE-4 interface

E^A (GPa)	32.5
E^M (GPa)	23.0
M_s (K)	264
M_f (K)	160
A_s (K)	217
A_f (K)	290
$\nu_A = \nu_M$	0.33
$C_A = C_M$ (MPa/K)	3.5
α_A ($1/^oC$)	32.0 x 10^{-6}
α_M ($1/^oC$)	21.0 x 10^{-6}

8.3.2 Results and Discussion

Figure 8.17 shows the load-displacement response from experiment in comparison to that obtained from the FEA of the hybrid DCB containing NiTi−T650-8HS/AFR-PE-4 interface with and without consideration of thermal residual stress due to curing. Both the original and shifted load-displacement curves from the FEA with consideration of thermal residual stress are presented in Figure 8.17. After undergoing thermal cooling and release of cooling constraint, the reaction force the specimen experienced was approximately 3 N. This is associated with thermal warping of the hybrid DCB containing NiTi−T650-8HS/AFR-PE-4 interface. However, this thermal warping is less significant compared to the DCB containing Ti−T650-8HS/AFR-

PE-4 interface analyzed and presented in Section 8.2. It should be noted that both the NiTi−T650-8HS/AFR-PE-4 and Ti−T650-8HS/AFR-PE-4 interfaces underwent the same thermal cooling since the same curing temperature was used. However, the mismatch between coefficients of thermal expansion (CTEs) of NiTi and PMC layers is less significant than that of Ti and PMC. The difference in warping curvature between the two FEA results for NiTi−T650-8HS/AFR-PE-4 and Ti−T650-8HS/AFR-PE-4 interfaces is supported by the observation of ultrasonic B-scan analyses of the Ti_PEI_16-hour and NiTi_PEI_16-hour specimens presented in section 6.

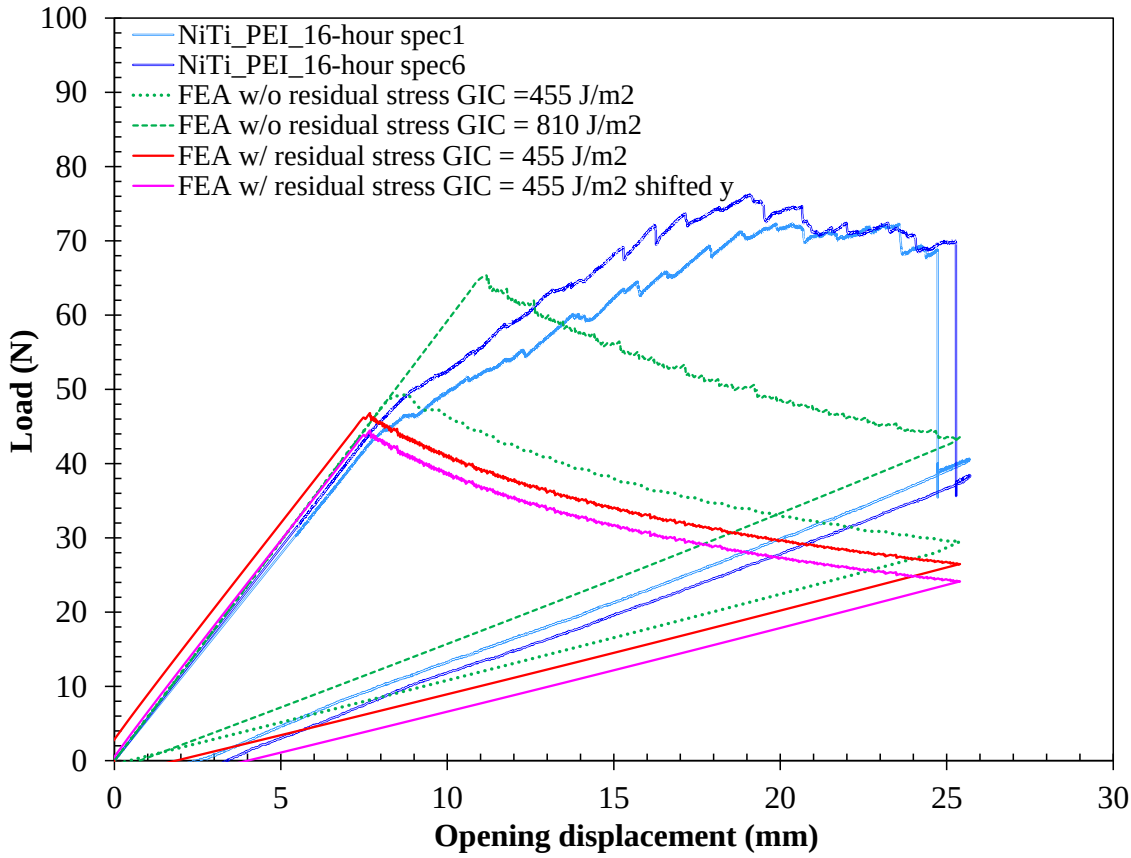

Figure 8.17: Load-displacement response from FE analysis of the hybrid DCB containing NiTi−T650-8HS/AFR-PE-4 interface with and without consideration of thermal residual stress due to curing.

The load-displacement curves obtained from FEA exhibited the initial slopes that are in good agreement with that of the experimental curves. It is observed that when the initiation fracture toughness value was used as G_{IC} in the FEA, the load and displacement at which the deviation from linearity occurred in the experiment were closely captured by the FEA. This deviation from linearity is associated with crack initiation and propagation from the initial crack tip. Beyond this deviation from linearity, the softening segment of the FEA load-displacement curves exhibited standard softening behavior as the crack propagated. This is in contrast with what observed from the experimental load-displacement curves, which exhibited toughening behavior. This toughening behavior could be attributed to the crack changing interfaces as the crack migrated from a location adjacent to the NiTi foil to into the first fabric layer next to the foil. This was discussed in section 6. The crack changing interfaces behavior is not modeled in this work. As a result, there is a discrepancy in the results obtained from experiment and FEA for the load-displacement response segment that associated with crack propagation.

Similar to the results presented in Section 8.2 for Ti−T650-8HS/AFR-PE-4 interface, the shifted load-displacement curve from the FEA with consideration of thermal residual stress show that as the specimen was fully unloaded, at zero load, the specimen exhibited non-zero displacement. This non-zero displacement value obtained from the FEA is in agreement with the experimental value.

Figure 8.18 and 8.19 show the evolution of martensitic volume fraction (MVF) during phase transformation occurring in the NiTi foil of the hybrid DCB containing NiTi−T650-8HS/AFR-PE-4 interface. The MVF profiles presented in Figure 8.18 and 8.19 were obtained from the FEA without consideration of thermal residual stress due to curing and $G_{IC} = 810\ J/m^2$ and $455\ J/m^2$, respectively. It is observed that as opening displacement was applied to the specimen, due to stress concentration near

the crack tip, the NiTi foil underwent stress-induced phase transformation in the crack tip vicinity. Prior to crack propagation, as higher displacement was applied, the NiTi foil transformed more near the crack tip. As the crack propagated, the transformed area of the NiTi foil also expanded with the movement of the crack tip. In the analysis where G_{IC} value of 810 J/m^2 was used, the maximum MVF value the specimen exhibited in the analysis was 12.6% as shown in Figure 8.18. Figure 8.19 shows that when the critical mode I strain energy release rate of 455 J/m^2 was used as input, the NiTi exhibited a maximum MVF of 6.5%. Maximum in-plane principal stress contour from this analysis is also presented in Figure 8.19. The maximum stress at the concentration site near the crack tip was 340 MPa. The reason for a lower value of MVF obtained from the FEA where $G_{IC} = 455\ J/m^2$ compared to that of the FEA with $G_{IC} = 810\ J/m^2$ is that for the former case, since a lower critical energy release rate was used, less energy was required to propagate the crack. As a result, the crack growth occurred at a lower applied load level. Consequently, the specimen experienced lower stress level and thus stress-induced phase transformation was less pronounced.

Figure 8.20 demonstrates the evolution of martensitic volume fraction during phase transformation occurring in the NiTi foil of the hybrid DCB containing NiTi−T650-8HS/AFR-PE-4 interface in the FEA with $G_{IC} = 455\ J/m^2$ and thermal residual stress due to curing was considered. Similar behavior as that described in Figure 8.18 was observed here. However, it should be noted that upon constrained cooling from the curing temperature, the NiTi foil underwent stress-induced phase transformation exhibited an MVF of 25 % prior to application of opening displacement or external load. As the crack propagated, the maximum MVF the foil displayed was approximately 35 %. The stress contour presented in Figure 8.21(b) shows that the NiTi foil exhibited a residual stress of 125 MPa due to curing. The profile of stress

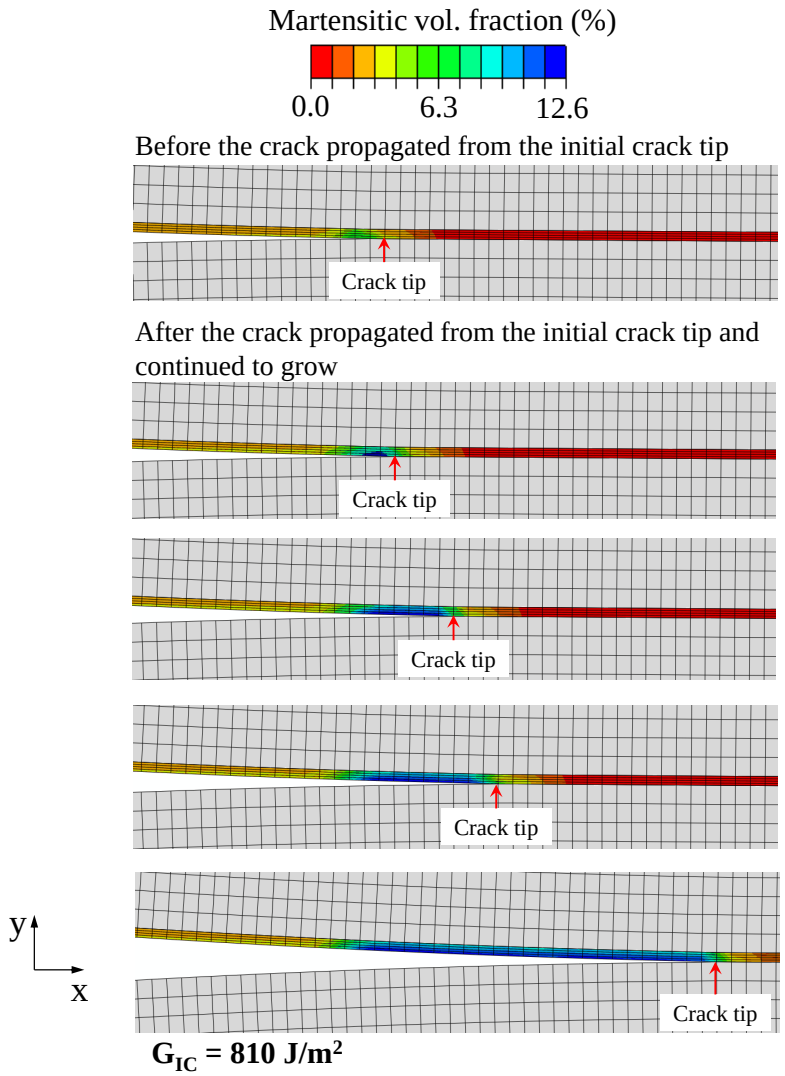

Figure 8.18: Evolution of martensitic volume fraction during phase transformation occurring in the NiTi foil of the hybrid DCB containing NiTi−T650-8HS/AFR-PE-4 interface. Analysis was performed without consideration of thermal residual stress due to curing and $G_{IC} = 810\ J/m^2$.

exhibited in the NiTi foil in the delaminated segment from the initial to the current crack tip locations are in agreement with the MVF profile shown in Figure 8.21(a).

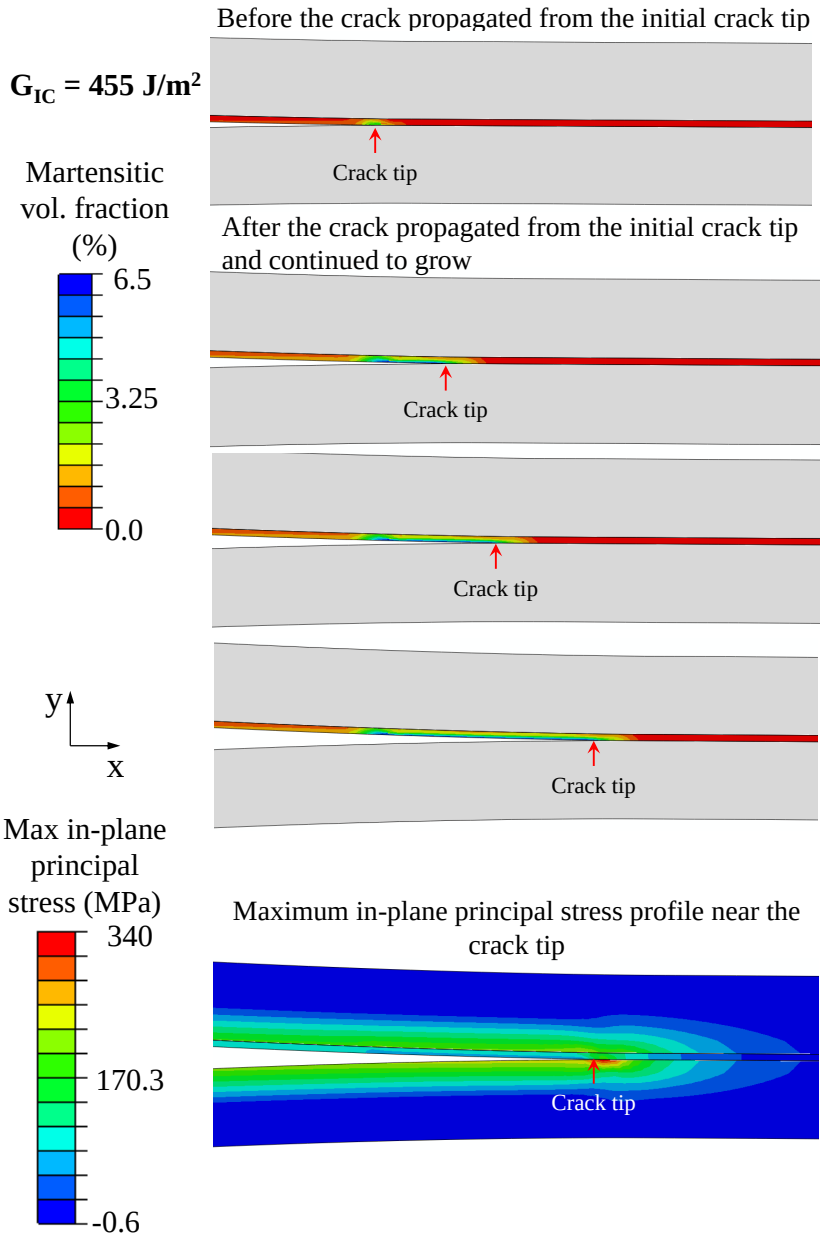

Figure 8.19: Evolution of martensitic volume fraction during phase transformation occurring in the NiTi foil of the hybrid DCB containing NiTi−T650-8HS/AFR-PE-4 interface. Analysis was performed without consideration of thermal residual stress due to curing and $G_{IC} = 455\ J/m^2$.

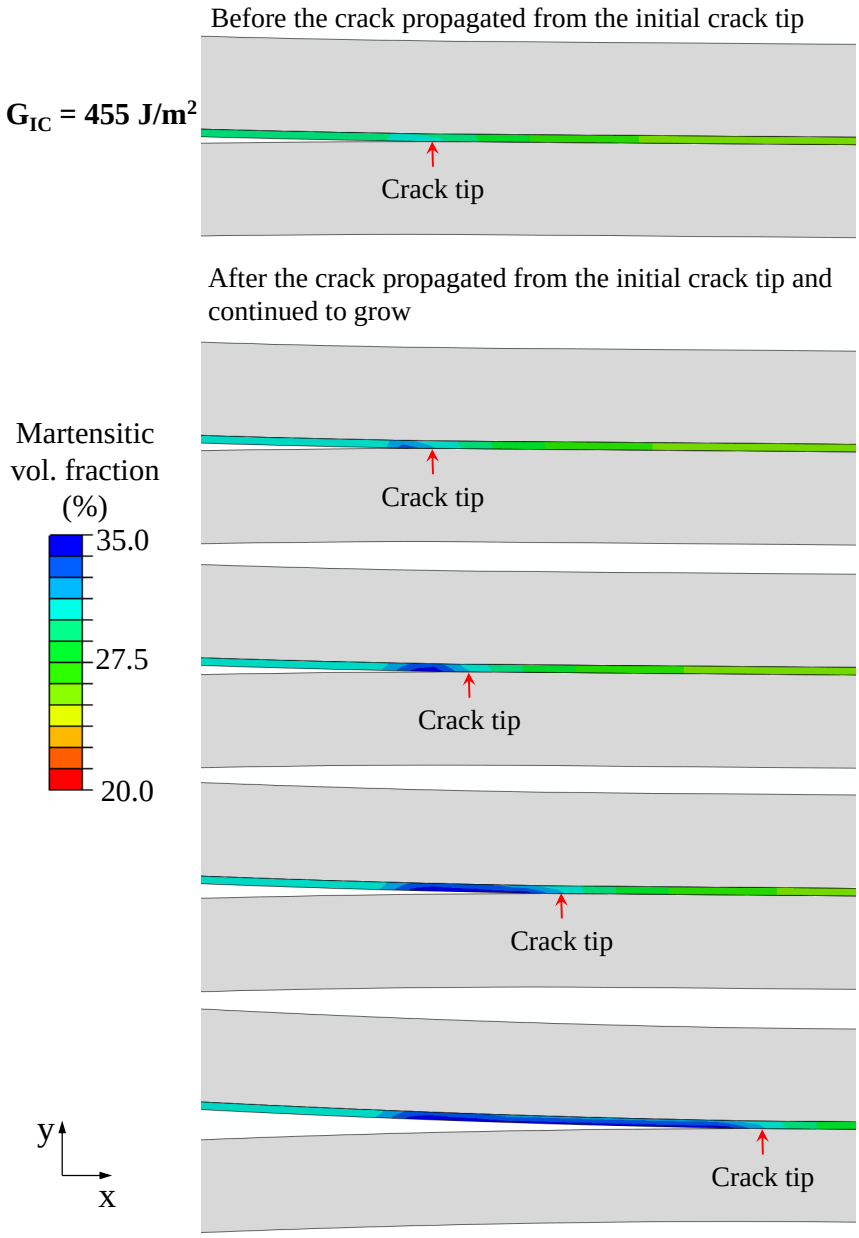

Figure 8.20: Evolution of martensitic volume fraction during phase transformation occurring in the NiTi foil of the hybrid DCB containing NiTi−T650-8HS/AFR-PE-4 interface. Analysis was performed with consideration of thermal residual stress due to curing and $G_{IC} = 455\ J/m^2$.

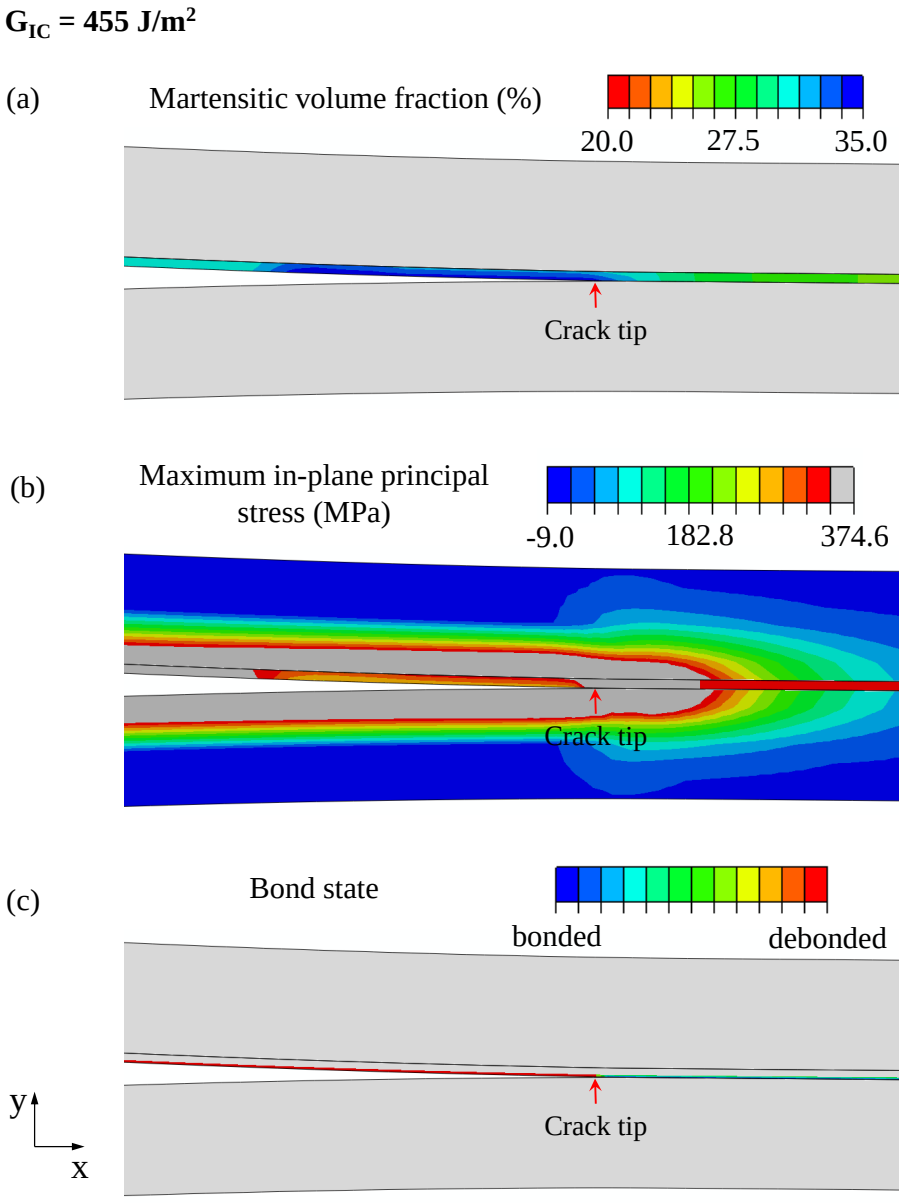

Figure 8.21: FEA results of the hybrid DCB containing NiTi−T650-8HS/AFR-PE-4 interface (a) Martensitic volume fraction during phase transformation occurring in the NiTi foil. (b) Maximum in-plane principal stress. (c) Bond state contour indicating the location of the crack tip. All contour plots in this figure were obtained at the same analysis time frame. Analysis was performed with consideration of thermal residual stress due to curing and $G_{IC} = 455\ J/m^2$.

9. MICRO-SCALE FINITE ELEMENT ANALYSES: THE EFFECT OF PATTERNED SURFACE ROUGHNESS

It is important to understand the effects of micro-scale surface roughness pattern created by laser ablation of the Ti and NiTi surfaces on the adhesion strength of ablated metallic surfaces with thermosetting polymer matrix. The effects of laser ablated micro-roughness on fracture behavior of the hybrid interface were investigated via finite element tools. The approach and results are presented herein.

9.1 Model Descriptions

Extended finite element method (XFEM) was used to model crack initiation and propagation at the hybrid interface. The microscale model simulating the ablation pattern was performed for hybrid interface between titanium and AFR-PE-4. The geometry of the laser ablated pattern was obtained from SEM images as shown in Figure 9.1.

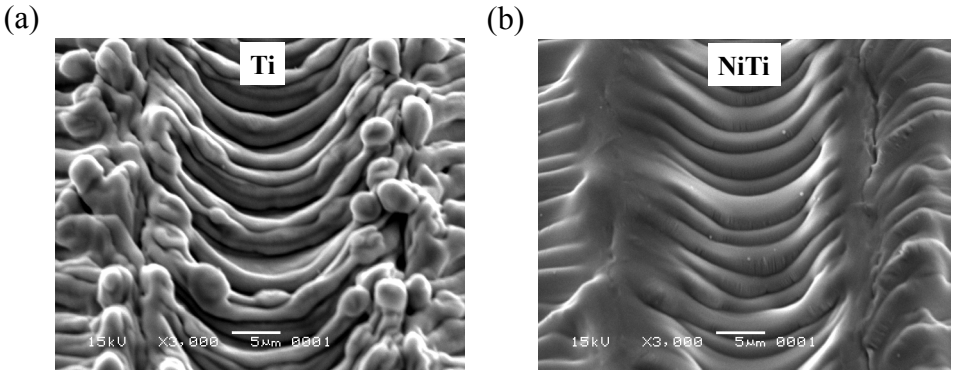

Figure 9.1: Laser ablated surfaces of (a) Ti (b) NiTi.

The interface between Ti and AFR-PE-4 resin as highlighted in blue on Figure 9.2(a) was assumed to be perfectly bonded. To model failure initiated in the AFR-PE-4 layer, this part was meshed with enriched finite elements. When the maximum principal in-plane stress in an element exceeds the tensile strength of AFR-PE-4 matrix, a crack was initiated inside that element. B-K mixed mode fracture criterion [111, 110] was assigned to model crack propagation. Thus, after initiation of the crack by XFEM, the crack propagated when the B-K fracture criterion was met. Four-node linear plane strain (CPE4) elements were used in the entire model.

Table 9.1: Material parameters used in XFEM microscale model

AFR-PE-4 matrix [53]	
E	3393.00 MPa
ν	0.33
σ_{ut}	72.05 MPa
G_{IC}=G_{IIC}	6.688 J/m^2
Titanium	
E	102000.00 MPa
ν	0.34

9.2 Boundary Conditions

To calibrate the cohesive zone parameters for mode I fracture analysis, the model was carried out with tensile loading boundary conditions as illustrated in Figure 9.2(b).

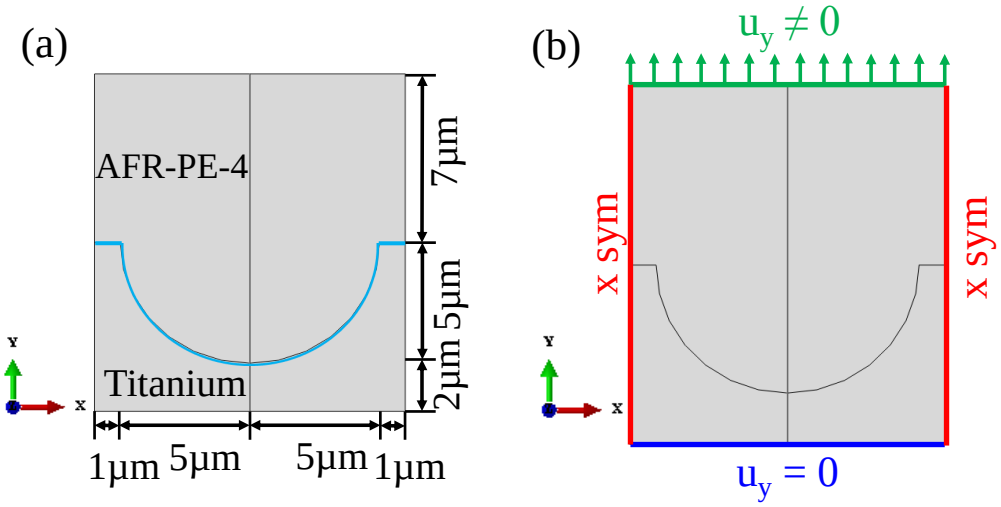

Figure 9.2: (a) Geometry of the model with interface highlighted in blue (b) Boundary condition in tensile loading case

9.3 Results and Discussion

The traction-separation from the tensile loading case was obtained and can be used to generate the mode-I parameters for the bilinear cohesive laws that govern the behavior of hybrid interfaces at the macroscale. Load-displacement results from this microscale FE analysis is presented in Figure 9.3. The results for the tensile loading case show that the crack was initiated in the polymer layer due to stress concentration created by the surface roughness pattern. As the crack propagated, it remained inside the polyimide layer without any sign of deflection to the interface with titanium, which is highlighted by the light blue curves. This lead to cohesive failure inside the polymer matrix. In Figure 9.4 (b) and (c), results for STATUSXFEM, status of an enriched element, are shown. The status of an enriched element was 1.0 if the element is completely cracked and 0.0 if the element contains no crack. If the element was partially cracked, the value of STATUSXFEM were between 1.0 and 0.0. Figure 9.5 shows evidence of microcrack formation during the fracture process

as observed experimentally on the fracture surface. These microcracks were formed on top of each laser ablation pattern due to stress concentration.

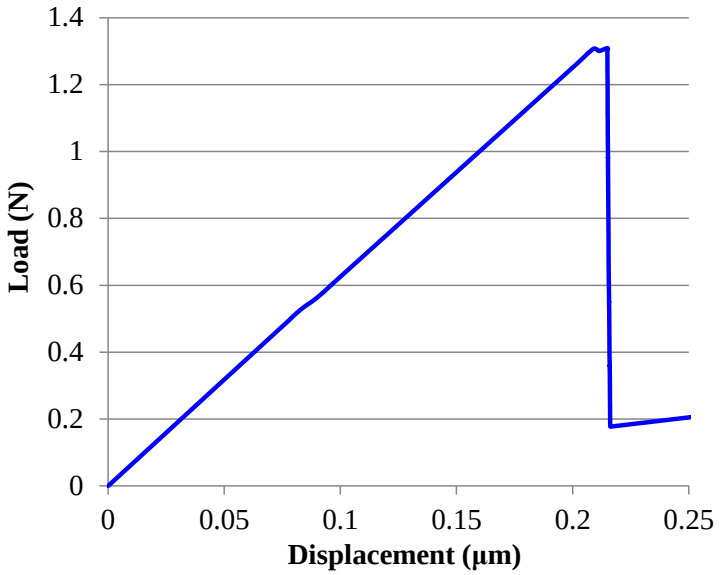

Figure 9.3: Load-displacement results from microscale FEA model. Tension boundary conditions were applied.

9.4 Summary

In this section, it was computationally proved that microscale surface roughness pattern created by laser ablation had an influence on the fracture behavior of the hybrid interface. Stress concentration sites induced by the presence of the regular roughness pattern caused the microcrack to initiated once the stress reached maximum allowable value of the polymer matrix. It should be noted that in the current model, the interface between the Ti ablated pattern and AFR-PE-4 resin was modeled as perfectly bonded. As such, the crack initiation and propagation was only

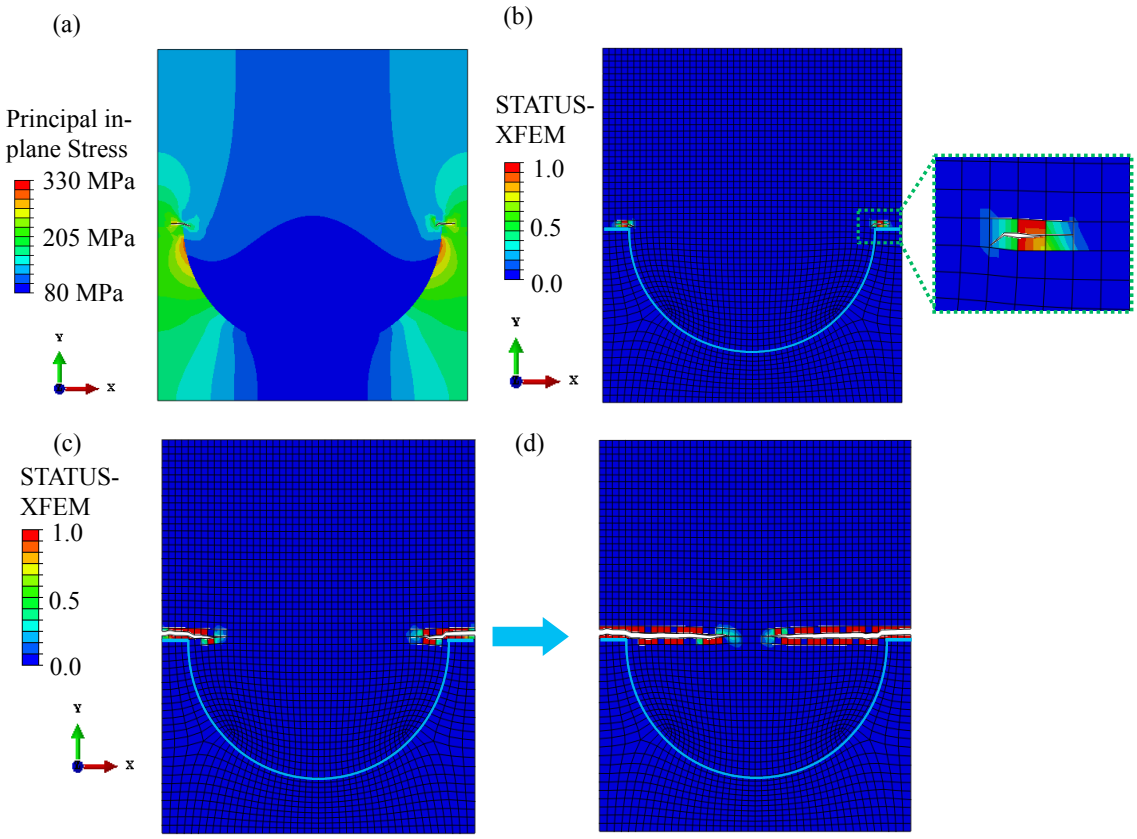

Figure 9.4: (a) Principal in-plane stress (b) - (d) Status XFEM variable status of the enriched element as the crack initiated and propagated in the AFR-PE-4 layer.

allowed in the enriched XFEM region, i.e. the polymer layer. This metal-resin interface could be modeled using cohesive elements or surface-based cohesive zone to study the effect of different interfacial adhesion strength on the overall response of hybrid interfacial region represented in this work. The competition between cohesive and adhesive failure of the laser-ablated interface could also be investigated. The effect of elevated temperature as well as different micro roughness pattern sizes and geometries on the performance of this interface are also of siginificant interest and importance. In addition, for future work, XFEM analyses should also be carried out for the shear loading case to study the effect of mode II loading configuration.

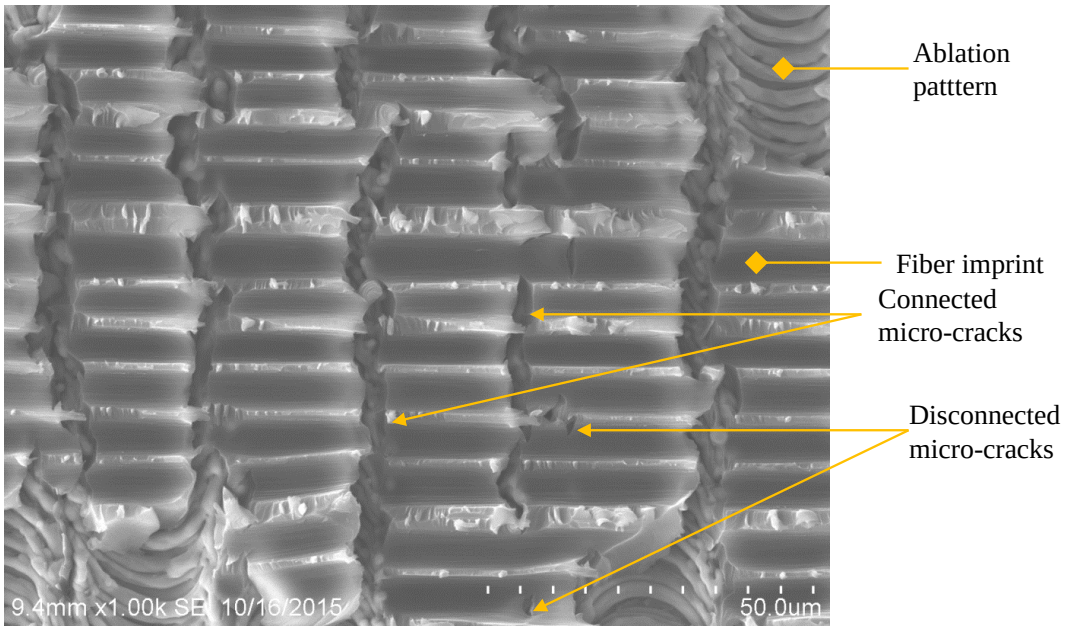

Figure 9.5: SEM image of microcrack formation on the fracture surface due to stress-concentration on top of trough of each laser ablation pattern.

Furthermore, different pattern geometries and parameters can be modeled with finite element tools and their effects on fracture behavior of the hybrid interface could investigated. Results from this work can help guide the design of laser ablated pattern and adjustment of ablation parameters to facilitate the creation of strong hybrid interfaces.

10. CONCLUSIONS AND RECOMMENDATIONS

10.1 Concluding Remarks

In this work, hybrid composite laminates were successfully created using out-of-autoclave processing techniques. The laminates contained one single layer of metal foil sandwiched between a number (four or eight) of layers of carbon fabric reinforcement that created a symmetric layup with respect to the metal foil. In these hybrid laminates, the hybrid interfaces between metal and polymer composite were created via co-curing. Different metal foils, fabric reinforcement types and polymer matrix were investigated. In addition, a variety of surface treatment techniques were employed on the metal foil prior to placing in in the hybrid laminate layup. The fracture behavior of the fabricated hybrid interfaces was investigated at both room and elevated temperature. Furthermore, physical, thermal-mechanical as well as microscopy of the laminates were performed.

It was found that in order to create strong hybrid metal-resin interface, the surface chemistry on the metal side plays a significant role. Robust hybrid interfaces should be created via formation of covalent bonds at the interface region. This could be achieved via sol-gel surface treatment method as demonstrated in this work. Other important aspects of consideration include not only thermal degradation of the surface treatment but also the compatibility of the sol-gel chemistry with the polymer resin.

It was shown in this work that the fracture behavior of the hybrid interfaces depends not only on the properties of polymer resin, which dictate whether the crack propagates in a stable or unstable manner, or whether the hybrid interface exhibits brittle or ductile-like failure, but also the architecture of the reinforcement

in the composite. Moreover, the loading configuration also has an important impact on the mode of failure at these hybrid interfaces. It was shown in sections 6 and 7 that the same hybrid interface (Ti_PEI_1-hour) that exhibits cohesive failure mode after the mode I fracture toughness test failed adhesively under mode II loading. In addition, surface roughness or architecture of metallic surface played an important role. Fracture toughness could be higher where rougher metallic surfaces are present at the hybrid interface. This is ascribed to the more energy released when microcracks formed during the fracture process due to stress concentration caused by the surface roughness.

One of the most significant contributions of this work is that for the first time, robust high temperature hybrid interfaces between metal (Ti)/shape memory alloy (NiTi) and polyimide matrix composite were successfully fabricated and tested. Laser ablation and a custom-synthesized sol-gel treatment was employed to prepare the Ti and NiTi foils surfaces for strong, direct adhesion with the polyimide AFR-PE-4 resin system. This high temperature interface could sustain temperature up to 250 ^oC. One interesting finding was revealed by SEM/EDS and nanoIR analysis of the hybrid interface cross-section where it was observed that Si from the sol-gel treatment solution clearly penetrated into the ablated Ti surface. This was attributed to the porosities on the Ti surface created during laser ablation. Evidence of covalent bonds formation between the sol-gel treatment solution and Ti foil was confirmed by nanoIR analysis. It was found that the degree of hydrolyzation of the custom-synthesized sol-gel treatment solution or the time associated with sol-gel hydrolysis was important. In this work, the best results were achieved with a 16 hour hydrolysis although further optimization could be possible.

It was also demonstrated in this work that in-situ Rayleigh backscattering fiber optics measurements were obtained during DCB experiments. This new technique

to measure distributed strains allows us to interprete the DCB experiment in a new way and enables the visualization of strain energy release upon crack propagation.

10.2 Recommendations

10.2.1 Contributions of in-situ DIC Measurements During DCB Testing

In-situ digital image correlation measurements were obtained in this work. Example of strain fields obtained from room temperature DCB test of non-hybrid T650/AFR-PE-4 specimen is presented in Figure 10.1. DIC results for displacement are much more reliable than the strain-field results. This is because although a standard DCB specimen size was prepared, the influence of edge-effect on the strain results could be significant. Thus, the strain field obtained at the edges of the specimen could be inaccurate. Thus, DIC displacement field could be used to validate the FEA results.

Girolamo *et al.* proposed a novel method that employed the DIC displacement field to calibrate cohesive zone parameters for finite element analysis. By using DIC analysis, the J-integral near the crack tip as a function of crack tip opening displacement could be obtained. Consequently, the traction-separation curve could be obtained and used to calibrate cohesive zone parameter [112]. However, the J-integral formula used Girolamo's work was derived for adhesive joint and symmetric DCB. For the current work, this formula is not applicable since asymmetry is presented in the hybrid DCB specimen where the crack propagates at a bi-material interface in sandwich configuration. Thus, a J-integral formula for asymmetric specimen for this method to be applicable. This is a future effort and could be a significant contribution to the research on hybrid interfaces both experimentally and computationally.

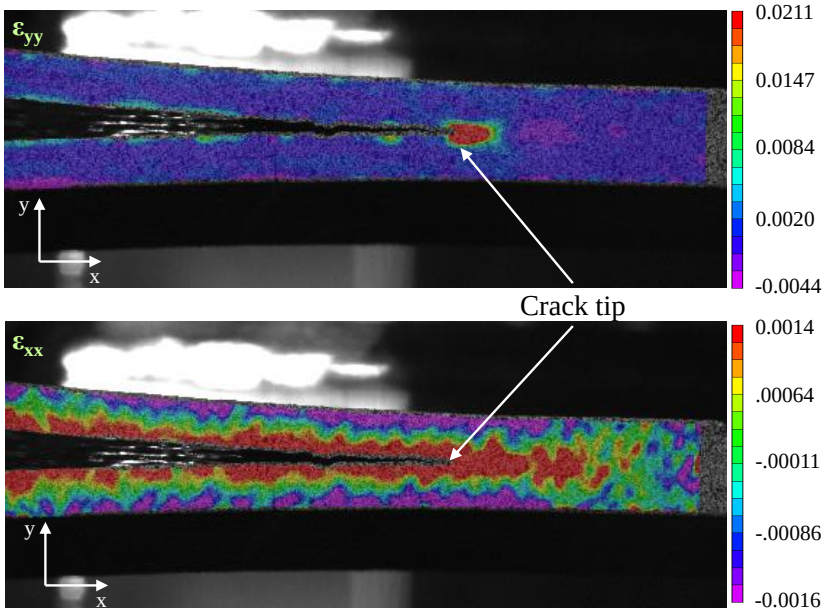

Figure 10.1: DIC strain fields obtained from room temperature DCB test of non-hybrid T650/AFR-PE-4 specimen.

10.2.2 Multi-scale Modeling of Hybrid Interfaces

As an attempt to create a cohesive linkage between the macroscale model presented in the previous FEA section and microscale model analyzed in this section, it is proposed herein a multiscale modeling scheme. Instead of utilizing the traction-separation curves and cohesive zones as the messenger between the two modeling scales, information from the microscale model can be transfered directly to the macroscale via sub-modeling technique. A microscale interfacial region similar to what analyzed in this section can be created and embedded at the crack tip in the macroscale model, i.e. the DCB or ENF model. The macroscale model is analyzed to provide the boundary conditions for the micro-scale model of the sub-region to be run. Various locations of the crack tip with respect to the interfacial architecture

features in the sub-region model can be used. VCCT technique can be employed to calculate strain energy release rate. Both the DCB and 4-ENF are analyzed to study the effects of mode-I and mode-II dominant loading conditions on the behavior at the hybrid interface where different interfacial architectures are present. This multiscale FEA scheme is illustrated in Figure 10.2.

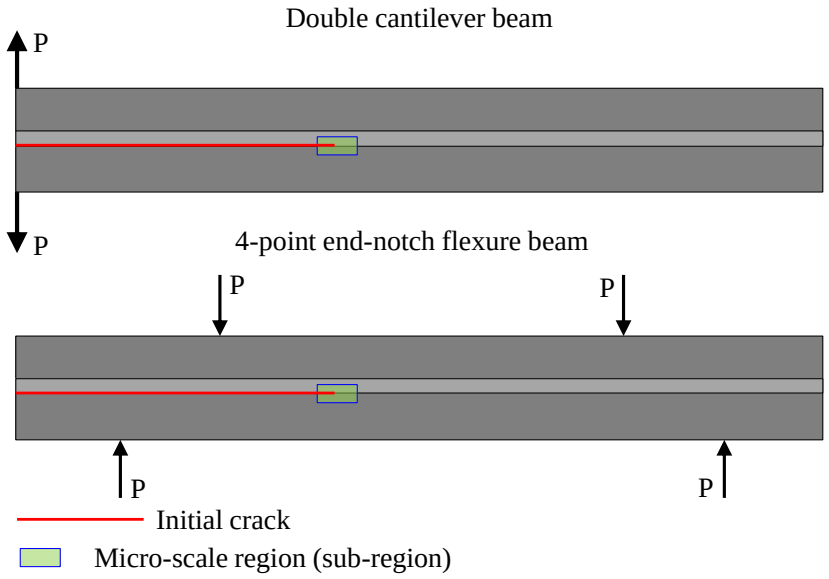

Figure 10.2: Schematic of boundary conditions on hybrid DCB and 4-ENF specimens with a micro-scale sub-modelling section at the crack tip.

Four different cases can be considered for the sub-region or the microscale region. They are illustrated in Figure 10.3 and described as follows.

- Case 1: flat metal surface, i.e. without ablation pattern. Properties of the composite in the model are homogenized, i.e. the effect of weave patterns are previously taken into account during homogenization.

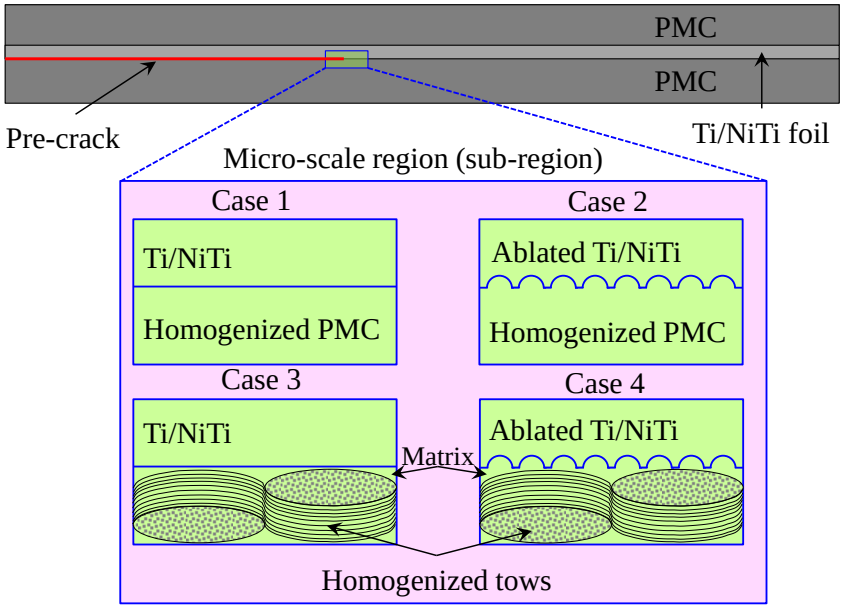

Figure 10.3: Detailed schematic of micro-scale submodel in multiscale FEA of hybrid DCB and 4-ENF specimens.

- Case 2: metal surface exhibiting ablation pattern. Properties of the composite in the model are homogenized.
- Case 3: flat metal surface, i.e. without ablation pattern. The weave pattern presented in the composite is considered and modelled in this case, where the tow properties are homogenized.
- Case 4: metal surface exhibiting ablation pattern. The weave pattern presented in the composite is considered and modelled in this case, where the tow properties are homogenized.

REFERENCES

[1] Yuntao Li. *Synthesis and cure characterization of high temperature polymers for aerospace applications*. PhD Dissertation, Texas A&M University, 2006.

[2] AC Long and LP Brown. Modelling the geometry of textile reinforcements for composites: Texgen. *Composite Reinforcements for Optimum Performance. Cambridge: Woodhead Publishing Ltd*, pages 239–64, 2011.

[3] Hieu TX Truong, Marcias J Martinez, Ozden O Ochoa, and Dimitris C Lagoudas. An investigation on hybrid interface using on-line monitoring experiment and finite element analyses. In *ICCM 20: 20th International Conference on Composite Materials, Copenhagen, Denmark, 19-24 July 2015*. ICCM, 2015.

[4] Lucio F Mondolfo. *Aluminum alloys: structure and properties*. Elsevier, 2013.

[5] John Whitcomb and Xiaodong Tang. Effective moduli of woven composites. *Journal of Composite Materials*, 35(23):2127–2144, 2001.

[6] Christoph Leyens and Manfred Peters. *Titanium and titanium alloys*. Wiley Online Library, 2003.

[7] Michel Barsoum and MW Barsoum. *Fundamentals of ceramics*. CRC press, 2002.

[8] W David Kingery. *Introduction to ceramics*. John Wiley & Sons, 1960.

[9] Michel W Barsoum and Tamer El-Raghy. The MAX phases: Unique new carbide and nitride materials-ternary ceramics turn out to be surprisingly soft and machinable, yet also heat-tolerant, strong and lightweight. *Am. Scientist*, 89(4):334–343, 2001.

[10] Miladin Radovic and Michel W Barsoum. MAX phases: bridging the gap between metals and ceramics. *American Ceramics Society Bulletin*, 92(3):20–27, 2013.

[11] Dimitris C Lagoudas. *Shape memory alloys: modeling and engineering applications*. Springer Science & Business Media, 2008.

[12] Vladimir Brailovski, SPTFT Prokoshkin, P Terriault, and F Trochu. *Shape memory alloys: fundamentals, modeling and applications*. École de technologie supérieure, 2003.

[13] Ankush Dilip Kothalkar, Rogelio Benitez, Liangfa Hu, Miladin Radovic, and Ibrahim Karaman. Thermo-mechanical response and damping behavior of shape memory alloy–MAX phase composites. *Metallurgical and Materials Transactions A*, 45(5):2646–2658, 2014.

[14] Brian T Lester, Yves Chemisky, and Dimitris C Lagoudas. Transformation characteristics of shape memory alloy composites. *Smart Materials and Structures*, 20(9):094002, 2011.

[15] Edwin A Peraza-Hernandez, Darren J Hartl, and Richard J Malak Jr. Design and numerical analysis of an SMA mesh-based self-folding sheet. *Smart Materials and Structures*, 22(9):094008, 2013.

[16] Edwin Peraza-Hernandez, Darren Hartl, Edgar Galvan, and Richard Malak. Design and optimization of a shape memory alloy-based self-folding sheet. *Journal of Mechanical Design*, 135(11):111007, 2013.

[17] DJ Hartl, DC Lagoudas, FT Calkins, and JH Mabe. Use of a ni60ti shape memory alloy for active jet engine chevron application: I. thermomechanical characterization. *Smart Materials and Structures*, 19(1):015020, 2009.

[18] Robert Saunders, Darren Hartl, Richard Malak, and Dimitris Lagoudas. Design and analysis of a self-folding SMA-SMP composite laminate. In *ASME 2014 International Design Engineering Technical Conferences and Computers and Information in Engineering Conference*, pages V05BT08A048–V05BT08A048. American Society of Mechanical Engineers, 2014.

[19] Darren J Hartl, Dimitris C Lagoudas, and FT Calkins. Advanced methods for the analysis, design, and optimization of SMA-based aerostructures. *Smart Materials and Structures*, 20(9):094006, 2011.

[20] Toshimichi Ogisu, Norio Ando, Junji Takaki, Tomonaga Okabe, and Nobuo Takeda. Improved surface treatment of SMA foils and damage suppression of SMA-foil embedded CFRP laminates. *Journal of Intelligent Material Systems and Structures*, 12(4):265–270, 2001.

[21] Lucas FM Da Silva and RD Adams. Adhesive joints at high and low temperatures using similar and dissimilar adherends and dual adhesives. *International Journal of Adhesion and Adhesives*, 27(3):216–226, 2007.

[22] Lucas FM Da Silva and RD Adams. Joint strength predictions for adhesive joints to be used over a wide temperature range. *International Journal of Adhesion and Adhesives*, 27(5):362–379, 2007.

[23] Lucas FM Da Silva and RD Adams. Techniques to reduce the peel stresses in adhesive joints with composites. *International Journal of Adhesion and Adhesives*, 27(3):227–235, 2007.

[24] MD Banea, LFM da Silva, and RDSG Campilho. Mode II fracture toughness of adhesively bonded joints as a function of temperature: experimental and numerical study. *The Journal of Adhesion*, 88(4-6):534–551, 2012.

[25] MD Banea, LFM Da Silva, and RDSG Campilho. Mode I fracture toughness of adhesively bonded joints as a function of temperature: experimental and numerical study. *International Journal of Adhesion and Adhesives*, 31(5):273–279, 2011.

[26] MD Banea, LFM da Silva, and RDSG Campilho. Effect of temperature on tensile strength and mode I fracture toughness of a high temperature epoxy adhesive. *Journal of Adhesion Science and Technology*, 26(7):939–953, 2012.

[27] T Zimmerman, K Blohowiak, M Dilligan, F Calkins, and J Mabe. Adhesive bonding of hybrid actuated shape memory alloy-composite structures. In *Proc. SAMPE Fall Technical Conf.(Salt Lake City, UT, Oct.)*, pages 1–13, 2010.

[28] S Ucsnik, M Scheerer, S Zaremba, and DH Pahr. Experimental investigation of a novel hybrid metal–composite joining technology. *Composites Part A: Applied Science and Manufacturing*, 41(3):369–374, 2010.

[29] PT Cheuk, L Tong, CH Wang, A Baker, and P Chalkley. Fatigue crack growth in adhesively bonded composite-metal double-lap joints. *Composite Structures*, 57(1):109–115, 2002.

[30] H Chai. On the correlation between the mode I failure of adhesive joints and laminated composites. *Engineering Fracture Mechanics*, 24(3):413–431, 1986.

[31] Jin-Hwe Kweon, Jae-Woo Jung, Tae-Hwan Kim, Jin-Ho Choi, and Dong-Hyun Kim. Failure of carbon composite-to-aluminum joints with combined mechanical fastening and adhesive bonding. *Composite Structures*, 75(1):192–198, 2006.

[32] Glyn Lawcock, Lin Ye, Yiu-Wing Mai, and Chin-Teh Sun. The effect of adhesive bonding between aluminum and composite prepreg on the mechanical properties

of carbon-fiber-reinforced metal laminates. *Composites Science and Technology*, 57(1):35–45, 1997.

[33] RD Adams and PDRD Cawley. A review of defect types and nondestructive testing techniques for composites and bonded joints. *NDT International*, 21(4):208–222, 1988.

[34] A Baldan. Adhesion phenomena in bonded joints. *International Journal of Adhesion and Adhesives*, 38:95–116, 2012.

[35] Reinhold H Dauskardt, Mark Oliver, Anay Kamer, Jeffrey Yang, and Linying Wang. Interphase thermomechanical reliability and optimization for high-performance ti metal laminates. Technical report, DTIC Document, 2011.

[36] Dennis A Burianek and S Mark Spearing. Delamination growth from face sheet seams in cross-ply titanium/graphite hybrid laminates. *Composites Science and Technology*, 61(2):261–269, 2001.

[37] Ming-Hwa R Jen, Che-Kai Chang, and Yi-Chun Sung. Fabrication and mechanical properties of ti/apc-2 hybrid nanocomposite laminates at elevated temperatures. *Journal of Composite Materials*, page 0021998315599590, 2015.

[38] Jacob M Hundley, H Thomas Hahn, Jenn-Ming Yang, Andrew B Facciano, et al. Multi-scale modeling of metal-composite interfaces in titanium-graphite fiber metal laminates part i: Molecular scale. *Open Journal of Composite Materials*, 1(01):19, 2011.

[39] Shi-Jun Guo, Qing-Sheng Yang, XQ He, and KM Liew. Modeling of interface cracking in copper–graphite composites by md and cfe method. *Composites Part B: Engineering*, 58:586–592, 2014.

[40] Jacob M Hundley, H Thomas Hahn, Jenn-Ming Yang, and Andrew B Facciano. Three-dimensional progressive failure analysis of bolted titanium-graphite fiber metal laminate joints. *Journal of Composite Materials*, page 0021998310391047, 2010.

[41] Mark S Oliver, Kay Y Blohowiak, and Reinhold H Dauskardt. Molecular structure and fracture properties of zrox/epoxysilane hybrid films. *Journal of Sol-gel Science and Technology*, 55(3):360–368, 2010.

[42] P Molitor, V Barron, and T Young. Surface treatment of titanium for adhesive bonding to polymer composites: a review. *International Journal of Adhesion and Adhesives*, 21(2):129–136, 2001.

[43] Kay Y Blohowiak, Joseph H Osborne, and Kenneth A Krienke. Sol-gel coated metal, 1999. US Patent 5,939,197.

[44] Frank L Palmieri, Kent A Watson, Guillermo Morales, Thomas Williams, Robert Hicks, Christopher J Wohl, John W Hopkins, and John W Connell. Laser ablative surface treatment for enhanced bonding of ti-6al-4v alloy. *ACS Applied Materials & Interfaces*, 5(4):1254–1261, 2013.

[45] Frank L Palmieri, Allison Crow, Anna Zetterberg, John Hopkins, Christopher J Wohl, John W Connell, Tony Belcher, and Kay Y Blohowiak. Further investigation into the use of laser surface preparation of ti-6al-4v alloy for adhesive bonding. In *Proceedings of Society for the Advancement of Material and Process Engineering (SAMPE) Conference. Seattle, WA*, 2014.

[46] Ronald Krueger. A summary of benchmark examples to assess the performance of quasi-static delamination propagation prediction capabilities in finite element codes. *Journal of Composite Materials*, 2014.

[47] Ronald Krueger. An approach to assess delamination propagation simulation capabilities in commercial finite element codes. *NASA Technical Report*.

[48] Huiming Ning, Takeharu Iijima, Ning Hu, Yaolu Liu, Liangke Wu, Feng Liu, and Masahiro Arai. Investigation on mode-ii interface fracture toughness of cfrp/al laminates toughened by vgcf interleaves. *Journal of Materials Science*, 50(4):1915–1923, 2015.

[49] Huiming Ning, Yuan Li, Ning Hu, Masahiro Arai, Naoya Takizawa, Yaolu Liu, Liangke Wu, Jinhua Li, and Fuhao Mo. Experimental and numerical study on the improvement of interlaminar mechanical properties of al/cfrp laminates. *Journal of Materials Processing Technology*, 216:79–88, 2015.

[50] Qizhou Yao and Jianmin Qu. Interfacial versus cohesive failure on polymer-metal interfaces in electronic packagingeffects of interface roughness. *Journal of Electronic Packaging*, 124(2):127–134, 2002.

[51] SPM Noijen, Olaf van der Sluis, PHM Timmermans, and GQ Zhang. Numerical prediction of failure paths at a roughened metal/polymer interface. *Microelectronics Reliability*, 49(9):1315–1318, 2009.

[52] Won-Seock Kim, Kyoung-Hwan Kim, Chang-Jae Jang, Hee-Tae Jung, and Jung-Ju Lee. Micro-and nano-morphological modification of aluminum surface for adhesive bonding to polymeric composites. *Journal of Adhesion Science and Technology*, 27(15):1625–1640, 2013.

[53] Jason E Lincoln. *Structure-property-processing relationships and the effects of physical structure on the hygrothermal durability and mechanical response of polyimides*. PhD Dissertation, 2001.

[54] Peter A Gustafson and Anthony M Waas. Experiments and cohesive zone model parameters for t650/afr-pe-4/fm680-1 at high temperatures. *Journal of Aerospace Engineering*, 24(3):285–297, 2011.

[55] Karen S Whitley and Timothy J Collins. Mechanical properties of t650-35/afr-pe-4 at elevated temperatures for lightweight aeroshell designs. In *Proceedings of the 47th AIAA/ASME/ASCE/AHS/ASC SDM Conference*, pages 2006–2202, 2006.

[56] E Sacher. A relation between toughness and the dynamic mechanical properties of polymer films. *Journal of Applied Polymer Science*, 19(5):1421–1425, 1975.

[57] Delmar C Timm, Ayodeji J Ayorinde, and Ralph F Foral. Epoxy mechanical properties: function of crosslink architecture. *British Polymer Journal*, 17(2):227–232, 1985.

[58] Anthony C Comer, Douglass S Kalika, Brandon W Rowe, Benny D Freeman, and Donald R Paul. Dynamic relaxation characteristics of matrimid® polyimide. *Polymer*, 50(3):891–897, 2009.

[59] Wenli Qu, Tze-Man Ko, Rohit H Vora, and Tai-Shung Chung. Effect of polyimides with different ratios of para-to meta-analogous fluorinated diamines on relaxation process. *Polymer*, 42(15):6393–6401, 2001.

[60] JP Habas, J Peyrelasse, and MF Grenier-Loustalot. Rheological study of a high-performance polyimide. interpretation of the secondary mechanical relaxations of a nadimide crosslinked system. *High Performance Polymers*, 8(4):515–532, 1996.

[61] Zhenhua Sun, Lisong Dong, Yugang Zhuang, Linying Cao, Mengxian Ding, and Zhiliu Feng. Beta relaxation in polyimides. *Polymer*, 33(22):4728–4731, 1992.

[62] Corine Bas, Cécile Tamagna, Thierry Pascal, and N Dominique Alberola. On the dynamic mechanical behavior of polyimides based on aromatic and alicyclic dianhydrides. *Polymer Engineering & Science*, 43(2):344–355, 2003.

[63] Kevin P Menard. *Dynamic mechanical analysis: a practical introduction*. CRC Press, 2008.

[64] RF Boyer. Dependence of mechanical properties on molecular motion in polymers. *Polymer Engineering & Science*, 8(3):161–185, 1968.

[65] Roger J Morgan and Lawrence E Nielsen. The dynamic mechanical properties of polymers at cryogenic temperatures. *Journal of Macromolecular Science, Part B*, 9(2):239–253, 1974.

[66] J Heijboer. Secondary loss peaks in glassy amorphous polymers. *International Journal of Polymeric Materials*, 6(1-2):11–37, 1977.

[67] GP Johari. Secondary relaxations and the properties of glasses and liquids. In *Molecular Dynamics and Relaxation Phenomena in Glasses*, pages 90–112. Springer, 1987.

[68] AF Yee and SA Smith. Molecular structure effects on the dynamic mechanical spectra of polycarbonates. *Macromolecules*, 14(1):54–64, 1981.

[69] Raymond F Boyer. Mechanical motions in amorphous and semi-crystalline polymers. *Polymer*, 17(11):996–1008, 1976.

[70] Jessica A Schroeder, Patricia A Madsen, and Robert T Foister. Structure/property relationships for a series of crosslinked aromatic/aliphatic epoxy mixtures. *Polymer*, 28(6):929–940, 1987.

[71] C Park, SE Lowther, JG Smith, JW Connell, PM Hergenrother, and TL St Clair. Polyimide–silica hybrids containing novel phenylethynyl imide silanes as cou-

pling agents for surface-treated titanium alloy. *International Journal of Adhesion and Adhesives*, 20(6):457–465, 2000.

[72] Cheol Park, Sharon E Lowther, and Terry L St Clair. Surface treatment, February 18 2003. US Patent 6,521,052.

[73] Dimitris Lagoudas, Darren Hartl, Yves Chemisky, Luciano Machado, and Peter Popov. Constitutive model for polycrystaline shape memory alloys with smooth transformation surfaces. *International Journal of Plasticity*, pages 32–33, 2012.

[74] ASTM Standard. Standard guide for preparation of metal surfaces for adhesive bonding. *ASTM Standard D*, 2651, 2008.

[75] ASTM Standard. Standard test method for mode I interlaminar fracture toughness of unidirectional fiber-reinforced polymer matrix composites. *ASTM Standard D*, 5528, 2013.

[76] M Martinez, A Beltempo, M Yanishevsky, R Rutledge, and B Rocha. Load monitoring on shm platform 1a using luna technologies, distributed sensing fibre optic system. *National Research Council of Canada, Unclassified Lab Technical Report, LTR-SMPL-2012-0047*, 2012.

[77] D Favier, Y Liu, L Orgeas, Arnaud Sandel, L Debove, and P Comte-Gaz. Influence of thermomechanical processing on the superelastic properties of a ni-rich nitinol shape memory alloy. *Materials Science and Engineering: A*, 429(1):130–136, 2006.

[78] KWK Yeung, KMC Cheung, WW Lu, and CY Chung. Optimization of thermal treatment parameters to alter austenitic phase transition temperature of niti alloy for medical implant. *Materials Science and Engineering: A*, 383(2):213–218, 2004.

[79] MC Carroll, Ch Somsen, and G Eggeler. Multiple-step martensitic transformations in ni-rich niti shape memory alloys. *Scripta Materialia*, 50(2):187–192, 2004.

[80] ZG Wang and XT Zu. Incomplete transformation induced multiple-step transformation in tini shape memory alloys. *Scripta Materialia*, 53(3):335–339, 2005.

[81] ASTM Standard. Standard test method for measuring the dynamic mechanical properties of plastics using three-point bending. *ASTM Standard D*, 5023, 2015.

[82] Yuntao Li and Roger J Morgan. Thermal cure of phenylethynyl-terminated afr-pepa-4 imide oligomer and a model compound. *Journal of Applied Polymer Science*, 101(6):4446–4453, 2006.

[83] Philip J Launer. Infrared analysis of organosilicon compounds: spectra-structure correlations. *Silicone Compounds Register and Review*, 100, 1987.

[84] DR Anderson and A Lee Smith. Analysis of silicones. *ed. Smith, A. Lee, Wiley-Interscience, New York*, 1974.

[85] LJNY Bellamy. *The infra-red spectra of complex molecules*. Springer Science & Business Media, 2013.

[86] Leah M Johnson, Lu Gao, C Wyatt Shields IV, Margret Smith, Kirill Efimenko, Kevin Cushing, Jan Genzer, and Gabriel P López. Elastomeric microparticles for acoustic mediated bioseparations. *Journal of Nanobiotechnology*, 11(1):22, 2013.

[87] Michael W Czabaj and Barry D Davidson. Determination of the mode I, mode II, and mixed-mode I–II delamination toughness of a graphite/polyimide composite at room and elevated temperatures. *Journal of Composite Materials*, page 0021998315602945, 2015.

[88] Nidal Alif, Leif A Carlsson, and John W Gillespie. Mode I, mode II, and mixed mode interlaminar fracture of woven fabric carbon/epoxy. In *Composite Materials: Testing and Design, Thirteenth Volume*. ASTM International, 1997.

[89] Ryan J Sager, Patrick J Klein, Daniel C Davis, Dimitris C Lagoudas, Graham L Warren, and Hung-Jue Sue. Interlaminar fracture toughness of woven fabric composite laminates with carbon nanotube/epoxy interleaf films. *Journal of Applied Polymer Science*, 121(4):2394–2405, 2011.

[90] Hieu Thi Xuan Truong. Processing, characterization and modeling carbon nanotube modified interfaces in hybrid polymer matrix composites. Master's thesis, Texas A&M University, 2012.

[91] Youjiang Wang and Dongming Zhao. Characterization of interlaminar fracture behaviour of woven fabric reinforced polymeric composites. *Composites*, 26(2):115–124, 1995.

[92] M Kotaki and H Hamada. Effect of interfacial properties and weave structure on mode I interlaminar fracture behaviour of glass satin woven fabric composites. *Composites Part A: Applied Science and Manufacturing*, 28(3):257–266, 1997.

[93] BD Davidson, M Kumar, and MA Soffa. Influence of mode ratio and hygrothermal condition on the delamination toughness of a thermoplastic particulate interlayered carbon/epoxy composite. *Composites Part A: Applied Science and Manufacturing*, 40(1):67–79, 2009.

[94] Hieu TX Truong, Dimitris C Lagoudas, Ozden O Ochoa, and Khalid Lafdi. Fracture toughness of fiber metal laminates: Carbon nanotube modified ti–polymer–matrix composite interface. *Journal of Composite Materials*, 48(22): 2697-2710, 2014.

[95] Hieu Truong, Marcias Martinez, Ozden Ochoa, and Dimitris Lagoudas. Experimental and computational investigations of hybrid interfaces in hybrid composite laminates. In *American Society of Composites-30th Technical Conference*, 2015.

[96] Piyush R Thakre, Dimitris C Lagoudas, Jaret C Riddick, Thomas S Gates, Sarah-Jane V Frankland, James G Ratcliffe, Jiang John Zhu, and Enrique V Barrera. Investigation of the effect of single wall carbon nanotubes on interlaminar fracture toughness of woven carbon fiber-epoxy composites. *Journal of Composite Materials*, page 0021998310389088, 2011.

[97] Nidal Alif, Leif A Carlsson, and Louis Boogh. The effect of weave pattern and crack propagation direction on mode I delamination resistance of woven glass and carbon composites. *Composites Part B: Engineering*, 29(5):603–611, 1998.

[98] Isabelle Paris, Pierre J Minguet, and TK O'Brier. Comparison of delamination characterization for im7/8552 composite woven and tape laminates. In *Composite Materials: Testing and Design, Fourteenth Volume*. ASTM International, 2003.

[99] Roderick H Martin. Delamination characterization of woven glass/polyester composites. *Journal of Composites, Technology and Research*, 19(1):20–28, 1997.

[100] George T Hahn, RG Hoagland, M Kanninen, AR Rosenfield, and R Sejnoha. Fast fracture resistance and crack arrest in structural steels. Technical report, 1973.

[101] Robert C Wetherhold and James A Forand. Improving stability in the double-cantilever-beam fracture test. *Materials Science and Engineering: A*, 147(1):L17–L20, 1991.

[102] T Baxevanis, AF Parrinello, and DC Lagoudas. On the fracture toughness enhancement due to stress-induced phase transformation in shape memory alloys. *International Journal of Plasticity*, 50:158–169, 2013.

[103] S Timoshenko. Analysis of bi-metal thermostats. *JOSA*, 11(3):233–255, 1925.

[104] Jiong Liu, Manoj K Chaudhury, Douglas H Berry, Jill E Seebergh, Joseph H Osborne, and Kay Y Blohowiak. Fracture behavior of an epoxy/aluminum interface reinforced by sol–gel coatings. *Journal of Adhesion Science and Technology*, 20(4):277–305, 2006.

[105] Leif A Carlsson, Donald F Adams, and R Byron Pipes. *Experimental Characterization of Advanced Composite Materials*. CRC Press, 2002.

[106] RH Martin and BD Davidson. Mode II fracture toughness evaluation using four point bend, end notched flexure test. *Plastics, Rubber and Composites*, 28(8):401–406, 1999.

[107] Peter Davies, GD Sims, BRK Blackman, AJ Brunner, K Kageyama, M Hojo, K Tanaka, G Murri, C Rousseau, B Gieseke, et al. Comparison of test configurations for determination of mode II interlaminar fracture toughness results from international collaborative test programme. *Plastics, Rubber and Composites*, 28(9):432–437, 1999.

[108] Clara Schuecker and Barry D Davidson. Evaluation of the accuracy of the four-point bend end-notched flexure test for mode II delamination toughness determination. *Composites Science and Technology*, 60(11):2137–2146, 2000.

[109] Emile Smith Greenhalgh. *Characterisation of mixed-mode delamination growth in carbon-fibre composites*. PhD Dissertation, Imperial College London (University of London), 1998.

[110] M Kenane and ML Benzeggagh. Mixed-mode delamination fracture toughness of unidirectional glass/epoxy composites under fatigue loading. *Composites Science and Technology*, 57(5):597–605, 1997.

[111] ML Benzeggagh and M Kenane. Measurement of mixed-mode delamination fracture toughness of unidirectional glass/epoxy composites with mixed-mode bending apparatus. *Composites Science and Technology*, 56(4):439–449, 1996.

[112] Donato Girolamo. Progressive damage analysis of bonded composite joints. Master's thesis, TU Delft, 2012.

APPENDIX A

SYNTHESIS OF PHENYLETHYNYL IMIDE SILANE SURFACE TREATMENT SOLUTION

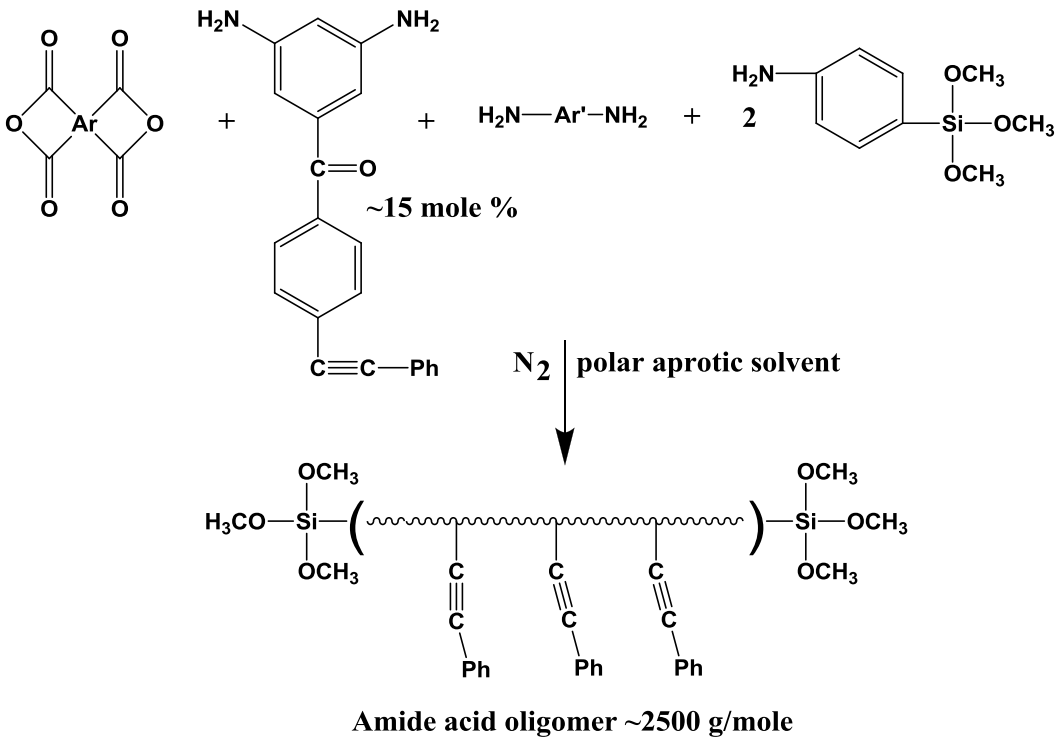

Figure A.1: Synthesis of amide acid oligomer

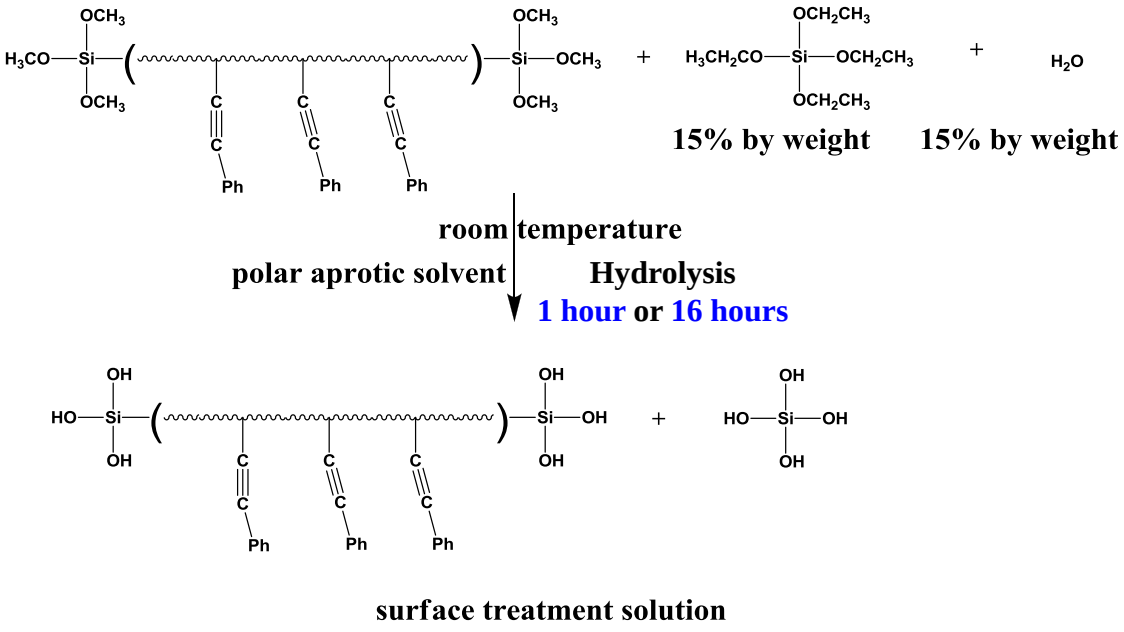

Figure A.2: Synthesis of phenylethynyl imide containing silane surface treatment solution

APPENDIX B

DIFFERENTIAL SCANNING CALORIMETRY ANALYSES ON THERMO-MECHANICALLY PROCESSED TI-50.8 AT%NI

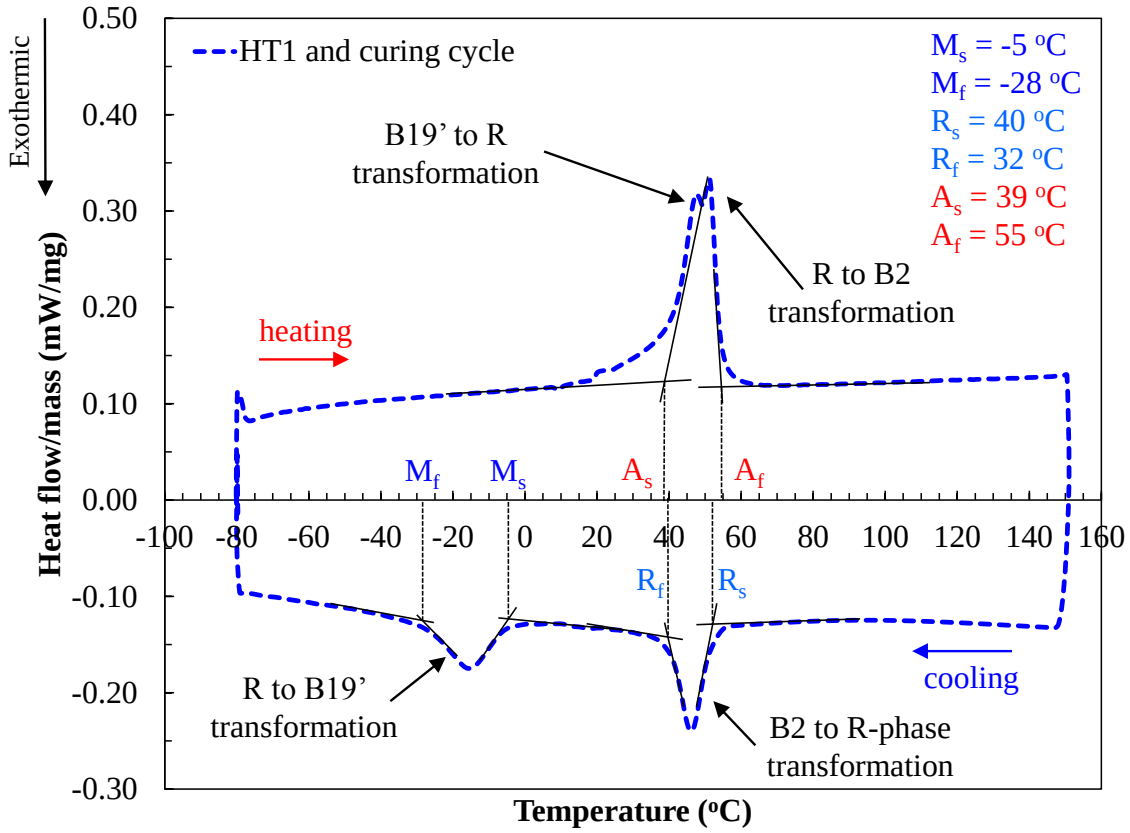

Figure B.1: DSC analysis of Ti-50.8 at%Ni foil after undergoing heat treatment 1 (aging for 30 min at 500 °C followed by water quenching) and curing cycle of T650-8HS/AFR-PE-4 laminates (illustrated in Figure 5.8).

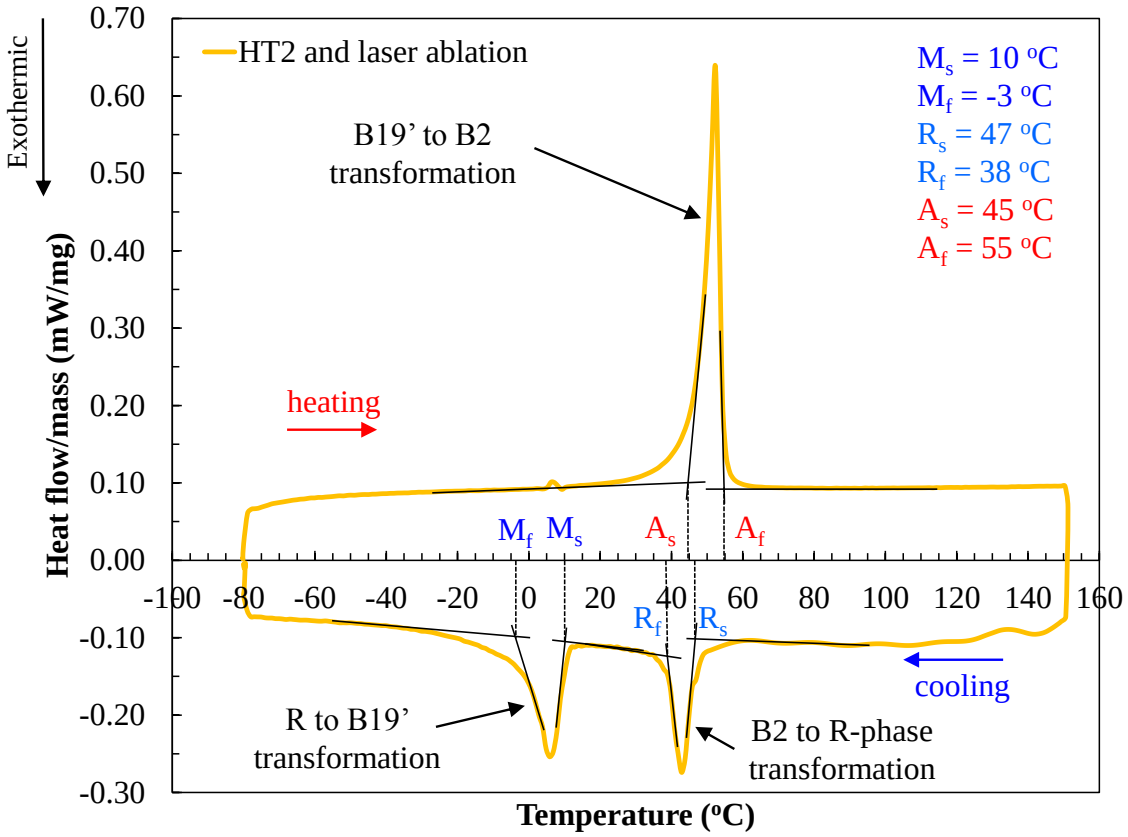

Figure B.2: DSC analysis of Ti-50.8 at%Ni foil after undergoing heat treatment 2 (aging for 1 hour at 500 °C and 45 min at 400°C followed by water quenching) and laser ablation on both surfaces.

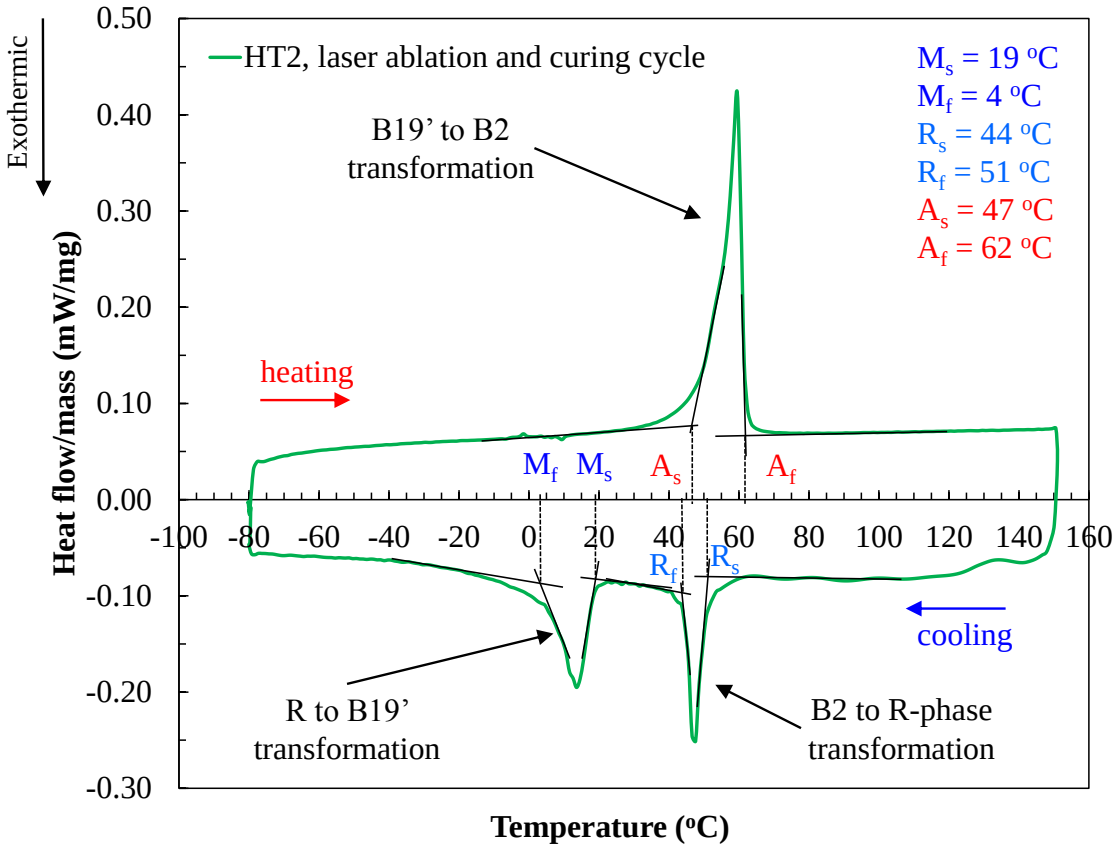

Figure B.3: DSC analysis of Ti-50.8 at%Ni foil after undergoing heat treatment 2, laser ablation on both surfaces, and curing cycle of T650-8HS/AFR-PE-4 laminates (illustrated in Figure 5.8).

APPENDIX C

ADDITIONAL RESULTS FROM DCB TESTS TI/NITI-AFR-PE-4 COMPOSITE

C.1 Ti-PEI-16hour

Load-displacement plots for all tested DCB specimens from AA-1hour panel.

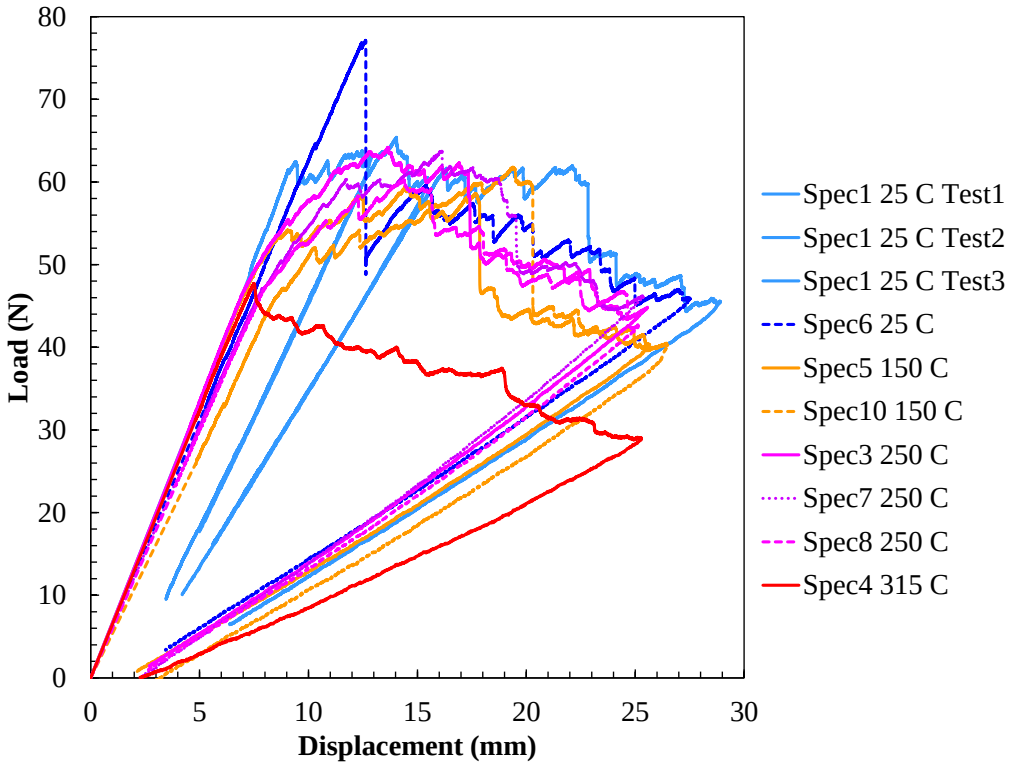

Figure C.1: Load-Displacement

C.2 Fracture Surfaces from Ti_EPII and Ti_AP DCB Tests

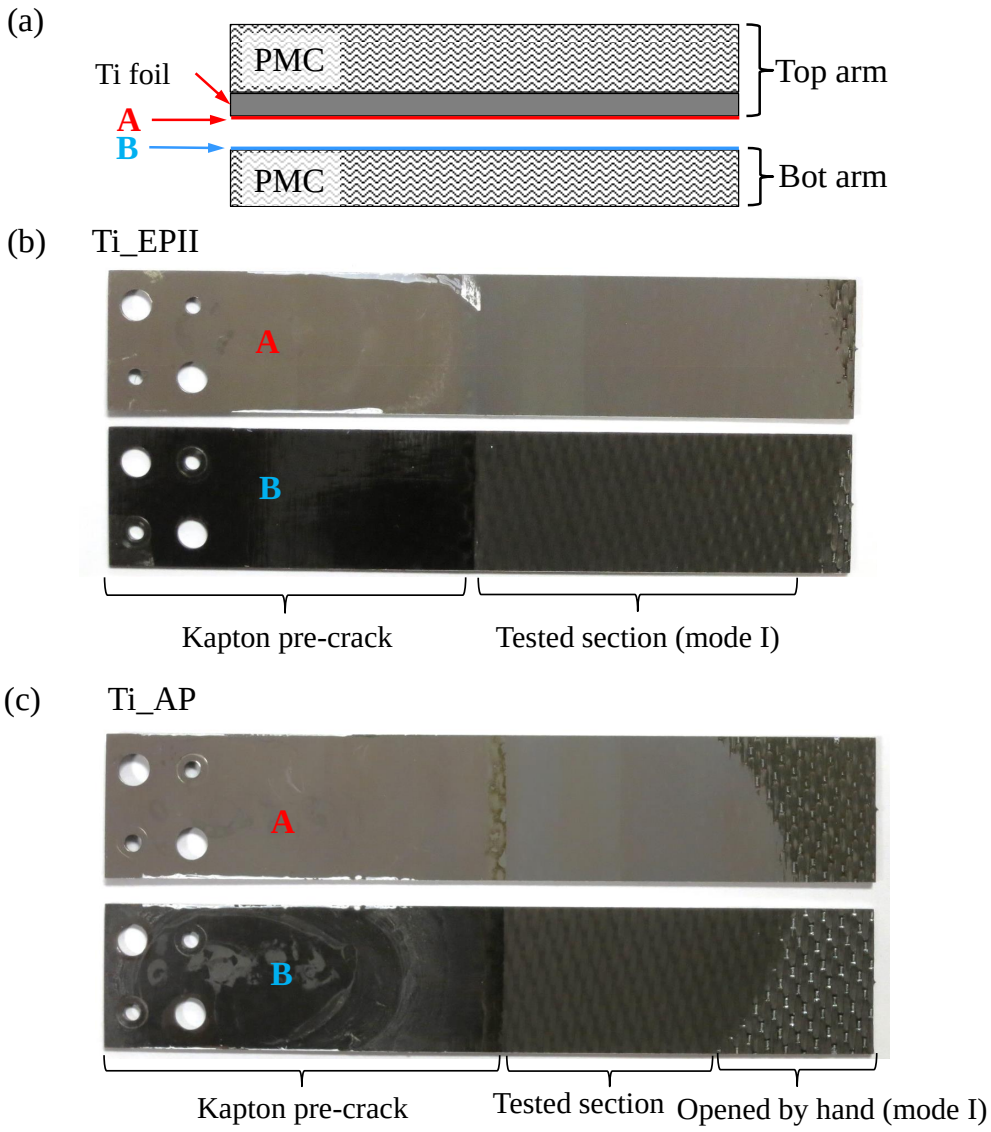

Figure C.2: (a) Schematic of tested DCB specimens and locations where fracture surfaces in (b) and (c) are shown. (b) Ti_EPII interface. (c) Ti_AP interface.

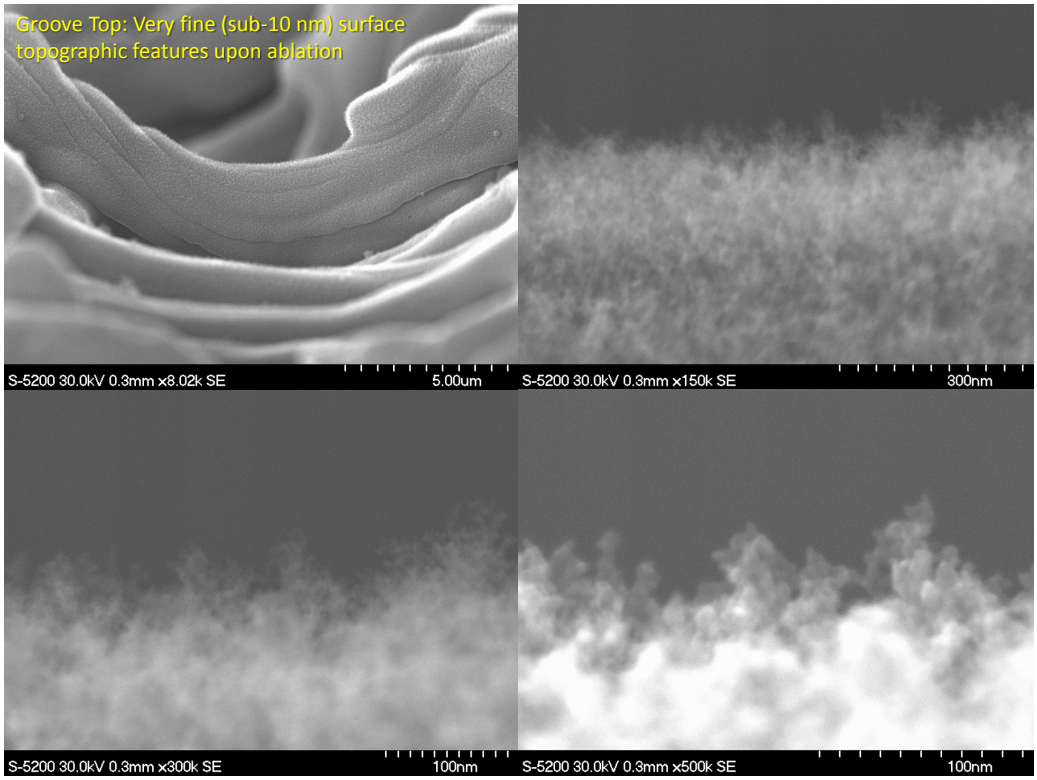

Figure C.3: High resolution SEM images of ablated Ti surface showing presence of porosities on the Ti surface after laser ablation (Courtesy of Dr. Yi Lin at NASA Langley Research Center, Hampton, VA).

APPENDIX D

ENGINEERING DRAWINGS FOR DCB SPECIMEN PREPARATION

D.1 DCB Tab Drilling

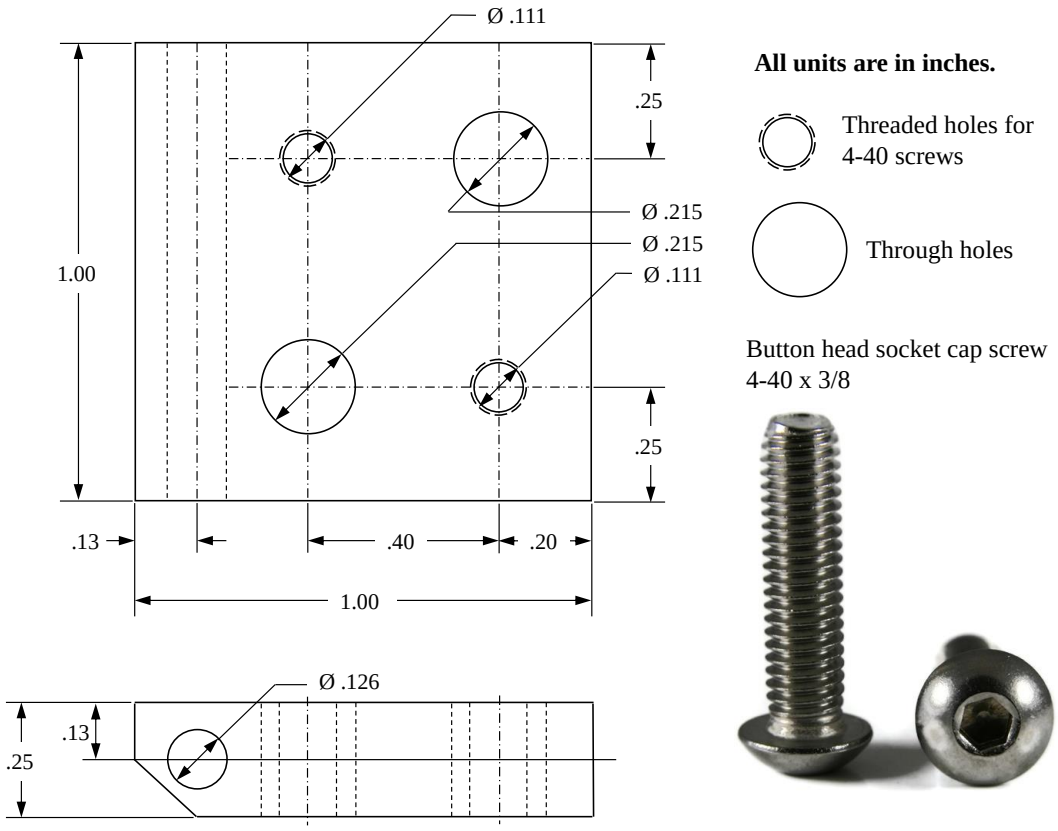

Figure D.1: Drawing for DCB tab drilling

D.2 DCB Specimen Drilling

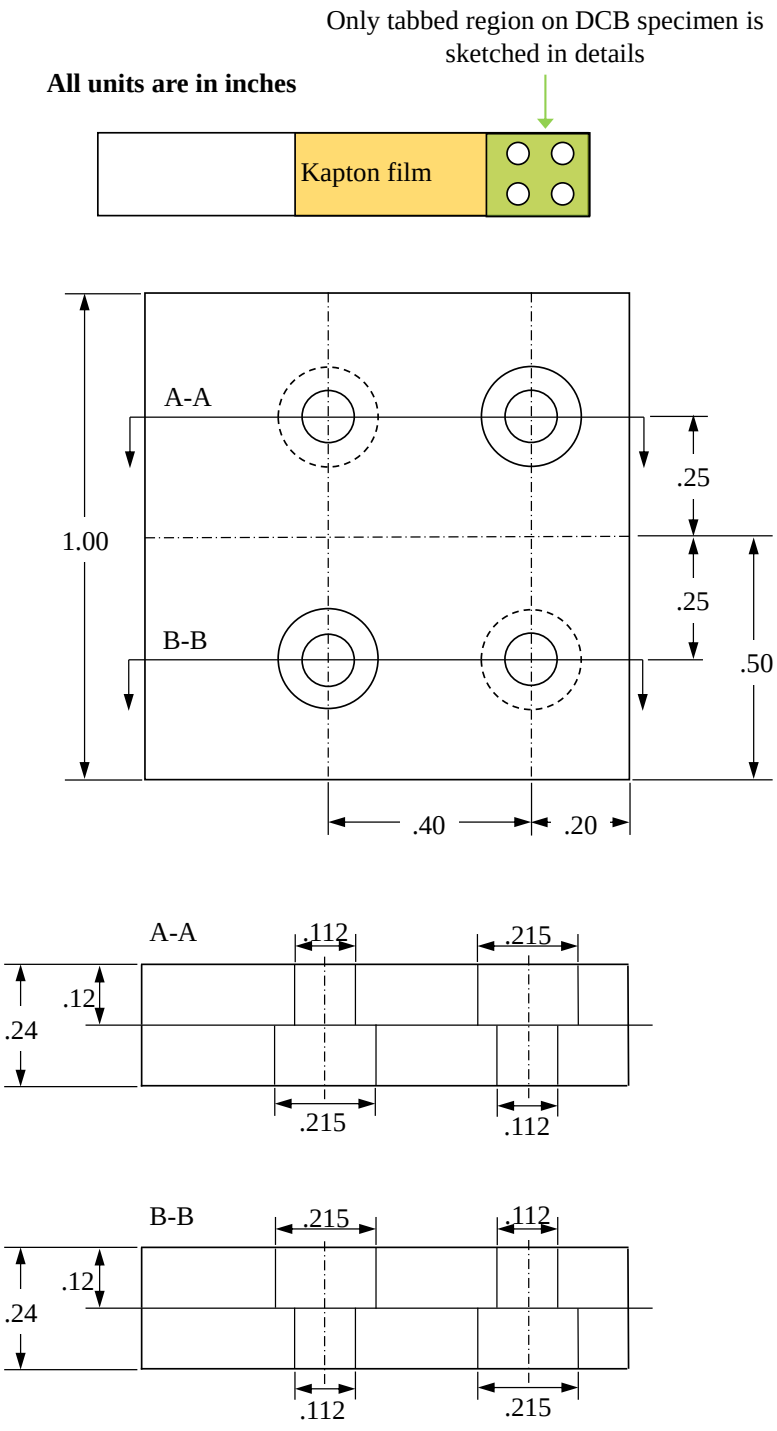

Figure D.2: Drawing for DCB specimen drilling